Volume 4 Issue 1 (2018) · ISSN 2424-7723

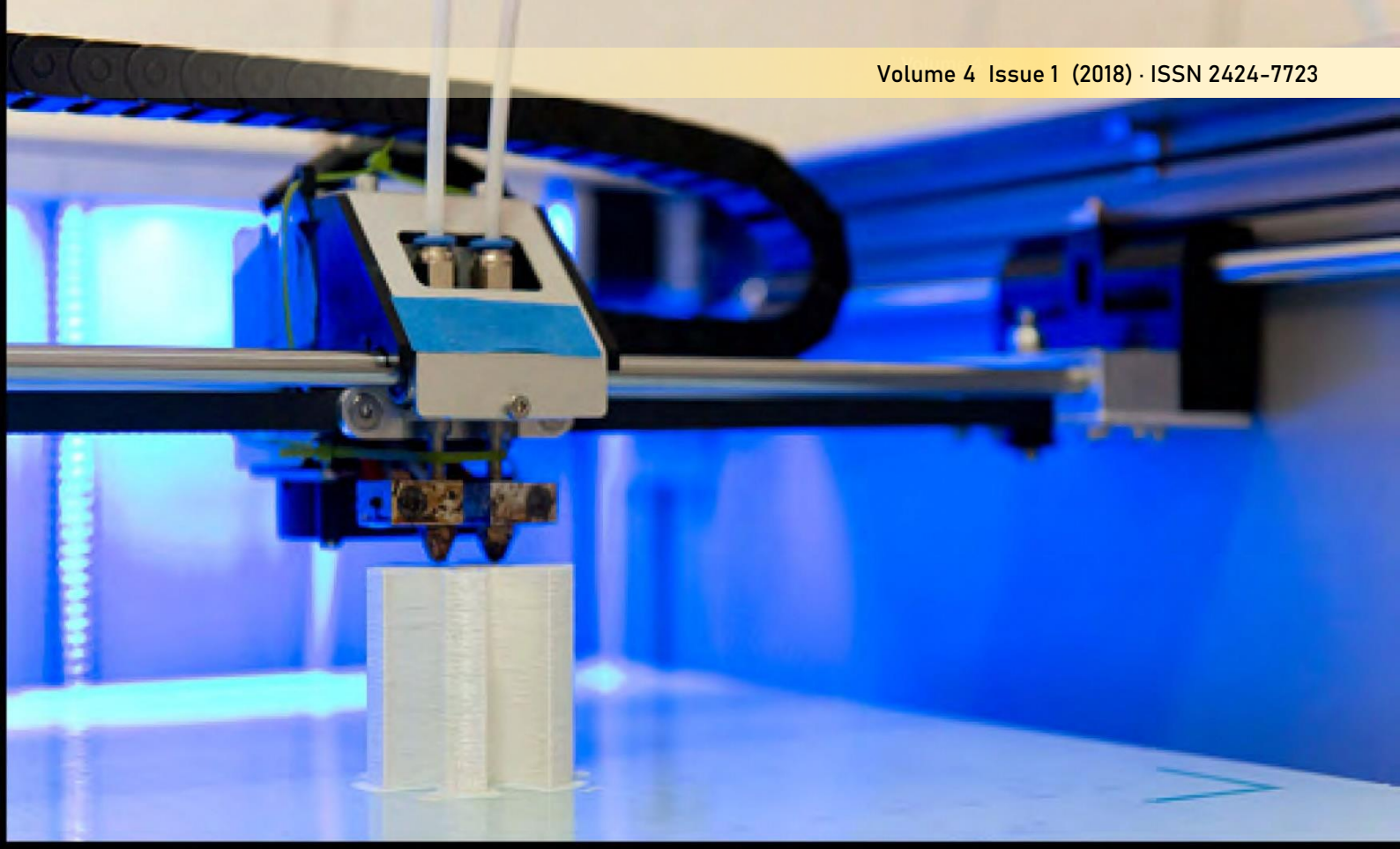

INTERNATIONAL JOURNAL OF BIOPRINTING

WHIOCE PUBLISHING PTE. LTD.
PROVIDING
FIRST-CLASS SCIENTIFIC INFORMATION
FOR TOP SCHOLARS

Volume 4 Issue 1 • 2018
ISSN 2424-7723 (print) ISSN 2424-8002 (online)

INTERNATIONAL JOURNAL OF BIOPRINTING

Editor-in-Chief
Chee Kai Chua
Nanyang Technological University, Singapore

WHIOCE PUBLISHING PTE. LTD.

Volume 4 | Issue 1 | 2018 |

International Journal of Bioprinting

https://ijb.whioce.com/index.php/int-j-bioprinting

CONTENTS

EDITORIAL

Call for 2nd Editorial Board Meeting: A milestone for IJB

Editor–in-Chief: Chee Kai Chua[1,2]

[1] Executive Director, Singapore Centre for 3D Printing, Singapore

[2] Professor, Manufacturing and Industrial Engineering Cluster, School of Mechanical and Aerospace Engineering, College of Engineering, Nanyang Technological University, Singapore

http://dx.doi.org/10.18063/IJB.v4i1.131.

Welcome to the year of 2018!

I am glad to announce that all papers published in IJB (since July 2015) are now indexed in Web of Science under the category of Emerging Sources Citation Index (ESCI). This will greatly increase the visibility of IJB, encourage future submissions and establish scientific impact. Meanwhile, IJB has been accepted for inclusion in Scopus since December 2017, the initiation of indexing process will take about three months. By March or April 2018, all papers published in IJB should be indexed in Scopus.

I am also glad to announce that the 3rd International Conference on Progress in Additive Manufacturing (PRO-AM) will be held at the Nanyang Technological University (NTU), Singapore on 14-17th May 2018. Prior to the conference, the 2nd Editorial Board Meeting of IJB will be held at the Singapore Centre for 3D Printing (within NTU) on the afternoon of 14th May. The main agenda are to hear and discuss the publisher's publication report on IJB and to make decisions on renewal of editorial board membership which is a 3-year contract. This meeting is a milestone for IJB because a new editorial board team will be formed to take care of the growing journal after its acceptance into both Web of Science and Scopus. It is a new era for IJB and many new challenges are ahead. We will make sure that IJB continues to perform in good hands. All in all, I am sincerely thankful to everyone who sees IJB as an added value to their publications.

This issue of IJB covers 1 review, 2 perspectives and 6 original research articles. Song presents recent advances in 3D printing of hydrogel composite systems for tissue engineering applications, with a focus on polymer- or hydrogel-hydrogel composites, particle-reinforced hydrogel composites, fiber-reinforced hydrogel composites, and anisotropic filler-reinforced hydrogel composites. While Lepowsky and Tasoglu argue that 3D printing for drug manufacturing is the future of pharmaceutical industries, owing to controlled release, personalised doses and on demand printing. Wang discusses recent progresses in organ 3D bioprinting and shares her perspective in this field. Shuai *et al*. reports an nMgO containing bone scaffold, which is antibacterial, degradable and biocompatible. Liang *et al*. present a coaxial nozzle-assisted electrohydrodynamic printing method to fabricate cell-laden 3D structures simultaneously with high resolution and high cell viability. Deng *et al*. discover that a corrosion resistant Mg alloy could be obtained for clinical applications when blending β-TCP with Mg-6Zn-1Zr (ZK60) and fabricating it using laser rapid solidification. Spriphutkiat *et al*. present how Standing Surface Acoustic Wave (SSAW) can be used to generate round shaped cell spheroids in a few minutes. Behbehani *et al*. show that 3D *in vitro* model can help evaluate the performance of different nerve guide conduits prior to animal testing.

PERSPECTIVE

3D printing for drug manufacturing: A perspective on the future of pharmaceuticals

Eric Lepowsky[1] and Savas Tasoglu[1,2,3,4,5*]

[1] Department of Mechanical Engineering, University of Connecticut, Storrs, CT, USA
[2] Department of Biomedical Engineering, University of Connecticut, Storrs, CT, USA
[3] Institute of Materials Science, University of Connecticut, Storrs, CT, USA
[4] Institute for Collaboration on Health, Intervention, and Policy, University of Connecticut, Storrs, CT, USA
[5] The Connecticut Institute for the Brain and Cognitive Sciences, University of Connecticut, Storrs, CT, USA

Abstract: Since a three-dimensional (3D) printed drug was first approved by the Food and Drug Administration in 2015, there has been a growing interest in 3D printing for drug manufacturing. There are multiple 3D printing methods – including selective laser sintering, binder deposition, stereolithography, inkjet printing, extrusion-based printing, and fused deposition modeling – which are compatible with printing drug products, in addition to both polymer filaments and hydrogels as materials for drug carriers. We see the adaptability of 3D printing as a revolutionary force in the pharmaceutical industry. Release characteristics of drugs may be controlled by complex 3D printed geometries and architectures. Precise and unique doses can be engineered and fabricated *via* 3D printing according to individual prescriptions. On-demand printing of drug products can be implemented for drugs with limited shelf life or for patient-specific medications, offering an alternative to traditional compounding pharmacies. For these reasons, 3D printing for drug manufacturing is the future of pharmaceuticals, making personalized medicine possible while also transforming pharmacies.

Keywords: three-dimensional (3D) printing; drug dosing and delivery; drug release characteristics; hydrogels; personalized medicine

*Correspondence to: Savas Tasoglu, Department of Biomedical Engineering and Department of Mechanical Engineering, University of Connecticut, Storrs, CT 06269, United States of America; savas.tasoglu@uconn.edu

Received: August 23, 2017; **Accepted:** September 18, 2017; **Published Online:** September 25, 2017

Citation: Lepowsky E and Tasoglu S, 2018, 3D printing for drug manufacturing: A perspective on the future of pharmaceuticals. *Int J Bioprint*, 4(1): 119. http://dx.doi.org/10.18063/IJB.v4i1.119

1. Introduction

Three-dimensional (3D) printing is an additive manufacturing method whereby successive layers of material are deposited/solidified to form a 3D structure. This technology has been applied in numerous fields, representing the large variety of possible applications, including the consumer goods industry[1], aerospace research[2,3], regenerative medicine[4–12], medical device development[13–19] and the automotive industry[20]. An emerging application of 3D printing is for drug manufacturing[21,22].

Interest in 3D printing of pharmaceutical products has been growing since the Food and Drug Administration (FDA) approved the first 3D printed drug in 2015[1,21]. Several methods and materials have since been investigated and demonstrated to serve this purpose[1,23–25]. Selective laser sintering (SLS) is the most analogous method to the common drug manufacturing process of powder pressing, in that it relies on loose powder that becomes joined into a solid object. Another powder-based method is binder deposition, in which a liquid binding solution is printed onto a bed of powder. Stereolithography, the selective solidification of a pool/bed of photosensitive material, may also be used for drug manufacturing. Inkjet printing offers high resolution

printing of viscous materials. Extrusion printing is another alternative method which is compatible with both viscous and solid materials. Furthermore, drug products can be printed using hydrogels or polymer-based filaments[1].

The rationales supporting the increasing research in 3D printing for drug manufacturing are noteworthy. In general, there is a demand for adaptability, a feature that is not often seen in pharmaceuticals[26]. This includes the ability to fabricate dosage forms with complex geometries and architectures, which directly correlates to increased complexity and control over release characteristics. The adaptability of 3D printing may also be applied for the precise and unique dosing of drugs, whereby drug doses can be printed with the safety of digital control. Additionally, multiple doses or multiple drugs can be printed together in a singular dosage form. Finally and importantly, 3D printing allows for drug products to be adapted for on-demand, prescription-specific production. The ability of on-the-spot drug fabrication will have major implications in emergency medicine and for medications with limited shelf-life[1]. Furthermore, 3D printing of drugs means that they can be manufactured for patients on an individualized basis. This capacity directly responds to the demand for individualized medicine and healthcare[1]. Patient-specific medicine entails the modification of drug dosing and combinations to meet the individual's needs. Conventional drug manufacturing methods lack the ability to fulfill this necessity, as they focus on large-scale batches[26]. There is little flexibility in the typical manufacturing process, requiring several steps which would be too difficult to tailor for a small batch. Conversely, 3D printing-based fabrication of drug products can be changed between prescriptions, also showing promise to transform pharmacy compounding.

Herein, we provide a case for the exploration of 3D printing for drug manufacturing. We first review 3D printing methods and materials that are applicable to drug manufacturing. Then, we elaborate on the benefits of this developing approach in pharmaceuticals, justifying why the FDA has encouraged continued development of 3D printed products[1,21]. We see the 3D printing of drug products as the next imminent revolution in the medicine and healthcare industries, and aim to demonstrate it as such.

2. Applicable 3D Printing Methods

For the purposes of printing drug products, we are concerned with 3D printing technology which utilizes bio-compatible materials that incorporate pharmaceutical elements. There are numerous 3D printing methods, many of which have previously been reported as adapted for bioprinting and drug manufacturing needs[23–25]. In particular, SLS (Figure 1A), binder deposition (Figure 1B), stereolithography (Figure 1C), inkjet printing

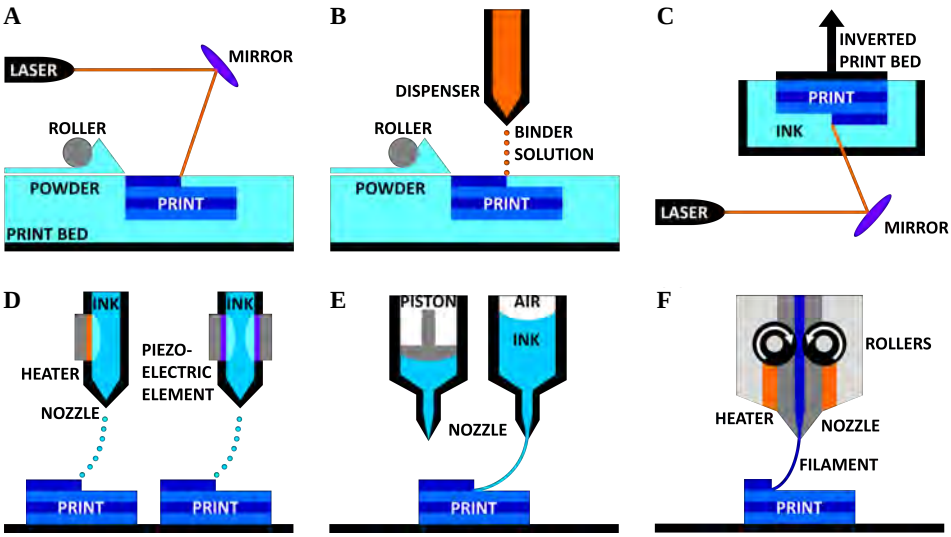

Figure 1. 3D printing methods for drug manufacturing. (**A**) Selective laser sintering. A laser is directed towards a bed of powder which is refilled by a roller system; the laser solidifies the powder to form the desired print. (**B**) Binder deposition. A binding solution is spotted onto a bed of powder which is refilled by a roller system; upon contact, the binder causes the powder to dissolve and re-crystalize. (**C**) Stereolithography. A laser is directed towards an inverted print bed which is submerged in a pool of photosensitive ink; the ink is cured and solidified by the laser. (**D**) Inkjet printing. On the left, a thermal inkjet nozzle uses a heating element to create a bubble in the continuous flow of ink, which generates a droplet. On the right, a piezoelectric element uses electrical pulses to create an acoustic wave which causes the formation of an air bubble, thereby generating a droplet. (**E**) Extrusion-based printing (of viscous materials). On the left, a piston is used to apply mechanical pressure to the ink to extrude a continuous stream. On the right, pneumatic pressure is applied from above to extrude the ink. (**F**) Fused deposition modeling (for solid materials). Solid filament is fed through the nozzle by rollers, then melted by heating elements within the nozzle, and extruded on the print bed.

(Figure 1D), and extrusion-based printing (Figures 1E and F) are ideal approaches for printing for drug manufacturing.

2.1 Powder-Based Printing

Powder-based printing methods are the most similar 3D printing method to the common drug manufacturing method of powder pressing, in which a bed of powder is pressed into a pre-fabricated mold. By the SLS method, a thermal-sensitive powder is spread over the build surface by a roller and pressed to form the appropriate layer thickness[27]. After the layer of powder is established, a laser supplies thermal energy to the powder to stimulate the melting and bonding of powder into the desired form[28]. This process of spreading powder followed by laser sintering is repeated for each successive layer. SLS also allows for partial sintering, and the encapsulation of non-sintered material within a sintered shell.

An additional powder-based method is binder deposition[29–31]. Following the same procedure for powder spreading, binder deposition is an additive method that builds from a bed of powder layers. Instead of a laser melting the powder as in SLS, a binder solution is spotted onto the powder. This binder solution dissolves the powder which then re-crystalizes to form the solid form. By this method, the drug ingredients may either be mixed in with the powder, or the drug may be mixed into the binder solution.

2.2 Stereolithography

Similar to SLS, stereolithography utilizes a laser or projector to solidify material while in a bulk setting. With stereolithography, also known more generally as photo-polymerization, the drug would be dissolved into a liquid pool of hydrogel or resin material[32,33]. The material of choice must be photosensitive. When the laser light shines onto the surface of the pool/bed of photosensitive, drug-loaded material, the material cures and solidifies. This method is extremely high resolution and considerably fast, but the nature of the pool of drug-loaded material has an inherent risk of cross-contamination between the fabrications of different drug products.

2.3 Inkjet Printing

Inkjet-based printing follows the same principles as a commercial inkjet printer for paper: ink is deposited onto a substrate by either a thermal-driven or piezoelectric-driven nozzle, offering high resolution printing capabilities. With the introduction of z-axis motion, 3D patterns may be fabricated by this method.

For the thermal inkjet printing approach, a thermal element within the print head generates droplets of ink. This heating element is electrically-controlled to cyclically produce brief spikes in thermal energy which is transferred to the ink[34]. The increase in thermal energy causes the formation of a small bubble, which provides a pulse of pressure to force ink out of the nozzle, thereby producing a droplet[4,35].

An alternative to thermal inkjet printing is the piezoelectric approach, which implements a piezoelectric actuator to form droplets. A piezoelectric crystal within the print head is stimulated when voltage is applied, which induces a rapid, reversible deformation[4]. This deformation propagates acoustic waves which supply the pulse of pressure needed to disrupt the flow of ink through the print head, thereby producing droplets.

The inkjet printing method can further be applied to microvalve-based 3D printing. Microvalve printing utilizes a motorized stage comprised of an array of microvalves which are capable of depositing droplets of material[36–38]. Each microvalve is connected to its own pressure regulator, allowing for individual control of each one. By controlling the stage and the pressure regulators in unison, various materials can be simultaneously deposited. This scheme has been previously applied to cell-laden bioprinting, whereby support material, growth media, and cell-laden material were printed together[37]. Microvalve-based 3D printing can be applied to drug fabrication by depositing various drug-loaded materials along with binders, scaffolds, and other biodegradable materials.

2.4 Extrusion-Based Printing

Extrusion-based printing entails the extrusion of a continuous stream of ink, as compared to the droplets which are formed *via* inkjet printing. By using this method, the substrate material is mixed with the drug of interest, and deposited by a nozzle or needle. The substrate may be a viscous liquid or a solid filament. Furthermore, advances in micro-extrusion allow for highly precise deposition of drug-loaded material for small-scale products[39].

3. Material Considerations

In discussing 3D printed pharmaceuticals, it is also important to consider the type of material – whether it be a powder, solid bulk, or liquefied substance – that is used to print the drug product[1]. SLS and binder deposition both require a powder substance. Compatible with extrusion-based printing, fused deposition modeling (FDM) relies on the extrusion of solid filaments loaded with the desired drug. Due to the reliance on solid polymer-based filaments, this method poses more challenges in making it appropriate for oral dosage medicines. Conversely, natural and synthetic hydrogels have a more viscous consistency that makes them more appropriate for oral drug products. Additionally, the

viscous nature of hydrogels allows for extrusion-based or inkjet-based printing. Finally, various forms of smart materials are described for drug delivery applications.

3.1 Materials for Powder-Based Printing

Materials used for powder-based printing methods must meet certain criteria for printability. With respect to binder deposition, the requirements and necessary parameters of the materials used are relatively straightforward. Factors that impact the printability include particle size, binder viscosity, droplet size of the binder solution, the concentration of the binder solutions, and the thickness of each powder layer[40]. The powder size must not be too small as to cause low flowability, nor may it be too large such that high density printed parts are not feasible. Additionally, the binder solution must be of low enough viscosity and high surface tension to precisely form small droplets, while also being able to penetrate the layer of powder. This is interdependent on the requirement that the powder layer be thin enough for binder saturation, but thick enough to prevent excessive binding. In most cases of binder deposition printing, the binder solution acts as a solvent for the powder, whereby the powder is dissolved upon contact with the binder[41,42]. The binder-powder mixture may either dry to form the solid part, or the materials may react to cause localized polymerization, curing or bonding. Examples of such powders may include soluble polymers, plastics and starches, while binders include chloroform and water, among other solvents.

Selective laser sintering has more complexity involved with material selection. Powders that have been previously studied include polyamides, poly-ε-caprolactone (PCL), hydroxyapatite (HA), polyethylene (PE) and poly(lactic acid) (PLA)[43–46]. By nature of SLS, a laser applies localized heat to selectively melt the powder where the laser strikes. To facilitate this process, the entire powder bed may be maintained at a temperature just below the melting point of the powder[27]. The powder material must withstand the elevated temperature of the print bed without degrading or agglomerating[47]. Ideally, the powder possesses a high melting point and a relatively lower glass transition temperature, which is often seen if the material exists as a semi-crystalline polymer at room temperature[28]. These thermal properties make the material suitable for printing at high temperatures. In the case of semi-crystalline polymers, the powder bed would be held at a temperature above the glass transition temperature, close to the melting point. At this state, the laser only needs to introduce enough energy to exceed the point of phase transition, while minimizing the temperature increase in the surrounding powder[47].

The powders used in SLS can range in particle size on the scale of microns to hundreds of microns[48]. For all particle sizes, the laser sintering causes the formation of necks between the particles; these necks, or linkages, remain small compared to the size of the particles themselves. This neck formation process is due to the surface heating of adjacent powder particles, and therefore is a function of particle size and shape, temperature, and the relative arrangement and density of particles. Particle size also contributes to another important material property, one which is shared with the binder deposition method: the flowability of the powder. Flowability refers to the ease of spreading precisely controlled layers of desired thickness; this parameter is directly related to the granulometry and morphology of the particles[47]. For instance, small particles at high density lead to lower flowability. On the other hand, high density powder is better suited for accuracy and strength of the sintered part. To balance these characteristics, particles are preferred to be near-spherical and flowability agents are often added[49].

3.2 Fused Deposition of Solid Materials

Fused deposition modeling (FDM) 3D printers are a specific category of extrusion-based printers which use a solid, polymer filament. The filament is fed through an electronically controlled nozzle which melts the filament and deposits it onto the print bed where the melted filament solidifies into the final 3D printed form. Such printers are simple and versatile, and are compatible with filaments such as poly(lactic acid) (PLA), poly(vinyl alcohol) (PVA), and ethylene vinyl acetate (EVA)[50–52]. Due to the polymer nature of the filaments, they exhibit considerable structural stability after printing and solidifying. These filaments are also largely water-soluble, and are capable of being loaded with a drug in solution. Filament can be loaded with varying concentrations of drugs for specified doses by dissolving the drug in an ethanolic solution and submerging the unprinted, solid filament in the solution[53,54]. Filament can also be loaded with drugs by melting the filament and re-solidifying it after the addition of the drugs[55]. Once the 3D printed drug product is placed *in vivo*, the drug itself will diffuse out of the print, while the biodegradable filament will dissolve over time.

3.3 Natural and Synthetic Hydrogels

As opposed to the solid nature of polymer-based filaments used in FDM printing, hydrogels are viscous and capable of being extruded or deposited as droplets *via* extrusion-based printing and inkjet-based printing, respectively. Implementing a controllable gelling hydrogel system, many layers of drug-loaded hydrogels can be printed into 3D structures, characterized by pores and channels which can be printed into the materials

according to programmable patterns[35]. Following printing, curing and soaking, the hydrogel patterns develop into water-swollen networks formed by the deposited hydrogel material[56–58]. These networks exhibit considerable porosity and high diffusion rates for various substances, and of particular interest is the ability to carry and release loaded drugs. Additionally, some hydrogels even respond to pH, temperature, or enzymatic activity, enabling controlled and targeted release of drugs[59–61].

Hydrogels may be formed with either naturally-derived or synthetic materials, each having nuanced properties and applications. Natural hydrogel materials include alginate, gelatin, agarose, fibrin and chitosan[57,62]. Synthetic materials include poly (ethylene glycol) (PEG), oligo(poly(ethylene glycol) fumarate) (OPF) and poly (acrylic acid) derivatives (PAA). PEG is a commonly used hydrogel material for drug delivery due to its non-toxic and non-adhesive properties, in addition to its compatibility with crosslinking which allows for more durable internal bonds to finalize the printed shape.

A more recent hydrogel contender in the field is gelatin methacryloyl (GelMA), which is an inexpensive biomaterial naturally derived from denatured collagen and chemically modified by the addition of a methacrylate group[63]. Similar to PEG, GelMA can be photo-crosslinked; when exposed to light in the presence of a photoinitiator, the methacrylate groups of the GelMA crosslink with each other, forming a gel. GelMA also exhibits the benefit of a temperature-dependent viscosity transition which makes it ideal for 3D printing. Furthermore, GelMA has been demonstrated as a drug delivery hydrogel by combining it with PAA, whereby the relative concentration of PAA controls the degree of and timing of drug release[64].

Pertaining to the formulation of all hydrogel materials, various parameters must be considered to achieve material properties suitable for high-resolution drug manufacturing. The type of crosslinking directly impacts the degradability and mechanical properties of the printed hydrogel[65–67]. Hydrogels can be chemically crosslinked – radical polymerization, reaction with complementary or end groups, and enzymatic activity – or physically crosslinked – crystallization, ionic interactions, hydrogen bonds, and protein interactions. Each form of crosslinking has varying levels of rigidity and degradability; stronger and greater numbers of bonds are associated with stronger printed products, but at the expense of lower degradability. For drug delivery application, the crosslinking bonds must be strong and plentiful enough to maintain the hydrogel for a given time period, but must also be weak and few enough to breakdown and degrade. In addition to the crosslinking, the combination of materials is also an important factor: multiple materials can be combined into a copolymer, in which case the relative ratios of each individual material tunes the final material properties[56,68,69]. Copolymers can also be utilized to control the drug release by leveraging hydrophobic and hydrophilic properties of both the individual hydrogel materials and of the added drug(s)[70,71]. For instance, the release of a hydrophilic drug can be controlled and slowed by embedding it within a hydrophobic hydrogel. An alternative example, a non-degrading hydrophobic hydrogel that has excellent thermo-mechanical properties can be modified to be biodegradable by the addition of hydrophilic material. Another consideration is the viscosity, surface tension, and temperature-dependent properties of hydrogels. These factors are crucial for finding or synthesizing materials that are appropriate for 3D printing[62,72]. A final limitation of practically all hydrogels that should be considered is the geometric precision during the 3D printing process. When printing drugs, accuracy is of utmost importance, yet due to the low viscosity during printing and the gelatinous consistency post-printing, accurately printing corners or small designs can be very difficult.

As for the loading of the drug into the hydrogel, two general methods have been presented: the printed hydrogel may be placed into a liquid medium saturated with the drug, or the drug may be pre-mixed into the hydrogel material[59]. These methods have been reported as diffusion and entrapment, respectively. Diffusion relies on the porosity of the hydrogel in order to take up and store the drug. Entrapment is more suitable for drugs with larger molecule sizes or for more careful and specific drug loading. Alternatively, drugs can also be directly deposited into the middle of a print, thereby entrapping the drug inside a hydrogel drug carrier. With both diffusion and entrapment, once the 3D printed drug-loaded hydrogel is placed *in vivo*, similar to a FDM-fabricated drug, the drug will diffuse out of the hydrogel network. The concentration gradient of the drug formed between the 3D print and the surrounding environment may cause an initial burst release or a triphasic release profile – burst release due to swelling and drugs eluted from the surface, followed by zero order release, and finished by a second phase of rapid release as the hydrogel degrades – dependent on various factors[59,73]. These factors include the size of the drug particles relative to the pore size of the hydrogel (if the drug is larger than the pores, diffusion is restricted, thereby reducing the burst release effect), the distribution of drug particles within the print (if the surface of the printed hydrogel contains a large concentration of the drug, a burst release is more likely), and whether the drug is loaded by mixing or bonding[58,73]. Herein lies another advantage of hydrogels over solid materials:

drugs can be covalently or physically linked to the hydrogel network to limit the drug's release, whereas this is impossible in FDM[74,75]. Drug release would only occur as the bond between the drug and hydrogel, or the hydrogel itself, degrades. It is important to note, though, that degradation of hydrogels often occurs primarily by bulk degradation, as opposed to surface degradation, due to high diffusion; surface erosion would be made possible by further modification and careful selection of the hydrogel materials[76–78].

3.4 Smart Materials for Drug Delivery

Drug delivery can greatly benefit from smart materials which are compatible with 3D printing. More specifically, smart materials of interest include shape memory materials and environment-stimulated materials such as pH- and temperature-sensitive materials. In general terms, degradable shape memory polymer (SMP) are multifunctional materials which are designed to conform to their therapeutically relevant shape and mechanical properties after implantation[79]. SMPs are considered active polymers, as they change from a temporary shape to their original, permanent shape upon exposure to a stimulus. This controllable, conformable change can be leveraged for drug delivery. Most commonly, the stimulus is in the form of a temperature change, *i.e.* the internal temperature of the human body compared to the outside temperature. pH-sensitive materials are also very useful in designing SMPs: due to the dependence on the physiological environment of the drug, pH sensitivity can act as a reversible switch for drug release as the drug form migrates through the body or as the environment changes in acidity/alkalinity[80]. Other possible stimuli include light, pressure, or a magnetic or electric field[81].

When considering the printing of SMPs, it is often referred to as four-dimensional (4D) printing, wherein the fourth dimension is time[82–85]. After 3D printing the drug form, the printed drug can change its shape or functionality when the external stimulus is applied. For instance, a drug form can be printed that has high surface area in its permanent shape but a compact, low surface area shape in its temporary shape; the drug would be ingested or implanted while in its compact shape, and once in the targeted location, external stimulus would cause the transformation to its high surface area shape to allow for high drug release rates.

Importantly, researchers have shown that the incorporation of drugs does not have a significant impact on the thermo-mechanical behavior and shape memory properties of the SMPs[86,87]. Furthermore, SMPs exhibiting biodegradability and zero-order drug release have also been developed[79,88]. By leveraging the elastic properties of particular SMPs combined with hydrophobic materials, SMPs can be designed to release drugs without an initial burst followed by hydrolytic degradation. Another exemplary implementation of SMPs is for double layer delivery systems[89]. A multilayer approach allows for finer tuning of drug release, while still maintaining the mechanical properties of an elastic material ideal for implantable applications. With a focus on drug eluting implants, SMP stents have been designed to perform a double duty: provide the mechanical function of an implantable stent while simultaneously delivery drugs[90]. By adding the drug eluting feature to SMPs, implants and stents can be designed with anti-inflammatory agents built-in[91].

4. Benefits of 3D printing for Drug Manufacturing

Once an appropriate 3D printing method is determined and the material best suited for the pharmaceutical application is selected, it is a matter of developing and printing the drug itself. It is at this stage in the drug manufacturing process where 3D printing presents itself as the ideal approach, attributed to some noteworthy benefits[92]. One of the primary considerations in the delivery of drugs is the release characteristics. 3D printing enables increased geometric and architectural complexity, facile fabrication of multi-layer delivery systems, and the application of various controlled release mechanisms. Printing as an approach for drug

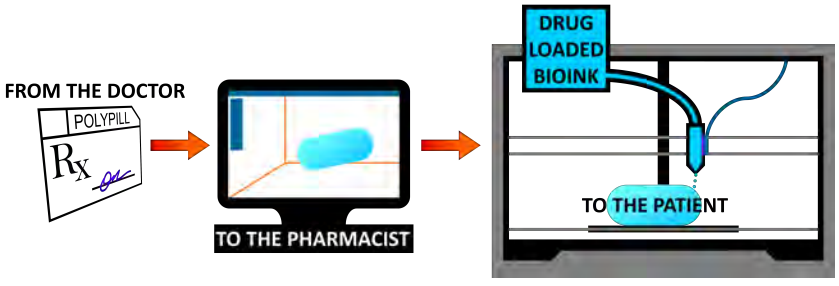

Figure 2. Theoretical scheme of 3D printing for drug manufacturing. Based on a patient's specific prescription from his doctor, a custom medication is designed *via* computer-aided design. The dosage form may be composed of complex geometries, multiple doses, or even multiple drugs. Drug-loaded bioink (biocompatible material) is then 3D printed on-demand.

manufacturing also introduces precise and unique dosing, and the ability to create multi-dose or multi-drug pharmaceutical products. Dosing may also be tailored specifically for individual patients. Similarly, the printing of drugs makes point-of-care, pharmacy-based drug production possible, without the risks and extensive fabrication time associated with compounding pharmacies. These benefits of 3D printing for drug manufacturing pave the way for the future of pharmaceuticals (Figure 2).

4.1 Release Characteristics of Drugs

The release characteristics of a drug refer to the quantity of the loaded drug that is emitted from the dosage form with respect to elapsed time. This has a significant impact on the application and relative effectiveness of the medication. One manner of manipulating the release characteristic of a drug is the geometric design and architectural complexity of the drug product. 3D printing is an ideal method for increasing the geometric and architectural complexity of dosage forms. 3D printing allows for custom-designed, discrete shapes to be fabricated, each with its own respective release timing. For instance, tablets of various shapes prepared with a constant surface area-to-volume ratio display different drug release rates, from fastest to slowest: sphere, cube, torus, cylinder and pyramid[93]. These findings are the result of drug diffusion and polymer dissolution[94,95]. The predominance of one of these factors over the other depends on the tablet shape and the solubility of the drug that is loaded in the tablet. This information can be leveraged with the capabilities of 3D printers to manufacture drugs with purposeful geometries for different release characteristics; in particular, by diverging away from typical spherical forms, 3D printing for drug manufacturing enables different and more precise drug delivery functions[96].

In addition to creating complex architectures of drug carriers, 3D printing is also capable of fabricating multi-layer delivery systems. Bilayer tablets are common for controlled release delivery systems, by incorporating instant-release and slow-release layers in the same dosage form. While bilayer tablets are not a novel pharmaceutical product, the ability to fabricate them in essentially a single step by means of a 3D printer may revolutionize the process[97]. Furthermore, controlling the release timing by printing the carrier in different shapes and densities may also contribute to greater control over burst release, which is the phenomenon of excess drug being released upon initial contact with the dissolution media[98].

A final and important consideration for the release characteristics of drugs is the material of the drug carrier. As described above, hydrogel is a great candidate for a 3D printing medium, as well as for a drug carrier. Hydrogels also exhibit a diverse range of controlled release functions[99]. As a material property, many hydrogels are biodegradable over time, which lends itself to taking advantage of polymer dissolution as a form of controlled release. Additionally, due to the high diffusion of hydrogels, they may also be leveraged for diffusion-controlled release and swelling-controlled release. Finally, hydrogels are also compatible with chemically-controlled release.

4.2 Precise and Unique Dosing

3D printing of drug products enables a newfound level of customization and personalization in drug dosing that is nearly impossible using typical commercial, mass-scale production methods. Presently, proper dosing is often imprecise, which can have costly results, in terms of both money and health[100]. While clinical pharmacology studies have been conducted to improve methods of drug dosing control and to help doctors prescribe the correct dose on a patient-to-patient basis, less work has focused on the production of the prescribed doses. 3D printing offers highly-precise fabrication, in addition to the capacity of unique dosing, all attributed to the free-form nature of 3D printing.

Exemplifying the application of 3D printing to provide precise dosing, a flexible-dose dispenser was developed that combines FDM 3D printing with hot melt extrusion (HME), which is a common pharmaceutical manufacturing process[101]. HME was implemented to produce drug-loaded filament by accurately mixing the drug with the filament material *via* a twin-screw compounder, thereby providing digital control over the concentration of drug melted into the filament. Following the HME process, the drug-loaded filament was used in a FDM printer to direct-write pharmaceutical tablets, which also introduces a high level of digital control through the design of the 3D printed tablets. Leveraging the linear relationship between the mass and volume of printed tablets, tablets of varying doses were able to be printed with high precision.

Digital control over drug dosing is not limited to FDM 3D printing; it has also been demonstrated with hydrogels which are compatible with inkjet printing. Following the deposition of drug-loaded hydrogel material, the hydrogel is cured by exposure to ultraviolet (UV) or near-UV light, which causes photo-initiator embedded within the material to crosslink. This photo-sensitive crosslinking may be utilized as a mean of digital drug dosing by using a projector to precisely cure a portion of the printed hydrogel[102]. The cured portion of the hydrogel forms the drug dose, while the uncured hydrogel can be washed away.

3D printing for drug manufacturing also advances

drug dosing by making multi-drug and multi-dose carriers not only possible, but simple to fabricate. So called "polypills" can be created by combining different drugs, materials with varying concentrations of the same or different drugs, and various materials with differing release characteristics into the same pill. 3D printing is the most effective and efficient method for accomplishing this[103,104]. Multiple drugs can be combined in a pill by printing with multiple filaments or inks, each loaded with a different drug. Likewise, multiple materials can be printed simultaneously to form a single pill comprising multiple release characteristics. These capacities come together to produce a myriad of possibilities, including, but not limited to: multiple layers, self-contained compartments, and inner-to-outer variation, each with either different doses or even different drugs. Such polypills made possible by 3D printing may very well be the future of precise and unique drug dosing.

4.3 On-Demand Capabilities

Point-of-care and pharmacy-based drug production may be the future of pharmaceuticals. 3D printing fulfills this niche portion of drug manufacturing. By implementing 3D printing as a fabrication method for pharmaceuticals, drugs can be on-demand in time-limited and resource-limited settings[1,105]. The on-demand capabilities are applicable to settings such as disaster relief, emergency and operating rooms, on board first response vehicles, or medical facilities for the military. Time is also a critical factor when fabricating and delivering low-stability drugs, which is another instance of an application for on-demand printing of drugs[97].

The printing of pharmaceutical products can also be implemented to produce drugs on-the-spot and in accordance with specific, individualized prescriptions, thereby revolutionizing pharmacy compounding[106]. Currently, patient-centered pharmaceuticals are limited to compounding pharmacies. Traditionally, pharmacy compounding is reserved for patients with special medical needs, offering custom medications which are not commercially available. In particular, pharmacists prepare small-scale batches based on individual prescriptions. However, the individual-centric practices of compounding pharmacies have associated risks[107].

Pharmacy compounding is traditionally reserved for cases in which a patient requires a dosage form, strength, or medicine cocktail that is not commercially available. In such cases, the risk-benefit ratio of using the compounded medicine is favorable for the patient[107]. However, the risk-benefit scale tips in the opposite direction for medications that have other more commercialized options. The reason for the variance in the merit of compounding is the inherit variability and likely imprecision involved in the pharmaceutical making process. Solving these potential risks is the precision of custom 3D printing drugs. Leveraging 3D printing's control over release characteristics of drugs and its ability to produce precise and unique doses, individualized medicine can provide prescription-based pharmaceutical products with the safety of digital control and the personalization of 3D printing.

5. Conclusion and Future Perspectives

Through this article, we have provided our perspective on the merits of 3D printing for drug manufacturing. Selective laser sintering, inkjet printing, and extrusion-based printing were presented as applicable 3D printing methods for drug manufacturing. Solid filament materials and natural and synthetic hydrogels were considered as possible materials for drug loading and printing. Various rationales for the 3D printing of drugs were also presented, including control over the release characteristics of drugs, the ability to print precise and unique doses, and the on-demand capabilities inherent with the printing approach.

3D printing for drug manufacturing represents the future of pharmaceuticals. While diverse industries across all of society are adopting 3D printing as a method for manufacturing, medicine and healthcare have yet to fully harness the capabilities of 3D printing for the direct-write fabrication of medications. With continued research, we believe personalized medicine will reach new levels of possibility, and pharmacies will be revolutionized by this particular application of 3D printing.

Conflict of Interest

No conflict of interest was reported by the authors.

Acknowledgments

S.T. acknowledges the American Heart Association Scientist Development Grant (15SDG25080056), Connecticut Innovations Biopipeline Award, and the University of Connecticut Research Excellence Program award for financial support of this research. S.T. is founder of, and have an equity interest in mBiotics, LLC, a company that is developing microfluidic technologies for point-of-care diagnostic solutions. S.T.'s interests were viewed and managed in accordance with the conflict of interest policies of the University of Connecticut. The authors have no other relevant affiliations or financial involvement with any organization or entity with a financial interest in or financial conflict with the subject matter or materials discussed in the manuscript apart from those disclosed.

References

1. Norman J, Madurawe R D, Moore C M V, *et al*., 2017, A new chapter in pharmaceutical manufacturing: 3D-printed drug products. *Adv Drug Deliv Rev*, 108(1): 39–50. http://doi.org/10.1016/j.addr.2016.03.001
2. Wong J Y and Pfahnl A C, 2014, 3D printing of surgical instruments for long-duration space missions. *Aviat Space Environ Med*, 85(7): 758–763. http://doi.org/10.3357/ASEM.3898.2014
3. Cesaretti G, Dini E, De Kestelier X, *et al*., 2014, Building components for an outpost on the Lunar soil by means of a novel 3D printing technology. *Acta Astronautica*, 93: 430–450. http://doi.org/10.1016/j.actaastro.2013.07.034
4. Murphy S V and Atala A, 2014, 3D bioprinting of tissues and organs. *Nat Biotechnol*, 32(8): 773–785. http://doi.org/10.1038/nbt.2958
5. Tasoglu S and Demirci U, 2013, Bioprinting for stem cell research. *Trends Biotechnol*, 31(1): 10–19. http://doi.org/10.1016/j.tibtech.2012.10.005
6. Park J H, Jang J, Lee J S, *et al*., 2017, Three-dimensional printing of tissue/organ analogues containing living cells. *Ann Biomed Eng*, 45(1): 180–194. http://doi.org/10.1007/s10439-016-1611-9
7. Lee V K and Dai G, 2017, Printing of three-dimensional tissue analogs for regenerative medicine. *Ann Biomed Eng*, 45(1): 115–131. http://doi.org/ 10.1007/s10439-016-1613-7
8. Knowlton S, Yenilmez B, Anand S, *et al*., 2017, Photocrosslinking-based bioprinting: Examining crosslinking schemes. *Bioprinting*, 5: 10–18. http://doi.org/10.1016/j.bprint.2017.03.001
9. Knowlton S, Yenilmez B and Tasoglu S, 2016, Towards single-step biofabrication of organs on a chip *via* 3D printing. *Trends Biotechnol*, 34(9): 685–688. http://doi.org/10.1016/j.tibtech.2016.06.005
10. Knowlton S, Joshi A, Yenilmez B, *et al*., 2016, Advancing cancer research using bioprinting for tumor-on-a-chip platforms. *Int J Bioprint*, 2(2): 3–8. http://doi.org/10.18063/IJB.2016.02.003
11. Knowlton S, Yu C H, Ersoy F, *et al*., 2016, 3D-printed microfluidic chips with patterned, cell-laden hydrogel constructs. *Biofabrication*, 8(2): 025019. http://doi.org/ 10.1088/1758-5090/8/2/025019
12. Knowlton S, Onal S, Yu C H, *et al*., 2015, Bioprinting for cancer research. *Trends Biotechnol*, 33(9): 504–513. http://doi.org/10.1016/j.tibtech.2015.06.007
13. Knowlton S M, Sencan I, Aytar Y, *et al*., 2015, Sickle cell detection using a smartphone. *Sci Rep*, 5: 15022. http://doi.org/10.1038/srep15022
14. Knowlton S, Yu C H, Jain N, *et al*., 2015, Smart-phone based magnetic levitation for measuring densities. *PLoS ONE*, 10(8): e0134400. http://doi.org/10.1371/journal.pone.0134400
15. Amin R, Knowlton S, Yenilmez B, *et al*., 2016, Smart-phone attachable, flow-assisted magnetic focusing device. *RSC Adv*, 6(96): 93922–93931. http://doi.org/10.1039/C6RA19483D
16. Amin R, Knowlton S, Hart A, *et al*., 2016, 3D-printed microfluidic devices. *Biofabrication*, 8(2): 022001. http://doi.org/10.1088/1758-5090/8/2/022001
17. Yenilmez B, Knowlton S, Yu C H, *et al*., 2016, Label-free sickle cell disease diagnosis using a low-cost, handheld platform. *Adv Mater Technol*, 1(5): 1600100. http://doi.org/10.1002/admt.201600100
18. Knowlton S, Joshi A, Syrrist P, *et al*., 2017, 3D-printed smartphone-based point of care tool for fluorescence- and magnetophoresis-based cytometry. *Lab Chip*, 17(16): 2839–51. http://doi.org/10.1039/C7LC00706J
19. Yenilmez B, Knowlton S and Tasoglu S, 2016, Self-contained handheld magnetic platform for point of care cytometry in biological samples. *Adv Mater Technol*, 1(9): 1600144. http://doi.org/10.1002/admt.201600144
20. Giffi C A, Gangula B and Illinda P, 2014, *3D opportunity for the automotive industry*. Deloitte University Press, New York.
21. Katstra W E, Palazzolo R D, Rowe C W, *et al*., 2000, Oral dosage forms fabricated by Three Dimensional Printing™. *J Control Release*, 66(1): 1–9. http://doi.org/10.1016/S0168-3659(99)00225-4
22. Ursan I D, Chiu L and Pierce A, 2013, Three-dimensional drug printing: A structured review. *J Am Pharm Assoc*, 53(2): 136–144. http://doi.org/http://dx.doi.org/10.1331/JAPhA.2013.12217
23. Chen C, Erkal J L, Gross B C, *et al*., 2014, Evaluation of 3D printing and its potential impact on biotechnology and the chemical sciences. *Anal Chem*, 86(7): 3240–3253. http://doi.org/10.1021/ac403397r
24. Singh M, Haverinen H M, Dhagat P, *et al*., 2010, Inkjet printing-process and its applications. *Adv Mater*, 22(6): 673–685. http://doi.org/10.1002/adma.200901141
25. Scoutaris N, Alexander M R, Gellert P R, *et al*., 2011, Inkjet printing as a novel medicine formulation technique. *J Control Release*, 156(2): 179–185. http://doi.org/10.1016/

j.jconrel.2011.07.033

26. Alhnan M A, Okwuosa T C, Sadia M, *et al*., 2016, Emergence of 3D printed dosage forms: Opportunities and challenges. *Pharm Res*, 33(8): 1817–1832. http://doi.org/10.1007/s11095-016-1933-1
27. Mazzoli A, 2013, Selective laser sintering in biomedical engineering. *Med Biol Eng Comput*, 51(3): 245–256. http://doi.org/10.1007/s11517-012-1001-x
28. Tan K H, Chua C K, Leong K F, *et al*., 2003, Scaffold development using selective laser sintering of polyetheretherketone-hydroxyapatite biocomposite blends. *Biomaterials*, 24(18): 3115–3123. http://doi.org/10.1016/S0142-9612(03)00131-5
29. Pardeike J, Strohmeier D M, Schrödl N, *et al*., 2011, Nanosuspensions as advanced printing ink for accurate dosing of poorly soluble drugs in personalized medicines. *Int J Pharm*, 420(1): 93–100. http://doi.org/10.1016/j.ijpharm.2011.08.033
30. Goole J and Amighi K, 2016, 3D printing in pharmaceutics: A new tool for designing customized drug delivery systems. *Int J Pharm*, 499(1–2): 376–394. http://doi.org/10.1016/j.ijpharm.2015.12.071
31. Sokolsky-Papkov M, Agashi K, Olaye A, *et al*., 2014, Polymer carriers for drug delivery in tissue engineering. *Adv Drug Deliv Rev*, 59(4–5): 187–206. http://doi.org/10.1016/j.addr.2007.04.001
32. Vehse M, Petersen S, Sternberg K, *et al*., 2014, Drug delivery from poly(ethylene glycol) diacrylate scaffolds produced by DLC based micro-stereolithography. *Macromol Symp*, 346(1): 43–47. http://doi.org/10.1002/masy.201400060
33. Xing J-F, Zheng M-L and Duan X-M, 2015, Two-photon polymerization microfabrication of hydrogels: An advanced 3D printing technology for tissue engineering and drug delivery. *Chem Soc Rev*, 44(15): 5031–5039. http://doi.org/10.1039/c5cs00278h
34. Xu T, Jin J, Gregory C, *et al*., 2005, Inkjet printing of viable mammalian cells. *Biomaterials*, 26(1): 93–99. http://doi.org/10.1016/j.biomaterials.2004.04.011
35. Boland T, Xu T, Damon B, *et al*., 2006, Application of inkjet printing to tissue engineering. *Biotechnol J*, 1(9): 910–917. http://doi.org/10.1002/biot.200600081
36. Horváth L, Umehara Y, Jud C, *et al*., 2015, Engineering an *in vitro* air-blood barrier by 3D bioprinting. *Sci Rep*, 5(1): 7974. http://doi.org/10.1038/srep07974
37. Ng W L, Wang S, Yeong W Y, *et al*., 2016, Skin bioprinting: Impending reality or fantasy? *Trends Biotechnol*, 34(9): 689–699. http://doi.org/10.1016/j.tibtech.2016.04.006
38. Lee W, Debasitis J C, Lee V K, *et al*., 2009, Multi-layered culture of human skin fibroblasts and keratinocytes through three-dimensional freeform fabrication. *Biomaterials*, 30(8): 1587–1595. http://doi.org/10.1016/j.biomaterials.2008.12.009
39. Panwar A and Tan L P, 2016, Current status of bioinks for micro-extrusion-based 3D bioprinting. *Molecules*, 21(6): 685. http://doi.org/10.3390/molecules21060685
40. Vaezi M and Chua C K, 2011, Effects of layer thickness and binder saturation level parameters on 3D printing process. *Int J Adv Manuf Technol*, 53(1–4): 275–284. http://doi.org/10.1007/s00170-010-2821-1
41. Lam C X F, Mo X M, Teoh S H, *et al*., 2002, Scaffold development using 3D printing with a starch-based polymer. *Mater Sci Eng C*, 20(1–2): 49–56. http://doi.org/10.1016/S0928-4931(02)00012-7
42. Giordano R A, Wu B M, Borland S W, *et al*., 1997, Mechanical properties of dense polylactic acid structures fabricated by three dimensional printing. *J Biomater Sci Polym Ed*, 8(1): 63–75. http://doi.org/10.1163/156856297X00588
43. Antonov E N, Bagratashvili V N, Whitaker M J, *et al*., 2005, Three-dimensional bioactive and biodegradable scaffolds fabricated by surface-selective laser sintering. *Adv Mater*, 17(3): 327–330. http://doi.org/10.1002/adma.200400838
44. Rimell J T and Marquis P M, 2000, Selective laser sintering of ultra high molecular weight polyethylene for clinical applications. *J Biomed Mater Res A*, 53(4): 414–420. http://doi.org/10.1002/1097-4636(2000)53:4<414::AID-JBM16>3.0.CO;2-M
45. Wiria F E, Leong K F, Chua C K, *et al*., 2007, Poly-ε-caprolactone/hydroxyapatite for tissue engineering scaffold fabrication *via* selective laser sintering. *Acta Biomater*, 3(1): 1–12. http://doi.org/10.1016/j.actbio.2006.07.008
46. Verbelen L, Dadbakhsh S, Van Den Eynde M, *et al*., 2016, Characterization of polyamide powders for determination of laser sintering processability. *Eur Polym J*, 75: 163–174. http://doi.org/10.1016/j.eurpolymj.2015.12.014
47. Drummer D, Rietzel D and Kühnlein F, 2010, Development of a characterization approach for the sintering behavior of new thermoplastics for selective laser sintering. *Phys Procedia*, 5(PART B): 533–542. http://doi.org/10.1016/j.phpro.2010.08.081
48. Gusarov A V, Laoui T, Froyen L, *et al*., 2003, Contact thermal conductivity of a powder bed in selective laser

sintering. *Int J Heat Mass Transf*, 46(6): 1103–9. http://doi.org/10.1016/S0017-9310(02)00370-8

49. Dupin S, Lame O, Barrès C, *et al*., 2012, Microstructural origin of physical and mechanical properties of polyamide 12 processed by laser sintering. *Eur Polym J*, 48(9): 1611–1621. http://doi.org/10.1016/j.eurpolymj.2012.06.007
50. Water J J, Bohr A, Boetker J, *et al*., 2015, Three-dimensional printing of drug-eluting implants: Preparation of an antimicrobial polylactide feedstock material. *J Pharm Sc*, 104(3): 1099–1107. http://doi.org/10.1002/jps.24305
51. Skowyra J, Pietrzak K and Alhnan M A, 2015, Fabrication of extended-release patient-tailored prednisolone tablets *via* fused deposition modelling (FDM) 3D printing. *Eur J Pharm Sci*, 68: 11–17. http://doi.org/10.1016/j.ejps.2014.11.009
52. Genina N, Hollander J, Jukarainen H, *et al*., 2016, Ethylene vinyl acetate (EVA) as a new drug carrier for 3D printed medical drug delivery devices. *Eur J Pharm Sci*, 90: 53–63. http://doi.org/10.1016/j.ejps.2015.11.005
53. Goyanes A, Buanz A B M, Basit A W, *et al*., 2014, Fused-filament 3D printing (3DP) for fabrication of tablets. *Int J Pharm*, 476(1): 88–92. http://doi.org/10.1016/j.ijpharm.2014.09.044
54. Goyanes A, Buanz A B M, Hatton G B, *et al*., 2015, 3D printing of modified-release aminosalicylate (4-ASA and 5-ASA) tablets. *Eur J Pharm Biopharm*, 89: 157–162. http://doi.org/10.1016/j.ejpb.2014.12.003
55. Okwuosa T C, Stefaniak D, Arafat B, *et al*., 2016, A lower temperature FDM 3D printing for the manufacture of patient-specific immediate release tablets. *Pharm Res*, 33(11): 2704–2712. http://doi.org/10.1007/s11095-016-1995-0
56. Ahmed E M, 2015, Hydrogel: Preparation, characterization, and applications: A review. *J Adv Res*, 6(2): 105–121. http://doi.org/10.1016/j.jare.2013.07.006
57. Drotleff S, Lungwitz U, Breunig M, *et al*., 2004, Biomimetic polymers in pharmaceutical and biomedical sciences. *Eur J Pharm Biopharm*, 58(2): 385–407. http://doi.org/10.1016/j.ejpb.2004.03.018
58. Hoare T R and Kohane D S, 2008, Hydrogels in drug delivery: Progress and challenges. *Polymer*, 49(8): 1993–2007. http://doi.org/10.1016/j.polymer.2008.01.027
59. Bhattarai N, Gunn J and Zhang M, 2010, Chitosan-based hydrogels for controlled, localized drug delivery. *Adv Drug Deliv Rev*, 62(1): 83–99. http://doi.org/10.1016/j.addr.2009.07.019
60. Qiu Y and Park K, 2012, Environment-sensitive hydrogels for drug delivery. *Adv Drug Deliv Rev*, 64(Supplement): 49–60. http://doi.org/10.1016/j.addr.2012.09.024
61. Gupta P, Vermani K and Garg S, 2002, Hydrogels: From controlled release to pH-responsive drug delivery. *Drug Discov Today*, 7(10): 569–579. http://doi.org/10.1016/S1359-6446(02)02255-9
62. Lee J M and Yeong W Y, 2016, Design and printing strategies in 3D bioprinting of cell-hydrogels: A review. *Adv Healthc Mater*, 5(22): 2856–2865. http://doi.org/10.1002/adhm.201600435
63. Yue K, Trujillo-de Santiago G, Alvarez M M, *et al*., 2015, Synthesis, properties, and biomedical applications of gelatin methacryloyl (GelMA) hydrogels. *Biomaterials*, 73: 254–271. http://doi.org/10.1016/j.biomaterials.2015.08.045
64. Serafim A, Tucureanu C, Petre D-G, *et al*., 2014, One-pot synthesis of superabsorbent hybrid hydrogels based on methacrylamide gelatin and polyacrylamide. Effortless control of hydrogel properties through composition design. *New J Chem*, 38(7): 3112–3126. http://doi.org/10.1039/c4nj00161c
65. Hennink W E and van Nostrum C F, 2012, Novel cross-linking methods to design hydrogels. *Adv Drug Deliv Rev*, 64(Supplement): 223–236. http://doi.org/10.1016/j.addr.2012.09.009
66. Berger J, Reist M, Mayer J M, *et al*., 2004, Structure and interactions in covalently and ionically crosslinked chitosan hydrogels for biomedical applications. *Eur J Pharm Biopharm*, 57(1): 19–34. http://doi.org/10.1016/S0939-6411(03)00161-9
67. Akhtar M F, Hanif M and Ranjha N M, 2016, Methods of synthesis of hydrogels … A review. *Saudi Pharm J*, 24(5): 554–559. http://doi.org/10.1016/j.jsps.2015.03.022
68. Yu L, Zhang Z, Zhang H, *et al*., 2009, Mixing a sol and a precipitate of block copolymers with different block ratios leads to an injectable hydrogel. *Biomacromolecules*, 10(6): 1547–1553. http://doi.org/10.1021/bm900145g
69. Peppas N A, Bures P, Leobandung W, *et al*., 2000, Hydrogels in pharmaceutical formulations. *Eur J Pharm Biopharm*, 50(1): 27–46. http://doi.org/10.1016/S0939-6411(00)00090-4
70. Qiao M, Chen D, Ma X, *et al*., 2005, Injectable biodegradable temperature-responsive PLGA-PEG-PLGA copolymers: Synthesis and effect of copolymer composition on the drug release from the copolymer-based hydrogels. *Int J Pharm*, 294(1–2): 103–112. http://doi.org/10.1016/j.ijpharm.2005.01.017

71. Molina I, Li S, Martinez M B, *et al*., 2001, Protein release from physically crosslinked hydrogels of the PLA/PEO/PLA triblock copolymer-type. *Biomaterials*, 22(4): 363–369. http://doi.org/10.1016/S0142-9612(00)00192-7
72. He Y, Yang F, Zhao H, *et al*., 2016, Research on the printability of hydrogels in 3D bioprinting. *Sci Rep*, 6: 29977. http://doi.org/10.1038/srep29977
73. Fu Y and Kao W J, 2010, Drug release kinetics and transport mechanisms of non-degradable and degradable polymeric delivery systems. *Expert Opin Drug Deliv*, 7(4): 429–444. http://doi.org/10.1517/17425241003602259
74. Duffy C V, David L and Crouzier T, 2015, Covalently-crosslinked mucin biopolymer hydrogels for sustained drug delivery. *Acta Biomater*, 20: 51–59. http://doi.org/10.1016/j.actbio.2015.03.024
75. Schoenmakers R G, van de Wetering P, Elbert D L, *et al*., 2004, The effect of the linker on the hydrolysis rate of drug-linked ester bonds. *J Control Release*, 95(2): 291–300. http://doi.org/10.1016/j.jconrel.2003.12.009
76. Shen W, Zhang K, Kornfield J A, *et al*., 2006, Tuning the erosion rate of artificial protein hydrogels through control of network topology. *Nat Mater*, 5(2): 153–158. http://doi.org/10.1038/nmat1573
77. Metters A T, Bowman C N and Anseth K S, 2000, A statistical kinetic model for the bulk degradation of PLA-*b*-PEG-*b*-PLA hydrogel networks. *J Phys Chem B*, 104(30): 7043–7049. http://doi.org/10.1021/jp000523t
78. Martens P, Metters A T, Anseth K S, *et al*., 2001, A generalized bulk-degradation model for hydrogel networks formed from multivinyl cross-linking molecules. *J Phys Chem B*, 105(22): 5131–5138. http://doi.org/10.1021/jp004102n
79. Wischke C, Neffe A T, Steuer S, *et al*., 2009, Evaluation of a degradable shape-memory polymer network as matrix for controlled drug release. *J Control Release*, 138(3): 243–250. http://doi.org/10.1016/j.jconrel.2009.05.027
80. Chen H, Li Y, Liu Y, *et al*., 2014, Highly pH-sensitive polyurethane exhibiting shape memory and drug release. *Polym Chemi*, 5(17): 5168–5174. http://doi.org/10.1039/C4PY00474D
81. Wang K, Strandman S and Zhu X X, 2017, A mini review: Shape memory polymers for biomedical applications. *Front Chem Sci Eng*, 11(2): 1–11. http://doi.org/10.1007/s11705-017-1632-4
82. Sydney Gladman A, Matsumoto E A, Nuzzo R G, *et al*., 2016, Biomimetic 4D printing. *Nat Mater*, 15(4): 413–418. http://doi.org/10.1038/nmat4544
83. Bakarich S E, Gorkin R III, in het Panhuis M , *et al*., 2015, 4D printing with mechanically robust, thermally actuating hydrogels. *Macromol Rapid Commun*, 36(12): 1211–1217. http://doi.org/10.1002/marc.201500079
84. Ge Q, Sakhaei A H, Lee H, *et al*., 2016, Multimaterial 4D printing with tailorable shape memory polymers. *Sci Rep*, 6: 31110. http://doi.org/10.1038/srep31110
85. Gao B, Yang Q, Zhao X, *et al*., 2016, 4D bioprinting for biomedical applications. *Trends Biotechnol*, 34(9): 746–756. http://doi.org/10.1016/j.tibtech.2016.03.004
86. Neffe A T, Hanh B D, Steuer S, *et al*., 2009, Polymer networks combining controlled drug release, biodegradation, and shape memory capability. *Adv Mater*, 21(32–33): 3394–3398. http://doi.org/10.1002/adma.200802333
87. Nagahama K, Ueda Y, Ouchi T, *et al*., 2009, Biodegradable shape-memory polymers exhibiting sharp thermal transitions and controlled drug release. *Biomacromolecules*, 10(7): 1789–1794. http://doi.org/10.1021/bm9002078
88. Kashif M, Yun B M, Lee K S, *et al*., 2016, Biodegradable shape-memory poly(ε-caprolactone)/polyhedral oligomeric silsequioxane nanocomposites: Sustained drug release and hydrolytic degradation. *Mater Lett*, 166: 125–128. http://doi.org/10.1016/j.matlet.2015.12.051
89. Musiał-Kulik M, Kasperczyk J, Smola A, *et al*., 2014, Double layer paclitaxel delivery systems based on bioresorbable terpolymer with shape memory properties. *Int J Pharm*, 465(1–2): 291–298. http://doi.org/10.1016/j.ijpharm.2014.01.029
90. Wache H M, Tartakowska D J, Hentrich A, *et al*., 2003, Development of a polymer stent with shape memory effect as a drug delivery system. *J Mater Sci Mater Med*, 14(2): 109–112. http://doi.org/10.1023/A:1022007510352
91. Xiao Y, Zhou S, Wang L, *et al*., 2010, Crosslinked poly(ε-caprolactone)/poly(sebacic anhydride) composites combining biodegradation, controlled drug release and shape memory effect. *Compos B Eng*, 41(7): 537–542. http://doi.org/10.1016/j.compositesb.2010.07.001
92. Banks J, 2013, Adding value in additive manufacturing: Researchers in the United Kingdom and Europe look to 3D printing for customization. *IEEE Pulse*, 4(6): 22–26. http://doi.org/10.1109/MPUL.2013.2279617
93. Goyanes A, Robles Martinez P, Buanz A, *et al*., 2015, Effect of geometry on drug release from 3D printed tablets. *Int J Pharm*, 494(2): 657–663. http://doi.org/10.1016/j.ijpharm.2015.04.069

94. Reynolds T D, Mitchell S A and Balwinski K M, 2002, Investigation of the effect of tablet surface area/volume on drug release from hydroxypropylmethylcellulose controlled-release matrix tablets. *Drug Dev Ind Pharm*, 28(4): 457–466. http://doi.org/10.1081/DDC-120003007

95. Kamaly N, Yameen B, Wu J, *et al*., 2016, Degradable controlled-release polymers and polymeric nanoparticles: Mechanisms of controlling drug release. *Chem Rev*, 116(4): 2602–2663. http://doi.org/10.1021/acs.chemrev.5b00346

96. Lee B K, Yun Y H, Choi J S, *et al*., 2012, Fabrication of drug-loaded polymer microparticles with arbitrary geometries using a piezoelectric inkjet printing system. *Int J Pharm*, 427(2): 305–310. http://doi.org/10.1016/j.ijpharm.2012.02.011

97. Khaled S A, Burley J C, Alexander M R, *et al*., 2014, Desktop 3D printing of controlled release pharmaceutical bilayer tablets. *Int J Pharm*, 461(1–2): 105–111. http://doi.org/10.1016/j.ijpharm.2013.11.021

98. Huang X and Brazel C S, 2001, On the importance and mechanisms of burst release in matrix-controlled drug delivery systems. *J Control Release*, 73(2–3): 121–136. http://doi.org/10.1016/S0168-3659(01)00248-6

99. Lin C C and Metters A T, 2006, Hydrogels in controlled release formulations: Network design and mathematical modeling. *Adv Drug Deliv Rev*, 58(12–13): 1379–1408. http://doi.org/10.1016/j.addr.2006.09.004

100. Bailey J M and Haddad W M, 2005, Drug dosing control in clinical pharmacology. *IEEE Control Syst Mag*, 25(2): 35–51. http://doi.org/10.1109/MCS.2005.1411383

101. Pietrzak K, Isreb A and Alhnan M A, 2015, A flexible-dose dispenser for immediate and extended release 3D printed tablets. *Eur J Pharm Biopharm*, 96: 380–387. http://doi.org/10.1016/j.ejpb.2015.07.027

102. Faralli A, Melander F, Larsen E K U, *et al*., 2014, Digital drug dosing: Dosing in drug assays by light-defined volumes of hydrogels with embedded drug-loaded nanoparticles. In Proceedings of the 2nd IEEE EMBS Micro and Nanotechnology in Medicine Conference.

103. Khaled S A, Burley J C, Alexander M R, *et al*., 2015, 3D printing of five-in-one dose combination polypill with defined immediate and sustained release profiles. *J Control Release*, 217: 308–314. http://doi.org/10.1016/j.jconrel.2015.09.028

104. Khaled S A, Burley J C, Alexander M R, *et al*., 2015, 3D printing of tablets containing multiple drugs with defined release profiles. *Int J Pharm*, 494(2): 643–650. http://doi.org/10.1016/j.ijpharm.2015.07.067

105. Srai J S, Badman C, Krumme M, *et al*., 2015, Future supply chains enabled by continuous processing-opportunities and challenges May 20–21, 2014 Continuous Manufacturing Symposium. *J Pharm Sci*, 104(3): 840–849. http://doi.org/10.1002/jps.24343

106. Alomari M, Mohamed F H, Basit A W, *et al*., 2015, Personalised dosing: Printing a dose of one's own medicine. *Int J Pharm*, 494(2): 568–577. http://doi.org/10.1016/j.ijpharm.2014.12.006

107. Gudeman J, Jozwiakowski M, Chollet J, *et al*., 2013, Potential risks of pharmacy compounding. *Drugs R D*, 13(1): 1–8. http://doi.org/10.1007/s40268-013-0005-9

REVIEW ARTICLE

Progress in organ 3D bioprinting

Fan Liu[1,2], Chen Liu[1], Qiuhong Chen[1], Qiang Ao[1], Xiaohong Tian[1], Jun Fan[1], Hao Tong[1], Xiaohong Wang[1,3*]

[1] Department of Tissue Engineering, Center of 3D Printing and Organ Manufacturing, School of Fundamental Sciences, China Medical University (CMU), Shenyang, China
[2] Department of Orthodontics, School of Stomatology, China Medical University, Shenyang, China
[3] Center of Organ Manufacturing, Department of Mechanical Engineering, Tsinghua University, Beijing, P.R. China

Abstract: Three dimensional (3D) printing is a hot topic in today's scientific, technological and commercial areas. It is recognized as the main field which promotes "the Third Industrial Revolution". Recently, human organ 3D bioprinting has been put forward into equity market as a concept stock and attracted a lot of attention. A large number of outstanding scientists have flung themselves into this field and made some remarkable headways. Nevertheless, organ 3D bioprinting is a sophisticated manufacture procedure which needs profound scientific/technological backgrounds/knowledges to accomplish. Especially, large organ 3D bioprinting encounters enormous difficulties and challenges. One of them is to build implantable branched vascular networks in a predefined 3D construct. At present, organ 3D bioprinting still in its infancy and a great deal of work needs to be done. Here we briefly overview some of the achievements of 3D bioprinting technologies in large organ, such as the bone, liver, heart, cartilage and skin, manufacturing.

Keywords: organ; 3D bioprinting; bone; heart; liver; cartilage; skin

*Corresponding to: Xiaohong Wang, Center of Organ Manufacturing, Department of Mechanical Engineering, Tsinghua University, Beijing 100084, P.R. China; wangxiaohong709@163.com; wangxiaohong@tsinghua.edu.cn

Received: October 16, 2017; **Accepted:** December 1, 2017; **Published Online:** January 9, 2018

Citation: Liu F, Liu C, Chen Q H, *et al.*, 2018, Progress in organ 3D bioprinting, *Int J Bioprint*, 4(1): 128. http://dx.doi.org/10.18063/IJB.v4i1.128

1. Introduction

It is widely believed that there are 79 organs in the human body[1]. Each of the organs consists of different tissues. Most of the tissues in the organs have heterogeneous structures that confers one or more highly-specific functions. Organs can be divided into several groups, such as sensory, internal and structural, according to their main functions[2]. The sensory organs include the eyes, nose, ears and tongue. The internal organs (also known as viscera) include the liver, lung, kidney, heart, esophagus, stomach and bowel, while the structural organs include the bones, cartilages and muscles.

With the advancement in modern science and technology, organ failure or deterioration caused by acute/chronic diseases, congenital malformations and traffic accidents have become one of the huge social problems[3]. According to the statistics, there are about 1.5 millions of patients who require organ transplantations in China every year, but only less than 1% of patients can obtain suitable organs[4]. Compared to the traditional artificial organs made from polymers or metals, bioartificial organs made from living cells and biomaterials have become more and more prevalent.

Currently, a variety of bioprinting strategies have been developed to tackle the challenges for manufacturing bioartificial organs with physiological functions[5–8]. A main character of these strategies is to build complex organ geometries *via* spatiotemporal pattern of heterogenoustypes of "bioinks", especially cells. These strategies can be classified into three main groups: multi-nozzle rapid prototyping (MNRP), decellularization organ regeneration and combined mold system. Each of them has its own

advantages and disadvantages in bioartificial organ manufacturing areas[9–11]. An obvious advantage of the MNRP technology is that it can produce bioartificial organs automatically mimicking their natural counterparts using heterogeneous cell types and other biomaterials. In this article, we highlight some of the three-dimensional (3D) achievements of various bioprinting technologies in five large organs, including the bone, liver, heart, cartilage and skin, manufacturing.

2. Different Types of Bioprinting

Given that working principles, five major types of 3D bioprinting technologies include inkjet-based bioprinting, extrusion-based bioprinting, laser-assisted bioprinting, stereolithography-based bioprinting and microvalve-based bioprinting[12–14]. Among these technologies extrusion-based bioprinting technologies have been widely used to build cell-laden 3D tissues and organs.

2.1 Inkjet-based Bioprinting

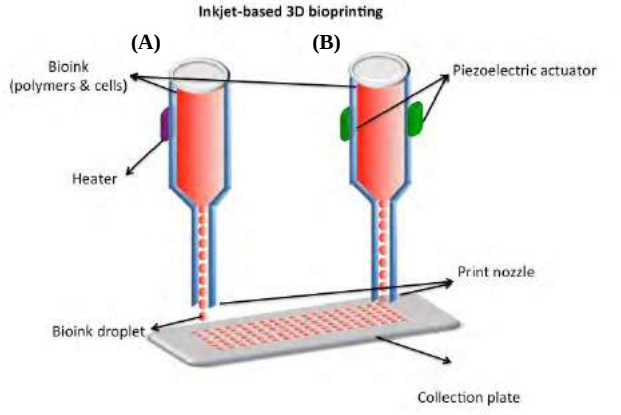

Figure 1. Schematic diagram of inkjet-based bioprinting (**A**: Heater; **B**: Piezoelectric actuator)

Inkjet-based bioprinting initially employed a commercial printer to spray cells (Figure 1)[15]. Inkjet bioprinters, known as droplet-based bioprinters, use thermal or acoustic force to eject liquid drops onto a substrate and build constructs layer-by-layer. In thermal inkjet bioprinting, "bioink" droplets are generated by electrically heating the print head to force cells in the liquid drops out of nozzle by increasing pressure[16]. Bioinks made of cells, scaffold materials and growth factors can be deposited accurately through controlling the droplet size and deposition rate[17]. During the inkjet bioprinting process, the heating temperature can reach approximate 300 °C. However, it lasts for very short of duration, resulting in the system temperature raising 4–10 °C with no obvious detrimental effect on cells. In piezoelectric inkjet bioprinting, bioink droplets are generated by acoustic wave induced by piezoelectric crystal inside the print head.

The advantages of inkjet-based bioprinting in organ 3D bioprinting contain the fast response speed, the high formation precision, and the high efficiency. These can be analysed through two aspects. On the one hand, the acoustic 3D bioprinters can be well-controlled through adjusting the jetting direction, droplet size, and cell viability. On the other hand, the thermal bioprinters can be well-controlled through adjusting the printing speed and cost. One obvious drawback of inkjet bioprinting in organ 3D bioprinting is that the "bioinks" should be in liquid forms with low viscosities[13]. This has greatly limited the height of the constructs. Only low concentration of polymeric bioinks with a low cell density (fewer than 10^6 cells/mL) can avoid nozzle clogging and reduce shear stress on cells[15–17]. Another obvious drawback of inkjet bioprinting in organ 3D bioprinting is the poor mechanical properties of the 3D constructs. Till now, most of the researchers in this field do their studies by modifying commercial inkjet printing systems to print living cells. This has greatly limited their development in soft and hardware as well as the complexity of printed constructs. Due to these drawbacks, inkjet-based bioprinting is still in its infancy stage for large organ 3D bioprinting whereas extrusion-based bioprinting has been prevalently used for numerous studies.

2.2 Extrusion-based Bioprinting

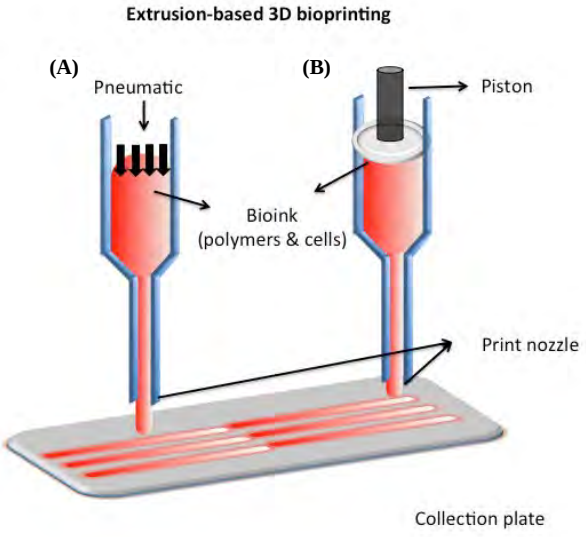

Figure 2. Schematic diagram of extrusion-based bioprinting (**A**: Pneumatic; **B**: Piston)

Extrusion-based bioprinting is a particular deposition process using fluidic polymeric solutions or hydrogels as bioinks (Figure 2)[18–24]. The extrusion-based bioprinters are normally consisted of a three-axis automatic extrusion system equipped with a fluid-dispensing nozzle (or head)[25–28]. During the extrusion processes, cell-laden bioinks are deposited in cylindrical filaments under the control of a computer-aided designing (CAD) model. At present, it is the only technology that can produce large scale-

Table 1. Comparison of different bioprinting techniques for organ manufacturing

Technique	Pros	Cons	References
Inkjet-based	High printing resolution (~20 μm); Several thermosensitive hydrogels can be printed; Simple sample-loading requirements; Low viscosity of cell suspensions (up to 10^6 cells/mL) or cell-laden hydrogels (3–30 mPs); Middle cell viability (> 70%).	Limited materials can be used; Complex 3D constructs are difficult to achieve; Limited height (< 10 μm); Potential cell desiccation; High shear stress endured by cells; Droplet instability at high printing speed; Poor cell sedimentation effects; Poor mechanical properties.	[13–17]
Extrusion-based	Easy updated soft and hardware; Flexible geometric shapes; Multiple biomaterials including cell types can be incorporated; Homogeneous and heterogeneous structures can be created; Good cell sedimentation effect; High cell viability (> 98%).	Material viscosity and temperature dependent; High viscosity hydrogels may affect cell activities.	[18–24]
Laser-assisted	Relatively high printing resolution (~40 μm); Wide range of printable viscosity; High cell viability (>90%).	High cost; Low efficiency; Difficult to incorporate multiple bioactive agents; Poor cell sedimentation effects; Poor cell homogeneity.	[39–42]
Stereolithography-based	Several photopolymerized materials can be used; High building velocity and accuracy; Multiple hydrogels can be printed simultaneously.	Cytotoxic of the laser beam and photo-initiators; Additional post-curing process may be necessary to remove the unpolymerized liquid resin; Poor cell sedimentation effects.	[43–46]
Microvalve-based	Relatively high printing resolution (~150 μm); Low viscosity of hydrogels (1–70 mPs); middle cell viability (> 80%); Middle cell sedimentation effect.	High shear stress suffered by cells; weak mechanical properties.	[50–53]

up cell-laden constructs containing both micro-/macro physiological environments in a controllable manner. Heterogeneous tissues and organs can be manufactured (*i.e.* produced) using either a single-nozzle 3D bioprinter with stem cells/heterogenous growth factors or a multi-nozzle 3D bioprinter with multiple cell lineages.

For extrusion-based bioprinting, the enabling 3D printers and biocompatible polymers are two major factors (*i.e.* elements) affecting the final 3D constructs. The resolution, shape and quality of the 3D constructs are mainly determined by the printability of the polymeric solutions or hydrogels, which has non-consistency with the cell viability. The viscosity of some of the polymeric "bioinks" may decrease when the shear stress of the printing system is increased. This may help to protect the cells and improve the resolution of the 3D constructs[29–34].

The advantages of extrusion-based bioprinting in organ 3D bioprinting include high cell densities, large 3D constructs and fast printing speeds. Beside polymeric solutions or hydrogels, extracellular matrices (ECMs) and cell aggregates can also be used as bioinks. The disadvantage of extrusion-based bioprinting in organ 3D bioprinting is that there are limited polymeric solutions or hydrogels that have good biocompatibilities and can be printed into large constructs in layers[35–38].

2.3 Laser-assisted Bioprinting

Laser-assisted bioprinting is based on the laser pulse to generate a high-pressure bubble between a solution and a piece of glass containing cells towards the collective substrate (Figure 3)[39,40]. It can produce micro cell-laden 3D constructs with a range of viscosities (1–300 mPa/s) of polymers in a high resolution[41,42].

The advantage of laser-assisted bioprinting in organ 3D bioprinting includes avoiding the problems of nozzle clogging with cells and/or polymeric biomaterials. The disadvantage of laser-assisted bioprinting in organ 3D bioprinting is the high cost of the laser-assisted 3D bioprinters.

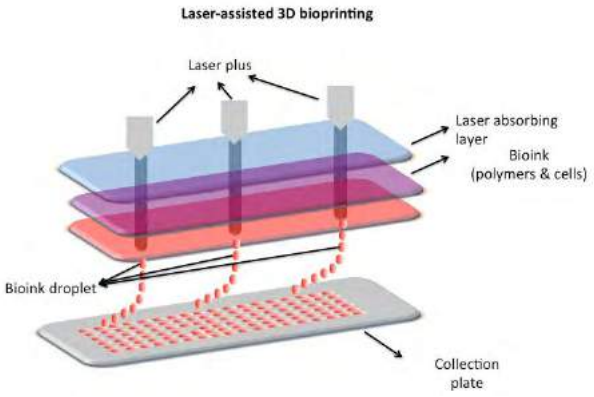

Figure 3. Schematic diagram of laser-assisted bioprinting

2.4 Stereolithography-based Bioprinting

Stereolithography (STL) technology is a solid free-form, nozzle-free technology based on photo-sensitive

macromolecule (or polymer) formulation[43]. It is a multi-layer procedure through the selective photo-initiated curing reaction of a low-molecular weight pre-polymer, additives and photo-initiators. Either a focused ultraviolet beam light or a mask-based irradiation can be used to selectively solidify the liquid photopolymer. Both single-photon polymerization and two-photon polymerization (2PP) can be induced at the printing stage[44]. A number of biomaterials can be added in the STL printing process. Optimal digital micromirror devices can work with wavelengths between 385–405 nm with expected lifetime of 2,000 h when exposed to a radiation with light intensities of 10 w/cm^2. Light-sensitive polymer hydrogels, such as hyaluronic acid, collagen, chitosan, diacrylate (PEGDA), containing cells can also be printed using these devices in a layer-by-layer manner[45,46]. The advantage of stereolithography-based bioprinting in organ 3D bioprinting is the high building velocity and accuracy. The disadvantages of stereolithography-based 3D bioprinting in organ 3D bioprinting is the high cost of the devices, and the cytotoxicity of the lights and photo-initiators[47–49].

2.5 Microvalve-based Bioprinting

Similar to inkjet-based bioprinting, microvalve-based bioprinting is a drop-on-demand technology. It comprises a three-axis movable robotic platform and an array of electromethanical microvalve heads[50]. Each of the microvalve head is connected to an individual gas regulator with pneumatic pressure. Liquid "bioinks" can be deposited when the pneumatic pressure overcomes the fluid viscosity and surface tension at the open orifice[51,52]. Cell viability and sedimentation effect during the printing process are the major issues in most of these bioprinting systems.

The main advantages of microvalve-based bioprinting in organ 3D bioprinting are the synchronized ejection of biomaterials including cells from different microvalve heads, the thin deposition layers (1–2 μm thickness), and the high throughput printing velocity (≈ 1000 droplets per second). The disadvantage of microvalve-based bioprinting in organ 3D bioprinting is that it can only print hydrogels within a limited range of viscosities (*e.g.* 1–200 mPa) and cell concentrations (up to 10^6 cells/mL)[53]. Cell viability and sedimentation effect depend largely on the employed liquid polymeric "bioinks".

No matter which bioprinting technology is applied in organ 3D bioprinting, good biocompatibility (or cytocompatiblity) of the polymeric solutions or hydrogels is a prior requirement for a successful 3D printable bioink, not only for the printing process, but also for the post-printing procedures, such as solvent exchanging, chemical crosslinking and polymeric degradation. The balance between a high cell viability and the physiological functionality realization of a supportive polymeric solution or hydrogel often need to be addressed before the 3D bioprinting process.

3. Large Organ 3D Bioprinting

A bone is a distinct rigid organ that constitutes part of the vertebrate skeleton (Figure 4)[54,55]. It is mainly composed of osteoblasts, osteoclasts and hard extracellular matrices (ECMs), such as collagen and hydroxyapatite. The bone has multiple functions, such as to support and protect various organs, produce red and white blood cells, store minerals, and enable mobility[56]. In the human body, different bones appear in a variety of shapes and sizes and have an intricate internal and external structure. These bones can be classified into five types: long, short, flat, sesamoid and irregular. There are blood vessels and marrow channels in the long bones which are difficult for the ordinary processing technologies to construct. Some large bones, such as the skull, radius and tibia, have complex shapes and contours. The contours may be strong angles, slightly concave or slightly convex, which need specific processing technologies to complete[57–60].

As early as in 1989, Madison first used rapid prototyping (RP) technology to diagnose bone diseases[61]. In 1998, Iseri *et al.* obtained a skull model of a 12-year-old girl using reverse engineering[62]. At the initial stage when RP technology was employed in 3D printing, researchers focused on matching the mechanical properties of bone *via* printing synthetic polymers to make 3D bone regenerative scaffolds. In 2002, Cheung *et al.* built a patient's maxillofacial region using the RP technique to provide a clear picture to guide the operation[63]. From then, various polymers in different states, such as thread, granular, solution, hydrogel, or slurry, were printed into porous structures under the instruction of CAD models. The porous scaffolds provided a favourable environment for cells to grow in. These works have provided a primary basis for large bone 3D bioprinting using either fused deposition modeling, extrusion-based or stereolithography-based printing technologies.

In recent years, a variety of 3D printing technologies have been further developed to construct bone repair

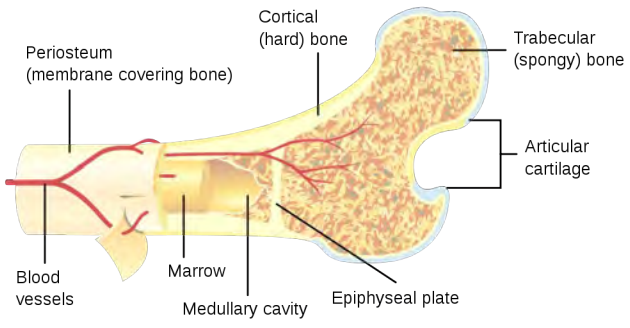

Figure 4. Cross-section of a large bone

materials mimicking the composition of bone tissues and the microenvironment of bony ECMs. For example, in 2002, Ang *et al.* at National University of Singapore printed a mesh hydroxyapatite-chitosan structure as bone repair fillers[64]. In 2005, Seitz *et al.* at Germany cooperated with Generis GmbH (Augsburg, Germany) company developed a 3D printed ceramic bone repair material[65]. In 2008, Kouhi et *al. at* Australia Swinburne University of Technology prepared a P400ABS plastic jawbone by fused deposition manufacturing[66]. In 2010, Smith *et al.* at nScrypt company in Orlando produced a hard tissue repair material using titanium and caprolactone[67]. In the same way, Lee *et al.* printed a porous calcium phosphate cement/alginate scaffold by depositing a solution of α-tricalcium phosphate-based powder and sodium alginate in a calcium chloride bath[68]. Comparing with the traditional metal or polymethyl methacrylate (mechanical and semi-mechanical) bone repair materials, most of the 3D printed bone repair materials have two obvious characteristics: one is made of biodegradable polymers, and the other is having go-through channels or pores. The predefined channels in the 3D printed construct are useful for nutrient supply and metabolite elimination for the in-growth of osteoblasts[69–73]. Some of the bone repair materials have showed good osteogenic effects and bone formation capabilities.

For large bone repair, a great deal pioneering work has been done in Tsinghua University using extrusion-based 3D printing technologies. Some ceramic materials, such as hydroxyapatite (HA) and beta-tricalcium phosphate (β-TCP), were incorporated into synthetic poly (lactic-co-glycolic acid) (PLGA) or poly-lactide (PLA) scaffolds to promote osteogenesis. Other biomaterials, such as collagen and bone growth factors could also be incorporated[76]. For example, In 2000, Yan *et al.* used a single nozzle low-temperature RP technology to prepare large bone repair materials with predefined (go-through) channels 200–500 μm in diameter which were hard to produce using traditional manufacturing technologies (Figure 5)[77]. Large scale-up cylindrical or grid PLA/HA or PLGA/HA scaffolds were produced for defect bone tissue regeneration. Similar research works were performed by other groups in American and Singapore with different biomaterials[78–80]. In 2009, Professor Wang in this group cooperated with Professor Qin in the Chinese University of Hong Kong constructed a large dual-functional bone repair material consisting of P-chitosan and S-chitosan through their home-made double-nozzle low-temperature deposition 3D bioprinter[81]. Multiple biochemical factors were entrapped in the synthetic polymeric scaffolds with precise predesigned (or predefined) patterns (or channels). Later in 2010, six mandible injury patients in Zhongshan People's Hospital were treated with the related 3D printed bone repair materials[82]. Multiple functional bone repair

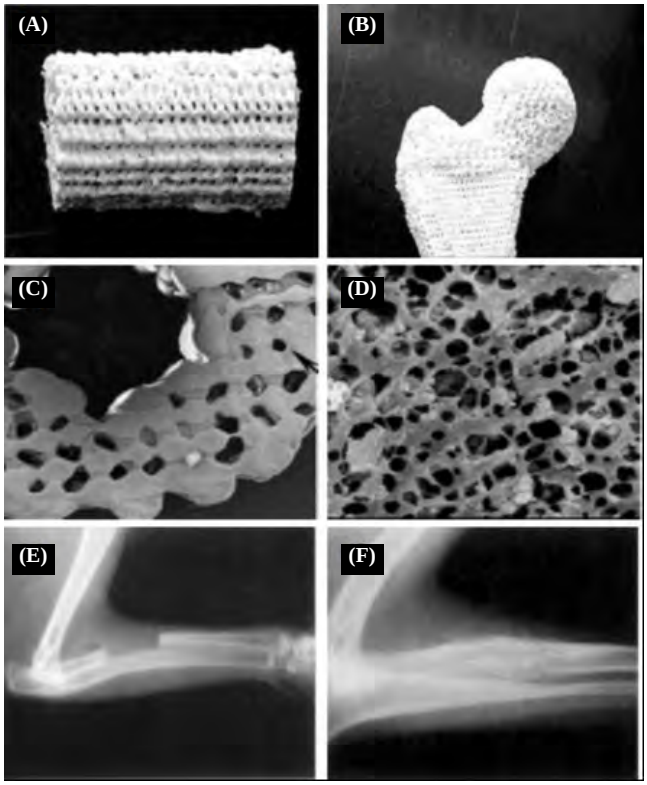

Figure 5. 3D bioprinted large bone repair materials for canine radius repairment, made of PLA (or PLGA)/HA with predefined internal morphology and macroscopic shapes.

materials with gradient structures were produced. The predefined channels could recapitulate the natural bony tissue microenvironment and promote the body fluid to diffuse. Nevertheless, most of the early 3D printed bone repair materials are made of synthetic polymers with no living cells involved in the 3D printing processes. These materials could act as bone tissue regenerative temporaries to promote cells growing in but not the real natural organ mimicking substitutes.

Compared with other organs, the composition of the bone is relatively simple and it is easy to be simulated. Until now, there are many reviews on this subject[83–89]. Numerous studies have focused on producing 3D printed bone regenerative scaffolds (or substitutes) in a custom-designed manner[90,91]. Most of the scaffolds are made of synthetic polymers, such as PLGA, polycaprolactone (PCL), with good mechanical properties, and ceramic materials, such as hydroxyapatite and beta-tricalcium phosphate (β-TCP)[92–95]. For example, in 2016 Jakus *et al.* developed an elastic construct for bone regeneration. They dissolved PCL or PLGA and HA in a trisolvent mixture as the printable "bioink". The printed 3D constructs can be handled versatilely, such as cutting, folding, rolling and suturing. Human mesenchymal stem cells (MSCs) seeded on the 3D constructs showed a significant up-regulation of pro-osteogenic genes,

collagen type I, osteocalcin, and osteopontin at day 28. When the 3D constructs were implanted in a macaque calvarial defect for 4 weeks, excellent new bone formation accompanying with the vascularization and integration of surrounding tissue[96]. At the same time, La *et al.* reported a bone substitute that replicates the micro- and mineralized environment through printing PCL/PLGA/TCP scaffolds, and then coating them with the bone dECM (bdECM) that was extracted from bovine tibiae. The PCL/PLGA/TCP/bdECM scaffolds exhibited significantly enhanced osteogenic gene expression and calcium deposition. These experiments have further certified the bone regenerative effects of the PLGA/HA scaffolds which have been printed more than ten years ago in Professor Wang's groups.

3.2 Liver 3D Bioprinting

The liver is a vital visceral organ in the human body (Figure 6). Unlike the structural organ bone, liver 3D bioprinting has several bottleneck problems to solve: one of them is how to construct the branched vascular and bile duct networks, another of them is how to distribute more than three cell types in a predefined 3D construct with a high cell density and make them develop to functional tissues[7].

There are several CAD models have been used to construct bioartificial livers. Some of the CAD models are made of experience. For example, in 2004 professor Wang and co-workers first assemble cell-laden gelatin-based hydrogels into large scale-up liver tissues with predefined structures (go-through channels) using a extrusion-based 3D printing system under the instruction of an experiential CAD model[16–19]. The predefined structures were printed via a pressure-controlled syringe. This technique allows the deposition of cell-laden hydrogels solutions with high concentration and velocity. Cylindrical channels with diameters ranging from 100 to 300 μm were produced. After 3D printing, the gelatin-based polymers in the cell-laden constructs were submitted to a chemical crosslinking process to stabilize the structures and improve the mechanical properties. Hepatocytes encapsulated in the gelatin-based hydrogels remained viable and produced hepatic ECMs during the 8 weeks' *in vitro* culture. This is a great breakthrough in tissue engineering field which has encountered numerous bottleneck problems in organ manufacturing areas. Thus difficult problems, such as large tissue formation and nutrient supply, have been solved therefore. In 2007, a large scale-up vascularized liver tissue was first produced in the same group using another experiential CAD model[29,30]. From then, actual bioartifical organ manufacturing has been put forward and developed very quickly. In 2009, a 3D printed complicated organ with a whole fluent of endothelial layer covered the inner channels of vascular network was produced[25–28]. It was possible to observe that endothelial cells aligned inside the surface of the predefined channels. More than three cell types formed functional tissues in a complex 3D construct. This technique has advanced other researches at least ten years in organ manufacturing areas[97,98].

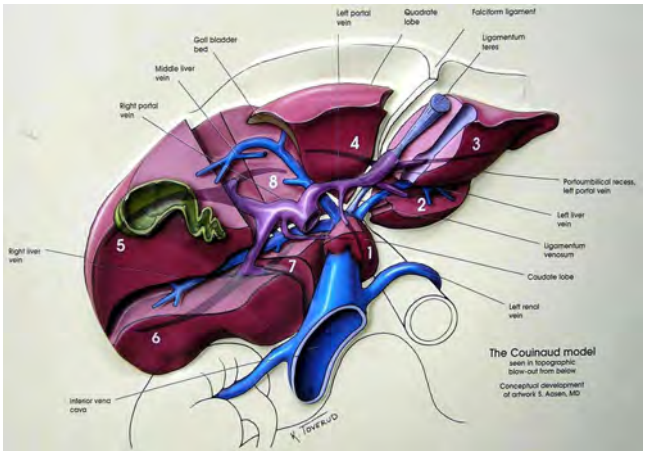

Figure 6. Schematic description the complex structure of the liver

At the same time, other groups throughout the world still devoted themselves in tissue engineered organ dreams with their porous scaffolds. For example, Huang *et al.* seeded hepatoma cells on a 3D printed branched vessel network which consists of avidin and biotin in 2007[99]. This is a typical traditional tissue engineering method to manufacture complex organs with a porous scaffold. Later in 2013, Organovo company in American printed a micro liver-tissue mimicking the techniques developed in Professor Wang' group. According to the British New Scientist magazine website report, the micro-liver tissue, 0.5 mm in thickness, 4 mm in square size, was created. To build the micro liver-tissue, two main cell types of the liver, *i.e.* hepatocytes and hepatic stellate cells, were printed into 20 layers[100]. Cells in the micro liver-tissue can survival for more than five days. Neovascularization played a role in the cell survival capabilities. In 2014, a bioartificial liver containing both vascular and nervous networks has been produced layer-by-layer using a combined MNRP under the instruction of a much more complex experienced CAD model[101]. The potential of this technology will eventually facilitate the manufacture of bioartificial livers, and make the liver 3D bioprinting an impending reality.

Currently, there is a trend that to make the CAD models from clinical patients. For instance, some current clinical diagnostic technologies, such as computer tomography (CT) and magnetic resonance imaging (MRI), have been explored to acquire liver image information of the patients. The CT and MRI image information are subsequently transformed into CAD models (*i.e.* liver manufacturing blueprints) and segregated into 2D horizontal slices to provide instructions to the 3D bioprinters.

For liver 3D bioprinting, two essential elements should be addressed: (1) a extrusion-based multi-nozzle 3D bioprinter with an appropriate soft/hardware. (2) multiple cell lineages from the liver or stem cells with proper growth factors. The extrusion-based multi-nozzle 3D bioprinter can print multiple cell types along with other biomaterials simultaneously in a layer-by-layer manner, which offers a great opportunity in manufacturing the complicated bioartificial livers with more than 6 cell types or tissues[102–106]. These technologies allow to use multiple polymeric hydrogels and growth factors to control the spatial distribution of cells and bioactive agents.

3.3 Heart 3D Bioprinting

The heart is one of the most important internal organ of human beings (Figure 7). It is composed of three different cardiac tissues: myocardium, pericardium and endocardium. The myocardium is the thick muscular layer of the heart wall which consists of cardiomyocytes, aligning themselves in an anisotropic manner and promoting the electrical activation of the cardiac muscles, and taking up to 30%–40% of the entire cell population. The pericardium is a conical, flask-like, double-wall fibroserous sac that encloses the blood vessels from the root of the heart. The endocardium is the endothelial lining of the innermost heart chambers and heart valves. It is primarily made up of endothelial cells that seal the heart and connect the surrounding blood vessels[107,108]. While the rest cell types of the heart are mainly non-myocyte fibroblasts[109]. The elasticity of the cardiomyocytes and their collagen-based ECMs in a normal heart are pliable and tough enough to generate actomyosin forces and pump the heart.

At present, there is limited literature for the whole heart 3D bioprinting. A number of 3D printing techniques have

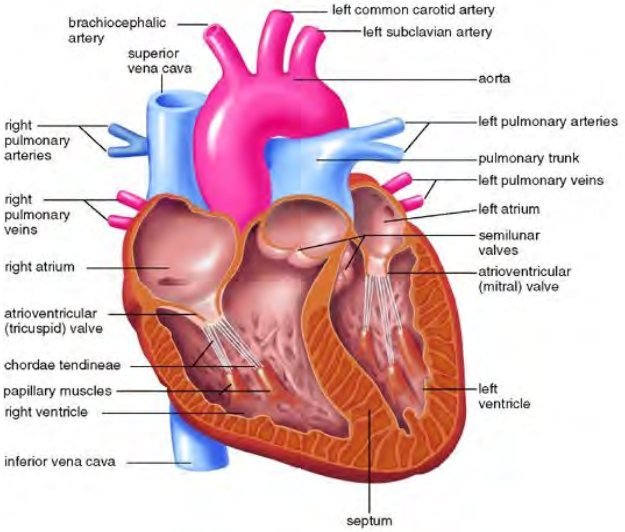

Figure 7. Schematic description of the heart

been developed to improve the functionality of the cardiac tissues. For example, in 2007, Marga *et al.* emitted a stream of cell-laden hydrogel microparticles in a well-defined topological pattern to form 3D myocardial patches using a inkjet-based bioprinting technique[110]. This technique is supported by the self-assembly and self-organizing capabilities of cells. In 2011, Gaebel *et al.* patterned human stem cells and endothelial cells with laser printing for cardiac regeneration[111]. In 2012, human cardiomyocyte progenitor cells (HCMPCs) in alginate hydrogel was printed by the same group[112]. HCMPCs in the alginate hydrogel showed an increase of cardiac commitment while at the same time maintaining viability and proliferation. In 2013, Duan *et al.* constructed trileaflet valve like conduits using sinus smooth muscle cells (SMCs) and alginate/gelatin hydrogels[113]. Cell viability in the alginate/gelatin hydrogels attained 81.4%. In 2014, similar study was carried out in the same group using human aortic vascular interstitial cells (HAVICs) in methacrylated hyaluronic acid (MeHA) or gelatin methacrylate (GelMA) hydrogels[114]. High HAVIC viability of the encapsulated cells (>90%) and promising remodeling potentials were obtained using this technology. The main concern of this technology is that polymethacrylate is an unbiodegradable polymer. It may hinder the cells to form functional tissues during the later cultures. In 2015, Hinton *et al.* created a heart CAD model using a reversible freeform embedding hydrogel[115]. A extrusion-based 3D bioprinting technology was used to produce a functional cardiac tissue, and particularly, a semilunar heart valve with three main components: a relatively stiff heart valve root populated by contractile SMCs, three thin flexible leaflets contain fibroblastic interstitial cells and three sinuses[116]. The semilunar heart valve can allows blood to be forced into the arteries and prevent the backflows. Hybrid hydrogel properties were studied by changing concentrations of the two compositions: MeHA and GelMA. The optimized hydrogel formulation was mixed with HAVICs. After 7 days in static culture, the 3D bioprinted valve showed well maintained structure, high viability of the encapsulated cells (> 90%), as well as promising remodeling potentials. In 2006, Chang *et al.* at the Cardiovascular Innovation Institute provided several sets of baseline parameters according to the different humidity of Pluronic F127 hydrogel for direct-write printing of the biomaterial, which was hoping to be used in heart tissue 3D bioprinting[117].

It should be aware of that either the semi-aortic valve or whole heart replacement is a dangerous procedure (a high-risk operation). Until present, the bioprinted aortic valve cannot open and close by itself without the presence of the rest of the heart. One reason is that the cardiac muscle cells are terminally differentiated cells that have no capability to regenerate and form new cardiac tissues. A number of techniques have thus been

developed to improve the functionality of engineered cardiac tissues. For example, to increase the mechanical properties, Hasan *et al.* developed an *in vitro* cell culture system to stimulate the physiological pressure and flow of the heart valve[118–120]. This stimulation could improve the strength of the heart valve before a possible implantation. A bioreactor system has been used to train printed heart valves, which could be beneficial for in vitro testing and maturation. Much more work needs to be done before the 3D printed bioartificial hearts to be applied clinically[121].

3.4 Cartilage 3D Bioprinting

Cartilage is a resilient and smooth elastic organ of the body, which protects the ends of long bones at the joints (*e.g.* the elbows, knees and ankles) (Figure 8). It is a structural component, made up of specialized cells called chondrocytes, of the rib cage, the ear, the nose, the bronchial tubes or airways, the intervertebral discs, and many other body components. The chondrocytes produce large amounts of ECM composed of proteoglycan, collagen and elastin fibers. Especially, there are no blood vessels in cartilage to supply the chondrocytes with nutrients. It is not as hard and rigid as bone, but it is much stiffer and much less flexible than muscle[123]. Like many other organs, cartilage exhibits multiple zonal organizations with highly coordinated cell distribution.

Cartilage can be categorized into three types: (1) hyaline cartilage with low-frication and wear-resistant properties; (2) elastic cartilage with flexible property; (3) fibrocartilage with tough and inflexible properties. Due to the lack of blood vessels, cartilage grows and repairs more slowly than other tissues/organs.

Through the research of cartilage regeneration is nearly as early as those in the bone, 3D printing technologies which have been used in cartilage regeneration is relatively late. For example, in 2014,

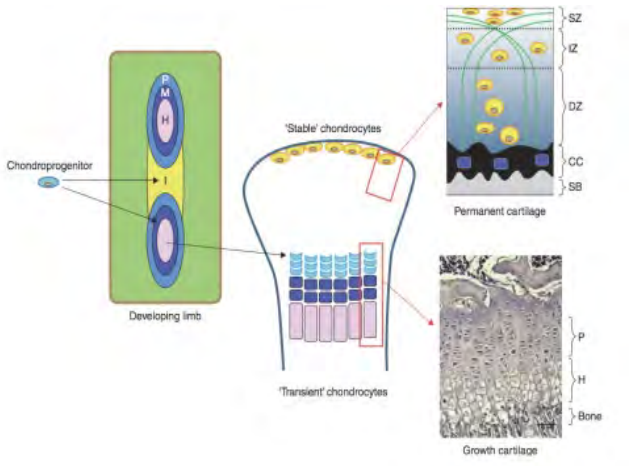

Figure 8. Schematic diagram of the developmental origins of articular and growth plate cartilage[122]

Lee *et al.* printed a meniscus scaffold with two different zones: the white zone, which is located at the inner zone of the meniscus, consists of chondrocyte-like cells with abundant collagen type II and glycosaminoglycans (GAG), whereas the red zone, which is in the other zone of the meniscus, contains fibroblast-like cells with collagen type I[124]. Human connective tissue growth factor and transforming growth factor β3 were then placed in the red and white zones respectively. The two zones spatiotemporally released the growth factors and induced the human synovium smooth muscle cells to form a zone-specific matrix, *i.e.* collagen type II in the white zone and collagen type I in the red zone. The zone-specific phenotypes were further exhibited in a 3-month implantation of a sheep partial meniscectomy model.

In 2015, Kundu *et al.* printed a hybrid cartilage construct containing chondrocyte, alginate, and PCL[125]. In 2016, the same group developed an autologous cartilage construct consisting of autologous chondrocyte, alginate, and PCL for auricular reconstruction[126]. The synthetic PCL was printed with alginate hydrogel and cells, which can provide the construct with long-term stability. The rigid properties of PCL may induce abrasion of the surrounding cartilage tissue. In the same year, Hung *et al.* fabricated a biodegradable polyurethane (PU) involving cartilage construct which exhibited a high strain recovery property[127]. Other bioactive compounds, such as hyaluronic acid and growth factors, can be encapsulated into the PU "bioink" and induce high GAG secretion at 4 weeks after implantation into rabbit osteochondral defects. The formation of cartilage was observed by safranin-O staining.

3.5 Skin 3D Bioprinting

The skin is the largest organ in the human body, which is accounting for about 15% body weight and maintains the body's temperature through sweat or other mechanism (Figure 9)[128]. Along with sweat glands, the skin contains oil glands to keep the skin from drying out and the hair from becoming brittle. The skin consists of three layers namely epidermis, dermis and hypodermis. Epidermis is the outer layer, consisting of keratinocytes (KCs), dermis is the middle layer, consisting of collagen and fibroblasts, hypodermis is the inner layer, consisting of lipocytes and collagen. There are about 19 million skin cells in every square inch of the human body! Although numerous studies have tried to generate full-thickness skin substitutes, most methods are dependent on the technique that seed cells on a porous scaffold, with which it is not easy to recapitulate the heterogeneity of skin comprising multiple types of cells. 3D bioprinting allows similar skin geometry to be built *via* the spatiotemporal pattern of the related cell types of the skin[129].

Traditional skin substitutes either are made of natural

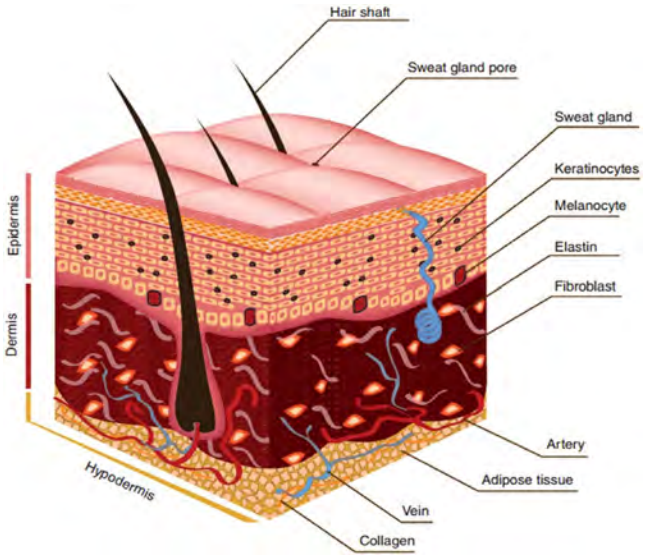

Figure 9. Schematic description of the skin

or synthetic polymers which could promote skin tissue regeneration to certain degree. These substitutes have been used in surgical therapies when autologous flap is not desirable. However, these substitutes have not been successfully used in clinical due to some technological limitations, such as the lack of multi-layer structures, vascularization and innervation[130].

In 2006, Ringeisen *et al.* printed living cells for skin regeneration using a laser-assisted technique[131]. The process employs radiation pressure from the scattering of energetic photons in a laser beam to deposit cell solutions with high concentration, rapid velocity (≥10 m/s) and micrometer resolution. Multiple skin cells were deposited with micron-scale resolution from a transfer layer or reservoir. In 2008, Saunders *et al.* delivered human fibroblasts using a piezoelectric drop-on-demand inkjet printing technique[132]. In 2009, Lee *et al.* used a extrusion-based printing system to fabricate skin substitutes using collagen, fibroblasts and keratinocytes[133]. In 2013,Michael *et al.* further printed skin substitutes using laser-assisted bioprinting techniques and transplanted them to skin wounds of nude mice[134]. It is expected that multiple scale characteristics of a natural skin can be mimicked through the combination of different bioprinting techniques[135].

Recently, skin 3D bioprinting has achieved a significant progress[136]. For example, in 2016 Pourchet *et al.* printed a full-thickness skin substitute containing dermis and epidermis layers[137]. A mixture of gelatin and fibrinogen was used as the "bioink". After 26 days of culture, the 3D printed skin substitute exhibited similar histological characteristics to human skin. Not only the main skin tissues but also the skin appendages, such as sweat glands, has been mimicked[138]. However, the regeneration of sweat glands has not been studied in depth due to the low regenerative ability and unknown induction niches of cellular differentiation. As a follow-up study, Liu *et al.* investigated the cellular niche by tailoring the architecture of a tissue construct *via* cell bioprinting[139]. The change of the geometry and architecture, such as the pore size of the tissue construct, has a strong influence on guiding sweat-gland morphogenesis and function[140]. The studies demonstrate that it is possible to print a bioartificial skin with the sweat-gland regenerative capability.

4. Conclusion

The advent of 3D bioprinting technologies has led to a significant progress in the manufacture of large bioartificial organs, such as the bones, livers, hearts, cartilages and skins, with heterogenic compositions. Various bioprinting techniques have provided a fully automated and advanced platform to deposit multiple cell types and ECM-like biomaterials to simulate the natural organs, a process that is lacking in conventional tissue-engineering approaches. Especially, with the helps of multi-nozzle 3D bioprinters and biocompatible polymers, the divergences between bioartificial organs and native counterparts are smaller and smaller. Nevertheless, there is still a long way to go to make the large bioartificial organs to be functional in clinical trials. It is believed that in the future combined multi-nozzle organ 3D bioprinting technologies will offer an unprecedented versatility and capability in mimicking the natural organs in every aspects, from the structural morphologies, to material compositions, and physiological functions. Further integrations among different sciences and technologies are still necessary to address the kernel issues in large organ 3D bioprinting areas.

Acknowledgments

The work was supported by grants from the National Natural Science Foundation of China (NSFC) (No. 81571832, 81271665, 81701033, 31600793 and 81571919) and the International Cooperation and Exchanges NSFC and Japanese Society for the Promotion of Science (JSPS) (No. 81411140040).

Author Contributions

Xiaohong Wang conceived, designed and wrote the main content; Liu Fan, Chen Liu, Qiuhong Chen, Qiang Ao, Xiaohong Tian, Jun Fan, Weijian Hou and Hao Tong contributed some detailed techniques.

Conflicts of Interest

The authors declare no conflict of interest. The founding sponsors had no role in the design of the study; in the collection, analyses, or interpretation of data; in the writing of the manuscript, and in the decision to publish the results.

References

1. Standring S2008, Gray's anatomy: The anatomical basis of clinical practice. *Reed Elsevier*, 978–0–8089–2371–8. https://doi.org/10.1016/s1479–666x(09)80013–9
2. Engeling C 2017, We got the mesentery news all wrong. Discover. Retrieved "https://en.wikipedia.org/w/index".
3. Chua C K, Yeong W Y, 2015, Bioprinting: principles and applications. *World Scientific Publishing Co*, https://doi.org/10.1142/9193
4. Wei D, Yin L, 1995, The situation and problems of human organs transplant technology in china. *Journal of Chinese Medical Ethics*, 6: 31–34.
5. Wang X, 2012, Intelligent freeform manufacturing of complex organs. *Artif Organs*, 36(11): 951–961. https://doi.org/10.1111/j.1525–1594.2012.01499
6. Wang X, Yan Y, Zhang R, 2010, Recent trends and challenges in complex organ manufacturing. *Tissue Eng Part B Rev*, 16: 189–197. https://doi.org/10.1089/ten.TEB.2009.0576
7. Wang X, Yan Y, Zhang R, 2007, Rapid prototyping as a tool for manufacturing bioartificial livers.*Trends Biotechnol*, 25(11): 505–513. https://doi.org/10.1016/j.tibtech.2007.08.010
8. Liu L, Wang X, 2015, Creation of a vascular system for complex organ manufacturing. *Int J Bioprint*, 1: 77–86. https://doi.org/ 10.1016/j.msec.2013.03.048
9. Mironov V, Kasyanov V, Markwald R R, 2011, Organ printing: From bioprinter to organ biofabrication line. *Curr Opin Biotechnol*, 22: 667–673. https://doi.org/10.1016/j.copbio.2011.02.006
10. Melchels F P W, Domingos M A N, Klein T J, *et al.*, 2012, Additive manufacturing of tissues and organs. *Pro in Polym Sci*, 37(8): 1079–1104. https://doi.org/10.1016/j.progpolymsci.2011.11.007
11. Li J, Chen M, Fan X, *et al.*, 2016, Recent advances in bioprinting techniques: approaches, applications and future prospects, *J Transl Med*, 14: 271. https://doi.org/10.1186/s12967-016-1028-0
12. Lei M, Wang X, 2016, Biodegradable polymers and stem cells for bioprinting. *Molecules*, 21(5): 539. https://doi.org/10.3390/molecules21050539
13. Cui X, Dean D, Ruggeri Z M, *et al.*, 2010, Cell damage evaluation of thermal inkjet printed Chinese hamster ovary cells. *Biotechnol Bioeng*, 106(6): 963–969. https://doi.org/10.1002/bit.22762
14. Demirci U, Montesano G, 2007, Single cell epitaxy by acoustic picolitre droplets. *Lab Chip*, 7(9): 1139–1145. https://doi.org/10.1039/b704965j
15. Saunders R E, Gough J E, Derby B, 2008, Delivery of human fibroblast cells by piezoelectric drop-on-demand inkjet printing. *Biomaterials*, 29(2): 193–203. https://doi.org/10.1016/j.biomaterials.2007.09.032
16. Kim J D, Choi J S, Kim B S, *et al.*, 2010, Piezoelectric inkjet printing of polymers: Stem cell patterning on polymer substrates. *Polymer*, 51(10): 2147–2154. https://doi.org/10.1016/j.polymer.2010.03.038
17. Phillippi J A, Miller E, Weiss L, *et al.*, 2008, Microenvironments engineered by inkjet bioprinting spatially direct adult stem cells toward muscle and bone-like subpopulations. *Stem Cells*, 26(1): 127–134. https://doi.org/10.1634/stemcells.2007-0520
18. Yan Y, Wang X, Pan Y, *et al.*, 2005, Fabrication of viable tissue-engineered constructs with 3D cell-assembly technique. *Biomaterials*, 26(29): 5864–5871. https://doi.org/10.1016/j.biomaterials.2005.02.027
19. Yan Y, Wang X, Xiong Z, *et al.*, 2005, Direct construction of a three-dimensional structure with cells and hydrogel. *J Bioact Compat Polym*, 20(3): 259–269. https://doi.org/10.1177/0883911505053658
20. Wang X, Yan Y, Pan Y, *et al.*, 2006, Generation of three-dimensional hepatocyte/gelatin structures with rapid prototyping system. *Tissue Eng*, 12(1): 83–90. https://doi.org/10.1089/ten.2006.12.83
21. Xu W, Wang X, Yan Y, *et al.*, 2007, Rapid prototyping three-dimensional cell/gelatin/fibrinogen constructs for medical regeneration. *J Bioact Compat Polym*, 22(4): 363–377. https://doi.org/10.1177/0883911507079451
22. Zhang T, Yan Y, Wang X, *et al.*, 2007, Three-dimensional gelatin and gelatin/hyaluronan hydrogel structures for traumatic brain injury. *J Bioact Compat Polym*, 22(1): 19–29. https://doi.org/10.1177/0883911506074025
23. Zhao X, Wang X, 2013, Preparation of an adipose-derived stem cell (ADSC)/fibrin-PLGA construct based on a rapid prototyping technique. *J Bioact Compat Polym*, 28(3): 191–203.
24. Zhao X, Liu L, Wang J, *et al.*, 2014, *In vitro* vascularization of a combined system based on a 3D printing technique. *J Tissue Eng Regen Med*, 10(10): 833–842. https://doi.org/10.1002/term.1863
25. Yao R, Zhang R, Yan Y, *et al.*, 2009, *In vitro* angiogenesis of 3D tissue engineered adipose tissue. *J Bioact Compat Polym*, 24(1): 5–24. https://doi.org/10.1177/0883911508099367
26. Wang X, Yan Y, Zhang R, 2010, Gelatin-based hydrogels for controlled cell assembly. *In: Biomedical Applications of*

Hydrogels Handbook (RM Ottenbrite ed.), Springer: New York, NY, USA, 269–284. https://doi.org/10.1007/978–1–4419–5919–5_14

27. Xu M, Wang X, Yan Y, *et al.* ,2010, A cell-assembly derived physiological 3D model of the metabolic syndrome, based on adipose-derived stromal cells and a gelatin/alginate/fibrinogen matrix.*Biomaterials*, 31 (14): 3868–3877. https://doi.org/10.1016/j.biomaterials.2010.01.111
28. Xu M, Yan Y, Liu H, *et al.*, 2009, Control adipose-derived stromal cells differentiation into adipose and endothelial cells in a 3-D structure established by cell-assembly technique. *Advances in Obstetrics & Gynecology*, 57 (1): 279–283.
29. Li S, Xiong Z, Wang X, *et al.*, 2009, Direct fabrication of a hybrid cell/hydrogel construct *via* a double-nozzle assembling technology. *J Bioact Compat Polym*, 24(3): 249–264. https://doi.org/10.1177/0883911509104094
30. Li S, Yan Y, Xiong Z, *et al.*, 2009, Gradient hydrogel construct based on an improved cell assembling system. *J Bioact Compat Polym*, 24(1): 84–99. https://doi.org/10.1177/0883911509103357
31. Xu Y, Wang X, 2015, Fluid and cell behaviors along a 3D printed alginate/gelatin/fibrin channel. *Bioeng Biotech*, 112(8): 1683–1695. https://doi.org/10.1002/bit.25579.
32. Zhao X, Du S, Chai L, *et al.*, 2015, Anti-cancer drug screening based on an adipose-derived stem cell/hepatocyte 3D printing technique. *J Stem Cell Res Ther*, 5(4): 273. https://doi.org/10.4172/2157–7633.1000273
33. Xu W, Wang X, Yan Y, *et al.*, 2008, Rapid prototyping of polyurethane for the creation of vascular systems. *J Bioact Compat Polym*, 23(2): 103–114. https://doi.org/10.1177/0883911507088271
34. Xu W, Wang X H, Yan Y N, *et al.*, 2008, A polyurethane-gelatin hybrid construct for the manufacturing of implantable bioartificial livers. *J Bioact Compat Polym*, 23(5): 409–422. https://doi.org/10.1177/0883911508095517
35. Kolesky D B, Truby R L, Gladman A S, *et al.*, 2014, Bioprinting: 3D bioprinting of vascularized, heterogeneous cell-laden tissue constructs. *Adv Mater*, 26(19): 3124–3130. https://doi.org/10.1002/adma.201305506
36. Melchels F P, Dhert W J, Hutmacher D W, *et al.*, 2014, Development and characterisation of a new bioink for additive tissue manufacturing. *J Mater Chem B*, 2(16): 2282–2289. https://doi.org/10.1039/C3TB21280G
37. Jungst T, Smolan W, Schacht K, *et al.*, 2016, Strategies and molecular design criteria for 3D printable hydrogels. *Chem Rev*, 116(3): 1496–1539. https://doi.org/10.1021/acs.chemrev.5b00303
38. Loo Y, Hauser C A, 2015, Bioprinting synthetic self-assembling peptide hydrogels for biomedical applications. *Biomed Mater*, 11(1): 014103. https://doi.org/10.1088/1748–6041/11/1/014103
39. Colina M, Serra P, Fernandez-Pradas J M, *et al.*, 2005, DNA deposition through laser induced forward transfer. *Biosens Bioelectron*, 20(8): 1638–1642. https://doi.org/10.1016/j.bios.2004.08.047
40. Barron J A, Ringeisen B R, Kim H, *et al.*, 2004, Application of laser printing to mammalian cells. *Thin Solid Films*, s453–454(2): 383–387. https://doi.org/10.1016/j.tsf.2003.11.161
41. Koch L, Kuhn S, Sorg H, *et al.*, 2010, Laser printing of skin cells and human stem cells. *Tissue Eng Part C Methods*, 16(5): 847–854. https://doi.org/10.1089/ten
42. Gruene M, Pflaum M, Hess C, *et al.*, 2011, Laser printing of three-dimensional multicellular arrays for studies of cell-cell and cell-environment interactions. *Tissue Eng Part C Methods*, 17(10): 973–982. https://doi.org/10.1089/ten
43. Matias J M, Bartolo P J, Pontes A V, 2009, Modeling and simulation of photofabrication processes using unsaturated polyester resins. *J Appl Polym Sci*, 114(6): 3673–3685. https://doi.org/10.1002/app.30405
44. Peltola S M, Melchels F P, Grijpma D W, *et al.*, 2008, A review of rapid prototyping techniques for tissue engineering purposes. *Ann Med*, 40(4): 268–280. https://doi.org/10.1080/07853890701881788
45. Bartolo P J, 2011, Stereolithography: Materials, processes and applications. Springer.
46. Chan V, Zorlutuna P, Jeong J H, *et al.*, 2010, Three-dimensional photopatterning of hydrogels using stereolithography for long-term cell encapsulation. *Lab Chip*, 10(16): 2062–2070. https://doi.org/10.1039/c004285d
47. Mironi-Harpaz I, Wang D Y, Venkatraman S, *et al.*, 2012, Photopolymerization of cell-encapsulating hydrogels: Crosslinking efficiency *versus* cytotoxicity. *Acta Biomater*, 8(5): 1838–1848. https://doi.org/10.1016/j.actbio.2011.12.034
48. Arcaute K, Mann B K, Wicker R B, 2006, Stereolithography of three-dimensional bioative poly(ethylene glycol) constructs with encapsulated cells. *Ann Biomed Eng*, 34(9): 1429–1441. https://doi.org/10.1007/s10439–006–9156–y
49. Wang S, Lee J M, Yeong W Y, 2015, Smart hydrogels for bioprinting. *Int J Bioprint*, 1: 3–14. https://doi.org/10.18063/IJB.2015.01.005
50. Ng W L, Lee J M, Yeong W Y, *et al.*, 2017, Microvalve-based bioprinting-process, bio-inks and applications. *Biomater Sci*,

5(4): 632–647. https://doi.org/10.1039/c6bm00861e

51. Gudapati H, Dey M, Ozbolat I, 2016, A comprehensive review on droplet-based bioprinting: Past, present and future. *Biomaterials*, 102: 20–42. https://doi.org/10.1016/j.biomaterials.2016.06.012
52. Mandrycky C, Wang Z, Kim K, Kim D H, 2016, 3D bioprinting for engineering complex tissues. *Biotechnol Adv*, 34(4): 422–434. https://doi.org/10.1016/j.biotechadv
53. Ng W L, Yeong W Y, Naing M W, 2017, Polyvinylpyrrolidone-based bio-ink improves cell viability and homogeneity during drop-on-demand printing. *Materials*, 10(2): 190. https://doi.org/10.3390/ma10020190
54. Hall J, 2011, Textbook of Medical Physiology (12th ed). Philadelphia: Elsevier. 957–960.
55. Wang X, Ma J, Wang Y, He B, 2001, Structural characterization of phosphorylated chitosan and their applications as effective additives of calcium phosphate cements. *Biomaterials*, 22(16): 2247–2255.
56. Laurin M, Canoville A, Germain D, 2011, Bone microanatomy and lifestyle: A descriptive approach. *Crpalevol*, 10(5): 381–402. https://doi.org/10.1016/j.crpv.2011.02.003
57. Wang X, Ma J, Wang Y, *et al.*, 2001, Progress in the research of bone substitutes. *J Biomed Eng*, 18(4): 647–652.
58. Wang X, 2014, 3D printing of tissue/organ analogues for regenerative medicine, in: *Handbook of Intelligent Scaffolds for Regenerative Medicine*, G Khang ed, the Second Edition, Pan Stanford Publishing, 557–570.
59. Wang X, Ao Q, Tian X, *et al.*, 2016, 3D bioprinting technologies for hard tissue and organ engineering. *Materials*, 9(11): 911. https://doi.org/10.3390/ma9110911
60. Liu L, Wang X, 2015, Hared tissue and organ manufacturing. in *Organ Manufacturing*, X Wang ed, Nova Science Publishers Inc, New York, 301–333.
61. Madison E, 1989, Computers in health care, *Englewood*, 10: 35–38.
62. Iseri H, Tekkaya A E, Oztan O, *et al.*, 1998, Biomechanical effects of rapid maxillary expansion on the craniofacil skeleton, studied by the finite element method. *Eur J Orthod*, 20 (4): 347–356.
63. Cheung L K, Wong M C, Wong L I, *et al.*, 2002, Refinement of facial reconstructive surgery by stereo-model planning. *Ann. R. Australas Coll Dent Surg*, 16: 29–32.
64. Ang T H, Sultana F S A, Hutmacher D W, *et al.*, 2002, Fabrication of chitosan-hydroxyapatite scaffolds using a robotic dispensing system. *Mat Sci Eng C*, 20(1): 35–42. https://doi.org/10.1016/S0928-4931(02)00010-3
65. Seitza H, Rieder W, Irsen S, *et al.*, 2005, Three-dimensional printing of porous ceramic scaffolds for bone tissue engineering, *J Biomed Mater Res B Appl Biomater*.74(2): 782–788. https://doi.org/10.1002/jbm.b.30291
66. Kouhi E, Masood S, Morsi Y, 2008, Design and fabrication of reconstructive mandibular models using fused deposition modeling. *Assembly Automation*, 28(3): 246–254. https://doi.org/10.1108/01445150810889501
67. Smith C M, Roy T D, Bhalkikar A, *et al.*, 2010, Engineering a titanium and polycaprolactone construct for a biocompatible interface between the body and artificial limb, *Tissue Eng Part A*, 16(2):717–24. https://doi.org/10.1089/ten
68. Lee G S, Park J H, Shin U S, Kim H W, 2011, Direct deposited porous scaffolds of calcium phosphate cement with alginate for drug delivery and bone tissue engineering. *Acta Biomater*, 7(8): 3178–3186. https://doi.org/10.1016/j.actbio.2011.04.008
69. Bose S, Roy M, Bandyopadhyay A, 2012, Recent advances in bone tissue engineering scaffolds. *Trends Biotechnol*, 30(10): 546–54. https://doi.org/10.1016/j.tibtech.2012.07.005
70. Wang X, Rijff B L, Khang G, 2015, A building-block approach to 3D printing a multi-channel organ regenerative scaffold. *J Tissue Eng Regen Med*, 11(5): 1403–1411. https://doi.org/10.1002/term.2038
71. Yeong W Y, Chua C K, Leong K F, *et al.*, 2006, Indirect fabrication of collagen scaffold based on inkjet printing technique. *Rapid Rrot J*, 12(4): 229–237. https://doi.org/10.1108/13552540610682741
72. Yang S, Leong K F, Du Z,*et al.*, 2002, The design of scaffolds for use in tissue engineering. Part II. Rapid prototyping techniques. *Tissue Eng*, 8: 1–11.
73. Ricci J L, Clark E A, Murriky A, *et al.*, 2012, Three-dimensional printing of bone repair and replacement materials: Impact on craniofacial surgery. *J Craniofac Surg*, 23(1): 304–308. https://doi.org/10.1097/SCS.0b013e318241dc6e
74. Kundu J, Shim J H, Jang J, *et al.*, 2013, An additive manufacturing-based PCL-alginate-chondrocyte bioprinted scaffold for cartilage tissue engineering. *J Tissue Eng Regen Med*, 9(11): 1286–97. https://doi.org/10.1002/term.1682
75. Langton C M, Whitehead M A, Langton D K, *et al.*, 1997, Development of a cancellous bone structural model by stereolithography for ultrasound characterisation of the calcaneus. *Med Eng Phys*, 19(7): 599–604.
76. Farzadi A, Hashjin M S, Eydivand M A, *et al.*, 2014, Effect of layer thickness and printing orientation on mechanical properties and dimensional accuracy of 3D printed porous

samples for bone tissue engineering. *Plos One*, 9(9): e108252. https://doi.org/10.1371/journal.pone.0108252

77. Yan Y, Cui F, Zhang R,*et al.*, 2000, Rapid prototyping manufacturing for artificial human bone. *Materials Review (Chinese)*, 14: 11–13.
78. Park A, Wu B, Griffith L G, 1998, Integration of surface modification and 3D fabrication techniques to prepare patterned poly (L-lactide) substrates allowing regionally selective cell adhesion. *J Biomater Sci Polym Ed*, 9(2):89–110.
79. Limpanuphap S, Derby B, 2002, Manufacture of biomaterials by a novel printing process. *J Mater Sci Mater Med*, 13(12):1163–6.
80. Lam C X F, Mo X M, Teoh S H, *et al.*, 2002, Scaffold development using 3D printing with a starch-based polymer. *Mater Sci Eng C*, 20(1): 49–56. https://doi.org/10.1016/S0928-4931(02)00012-7
81. He K, Wang X, Kumta S, *et al.*, 2009, Fabrication of a two-level tumor bone repair biomaterial based on a rapid prototyping technique. *Biofabrication*, 1(2): 025003. https://doi.org/10.1088/1758–5082/1/2/025003
82. Yu J, Wen T, Hu Q X, 2010, Research on automatic planning of main clamping points in rapid fixture design system. *Conference: Fuzzy Systems and Knowledge Discovery*, 6: 2657–2661. https://doi.org/10.1109/FSKD.2010.5569803
83. Hollister S J, 2005, Porous scaffold design for tissue engineering. *Nat Mater*, 4(7): 518–524. https://doi.org/10.1038/nmat1421
84. Bose S, Vahabzadeh S, Bandyopadhyay A, 2013, Bone tissue engineering using 3D printing. *Materials Today*, 16(12): 496–504.
85. Fedorovich N E, Alblas J, Hennink W E, *et al.*, 2011, Organ printing: The future of bone regeneration? *Trends Biotechnol*. 29(12): 601–606. https://doi.org/10.1016/j.tibtech.2011.07.001
86. Inzana J A, Olvera D, Fuller S M, *et al.*, 2014, 3D printing of composite calcium phosphate and collagen scaffolds for bone regeneration. *Biomaterials*, 35(13): 4026–4034. https://doi.org/10.1016/j.biomaterials.2014.01.064
87. Xue W, Krishna B V, Bandyopadhyay A, *et al.*, 2007, Processing and biocompatibility evaluation of laser processed porous titanium. *Acta Biomater*, 3(6): 1007–1018. https://doi.org/10.1016/j.actbio.2007.05.009
88. Hull C W, 1986, Apparatus for production of three-dimensional objects by stereolithography, US Patent 4575330, fabbster.com.
89. Wilson C E, de Bruijn J D, van Blitterswijk C A, *et al.*, 2004, Design and fabrication of standardized hydroxyapatite scaffolds with a defined macro-architecture by rapid prototyping for bone-tissue-engineering research. *J Biomed Mater Res A*, 68(1): 123–132. https://doi.org/10.1002/jbm.a.20015
90. Daly A C, Cunniffe G M, Sathy B N, *et al.*, 2016, 3D Bioprinting of developmentally inspired templates for whole bone organ engineering. *Advanced Healthcare Materials*, 5(18): 2353–2362. https://doi.org/10.1002/adhm.201600182
91. La W G, Jang J, Kim B S, *et al.*, 2016, Systemically replicated organic and inorganic bony microenvironment for new bone formation generated by a 3D printing technology. *RSC Advances*, 6(14): 11546–11553. https://doi.org/10.1039/C5RA20218C
92. Hutmacher D W, 2000, Scaffolds in tissue engineering bone and cartilage. *Biomaterials*, 21(24): 2529–2543. https://doi.org/10.1016/S0142-9612(00)00121-6
93. Williams J M, Adewunmi A, Schek R M, *et al.*, 2005, Bone tissue engineering using polycaprolactone scaffolds fabricated *via* selective laser sintering. *Biomaterials*, 26(23): 4817–4827. https://doi.org/10.1016/j.biomaterials.2004.11.057
94. Tan K, Chua C, Leong K, *et al.*, 2003, Scaffold development using selective laser sintering of polyetheretherketone-hydroxyapatite biocomposite blends. *Biomaterials*, 24(18): 3115–3123.
95. Mondrinos M J, Dembzynski R, Lu L, *et al.*, 2006, Porogen-based solid freeform fabrication of polycaprolactone-calcium phosphate scaffolds for tissue engineering. *Biomaterials*, 27(25): 4399–4408. https://doi.org/10.1016/j.biomaterials.2006.03.049
96. Jakus A E, Rutz A L, Jordan S W, *et al.*, 2016, Hyperelastic "bone": A highly versatile, growth factor-free, osteoregenerative, scalable, and surgically friendly biomaterial. *Sci Transl Med*, 8(358): 358ra127. https://doi.org/10.1126/scitranslmed.aaf7704
97. Wang X, He K, Zhang W, 2013, Optimizing the fabrication processes for manufacturing a hybrid hierarchical polyurethane-cell/hydrogel construct. *J Bioact Compat Polym*, 28(4): 303–319. https://doi.org/10.1177/0883911513491359
98. Huang Y, He K, Wang X, 2013, Rapid Prototyping of a hybrid hierarchical polyurethane-cell/hydrogel construct for regenerative medicine. *Mater Sci Eng C*, 33(6): 3220–3229. https://doi.org/10.1016/j.msec.2013.03.048
99. Wang J, Wang X, 2014, Development of a combined 3D printer and its application in complex organ construction, *Master's Thesis, Tsinghua University, Beijing, China*.
100. Huang H, Oizumi S, Kojima N, *et al.*, 2007, Avidin-biotin binding-based cell seeding and perfusion culture of liver-derived cells in a porous scaffold with a three-

dimensional interconnected flow-channel network. *Biomaterials*, 28(26): 3815–3823. https://doi.org/10.1016/j.biomaterials.2007.05.004

101. Coghlan A, 2013, 3D printer makes tiniest human liver ever, *New Scientist April*. http://www.newscientist.com/article/dn23419-3d-printer-makes-tiniest-human-liver-ever. html#.Ui2l7kDEfn4.
102. Wang X, 2014, Spatial effects of stem cell engagement in 3D printing constructs. *Stem Cells Res Rev & Rep*, 1: 5–9.
103. Wang X, Tuomi J, Mäkitie A, *et al.*, 2013, The integrations of biomaterials and rapid prototyping techniques for intelligent manufacturing of complex organs, in *Advances in Biomaterials Science and Applications in Biomedicine,* R Lazinica ed, InTech, Rijeka, 437–463. https://doi.org/10.5772/53461
104. Wang X, 2013, Overview on biocompatibilities of implantable biomaterials. *Advances in Biomaterials Science and Biomedical Applications in Biomedicine*, 111–155. https://doi.org/10.5772/53461
105. Wang X, Zhang Q, 2011, Overview on "Chinese-Finnish workshop on biomanufacturing and evaluation techniques". *Artificial Organs*, 35: E191–E193.
106. Xu Y, Li D, Wang X, 2015, Liver manufacturing approaches: the thresholds of cell manipulation with bio-friendly materials for multifunctional organ regeneration, in *Organ Manufacturing*, X Wang ed, Nova Science Publishers Inc, New York, 201–225. http://www.cartilagehealth.com/images/artcartbiomech.pdf
107. Walther G, Gekas J, Bertrand D F, 2009, Amniotic stem cells for cellular cardiomyoplasty: Promises and premises. *Catheter and Cardiovasc Interv*, 73(7): 917–924. https://doi.org/10.1002/ccd.22016
108. Nag A C, 1979, Study of non-muscle cells of the adult mammalian heart: A fine structural analysis and distribution. *Cytobios*, 28(109): 41–61
109. Tomanek R J, Runyan R B, Tomanek R J, 2001, Formation of the heart and its regulation. *Boston Birkhäuser*, 28(7): 2008–2013.
110. Marga F, Neagu A, Kosztin I, *et al.*, 2007, Developmental biology and tissue engineering. *Birth Defects Res C Embryo Today*, 81(4): 320–328. https://doi.org/10.1002/bdrc.20109
111. Gaebel R, Ma N, Liu J, *et al.*, 2011, Patterning human stem cells and endothelial cells with laser printing for cardiac regeneration. *Biomaterials*, 32(35): 9218–9230. https://doi.org/10.1016/j.biomaterials.2011.08.071
112. Gaetani R, Doevendans P A, Metz C H, *et al.*, 2012, Cardiac tissue engineering using tissue printing technology and human cardiac progenitor cells. *Biomaterials*, 33(6): 1782–1790. https://doi.org/10.1016/j.biomaterials.2011.11.003
113. Duan B, Hockaday L A, Kang K H, *et al.*, 2013, 3D bioprinting of heterogeneous aortic valve conduits with alginate/gelatin hydrogels. *J Biomed Mater Res A*, 101(5): 1255–1264. https://doi.org/10.1002/jbm.a.34420
114. Duan B, Kapetanovic E, Hockaday L A, *et al.*, 2014, Three-dimensional printed trileaflet valve conduits using biological hydrogels and human valve interstitial cells. *Acta Biomater*, 10(5): 1836–1846. https://doi.org/10.1016/j.actbio.2013.12.005
115. Hinton T J, Jallerat Q, Palchesko R N, *et al.*, 2015, Three-dimensional printing of complex biological structures by freeform reversible embedding of suspended hydrogels. *Sci Adv*, 1(9): e1500758. https://doi.org/10.1126/sciadv.1500758
116. Visser J, Melchels F, Jeon J E, *et al.*, 2015, Reinforcement of hydrogels using three-dimensionally printed microfibers. *Nat. Commun*, 6: 6933. https://doi.org/10.1038/ncomms7933
117. Kang H W, Lee S J, Ko I K, *et al.*, 2016, A 3D bioprinting system to produce human-scale tissue constructs with structural integrity. *Nat Biotechnol*, 34(3): 312–319. https://doi.org/10.1038/nbt.3413
118. Hasan A, Ragaert K, Swieszkowski W, *et al.*, 2014, Biomechanical properties of native and tissue engineered heart valve constructs. *J Biomech*, 47: 1949–1963. https://doi.org/10.1016/j.jbiomech.2013.09.023
119. Xu Y, Li D, Wang X, 2015, Liver manufacturing approaches: The thresholds of cell manipulation with bio-friendly materials for multifunctional organ regeneration, in: *Organ Manufacturing*, X Wang ed, Nova Science Publishers Inc, New York, 201–225. http://www.cartilagehealth.com/images/artcartbiomech.pdf
120. Lei M, Wang X. 2015, Uterus Bioprinting, in: *Organ Manufacturing*, X Wang ed, Nova Science Publishers Inc, New York, 335–355. http://www.cartilagehealth.com/images/artcartbiomech.pdf
121. Xu Y, Li D, Wang X. Current trends and challenges for producing artificial hearts, in: *Organ Manufacturing*, X Wang ed, Nova Science Publishers Inc, New York, 101-125. http://www.cartilagehealth.com/images/artcartbiomech.pdf
122. Staines K A, Pollaod A S, McGonnell I M, *et al.*, 2013, Cartilage to bone transitions in health and disease. *J Endocrinology*, 219(1): R1–R12. https://doi.org/10.1530/JOE–13–0276
123. Liu L, Wang X, 2015, Organ manufacturing. in: *Organ Manufacturing*, X Wang ed, Nova Science Publishers Inc, New York, 1–28. http://www.cartilagehealth.com/images/

artcartbiomech.pdf

124. Lee C H, Rodeo S A, Fortier L A, *et al.*, 2014, Protein-releasing polymeric scaffolds induce fibrochondrocytic differentiation of endogenous cells for knee meniscus regeneration in sheep. *Sci Transl Med*, 6(266): 266ra171. https://doi.org/10.1126/scitranslmed.3009696
125. Kundu J, Shim J H, Jang J, *et al.*, 2015, An additive manufacturing-based PCL-alginate-chondrocyte bioprinted scaffold for cartilage tissue engineering. *J Tissue Eng Reg Med*, 9(11): 1286–1297. https://doi.org/10.1002/term.1682
126. Hung K C, Tseng C S, Dai L G, *et al.*, 2016, Water-based polyurethane 3D printed scaffolds with controlled release function for customized cartilage tissue engineering. *Biomaterials*, 83: 156–168. https://doi.org/10.1016/j.biomaterials.
127. Park J H, Hong J M, Ju Y M, *et al.*, 2015, A novel tissue-engineered trachea with a mechanical behavior similar to native trachea. *Biomaterials*, 62: 106–115. https://doi.org/10.1016/j.biomaterials.2015.05.008
128. Mak H C, 2011, Trends in computational biology–2010. *Nat Biotechnol*, 29(1): 45–49. https://doi.org/10.1038/nbt0111–45b
129. Ng W L, Wang S, Yeong W Y, *et al.*, 2016, Skin bioprinting: Impending reality or fantasy? *Trends in Biotechnology*, 34(9): 689–699. https://doi.org/10.1016/j.tibtech.2016.04.006
130. Lee V, Singh G, Trasatti J P, *et al.*, 2014, Design and fabrication of human skin by three-dimensional bioprinting. *Tissue Eng Part C Methods*, 20(6): 473–484. https://doi.org/10.1089/ten
131. Ringeisen B R, Othon C M, Barron J A, *et al.*, 2006, Jet-based methods to print living cells. *Biotechnol J*, 1(9): 930–948. https://doi.org/10.1002/biot.200600058
132. Saunders R E, Gough J E, Derby B, 2008, Delivery of human fibroblast cells by piezoelectric drop-on-demand inkjet printing. *Biomaterials*, 29(2): 193–203. https://doi.org/10.1016/j.biomaterials.2007.09.032
133. Lee W, Debasitis J C, Lee V K, *et al.*, 2009, Multi-layered culture of human skin fibroblasts and keratinocytes through three-dimensional freeform fabrication. *Biomaterials*, 30(8): 1587–1595. https://doi.org/10.1016/j.biomaterials.2008.12.009
134. Michael S, Sorg H, Peck C T, *et al.*, 2013, Tissue engineered skin substitutes created by laser-assisted bioprinting form skin-like structures in the dorsal skin fold chamber in mice. *PLoS ONE*, 8(3): e57741. https://doi.org/10.1371/journal.pone.0057741
135. Huang H, Sharma H S, 2013, Neurorestoratology: One of the most promising new disciplines at the forefront of neuroscience and medicine. *J Neurorestoratology*, 2013(default): 37–41. https://doi.org/10.2147/JN.S47592
136. Zhou X, Wang X, 2015, Skin Substitute Manufacturing, in: *Organ Manufacturing*, X Wang ed, Nova Science Publishers Inc, New York, 385–408. http://www.cartilagehealth.com/images/artcartbiomech.pdf
137. Pourchet L J, Thepot A, Albouy M, *et al.*, 2016, Human skin 3D bioprinting using scaffold-free approach. *Adv Healthc Mater*, 6(4). https://doi.org/ 10.1002/adhm.201601101
138. Lu C P, Polak L, Rocha A S, *et al.*, 2012, Identification of stem cell populations in sweat glands and ducts reveals roles in homeostasis and wound repair. *Cell*, 150(1): 136–150. https://doi.org/10.1016/j.cell.2012.04.045
139. Liu N, Huang S, Yao B, *et al.*, 2016, 3D bioprinting matrices with controlled pore structure and release function guide *in vitro* self-organization of sweat gland. *Sci Rep*, 6: 34410. https://doi.org/10.1038/srep34410
140. Huang S, Yao B, Xie J, *et al.*, 2016, 3D bioprinted extracellular matrix mimics facilitate directed differentiation of epithelial progenitors for sweat gland regeneration. *Acta Biomater*, 32: 170–177. https://doi.org/10.1016/j.actbio.2015.12.039

REVIEW ARTICLE

3D printing of hydrogel composite systems: Recent advances in technology for tissue engineering

Tae-Sik Jang[1#], Hyun-Do Jung[2#], Houwen Matthew Pan[1], Win Tun Han[1], Shengyang Chen[1], Juha Song[1*]

[1] School of Chemical and Biomedical Engineering, Nanyang Technological University, Singapore
[2] Liquid Processing & Casting Technology R&D Group, Korea Institute of Industrial Technology, Incheon, Republic of Korea

Abstract: Three-dimensional (3D) printing of hydrogels is now an attractive area of research due to its capability to fabricate intricate, complex and highly customizable scaffold structures that can support cell adhesion and promote cell infiltration for tissue engineering. However, pure hydrogels alone lack the necessary mechanical stability and are too easily degraded to be used as printing ink. To overcome this problem, significant progress has been made in the 3D printing of hydrogel composites with improved mechanical performance and biofunctionality. Herein, we provide a brief overview of existing hydrogel composite 3D printing techniques including laser based-3D printing, nozzle based-3D printing, and inkjet printer based-3D printing systems. Based on the type of additives, we will discuss four main hydrogel composite systems in this review: polymer- or hydrogel-hydrogel composites, particle-reinforced hydrogel composites, fiber-reinforced hydrogel composites, and anisotropic filler-reinforced hydrogel composites. Additionally, several emerging potential applications of hydrogel composites in the field of tissue engineering and their accompanying challenges are discussed in parallel.

Keywords: hydrogel composites; 3D printing; tissue engineering

*Correspondence to: Juha Song, School of Chemical and Biomedical Engineering, Nanyang Technological University, 70 Nanyang Drive, 637457, Singapore; songjuha@ntu.edu.sg

#The co-authors have equally contributed to the manuscript

Received: September 30, 2017; **Accepted:** November 22, 2017; **Published Online:** January 19, 2017

Citation: Jang T-S, Jung H D, Pan H W, *et al.*, 2018, 3D printing of hydrogel composite systems: Recent advances in technology for tissue engineering. *Int J Bioprint*, 4(1): 126. http://dx.doi.org/10.18063/IJB.v4i1.126

1. Introduction

Since the advent of the first three-dimensional (3D) printing system, formerly known as additive manufacturing or rapid prototyping, in 1986, the manufacturing industry has undergone significant transformations, requiring now less time, energy, and producing less waste with the ability to directly fabricate 3D prototypes from computer-aided designs[1–3]. This fascinating ability to create 3D structures has already taken fabrication technology to a new level, especially in the field of tissue engineering. Over the past two decades, with the development of medical imaging technologies, such as ultrasound, magnetic resonance imaging (MRI), and computed tomography (CT), there has been multiple attempts to replicate the complexity of anatomical systems in the human body for tissue replacement and regeneration which requires complete restoration of 3D anatomical geometry[2,4]. However, without artificial or transplant supports, rapid and extensive reconstruction of vital organs in the human body remains a daunting challenge in tissue engineering[5].

3D printed scaffolds play an essential role in supporting cell adhesion and promoting cell infiltration within their porous matrix[6]. Moreover, during the tissue reconstruction process, scaffolds are able to provide mechanical support against stressful environments of the human body maintaining sufficient space for the tissue reconstruction and remodeling[7]. Currently, the most widely used scaffold

materials for 3D printing are hydrogels because they can be easily functionalized or modified, without complex synthesis steps, to replicate the physicochemical properties of most biological tissues[8,9]. They possess a highly hydrated polymeric structure, exhibiting up to 40-fold change in volume as they swell or shrink in the presence or absence of water, respectively, and can be modified to respond to various physical and biological stimuli such as temperature, light, pH, ions, and biochemical signals[9,10]. These unique features make hydrogels excellent environments for cell attachment and proliferation within their hydrated hydrogel networks, which offer abundant space for cell growth while facilitating the transportation of essential metabolites and nutrients to the encapsulated cells[8,11]. However, most hydrogels suffer from a lack of mechanical strength and unsuitable degradation behavior compared with native tissues such as ligament, tendon, muscle, or cartilage. Therefore, augmenting the mechanical properties and bioactivity of hydrogel have been a challenging task for material scientists[8].

Hydrogel composite system is one of the most suitable strategy for incorporating and combining various hydrogel functions and properties, not attainable by any single hydrogel alone[11]. Over the past few decades, a diverse range of reinforcements have been proposed utilizing various composite designs such as particle-, anisotropic filler-, and fiber-hydrogel composite systems in which reinforcements are stabilized and immobilized via physical or chemical interactions in the hydrogel matrix[8,9,11,12]. In the case of hydrogel-hydrogel composite system, the interpenetration between the two polymer networks forms a mechanical anchoring behavior, and these complexes strongly affect the hydrogel rheology, degradation rate, permeability, and mechanical properties[13]. Conventional inorganic reinforcements are based on physical interactions with the hydrogel matrix in which secondary or van der Waals forces including London dispersion forces, dipolar interactions and hydrogen bonding are involved[14]. These physical interactions generate strong adhesion between the reinforcements and hydrogel matrix, and the enhancement of hydrogel properties are dependent on the amount of reinforcements and the volume ratio of physically interacted- and non-interacted-polymer networks[15]. In the case of chemical modifications, the introduction of chemical groups and the covalent bonding formations at the interface induce superior interfacial bonding strength of which energy is generally in between the 40 to 400 kJ/mol *i.e.* much higher than physical interaction (8–16 kJ/mol)[14]. Thus, it is possible to provide substantial increase of mechanical strength to the hydrogel composite system.

While the hydrogel composite has attracted a lot of attention due to its superior properties, most review articles report on conventional fabrication techniques such as molding or casting[5,7]. Compared with well-understood and evaluated conventional manufacturing processes, hydrogel composite 3D printing systems remain a relatively new area of research and much more can be studied with regards to their physicochemical properties such as viscosity, dispersion, reinforcement, and its size and shape[16,17]. In recent years, significant progress has been made in the development of 3D printing systems for hydrogel composites with improved mechanical performance and biofunctionality[1,16,17].

Herein, we first provide a brief introduction of hydrogel composite 3D printing techniques and their application in the field of tissue engineering. We shall categorize 3D printing into (a) laser based-3D printing, (b) nozzle based-3D printing, and (c) inkjet printer based-3D printing systems, and discuss their working principles and recent trends. In particular, we will discuss four different hydrogel composite systems: i) polymer- or hydrogel-hydrogel composite, ii) particle-reinforced hydrogel composite iii) fiber-reinforced hydrogel composite, and iv) anisotropic filler-reinforced hydrogel composite, and highlight tailored physical properties and their functionality. Additionally, several emerging potential applications of hydrogel composites in the field of tissue engineering and their accompanying challenges are discussed in parallel.

2. 3D Printing Technology for Hydrogels Composite

2.1 Laser-based Hydrogel 3D Printing Systems

Most laser-based 3D printing systems are applicable for the hydrogel composite fabrications, which builds a 3D structures in a vat of photocurable hydrogels under the deposition of laser energy, usually UV range, in specific designed patterns[3]. The exposure of UV laser on to the surface of photocurable liquid causes gel-formation of a thin single layer, and it is sequentially moved upward or downward with the sample stage to allow the next layer formation on top of preformed structure. During this process, designed 3D structures are directly materialized in the liquid vat that means the hydrogel composites can be built within the photocurable organic-inorganic solution[3,18,19].

Since the development of laser-based 3D printing in 1980s, several other commercially available techniques have emerged, and they are widely used for biomedical applications such as scaffolds, drug delivery, implants, and devices[2,18]. Laser-based 3D printing system can be divided into several categories based on the type of laser source, beam delivering system, method of scanning or exposure, and type of stage movement system. However, most of these techniques require post-processing such as support removal and other unwanted materials. In addition, a post-curing procedure is necessary to completely cure the built structure for intact mechanical

stability. In this chapter, basic principle of popular laser-based 3D printing techniques for the hydrogels will be further discussed.

2.1.1 Stereolithography Apparatus

Stereolithography apparatus (SLA) is one of the most widely used 3D printing systems based on the layer-by-layer solidification of a liquid photocurable hydrogel. Computer-controlled UV-laser is scanned across the surface of the liquid hydrogel in a vat, and that leads to the formation the covalent bonds between the adjacent chains of photocurable polymers resulting a solidified single layer of the designed 2D pattern. The platform then descends a distance equal to the thickness of a single layer of the design to fully re-coat the surface of preformed 2D pattern with fresh liquid hydrogel[3]. This procedure is repeated until the 3D object is complete, as shown in (Figure 1A). Interconnection between the 2D patterns of each layer can be achieved in the precisely controlled optical scanning system with slightly larger focusing depth than the one-layer height[3,18].

Generally, SLA 3D printing system has many advantages such as wide range of building volume (from 200 to 2000 mm), high structural resolution, and good quality surface finishes. In addition, high accuracy and consistency of 3D printed objects could be achievable by controlling UV-laser power, scanning speed, exposure time, spot size, and wavelength[2,18]. Despite its advantages, the limited range of photocurable hydrogels, requirement of support structures, and post-curing process are the major drawbacks of SLA techniques in hydrogel composite fabrication.

More recently, the resolution of SLA has been improved by a complex optical system for the beam delivery. With this micro fabrication technique of SLA, also known as micro-stereolithography (μSLA), light beam can be focused into a spot size of few micrometers, which requires

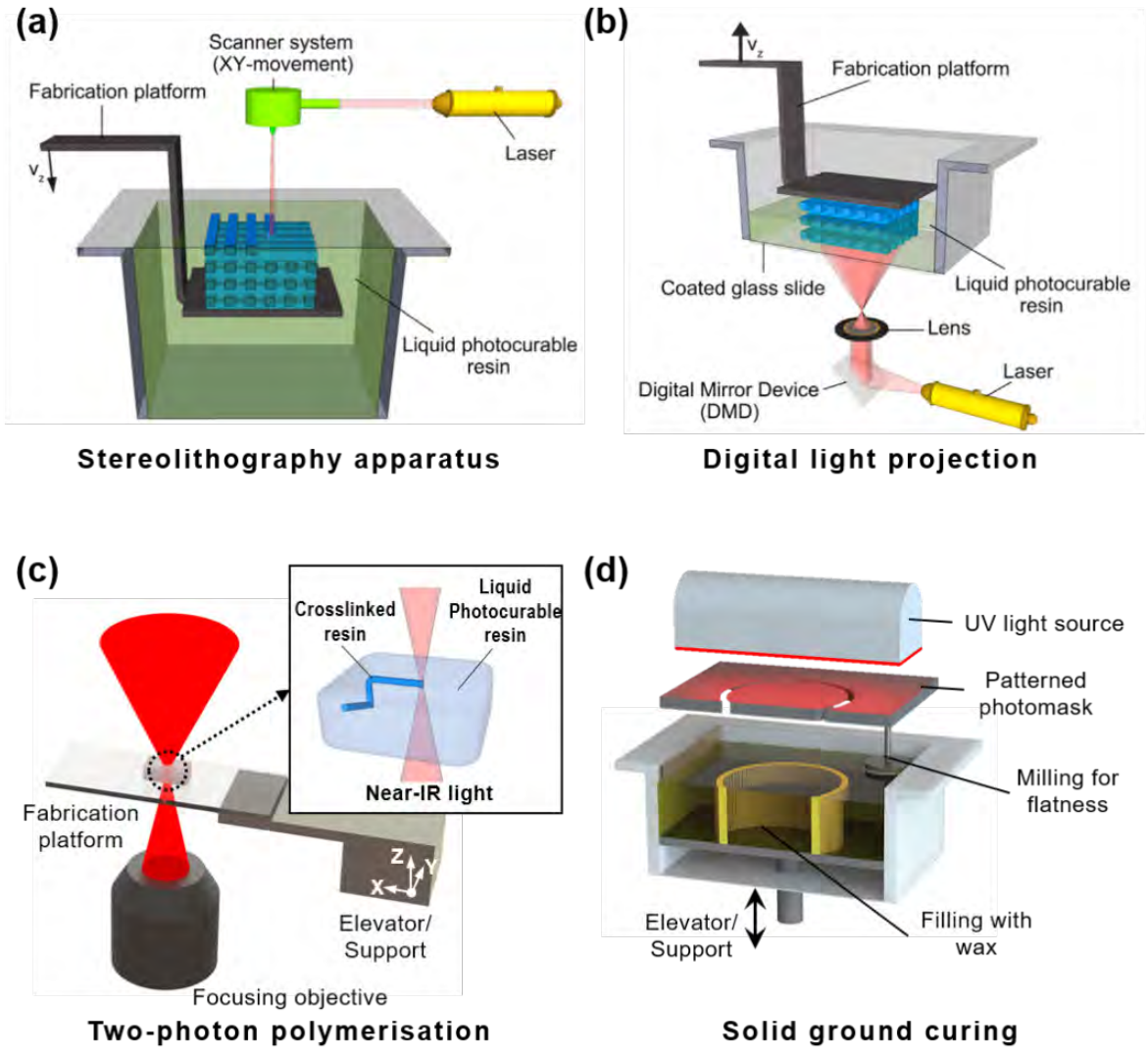

Figure 1. Schematic images of laser based hydrogel 3D printing systems.(reproduced with permission from [3]. Copyright 2012, Elsevier Ltd).

precise beam controlling and scanning system[19]. So far, μSLA can be categorized into (i) scanning μSLA system and (ii) mask (or integral) projection μSLA system. In the scanning μSLA, UV beam is fixed with a stationary spot position onto the liquid hydrogel surface, and scanning is conducted by moving the work piece stage including the vat, which can eliminate the unstable mobile optical elements leading to focusing errors and poor resolution[20,21]. In the mask projection system, light beam exposure of each liquid hydrogel layers is conducted in a single radiation using dynamic pattern generator mask. The sliced 2D patterns of 3D structure is converted into a data file and input to the light beam mask, which can generate the precise patterns corresponding to the each layer of structure[22,23]. The patterned beam is focused by the computer-controlled focusing optical components to reduce the whole pattern size into micrometers. The highly precise 3D structure containing complex engineered shapes can make a unique interface between the nano-scale functional second materials and macro-scale hydrogel molecules, which provides an engineering platform for various industries, such as tissue engineering, photonics, and microelectromechanical system (MEMS)[19,23].

2.1.2 Digital Light Projection

Digital light projection (DLP) is developed from the mask projection system of SLA. However, in this 3D printing system, digital mirror device or liquid crystal displays play a role of dynamic pattern generator mask, which consists of several millions of arrayed mirror or LCD pixel units to generate an individual on-off beam signal (Figure 1B). The DLP light source allows fabrication of the 3D structure with high resolution between 25 and 150 μm, which can be further enhanced with additional multi lens components to focus the light beam sources[2,3,18]. In comparison to other 3D printing systems that have bottom-up construction approach, DLP is based on a top-down working principle[24]. The beam source is placed at the bottom part of system, photocurable liquid hydrogel is exposed by the beam through the transparent contact window underneath the vat. The building plate or carrier is immersed into the liquid hydrogel and moves vertically upward direction after each layer is polymerized. In this process, fresh liquid hydrogel is automatically supplied to the bottom layer through the capillary action, and each repetitive processing steps can be conducted within 15 seconds[2,3]. In the DLP system, any planarization or levelling process is not required which allows to increase the building speeds and thus eliminate the fabricated parts from damaging during the wiping actions.

2.1.3 Two-Photon Polymerisation

Two-photon polymerisation (TPP) is an entirely new stereolithographic strategy to fabricate nanoresolution structures without undergoing the layer-by-layer process. The light source of TPP system is femtosecond infrared laser pulses that is focused into the volume of photocurable liquid materials, and initiates photolytic polymerization process without any masks[3,18,25]. In contrast to the UV light, nonlinear behavior and existence of polymerization threshold intensity of infrared light allow direct fabrication of complex 3D structure inside the photosensitive liquid with much higher structural resolution as high as 200 nm. Thus, 3D printed objects by TPP obtain better quality than the parts fabricated by conventional stereolithography techniques, as shown in (Figure 1C)[3,18]. Because of its ultra-small focusing spot size, the scanning of tightly focused beam of ultra-short laser pulse is precisely controlled by a computer positioning system combined with piezoelectric stages and/or optical scanning systems. The high intensity of photons from the two-focused beam source causes excitation of the photoinitiator molecules resulting in the creation of free radicals. These free radicals break the unstable bond of monomers and initiate the polymerization process. As a result, polymer chains can be formed and grown by combining monomers and adding to the chains. Although conventional photosensitive materials and initiators have been developed, such polymer still suffers from the insufficient free radical density within the extremely small cross-sectional focusing area for two-photons[26,27]. Thus, enough duration of each scan position, high density of photoinitiator, and intensity of focused light beam are most important parameters to terminate the photopolymerization procedure with enough crosslinking density.

TPP is promising 3D printing technique for biological applications, such as drug delivery, implants, biosensors, and tissue engineering. Since infrared light does not cause any harmful effect to the living cells or organisms, customized 3D scaffold structure can be directly fabricated in the presence of living cells[28]. Furthermore, it allows the introduction of pores at any location within the structure, which enables precise control of the cell position, movement, interaction, and organization inside the scaffold and, consequently, integrity with host tissue inside the body[18,27,28]. For the practical application in tissue engineering, hybrid materials with either organic/organic or organic/inorganics are consistently introduced for the better cell affinity and biocompatibility of 3D printed scaffolds.

2.1.4 Solid Ground Curing

Solid ground curing (SGC) is one kind of projection beam systems developed by Cubital Inc. in 1986. In this system, the fabrication of the each layer patterns of 3D object is done by a high-powered UV lamp in the presence of the patterned mask over the surface of photocurable materials[18,29,30]. The patterned mask is

built by the machine prints on the glass plate, and placed in between the light source and the fabrication platform. The fabrication principle of this technique resembles the previous SL printers, but it has unique features of process and support material design. Every fresh photocurable materials are coated on top of fabricated structure by spraying method. After UV light irradiation on the liquid materials, uncured material is removed by vacuum and filled with a wax as a supporter for the next layer (Figure 1D). During these repeating this process, planarization or levelling procedure of coated new layer is necessary for the accurate and reliable finishing. After printing, the wax is melted away from the 3D structure[18,29].

2.2 Nozzle-based Hydrogel 3D Printing Systems

Nozzle-based printing method is the most popular technique to build hydrogel based scaffolds. The melted polymers or viscous liquids are forced and extruded out of a nozzle, syringe or orifice and solidified onto a building stage as shown in (Figure 2A). 3D structures are constructed through sequential extruding material layer-by-layer which follows a predesigned path constructed by computer modelling. The key to successful 3D printed structures using this method is good interlayer adhesion between layers. Hence, various parameters of hydrogels such as solidification temperature, rheological properties and the gel setting mechanism are critically important. In extrusion-based printing, polymers must be either viscous or viscoelastic initially. These printed layers are cured and become self-supporting hydrogels before next layers are printed.

Nozzle-based printing can be categorized into two groups: techniques with melting process and techniques without melting process. Nozzle-based printing with melting process include fused deposition modelling (FDM), precise extrusion manufacturing (PEM), multiphase jet solidification (MJS), precision extrusion deposition (PED), and 3D fiber deposition[31–34]. FDM technique is the most commonly used nozzle based 3D printing method in which thermoplastic filaments such as poly(lactice acid) (PLA) and acrylonitrile-butadiene-styrene (ABS) are melted by heating and extruded on the build plate[35]. However, all techniques with a melting process are not suitable processes to deposit hydrogel since applying heat to hydrogel can cause a decrease in biocompatibility and thermal degradation[3,36]. Heat treatment for sol-gel transition of hydrogels at elevated temperatures induces critical damage to cells loaded in the hydrogels, resulting in acute cell death[37]. In addition, unlike thermoplastic polymers, hydrogels are in the form of viscous liquid and cannot be used as materials for FDM as they cannot be shaped into filament due to their poor mechanical properties.

Therefore, most of hydrogel-based 3D printings studies are performed by printing techniques without melting process including five major categories, 3D bioplotting, pressure-assisted microsyringe (PAM), direct ink writing (DIW), low-temperature deposition modelling (LDM), and robocasting, based on the proposed categorization of nozzle-based printing systems by Billiet *et al.*[3] These printing techniques allow rapid fabrication of structure with improved mechanical integrity. Moreover, they have been widely used for extrusion of hydrogel-based composites as well as hydrogels with drug or cell delivering capabilities. These techniques without melting process can be further classified by their working principles such as mode of extrusion, nozzle design, and type of materials as described in the following section.

2.2.1 3D Plotting

In 2000, Freiburg Materials Research group first developed 3D plotting method to produce scaffolds for soft tissue engineering[38]. 3D plotting method uses viscous hydrogels which are initially loaded in a syringe and injected through a micro-needle used as the extrusion nozzle into a liquid solution with a density similar to that of the hydrogel. The hydrogel from a pressurized syringe can be deposited as a single continuous microstrand or as individual

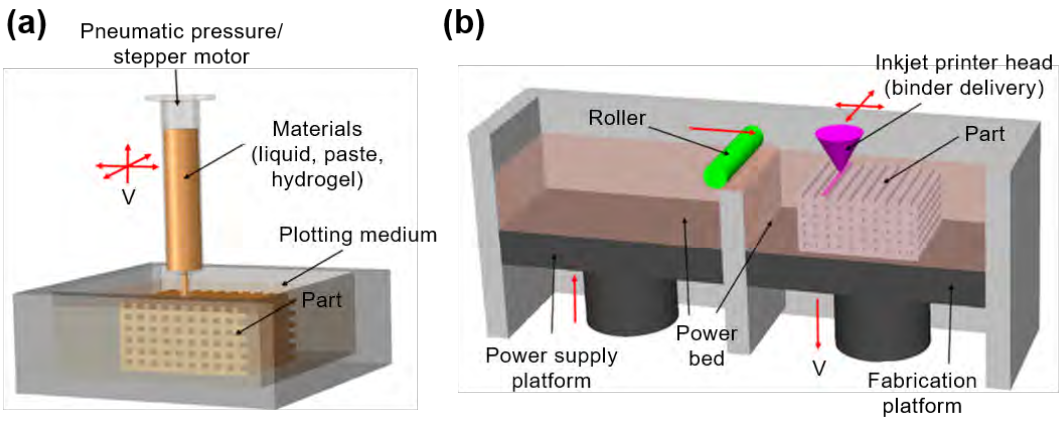

Figure 2. Schematic images of (**A**) nozzle and (**B**) inkjet printer based hydrogel 3D printing systems. (reproduced with permission from [1]. Copyright 2017, Elsevier Ltd)

microdots. The thickness of microstrand can be controlled by the viscosity of hydrogel, deposition rate, diameter of nozzle, and applied pressure. The material dispensing head generally moves in x, y, z directions, while the build platform is kept in place. Liquid flow is generated by working stepper motor (volume-driven injection nozzle) or filtered air pressure (pneumatic nozzle). The key point of this technique is to plot hydrogel into a liquid solution with a carefully designed density that matches that of the hydrogel.

Various materials can be used in 3D plotting system such as hydrogels, nanocomposite hydrogels, polymer sol, and bioactive polymers such as proteins[39–42]. Materials with low viscosity can also be used in plotting since deposition takes place in a liquid medium with a matching density. Moreover, thermal sensitive biocomponents such as growth factor and even cells can be incorporated into hydrogels because heating is not required. Extruded hydrogels can be cured by plotting in a reactive solution or by using mixing nozzles with multiple dispensing component. However, the microstrands of scaffolds constructed by 3D plotting technique normally possess smooth surfaces, which cause unfavorable environment for initial cell adhesion. Thus additional surface treatment has been researched for fabricating the favorable surface with modified initial cell adhesion[43].

2.2.2 Direct Ink Writing (DIW)

Direct ink writing (DIW) or direct write assembly (DWA) was first investigated by Lewis *et al.*[44] A variety of inks such as hydrogels, nanoparticle filled inks, colloidal suspensions and gels, and organic inks can be printed in 2D and 3D patterns with feature sizes ranging from 100 nm to 1000 μm. Components of DIW apparatus are the three-axis translation platform, compressed air supply, cylindrical nozzle, and optical microscope for real-time monitoring. The hydrogels are stored in each orifice mounted on the Z direction motion stage and printed through a nozzle onto a moving XY stage. The pressure of orifice and printing speed depend on nozzle diameter and rheology of hydrogel, respectively.

There are two important considerations regarding the hydrogels used in DIW technique. First, they must obtain self-supporting ability and spanning shapes with controlled viscoelastic characteristics. Therefore, extruded hydrogels should set instantly to enable feature retention of the printed structures. Second, high concentration of nanoparticle or colloid in hydrogels is preferred to reduce shrinkage during the drying process of the completed assembly. Generally, 70–85 wt% of solid loadings in hydrogels are preferred for assembling planar and spanning filaments[45]. The nanoparticle or colloid network in hydrogels is able to resist compression stress caused by capillary tension, thereby preventing spreading during extrusion.

2.2.3 Pressure-assisted Microsyringe (PAM)

The PAM technique, similar to FDM without heating system is first proposed by Vozzi in 2002[46]. In the initial stage, pneumatic driven glass capillary microsyringe which moves in the vertical plane was used to deposit materials on a substrate. Vozzi and his research group modified PAM systems for hydrogel microfabrication[47]. Compressed air and pneumatic driven microsyringe were replaced with a stepper motor and piston assisted microsyringe, respectively. Moreover,a temperature controlled syringe module with an aluminum jacket was added to control the temperature of deposit materials.

2.2.4 Low-temperature Deposition and Manufacturing (LDM)

Xiong *et al.* designed LDM systems to overcome heating process[48]. In this technique, temperature is decreased to solidify materials. Materials such as hydrogels are embedded in feeder connected to a screw pump nozzle and injected from the nozzle that can move along the XY axis onto a building stage at a temperature below 0 °C. Printed scaffolds are necessary to undergo freeze-drying process to remove the solvent. Modified LDM technique, called multinozzle low-temperature deposition and manufacturing (M-LDM) was developed by incorporating multiple nozzles with different types [49]. They are used for fabrication of scaffolds with gradient structures and materials by the incorporation of additional jetting nozzles into the LDM process.

2.2.5 Robocasting

Robocasting is also a nozzle based process which was originally adapted to produce ceramic scaffold using highly loaded ceramic slurries[50]. The system is composed of stationary dispensing head and movable platform that can move in X, Y and Z axis. The slurry injected layer by layer from a syringe has to sustain their weight and the weight of next layers to sustain the printed features. Thus, low viscous slurry or hydrogel alone are inadequate for robocasting technique. Recently, hydrogels were applied as carriers for ceramic powder in this system. Although the final product is a ceramic scaffold that is formed through burning out hydrogels, this result indicates the great potential of robocasting process in fabrication of hydrogel-based composites.

2.2.6 Other Apparatus

Nozzle-based 3D printing process is a promising technique to fabricate hydrogel-based composite scaffolds due to its versatility in various printing conditions. This technique is capable of printing large porous structures for infiltrating body fluid and controlling mechanical and biological properties, which cannot be carried out by other hydrogel

3D printing techniques. However, there are some drawbacks such as limitation of material type, nozzle condition, and natural ability of this process hinder its potential.

To date, scaffolds fabricated by nozzle based 3D printing technique show low resolution and poor mechanical properties. Compared to laser based 3D printing and droplet based 3D printing technologies, the resolution of nozzle based 3D printing is relatively low. Moreover, the resolution is dependent on the solid loading or particle size on hydrogel-based composites. As the hydrogel is extruded from the nozzle, it does not have the material strength to maintain the structure and result in sagging or collapse of unsupported parts. This phenomenon of mechanical property deterioration is aggravated during the printing process of scaffolds without the assistance of supporting materials or liquid medium. When the hydrogel materials possess sensitive biocomponents such as cells or ECM or growth factor, low printing speed and external pressure on materials may lead to function loss or damage of biocomponents.

For solving these disadvantages, other improved and combined nozzle based systems have also been reported steadily. Multi-head deposition system (MHDS), bioExtruder, screw extrusion system (SES), combined rapid freezing and plotting system, modified plotting system and porogen-based extrusion system are some of the novel attempts[51–56]. These techniques were investigated to enhance manufacturing flexibility by increasing the capability of deposition in accomplishing optimum scaffold requirements.

2.3 Inkjet Printer-based Hydrogel 3D Printing Systems

3D printing technology, also known as additive manufacturing, originated from 2D inkjet-based printer. It was first developed at the Massachusetts Institute of Technology (MIT) in 1993 by depositing liquid binder onto a powder bed[57]. Inkjet printer is a non-contact technology which prints droplets of ink onto a material platform. It is composed of a printer head which possesses liquid binder cartridge and moves in the XY plane and a build platform that is movable along the Z axis as shown in (Figure 2B).

Inkjet printing process can be divided into two types; continuous inkjet (CIJ) printing and drop-on-demand (DOD) printing[58,59]. In CIJ printing, liquid binder emerges continuously from a nozzle to form a jet which breaks up into droplets by the Rayleigh instability, whereas individual droplets are ejected only when electrical signals result from thermal or piezoelectric effect in DOD printing. Both systems offer droplets ranging in size from 15 to several hundred microns. However, DOD printing is preferable for fabricating biological structures of soft tissue engineering applications due to the reduced possibility of contamination and good controllability[60].

As mentioned above, piezoelectric or thermal force is used to eject liquid drops in DOD printing systems. In piezoelectric inkjet printer, the application of external voltage to piezoelectric actuator generate pressure to eject droplets from nozzle. Thermal inkjet printer, which possesses low cost, high print speed, and wide availability, uses an electrical heating to generate pulses of pressure that leads to the vaporization of liquid. Application of air-pressure pulses eject small droplets from the nozzle. Heating temperature is usually in the range from 200 °C to 300 °C, which can lead to denaturalization of hydrogels or biocomponents in hydrogels. However, due to the short heating time (~2 μs) in the printing process, heating has shown no detrimental effect on the stability of biocomponents in recent studies[61].

Similar to other 3D printing techniques, hydrogel scaffolds predesigned by computer modeling are constructed layer-by-layer with deposition materials. And there are a variety of material that can be used in inkjet 3D printer. These can be categorized in two types by starting materials on platform as described in the following section.

2.3.1 Inkjet Based 3D Printer with Powder (I3DP-P)

I3DP-P system (Figure 3A) is the representative solid-phase rapid prototyping technology. This system can use various materials including ceramic, metals, polymers as well as hydrogels[62–65]. The process is a 3-step process. The first step in 3D printing is the spreading of powder onto a platform with a roller. Second step is the deposition liquid binder from inkjet print head with a 2D pattern onto the powder layer by bonding the adjacent powder particles together. The final step involves lowering the layer and filling the powder on the next layer. This process is repeated until the fabrication process is completed. The unreacted powder with binders can support the bonded structures, thus no supporting material is needed. Various types of powder such as a single powder, surface-coated powder, and a mixture of different powders are used in this system. Selection of suitable biocompatible powder and binder is the most important part in I3DP-P system.

2.3.2 Inkjet-based 3D Printer with Liquid (I3DP-L)

There are two types of I3DP-L (Figure 3B). The working principle of the first type is similar to the I3DP-P system but the powder bed is replaced by liquid materials[66], and the second type is a direct inkjet writing system which generally uses photosensitive resins[67]. In the case of the former system, uncrosslinked hydrogels are filled in bed platform which moves along Z-axis and the liquid crosslinker ink such as calcium chloride are printed from the print head. In direct inkjet writing systems, photosensitive resin ejected from inkjet printer head build are constructed by simultaneous curing with light. Compared with I3DP-P, fabricated scaffolds shows high

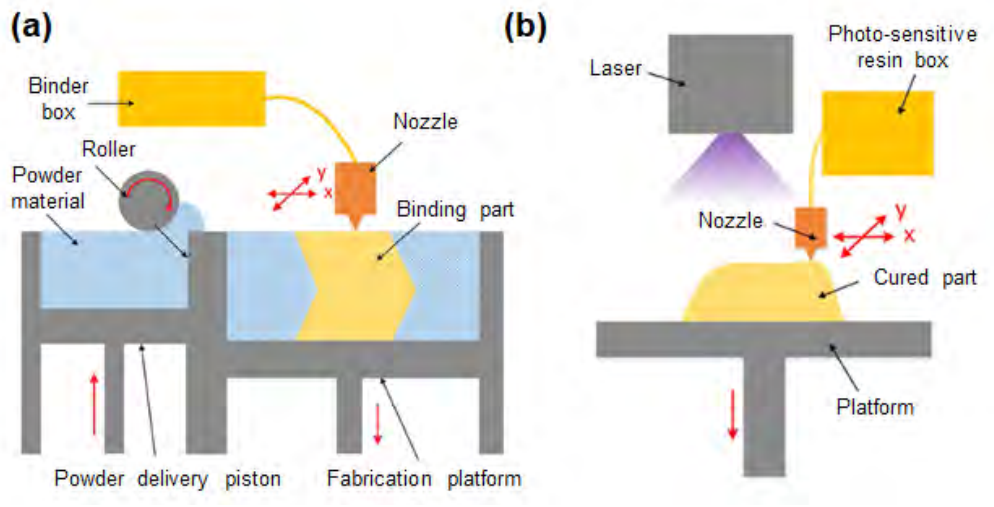

Figure 3. The schematic images of (**A**) I3DP-P and (**B**) I3DP-L printer based inkjet 3D printing system.(adapted with permission from [139]. Copyright 2016, John Wiley & Sons, Ltd).

accuracy, but the cost of I3DP-L is higher.

A wide range of materials can be used with both Inkjet-based 3D Printer with powder and liquid as these processes are done in room temperature. Moreover, these techniques offer more options for soft tissue engineering and bioprinting because incorporated biocomponents are not subjected to deleterious effects of laser-mediated fusion or force by extrusion. However, post processing is required as water soluble liquid binders often remain after 3D printing. In addition, it is difficult to remove internal unbound powder or liquid which were trapped in the negative spaces such as hollow structures.

3. 3D Printing of Hydrogel Composites

Hydrogels provide many advantages for tissue engineering and cell delivery applications owing to their tunable degradability, biocompatibility, and capacity to be modified. However, their inherently poor mechanical properties make them unsuitable for applications requiring strength such as load bearing components. The rapid biodegradation behavior of hydrogels also has greatly limited their further application in the tissue engineering. In addition, in the case of biodegradable synthetic hydrogels with polyester chains, acidic by-products during the hydrolysis degradation process of ester bonds were found to induce the side effects to the cells[68]. Therefore, the addition of materials including metals, ceramics and polymers were essential to improve some of the limitation of hydrogels.

Printability is one of the most important criteria to consider for 3D-printing of hydrogel based composites. It plays a critical role in determining the degree of accuracy and precision relative to the computed spatial and temporal design. The printability of hydrogel composites requires stimuli-dependent viscosity to be used in various printing methods which may involve changes in temperature and shear thinning to prevent the nozzle from clogging and to maintain the intended shape after printing. Research has reported the addition of ceramic or metal based nano or microparticles as rheology modifiers often interrupt the crosslinking of hydrogels, thus decreasing the printability of materials[69]. In addition, the incorporation of these additives may lead to a decrease in the accuracy of printed scaffolds due to an increase in nozzle size or even make the resulting material completely unusable. Therefore, many studies have tried to print hydrogel scaffolds by incorporating additional hydrogels, soft polymers or inorganic second phases.

3D printing techniques for the fabrication of hydrogel composites can be categorized into (i) polymer or other hydrogel reinforced composite (ii) particle-reinforced composite (iii) anisotropic filler-reinforced composite, and (iv) fiber-reinforced composite hydrogel printing systems, as represented in Table 1. It should be noted that for the category (i), hydrogel-reinforced composites, matrix and reinforcement materials were defined based on the volume fraction of hydrogels in the composites according to our framework. For instance, if gelatin has a higher volume fraction than alginate does in their composite, we assume that gelatin is the matrix and alginate is the reinforcement for this gelatin-alginate composite. These categories will provide a platform for designing an appropriate combination of materials and 3D printing technique for achieving the desired properties. Each system involves an innovative combination of reinforcement and hydrogel matrix that generate not only mechanical strengthening but also a plurality of property enhancements such as biological activity, degradation tunability, and enzyme sensitivity.

Table 1. The summary of methods and materials for 3D printing of various hydrogel composites

Reinforcement type	3D printing methods	Matrix materials	Reinforcement materials	Properties	Potential application	Ref.
Gel	3D plotting	Alginate	Poly(acrylamide)	Improved tensile properties	Tendon	[70]
	3D plotting	Gelatin	Alginate	Maintained tensile biomechanics	Aortic heart valve	[17]
	3D plotting	Collagen	Gelatin	Formed vascular construct with cell	Vascular tissue	[71]
	3D plotting	PEGDA	Alginate	Improved toughness	General	[72]
	3D plotting	Alginate	Nanocellulose	Improved storage modulus	Cartilage (Ear)	[73]
	3D plotting	PEGX	Gelatin	Improved storage modulus and critical strain	General	[74]
	3D plotting	Gelatin-alginate	Fibrinogen	Improved cell differentiation and self-organization	Drug discovery	[75]
	3D plotting	Alginate	Gellan gum	Improved swelling ratio and stiffness	General	[76]
	3D plotting	PCL	PEG, HAc	Improved storage modulus	General	[77]
	3D plotting	PEG	P(HPMAm-lactate)	Improved rheological properties and degradation rate	Cartilage	[78]
	DIW	HAc	Glycidyl methacrylate	Improved mechanical properties	General	[79]
	LDM	Collagen	PU	Improved nerve regeneration capability	Nerve conduit	[80]
	Robocasting	Chitosan	Alginate	Large-scale structures	General	[81]
	Inkjet printer	Alginate	Gelatin	Cell printing	General	[66]
	Inkjet printer	Starch	Cellulose, Dextrose	Improved elongation	General	[65]
	DLP	PU	HAc	Improved degradation rate	Cartilage	[82]

Table 1. (continued).

Reinforcement type	3D printing methods	Matrix materials	Reinforcement materials	Properties	Potential application	Ref.
Particle	3D plotting	Alginate, Gelatin	Bioglass (55 nm)	Improved cell proliferation and mineralization	Bone	[83]
	3D plotting	Methacrylated chitosan	Graphene oxide (430–460 nm)	Improved elastic modulus, tensile strength and conductivity	Biomedical device	[84]
	3D plotting	Alginate, Gelatin	Hydroxyapatite (183 nm)	Improved mechanical properties and biological properties	Bone	[85]
	3D plotting	Thiol-modified hyaluronic acid	Gold nanoparticle (24 nm)	Decreased gelation time, and improved mechanical properties	Vessel	[86]
	3D plotting	Alginate	Biphasic calcium phosphate (106–212 μm)	Improved biological properties	Bone	[87]
	Inkjet printer	Natural polysaccharides gums	Carbone nanotube (10 nm)	Improved radiopacity and conductivity	Biomedical device	[88]
	Casting + FDM	GelMA	PLA 3D structure (200 μm)	Improved mechanical properties	Bone	[89]
	SLA	PEGDA	Hydroxyapatite (50–100 nm)	Improved biological properties	Bone	[90]
	SLA	PEGDA	Hydroxyapatite (80–100 nm)	Improved mechanical properties and biological properties	Cartilage	[91]
Fiber	3D plotting	Acrylamide	Cellulose short fibril	Anisotropic swelling behaviors	4D printing	[92]
	3D plotting	Alginate	PLA continuous nanofiber	Improved mechanical properties and biological properties	Cartilage	[93]
	Casting + 3D plotting	PEGDGE, Acrylamide	PU continuous microfiber	Improved mechanical properties	General	[94]
	3D plotting	Alginate, Acrylamide	Emax (UV-curable epoxy)	Improved mechanical properties	Cartilage	[95]
Anisotropic filler	DIW	PEGDA, alginate, gelatin	Laponite RD, Laponite XLG	Improved self-supporting capacity and young's modulus	General	[96]
	3D plotting	N-acryloyl glycinamide	Laponite XLG	Improved tensile and compression properties and biological properties	Bone	[97]
	3D plotting	Alginate-methylcellulose	Laponite	Improved shape fidelity and sustained drug delivery	Bone	[98]

3.1 Polymer or Other Hydrogel Reinforced Hydrogel Composites 3D Printing

Hydrogels for 3D printing can be divided into protein-based natural hydrogels such as gelatin, collagen, silk or polysaccharide-based natural hydrogels such as chitosan, agarose, hyaluronic acid (HAc), alginate, cellulose, or synthetic hydrogels such as poly(ethylene glycol) (PEG), polyurethane, polyacrylamide. Alginate, a common hydrogel crosslinked by ionic interactions or phase transition, has been widely used in the field of soft tissue engineering owing to their biodegradability and low toxicity. However, alginate limits cellular adhesion due to the lack of adhesion sites for cells. Markstedt *et al.* investigated 3D printing materials for cartilage tissue engineering applications by combining alginate and nanofibrillated cellulose[73]. Their rapid cross-linking ability and the shear thinning properties make the scaffolds fabricated by 3D plotting method stable. Human nasoseptal chondrocytes encapsulated in nanofibrillated cellulose/alginate hydrogels exhibited

86% of viability at day 7 after 3D culturing. Xu *et al.* fabricated a composite extracellular matrix by printing alginate/gelatin hydrogels with incorporating fibrin which is a natural scaffold material[75]. Fibrin acted as an important component to regulate self-organization and differentiation of adipose derived stromal cell. This printed hydrogel composite functions as an extracellular matrix that can offer an environment for cell growth and a platform for drug delivery in soft tissue engineering. The gellan gum, a versatile gelling agent, was introduced as compounding materials in 3D plotting method by Akkineni *et al.*[76] They mixed high concentration of alginate and 2–3 wt % of gellan gum. The addition of gellan gum prevents rapid swelling and thus improves the shape fidelity of printed scaffolds. Moreover, human mesenchymal stem cells on alginate/gellan gum composites displayed higher degree of cytocompatibility compared with pure alginate. The study explained that the improved initial cell attachment was related to the mechanical properties of hydrogels; stem cells preferred stiffer gels. Many researchers have highlighted that the cytocompatibility of gels is highly dependent on the mechanical properties of the hydrogel matrix.

In attempts to enhance the mechanical properties of hydrogel, two-component hydrogels consisting of a thermoresponsive polymer mixed with PEG or HAc were printed by 3D plotting[77]. Starting materials were crosslinked by chemoselective reaction and extruded hydrogels showed mechanically stable hydrogels with a storage modulus of 9 kPa after 3 h. The hydrogel composite containing HAc exhibited high cell viability of chondrocytes. Hong *et al.* developed 3D printed PEG/alginate hydrogel composite with stretchiness and toughness[72]. Fabricated hydrogel composites had higher fracture energy than the value of cartilage and high cell viability after 7 days of culturing. The toughness of this hydrogel composite is attributed to the reversibly crosslinked calcium ions dissipating the mechanical energy and the covalently crosslinked PEG chains contributing to high elasticity.

Another method to tailor the mechanical strength is to co-print hydrogel with a stiffer polymer. Hyaluronic acid, the main ECM component of cartilarge, with photi-reactive glycidyl methacrylate was printed as a porous scaffold by direct ink writing technique[79]. The stiffness of scaffold increased as the contents of functionalized glycidyl methacrylate increased. When implanted in a porcine mandibular model, it showed good cell compatibility and enhanced tissue growth. Bakarich *et al.* blended alginate/poly(acrylamide) with acrylated urethane UV-curable adhesive (Emax 904) to fabricate biomimetic hydrogel composites[70]. They adjusted the ratio of components by controlling the rates at which two materials stored in two separate syringes are dispensed into a single mixing nozzle (Figure 4A). As the volume content of Emax 904 increased, the tensile strength and elastic modulus also increased and this trend was in accordance with the rule of mixtures theory. Finally, they incorporated varying gradients into the printed scaffold to mimic living tissue such as tendon which links soft muscles to hard bone (Figure 4B).

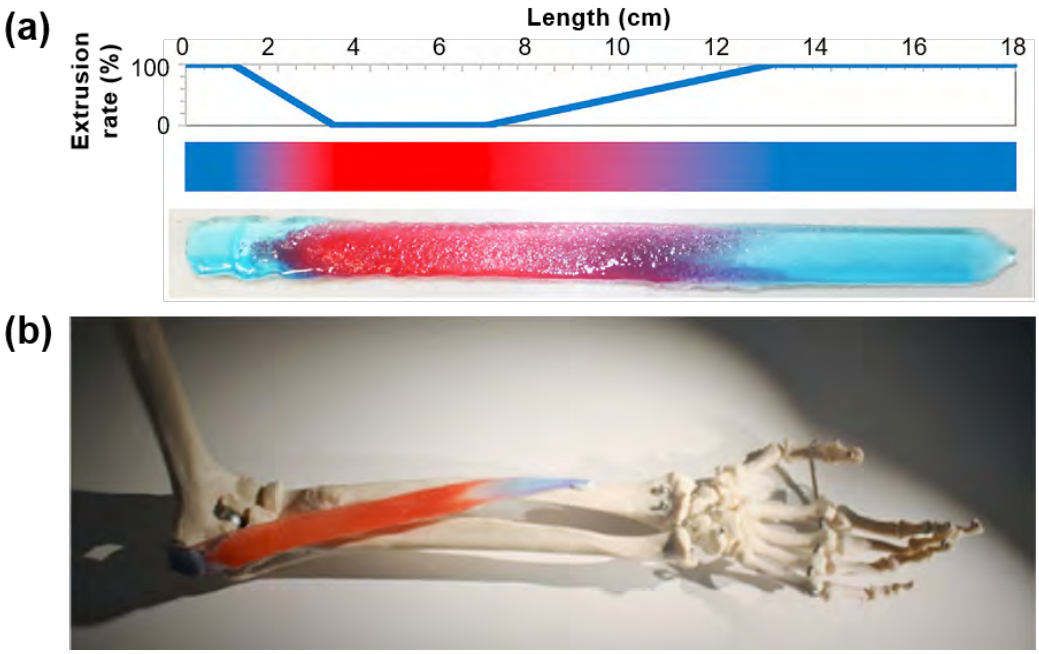

Figure 4. (**A**) The extrusion rate of Emax 904 as a function of the length and image of extruded gradient gel stained with red and blue dye. (**B**) Application of gradient gel which mimics the human tendon-muscle-tendon system in the place of pronator teres. (reproduced with permission from [70]. Copyright 2017, Elsevier Ltd).

A tunable degradation rate for hydrogels has also been thoroughly investigated so as to provide a tissue scaffold platform which gradually degrades over a few months as well as sufficient mechanical resistance. p(HPMAm-lactate)/PEG hydrogel composites are printed with 3D plotting method by Censi *et al.*[78] These hydrogel composites were crosslinked by thermal gelation and chemical crosslinks to stabilize the structure. Complete degradation of the printed scaffold was achieved in 190 days. In addition, the fabricated scaffolds showed similar mechanical characteristic with natural semi-flexible hydrogels such as collagen and displayed high chondrocytes viability after 1 and 3 days. Shie *et al.* also attempted to modify the degradation rate of hydrogels through a 3D printed polyurethane (PU)/HAc scaffold for use in cartilage tissue engineering[82]. The water-based polyurethane (PU) with varying contents of HAc were printed by DLP process. The diametral tensile strength and elastic modulus of PU/HAc hydrogel composite are higher than those of pure PU hydrogel. After 28 days of degradation test, PU/HAc hydrogel composites with varying concentrations of HAc all exhibited similar degradation profiles. However, in the case of PU/HAc hydrogel composite scaffolds with over 2% of HAc, scaffolds showed ductile behavior even after 28 days of degradation. Meanwhile PU hydrogel and PU/1% HAc hydrogel demonstrated brittle behavior after degradation suggesting that the addition of HAc facilitated the stable degradation of hydrogel composite scaffolds.

3.2 Particle-reinforced Hydrogel Composites 3D Printing

Incorporation of micro- or nanoparticles into the hydrogel is widely used to enhance the mechanical and biological properties of pure hydrogels due to their low cost, ease of preparation, and isotropic strengthening behaviors[11,12]. A particle-reinforced hydrogel composite is often formed from *ex situ* process in which the pre-formed or pre-purchased particles are dispersed into a hydrogel-forming liquid to be used for 3D printing (Figure 5A). This approach allows excellent control over the quantity of incorporated particles and greatly facilitates the study of optimal experiment conditions. Most particle-reinforced hydrogel composites are fabricated by this approach. For example, Fedorovich *et al.* used biphasic calcium phosphate (BCP) microparticles in the range of 106–212 μm for composite reinforcement and Matrigel or alginate as the hydrogel matrix. This particle-reinforced hydrogel composite was implanted in bone defects and used as an osteoinductive bone filler. Within 6 weeks of implantation, early osteogenesis of incorporated multi-potent stromal cells (MSCs) was induced. For 3D printing of particle-reinforced composites, nozzle sizes bigger than the microparticle size (420 um internal diameter) were used and a 10-layer 3D scaffold (10 × 20 × 1 mm) was fabricated *via* a 3D-bioplotter system. In the case of coarse microparticle-hydrogel composites, the mechanical enhancement is much lower compared to composites containing nano-sized particles, but it is easier to get a uniform particle distribution within the hydrogel through simple mixing due to its relatively low surface-to-volume

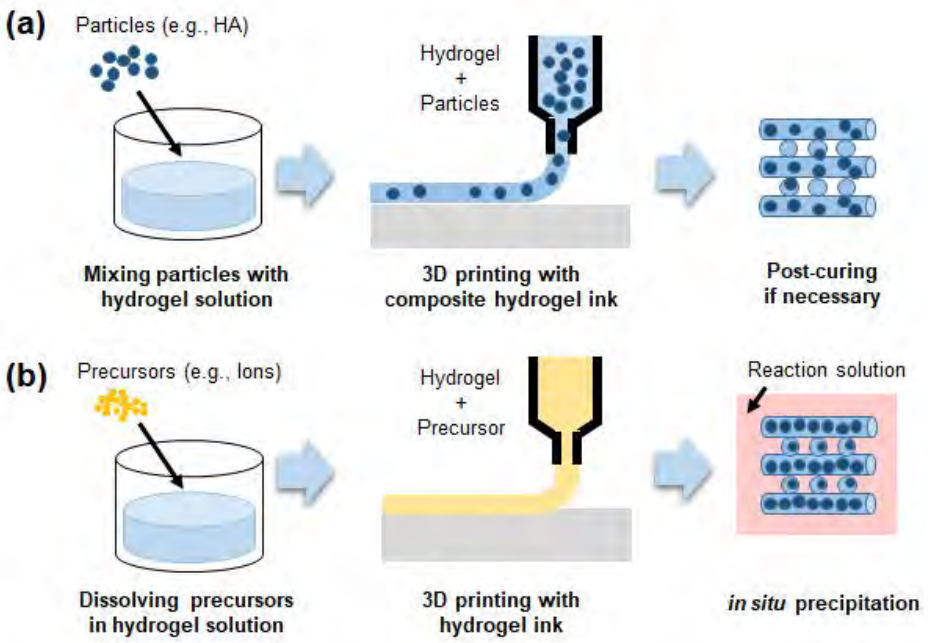

Figure 5. Schematic diagram of *ex-situ* and *in-situ* approaches for particle-reinforced hydrogel composite fabrication

ratio[87].

Nanoparticle-reinforced hydrogels offer better mechanical and biological properties than microparticle-reinforced hydrogels. For example, Wüst *et al.* added HAp nanoparticles to a gelatin/alginate hydrogel system for bone tissue engineering applications, as shown in (Figure 6A). Gelatin provided the initial viscosity and mechanical stability required for the hydrogel ink to be printable due to its temperature-dependent physical crosslinking behavior. The long-term stability of the printed structure is achieved by the ionic crosslinking of alginate (Figure 6B). They fabricated simple structures using 3D-bioplotter printing which was modified with an in-house-fabricated heatable cartridge up to 40 °C to enhance the printability of composite hydrogels. By adding HAp nanoparticles (8% w/v), the Young's modulus was significantly increased with during the 3 day incubation period (Figure 6C). However, varying HAp concentrations from 0 to 4% did not induce a significant enhancement in the mechanical properties. Incorporation of HAp nanoparticles additionally led to radiopacity and thus visibility of constructed scaffolds under X-ray based medical detection, as shown in Figure 6D[16]. Wang *et al.* investigated the effect of bioglass nanoparticles, with the size of 55 nm, on encapsulated SaOS-2 cells. An alginate/gelatin/SaOS-2 cell suspension supplemented with bioglass nanoparticles was placed into sterile 3D-bioplotter printing cartridges, and printed into a hydrogel scaffold (13 × 13 × 1.5 mm). During the incubation periods of 3 and 5 days, bioglass-reinforced alginate/gelatin hydrogel composites showed significant enhancement of proliferation and mineralization of bioprinted SaOS-2 cells[83].

In spite of the superior mechanical and biological performances of inorganic particles, the major problem of the *ex situ* incorporation approach is the limit on the maximum amount of particles that can be added to the hydrogel; introducing nanoparticles into the hydrogel rendered the printing ink more viscous and harder to print in the desired way. In previous studies, maximal nanoparticle inclusion to ensure proper printability and structural accuracy was found to be limited to 10%. Nearing the 10% nanoparticle inclusion, slight irregular filament shape and ununiform size distribution were induced[16]. Skardal *et al.* introduced gold nanoparticles (AuNPs) into semi-synthetic extracellular matrix (sECM) hydrogel composites which can generate dynamic crosslinking between intra-gel and inter-gel during and after printing. In particular, 2.5% w/v of 25 nm gold nanoparticle provided enough mechanical stability to support multilayered 3D structures by the physical reinforcement effect, and after 60 min of printing, adjacent filaments were completely joined by slow rate of inter-filament crosslinking between AuNP and sECM hydrogel[86]. This dynamically crosslinked AuNP-sECM hydrogel may provide new strategies in the *ex situ* particle incorporation approach for the 3D printing hydrogel composite system.

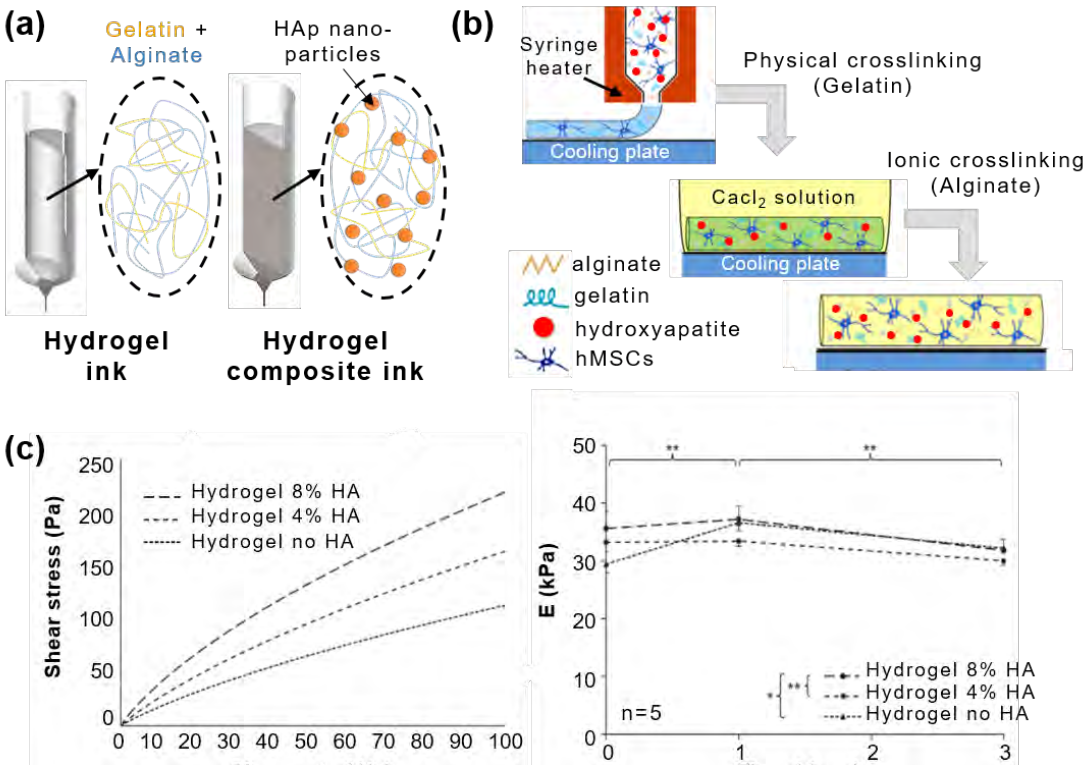

Figure 6. Schematic images of (**A**) gelatin/alginate hydrogel and its composite with Hap nanoparticles and (**B**) two-step hydrogel gelationprocess. (**C**) Rheological properties of hydrogel composites (left: shear stress plotted over a shear rate, right: elastic modules over 3 day). (**D**) Opticalmicroscopic and micro-CT images of 3D printed patterns. (reproduced with permission from [16]. Copyright 2014, Elsevier Ltd).

The *in situ* incorporation of particles into hydrogel scaffolds during and/or after 3D printing is more-effective approach than the *ex situ* method for achieving uniform distribution and high loadings, because post-loaded particles do not hinder the printing process (Figure 5B). Jeong *et al.* proposed a great potential of in situ precipitation process for high- and uniform-loading capacity with minimal agglomeration into a polymer matrix . Precipitated calcium phosphate (CaP) nanoparticles with 200–350 nm were easily formed and incorporated from calcium chloride and phosphoric acid mixed solutions. Compared with same concentration of pre-mixed CaP nanoparticles, precipitated HAc-CaP composite hydrogels exhibited homogeneous distribution and approximately five times higher storage moduli values. In addition, mechanical properties were continuously increased by increasing concentration of precipitated CaP up to 40 wt%[15]. Very recently, Egorov *et al.* combined *in situ* mineralization with 3D printing in which calcium chloride and ammonium hydrogen phosphate solutions were mixed with sodium alginate slurry and then 3D-bioplotter printing was employed to fabricate a cubic-shaped 3D composite structure (8 × 8 × 5 mm). The compressive strength of composite hydrogels were gradually increased from 0.4 to 1.0 MPa with increasing concentration of precipitated CaP up to 2.0 wt%. However, overall mechanical properties of 3D printed scaffold were relatively low due to the weak bonding between filaments, which is a major limitation of the in situ particle incorporation approach for composite hydrogel systems[99].

3.3 Fiber-reinforced Hydrogel Composites 3D Printing

Fiber reinforcements can also improve mechanical properties of hydrogel matrix in which the fiber contents and its distribution inside its matrix determine mechanical properties such as stiffness and strength of composites[92–95]. In the case of common 3D printing systems, short fiber reinforcements are the most commonly used due to its easy processing procedure at low cost. The fibers can be directly incorporated into the hydrogel matrix *via* simple mixing and transferred into the syringe for printing. Gladman *et al.* proposed stiff cellulose fibrils as a short fiber reinforcement and printed cellulose-acrylamide composite hydrogel 3D structures. For ensuring smooth, clog-free print behavior of composite ink, the maximum concentration of nanofibrillated cellulose inside a soft acrylamide matrix should not exceed 0.8 wt%, which was then transferred into the 3D-bioplotter cartridge and injected through stainless steel commercial nozzles of varying diameters. During the printing process, short fibers inside the composite ink undergo shearing forces due to the small nozzle size and orientate themselves along the printing direction, as shown in Figure 7A. This in turn induces anisotropic mechanical properties of printed filaments such as anisotropic stiffness and swelling behaviors[92].

In the case of long and continuous fiber-reinforced hydrogel systems, research has shown substantially improved mechanical performances due to the continuous fiber-hydrogel matrix interactions as opposed to disconnected interactions in short-fiber-reinforced hydrogels. As such, the load transmittance from the matrix to each fiber also becomes more continuous. However, in spite of its outstanding performance, the most challenging issue for applying this composite system to the 3D printing process are practical ways to achieve an uniform distribution and intended alignment of continuous fibers within the hydrogel matrix. Narayanan *et al.* tried to fabricate alginate-nanofiber bioink for 3D-bioprinting which could provide protection for encapsulated cells during the digitally driven fabrication process[93]. To prepare the composite hydrogel, pre-fabricated portions of PLA nanofiber was mixed with alginate (ratio 1:5, w/w), and agitated in a vortex mixer, and finally sonicated for 2 hours. Despite all these efforts, continuous PLA nanofibers were aggregated and poorly distributed within hydrogel matrix, which is mainly attributed to the strong van der Waal's attraction between the sub-micron scaled aggregated fibers (Figure 7B). In this paper, they could not prove there were any mechanical enhancement of nanofiber-reinforced composite hydrogels, but the nanofiber-reinforced bioink showed better cell proliferation and metabolic activity levels of human adipose-derived stem cells (hASC) within printed 3D structure that were encapsulated with cells[93].

Agrawal *et al.* approached this issue from a different angle. To build continuous fiber-PEG composite scaffold, elastic polyurethane (PU) fibers are printed first to form a "log-pile" structure, and then fabricated continuous fibers were impregnated with the PEG gel. The PU polymer solution was placed into a pressure-driven syringe fitted with a 100 μm needle, and mounted on the dispensing 3D printing system. The entire printing process was performed under water to form a continuous elastic micro fiber rapidly though solvent exchange. As with 24 wt% continuous fibers, the elastic modulus of composites were two-times higher, and the maximum strain-to-break ratio was greatly improved compared to that of pure hydrogels[94]. Bakarich *et al.* developed a more advanced technique for fiber-reinforced hydrogel composite system using a one-step process[95]. The previous approach requires at least a two-step fabrication process involving the 3D printing of continuous fiber scaffold structure followed by immersion of the scaffold into a hydrogel precursor solution, and crosslinking. However, recent development of UV curable material and light system of 3D printing have made it possible to fabricate fiber reinforced hydrogel composites using a one-step 3D-bioplotter process. This composite was printed by selectively patterning a combination of two different UV curable inks: one is alginate/acrylamide gel solution for the matrix, and the other is adhesive epoxy

resin (Emax 904 Gel-SC) for the reinforcement. Composite digital models of hydrogel matrix and fiber reinforcement were constructed using computer-aided designs and the printing path was also precisely generated by the software. For evaluating mechanical properties of fiber reinforced composite hydrogel, a dog-bone shaped tensile strength specimen with uniaxial oriented continuous epoxy fiber was successfully fabricated as shown in (Figure 7C). The printed composite hydrogels showed a combination of properties in between pure hydrogel and epoxy resin, and its elastic modulus, failure strength, failure strain properties were gradually increased by increasing the relative volume of epoxy fibers. A noticeable finding in this study is that there is no limitation of fiber reinforcement amount inside the hydrogel matrix. They showed extremely wide range of fiber volume fraction from 0 to 100% inside alginate hydrogel matrix, and the bone between the hydrogel and fiber is stronger than pure hydrogel so that under the applied stress, matrix and fibers were equally deformed without any interfacial slipping between them. The reinforced fibers experience a greater stress than the hydrogel matrix[95]. So far, these studies have only demonstrated the feasibility of 3D printing for fiber-reinforced composite hydrogel, but the further development of composite 3D printing techniques is crucial before they can be applied to various tissue engineering applications such as biofabrication of skin, muscle, tendons, and cartilage in the near future.

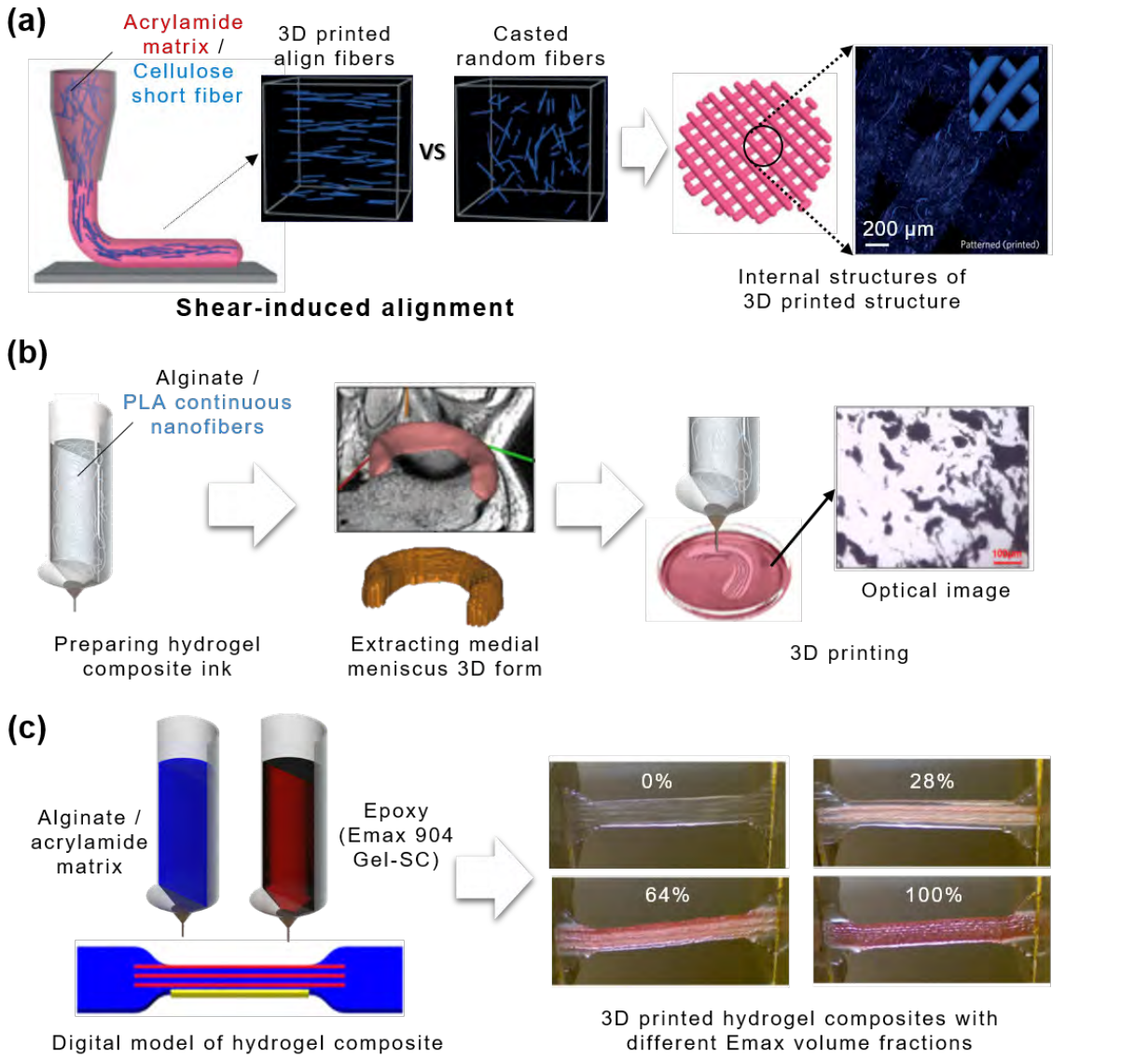

Figure 7. (**A**) Schematic images of cellulose short fiber alignment during the 3D printing (reproduced with permission from [92]. Copyright 2016, Macmillan Ltd). (**B**) Overview of 3D printing process of PLA nanofiber-alginate hydrogel composite, and its internal structure (reproduced with permission from [93]. Copyright 2016, ACS Publications). (**C**) Schematic image of the fabrication of hydrogel composite tensile specimen, and its photographs with different Emax volume fractions (reproduced with permission from [95]. Copyright 2014, ACS Publications).

3.4 Anisotropic Filler-Reinforced Hydrogel Composites 3D Printing

Nanoclay is a nanoparticle which is composed of layered hydrous silicate. It has been used in a wide range of applications such as pharmacy, paints, cosmetics as well as catalysis owing to their good surface properties and excellent rheology controllability. Depending on the type of clay, each layer consists of two or more sheets of either $(AlO_3(OH)_3)_6$ octahedra or $(SiO_4)_4$-tetrahedra. Nanoclays are classified into several classes such as Laponite, montmorillonite, bentonite, nontronite, saponite, kaolinite, hectorite, and halloysite by their geometrical shape and chemical composition which can affect biocompatibility. Rawat *et al.* investigated the cytotoxicity and antimicrobial properties of various shape and concentration of nanoclays[100]. They prepared Laponite with an aspect ratio of 25:1 and montmorillonite (MMT) with an aspect ratio of 300:1, The cytotoxicity and antimicrobial properties of both nanoclays with various concentration from 0.00005 ug/mL to 0.0125 ug/mL were assessed by eukaryotes-human embryonic kidney (HEK), and cervical cancer SiHa cell and Kirbey-Bauer protocol method, respectively. Laponite exhibited good antimicrobial properties, while MMT showed better cytotoxicity. Their explanation behind this finding is due to the difference in charge density and anisotropy of the clays. Modification of nanoclays as organic-inorganic hybrid nanomaterials have potentials for use as rheological modifiers, gas absorbents and drug delivery carriers in customizing polymer composites.

Laponite, a synthetic magnesium silicate, is well known as a nano biofiller in cosmetics. The potential use of Laponite as tissue engineering constructs has been discussed because they enhance cell spreading and promote osteogenesis. The crystal structure of Laponite is a disc-shaped layered magnesium silicate with a particle size of approximately 25 nm in diameter and 1 nm in thickness as shown in (Figure 8A). These ultrathin structures with a high degree of anisotropy and functionality enhance their surface interactions. In addition, Laponite is negatively charged on its face and positively on the rim thus undergoes self-assembly through electrostatic interactions to form a shear thinning gel state with a "house-of-cards structure" (Figure 8B)[101]. Therefore, many studies have been carried out on blending Laponite with polymers for improving mechanical and biological properties. Hydrogels with poor mechanical properties can yield these properties by forming strong interaction between chains of hydrogel and monodispersed Laponite. Su *et al*. fabricated silk fibroin hydrogel composites with Laponite for bone defect repair application[102]. As the concentration of Laponite increased from 0 to 5%, rheological properties of hydrogel composites increased from 30 to 200 kPa. Osteoblasts cell proliferation and differentiation also increased with the addition of Laponite. Injectable hydrogel naoncomposite was investigated by combining Laponite and dopamine-

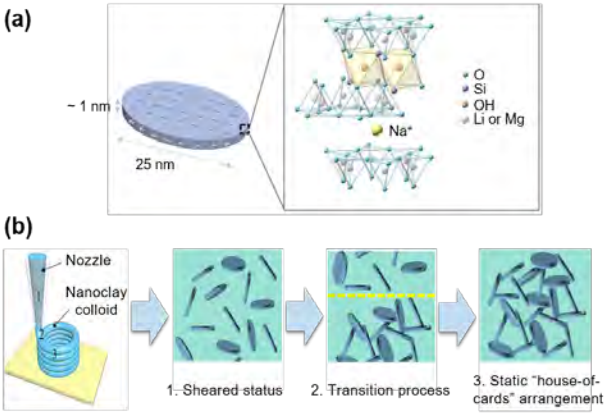

Figure 8. (**A**) The structure and composition of Laponite nanoclay as an anisotropic filler and (**B**) "house-of-cards" mechanism of self-assembling printed hydrogels including Laponite. (reproduced with permission from [96]. Copyright 2017, ACS Publications).

modified four-armed poly(ethylene glycol) (PEG-D4) Liu *et al.*[103] The introduction of Laponite did not change the degradability and cytocompatibility of PEG-D4. However, the curing time, mechanical and adhesive properties were significantly increased. Consequently, PEG-D4/Laponite hydrogel nanocomposites minimized inflammatory response and improved cellular infiltration in vivo as compared to Laponite-free specimens.

Recently, a variety of Laponite incorporated hydrogel composites are 3D-printed for hard tissue engineering. Jin et al. proposed a direct hydrogel printing approach without any supporting bath by using self-supporting nanoclay[96]. Laponite RD and XLG were mixed with three types of hydrogels including poly(ethylene glycol) diacrylate (PEGDA), alginate, and gelatin. Each prepared composites were extruded by direct ink writing with appropriate crosslinking methods, respectively. Laponite-incorporated hydrogels were readily printed through a nozzle and solidified after extrusion in the air. The addition of Laponite improved the mechanical properties of extruded scaffolds and also adjusted the degradation rates. The elastic modulus of PEGDA-Laponite, alginate-Laponite, and gelatin-Laponite scaffolds increased 1.9, 7.4 and 3.3-fold than each pure hydrogels without Laponite, respectively. The cytocompatibility of PEGDA-Laponite was confirmed by fibroblast cell adhesion and proliferation.

Zhai *et al.* reported that the physical crosslinking of hydrogel chain-clay coupled with hydrogen bonding remarkably increased the mechanical performance of hydrogel scaffolds[97]. N-acryloyl glycinamide (NAGA) was dissolved in deionized water with varying concentrations from 10 to 30%, and then mixed with different quantities of Laponite XLG. The mixed solutions were extruded by 3D plotting method and printed specimens were cured in a cross-link oven. Fabricated PNAGA-Clay scaffolds showed homogeneous structures and the mechanical properties of

scaffolds in tension and compression tests significantly increased with the addition of Laponite XLG. The release of silicon and magnesium ions from Laponite XLG promoted the proliferation and differentiation of primary rat osteoblast (ROB) cells. PNAGA-clay hydrogel scaffolds implanted in tibia defects of rats effectively induced new bone formation.

The possibilities of bioprinting and growth factor delivery of hydrogel-nanoclay composites were verified by Ahlfeld *et al.*[98] Laponite XLG was blended with various compositions of alginate-methylcellulose hydrogels. The pastes were printed by 3D plotting method and incubated in $CaCl_2$ solution. Human telomerase reverse transcriptase-mesenchymal stem cells (hTERT-MSC) were mixed with prepared hydrogel composite pastes before printing for cell plotting. Bovine serum albumin (BSA) and vascular endothelial growth factor (VEGF) were also loaded in advance into hydrogel composite pastes for release tests. Scaffolds were well-extruded with high shape fidelity by the addition of nanoclay. After 21 days, the printed hTERT-MSC showed cell viability of approximately 70%–75%. Continuous release of BSA and VEGF, from the hydrogel composite scaffolds, was observed even after 21 and 7 days, respectively.

4. Applications and Challenges

4.1 Hard Tissue Engineering Application

3D printing technologies have been used by medical professionals in a wide range of applications. Initially, only visual models and functional prototypes were fabricated by 3D printers. However, with improved accuracy of 3D printing process as well as the development of medical imaging, or radiology equipment such as magnetic resonance imaging (MRI) and computed tomography (CT), 3D printing technologies can now be used to produce tissues or organs which are directly implanted into the human body. The customized implantable scaffolds for patients are designed to better fit the affected site using reconstructed MRI and CT images. In particular, porous scaffolds which induce cell infiltration and proliferation are more easily produced by 3D printers as compared to other traditional processes such as subtractive manufacturing.

As mentioned before, pure hydrogels have poor mechanical properties. Therefore, in order to match the mechanical properties of tissues or organs, the integration other materials to form hydrogel composites is essential. Hard tissue engineering such as bone regeneration is one of biomedical fields that require these composites (Figure 9). The material needs sufficient strength and elastic modulus as well as good biocompatibility. HAp, the main component of bone, is a promising reinforcement that can be used to improve these conditions. Various sizes of HAp particles from nano to micro scale were

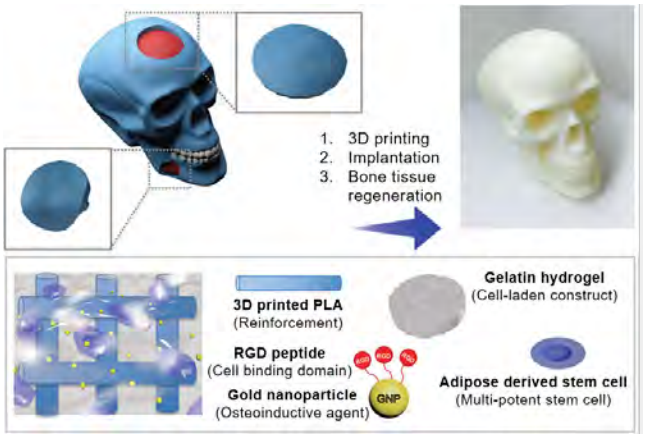

Figure 9. Customized bone defect regeneration using a extruded PLA and gelatin hydrogel composite with incorporated human adipose derived stem cells and gold nanoparticles (reproduced with permission from [89]. Copyright 2017, Royal society of chemistry).

dispersed in hydrogels and printed as bone substitute scaffolds. Demirtas *et al.* printed chitosan-HA hydrogels using a 3D plotting method and compared them with alginate-HAp hydrogels[104]. With the addition of about 180 nm HAp particles, elastic modulus of alginate-HAp hydrogels and chitosan-HAp hydrogels increased approximately 3-and-5 fold compare to pure alginate and chitosan hydrogels. The hydrogels loaded with pre-oseteoblast cells, chitosan-HAp hydrogels showed higher expression of osteogenic differentiation marker on day 21 when compared with other hydrogels. Other calcium phosphate materials including bicalcium phosphate (BCP) and tricalcium phosphate (TCP) are also proposed as hydrogel fillers for bone tissue engineering. Diogo *et al.* mixed alginate with beta-TCP and extruded by 3D plotter[105]. Various composition of beta-TCP/alginate of 50/50% (w/w), 30/70% (w/w) and 20/80% (w/w) were evaluated. As the beta-TCP contents in alginate matrix increased, the accuracy of printing increased due to increase in the viscosity of hydrogel composites. 50/50 beta-TCP/alginate scaffolds had the highest compression strength and Young's modulus and these values are higher than those of trabecular bones. Furthermore, biological test using osteoblast cells suggested that 50/50 beta-TCP/alginate scaffolds have potential as composite scaffolds in bone regeneration applications.

Similarly, studies were also carried out on bioglass incorporated hydrogel composites[106]. 3D printed collagen/alginate was coated with silica by soaking the scaffolds in tetraethyl orthosilicate (TEOS) with various concentrations[107]. The scaffolds were more mineralized in simulated body fluid solution as the fractions of silica in collagen/alginate scaffolds increased. The degradation rate of silica coated collagen/alginate scaffolds was significantly reduced while the elastic modulus of silica coated collagen/

alginate scaffolds increased. *In vitro* cellular response using pre-osteoblast cells exhibited that silica coated collagen/alginate scaffolds had higher value of proliferation and gene expression than pure hydrogel scaffolds. Wang et al. added various kinds of bioglass including polyphosphate (polyP), polyP*Ca^{2+}-complex, silica, and biosilica produced by sol-gel method in to alginate/gelatin/SaOS-2 bone cell hydrogels composites[108]. Each of the mixed pastes were extruded by 3D bioplotter and results showed that the added polyP and biosilica increased the proliferation and mineralization of bone cells.

4.2 Soft Tissue Engineering Application

Cartilage is a kind of soft tissue, which is a complex structure composed of interstitial fluid, collagen and chondrocytes. Cartilage tissue engineering has been widely investigated because the injured cartilage does not heal or regenerate by itself[109]. Hydrogels are excellent alternatives for use in cartilage engineering since they are highly hydrated with a cross-linked architecture that can be filled with cells. These hydrogels scaffolds can be easily prepared by 3D printing but their poor mechanical stability remains a big challenge. Therefore, many researchers have put in efforts to overcome this limitation by mixing pure hydrogels and fillers.

Bartnikowski fabricated multi-layered hydrogel composites comprising functionalized gelatin methacrylamide (GelMA) or GelMA with hyaluronic acid methacrylate (HAMA) on pure alginate or alginate/hydroxyapatite (HAp) composites by 3D plotting[110]. Incorporation of hydroxyapatite increased the elastic modulus of printed hydrogel composites and HAMA in GelMA hydrogels improved chondrogenesis. The polycaprolactone (PCL) and alginate were printed layer-by-layer with a multihead deposition system as shown in (Figure 10A)[111]. These hydrogel composites combined chondrocyte cells and transforming growth factor beta (TGF-beta) to mimic the properties of cartilage. PCL/alginate scaffolds with TGF-beta showed higher cartilaginous ECM formation. In vivo test using dorsal subcutaneous zone of nude mouse showed that the amounts of collagen fibers and cartilaginous tissue formation of chondrocyte encapsulated PCL/alginate scaffolds with TGF-beta were higher than other control hydrogels. PCL was also used as composite material for cartilage tissue engineering applications[112]. Electrospun PCL and fibrin/collagen hydrogel containing chondrocytes were fabricated layer by layer by hybrid inkjet printing/electrospinning system. The printed hybrid composite scaffolds showed higher tensile properties compared with each of the PCL and fibrin/collagen hydrogels alone. Printed chondrocytes cells maintained more than 80% of viability *in vitro* and large amounts of collagen and glycosaminoglycans which are similar to elastic cartilage were produced *in vivo*. In order to fabricate tough hydrogels for cartilage tissue engineering applications, agar was combined with alginate by Wei *et*

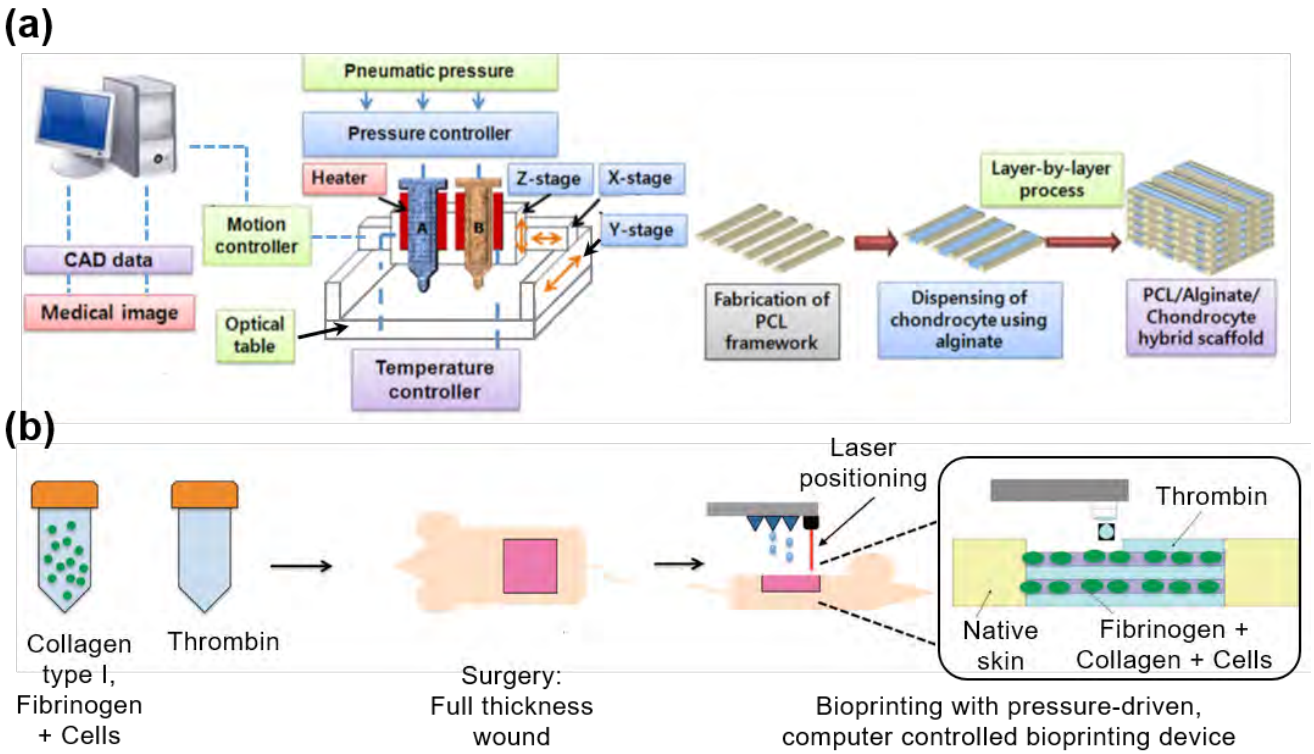

Figure 10. Schematics of (**A**) the 3D printing process of chondrocyte-incorporated alginate-PCL hybrid scaffold for cartilage application (reproduced with permission from [111]. Copyright 2013, John Wiley & Sons, Ltd) and (**B**) the direct bioprinting process of collagen-fibrinogen with stem cells onto skin wound of rat (reproduced with permission from [116]. Copyright 2012, AlphaMed Press).

al.[113] The addition of alginate not only improved the hydrogel viscosity and shape fidelity, but also increased the tensile strength and toughness of hydrogels.

The skin is the largest organ that covers the human body and it plays an important role in regulating temperature, controlling evaporation as well as protecting from pathogens and external environment. It is a complex structure with three sequential layers including epidermis which is the outer layer, dermis that is permeated by a complex nervous and blood vessel, and hypodermis consisting of subcutaneous tissue[114]. Therefore, in skin tissue engineering, many researchers tried to substitute this complex and important organs with artificial skin grafts such as hydrogels for curing skin wounds and diseases[115]. With recent advances in hydrogel printing technique which moved from 2D to 3D printing allow more flexibility in controlling the micro/nano level structure. Moreover, studies are focused on 3D printing hydrogel composites to functionalize hydrogel scaffolds that are closely mimicking real skin tissue.

Skardal *et al.* investigated the possibility of skin regeneration of mouse skin wound by printed amniotic fluid-derived stem (AFS) cells incorporated hydrogels[116]. They used fibrinogen/collagen mixed with 50:50 volume ratio as hydrogel composites and hydrogel composites including AFS cells and mesenchymal stem cells (MSCs). Fibrinogen/collagen hydrogel composites with cells and thrombin were directly printed on the skin wound of nude mouse layer-by-layer by inkjet 3D printer (Figure 10B). The wounds treated by composite with AFS cell and MSC cells showed better wound closure and re-epithelialization results up to 14 days than those of fibrin/collagen gel up to 14 days with increased vessel density and enlarged capillary diameters.

Chitosan and graphene were used as hydrogel composite materials for tissue engineering[84,117]. Chitosan has been used in artificial skin and wound dressing with its similarity in hyaluronic acid content and glycosaminoglycans in joints[118]. The limitations of chitosan are its poor mechanical properties and slow gelation rate. In Sayyar's studies, chitosan or methacrylated chitosan (ChiMA) were mixed with various contents of graphene and extruded by modified computer numerical control (CNC) machine. Both graphene/chitosan and graphene/ChiMA hydrogels showed tunable swelling properties and good biocompatibility which was confirmed with fibroblast cell adhesion and proliferation test on the hydrogel composites. As the contents of graphene in chitosan or ChiMA increased, tensile strength and conductivity remarkably increased.

For 3D printing of soft tissue engineering scaffolds, cell-laden bioinks are often used. Despite of numerous advantages of bioprinting, the harsh conditions imposed by the printing process have led to the rise of new challenges regarding the processing of sensitive cells and biomolecules due to 3D printing conditions required by different types of 3D printers and the chosen bioink[119]. In thermal, laser and piezoelectric inkjet, cell damage mainly results from the thermal heating during the printing process, whereas in extrusion bioprinting, compression forces and shear stresses generated during the printing causes damage to cells[120]. On the other hand, biocompatible hydrogels widely used for matrix materials of cell-laden bioinks or supporting materials of printed cells require solidification strategies, *e.g.*, photo-crosslinking, *in situ* chemical crosslinking, physical crosslinking or shear-thinning[121-124]. Integration of those solidification methods into bioinks is challenging, particularly in case of cell-laden hydrogel bioinks where the hydrogel gelation process should minimize the potential damage of encapsulated cells[121–123,125,126]. Particularly, UV-based photopolymerization reactions of bioactive hydrogels (*e.g.*, gelatin, collagen, chitosan) are commonly coupled with bioprinting, employed either during the printing process[127] or after the deposition of bioinks[39] to produce stable 3D hydrogels with intricate architectures for cell encapsulation. However, the deleterious effects of UV light irradiation and cytotoxicity of radicals generated by photoinitiators lead to a decrease in cell viability and ultimately DNA damage[128].

4.3 Vascular Application

Fabrication of vascular system is one of the main challenges in 3D printing, because isolated cells cannot live in spaces of less than 3 mm^3 of volume[129]. Vascular channels transport oxygen, growth factors and nutrients and remove the waste solutions for living cells. Therefore, well-designed blood vessel tree of capillaries and micro-vessels are required for operating large tissues or organs. Moreover, sufficient mechanical properties are also needed for vascular tissue engineering to tolerate physiological pressures and surgical connections.

To achieve this goal, double-nozzle assembling method was adapted to 3D-print vascular for liver by Li's group[130]. Li fabricated gelatin/alginate/chitosan (GAC) hydrogel composites combined with adipose-derived stromal cells (ADSC) and printed them to form vascular networks. Gelatin/alginate/ fibrinogen (GAF) hydrogel was also combined with hepatocytes and placed around the printed ADSC/GAC hydrogel composites to mimic anatomical liver structure. The vascular channels were crosslinked with thrombin, $CaCl_2$, $Na_5P_3O_{10}$ and glutaraldehyde and were well maintained for more than 2 weeks. Printed ADCSs differentiated into mature endothelial cells and the albumin secretion value of the hepatocytes increased after 2 weeks of culturing. In a similar way, the production of perfusable vascular systems with highly ordered arrangements was achieved by a multiple coaxial nozzle as shown in (Figure 11A)[131]. They mixed gelatin methacryloyl (GelMA) and 4-arm poly(ethylene glycol)-tetra-acrylate (PEGTA) for fixing the morphologies of the constructs permanently and sodium alginate for maintaining the shape by fast

ionic crosslinking. The perfusable structures with multiple layers and various diameters were formed by coaxial nozzle systems in a one-step process. The rheological and mechanical properties of the printed hydrogel composites were tunable by PEGTA and endothelial and mesenchymal stem cells incorporated hydrogel composites also showed favorable biological responses which demonstrated the formation of vessels resembling early maturation of the native vasculature.

PEG derivatives were used as crosslinkers to develop bioartificial vessel-like grafts. Different four-armed polyethylene glycol(PEG) derivatives called TetraPEG8 and TetraPEG13 were converted to tetra-acrylate derivatives (TetraPAcs) and these were co-crosslinked with hyaluronan acid and gelatin hydrogels into synthetic extracellular matrices (sECMs) by Skardal *et al.* (Figure 11C)[132]. The crosslinked hydrogel composites showed improved rheological properties which are more suitable for bioprinting when compared with sECM hydrogels crosslinked with PEGDA. Bioprinted hydrogel composites containing NIH3T3, HepG2 C3A, and Int407cells exhibited microcapillary tube structure with cells viability up to 4 weeks.

Dolati proposed bioprintable vascular conduits reinforced by carbon nanotubes[133]. Multiwalled carbon nanotubes (MWCNTs) were dispersed in alginate hydrogels and human coronary artery smooth muscle cells (HCASMCs) encapsulated hydrogel composites were extruded by coaxial nozzle. As contents of MWCNTs increased, the mechanical properties of hydrogel composites increased. However, in long-term biological responses, MWCNT-added hydrogel composites induced cell toxicity.

4.4 4D printing

The applications of the hydrogel composite systems are not only limited to mechanical strengthening or biological performance. They are also valuable model systems for stimuli-responsive smart materials, also known as 4D printing. 4D printing involves materials that are responsive to external stimuli such as electricity, light, ions, temperature, and water, such that the pre-printed 3D configuration changes over time[92,134–138].

In general, shape memory polymers (SMPs) are popularly used for the 4D printing which have permanent shape by a cross-linked polymer network, and can be deformed into a temporary shape *via* reversible interactions between the networks. When exposed to external stimuli, the material can recover its original shape. However, most SMPs only possess 3D printability with laser-based printing systems such as Polyjet or SLA 3D printing[135,136]. Therefore, there are severe limitations on the choice of material and function for tissue engineering applications.

In the case of hydrogel composite, they have a great potential as a platform technology to extend material choice for 4D printing with their highly tunable functionalities. For example, it is possible to utilize hydrogel composites for water-activated 4D printing. In general, reinforcements such as inorganic particles or fillers do not or exhibit less swelling behavior in water as compared to hydrogels (Figure 12A). The orientation or distribution of reinforcements within the hydrogel composite generates controllable

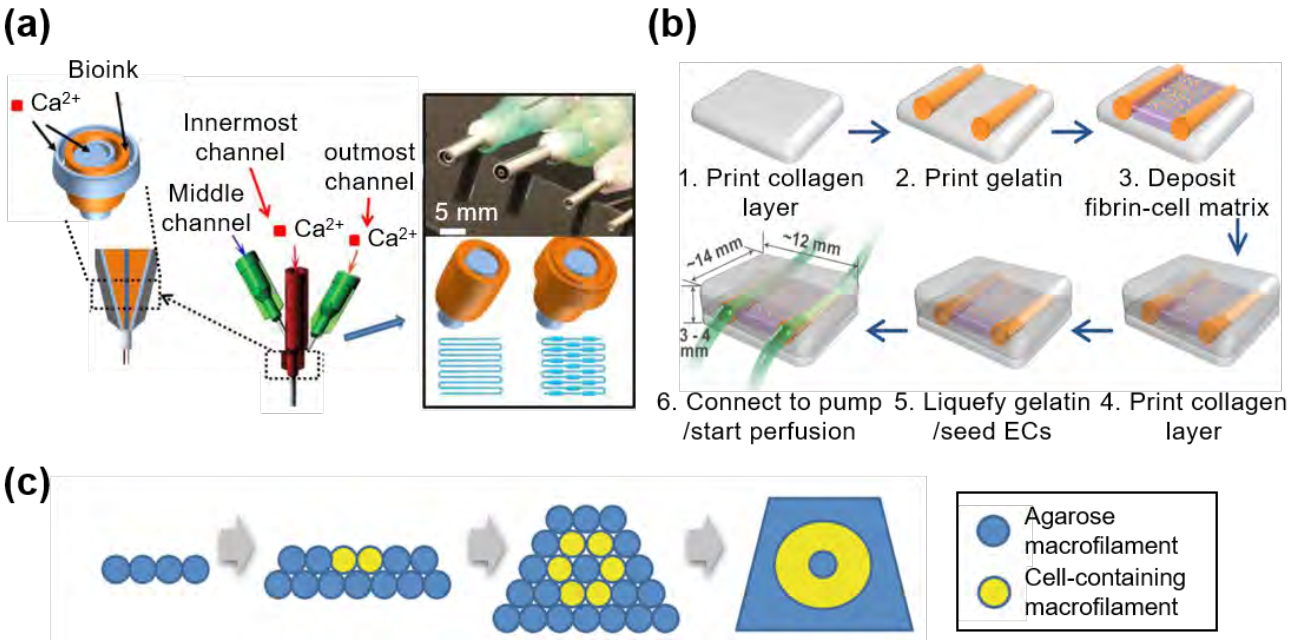

Figure 11. Various strategies of constructing vascular system (**A**) using a multiple coaxial nozzle with alginate, GelMA, and 4-arm PEGTA (reproduced with permission from [131]. Copyright 2016, Elsevier Ltd), (**B**) bioprinting layer-by-layer with collagen, fibrin-cell mixture, and sacrificial gelatin, (reproduced with permission from [140]. Copyright 2017, Springer International Publishing AG.) and (**C**) by stacking hydrogel macrofilaments to form a cellularized tubular structure(reproduced with permission from [132]. Copyright 2010, Elsevier Ltd).

anisotropic swelling and allows precise control over the printed structure's curvature (Figure 12B)[92]. Thus, by utilizing the swelling behaviors of hydrogel composite structures, bio-origami hydrogel scaffolds can be developed with self-folding behavior under the appropriate external stimuli, which can greatly contribute to the fabrication of functional 3D tissues.

4D printing technique is also attractive for drug delivery systems in which precise control over the shape of the carrier is desirable to release drugs or cells in a programmable manner. For example, in the case of mucoadhesive drug delivery systems, hydrogel bilayer structures composed of two differentially swelling layers can induce self-folding property, which makes it more likely to stick to the mucus tissue. The less or non-swelling layer acts as a diffusion barrier and incorporated drugs can be released unidirectionally towards the adhered tissues, which minimizes drug leakage and enhances drug delivery efficiency[134,137].

Until now, existing self-assembly or self-folding 4D printing systems are limited to macroscale deformations, which restricts the precise spatial manipulation of 4D-printed structures. In addition, most responsive materials only respond to one type of external stimulus. For tissue engineering applications, printed scaffolds need to adapt to complicated microenvironments of within the human body[134,138]. Therefore, the future of 4D printing requires a stronger focus on microscale controllability over the shape, orientation, or biocompatibility of printed structures. This can be achieved by improving printing resolution and material design in response to multiple physiological signals.

5. Conclusion and Future Outlook

In this paper, the pros and cons of utilizing hydrogel composite materials as printing ink in 3D printing systems has been thoroughly discussed. This information will be useful for selecting the printing method and appropriate materials for the desired biological performances. The recent developments of 3D printing system tend to bring the hydrogel-based tissue engineering on the next level. In recent years, hydrogel composite 3D printing techniques have gone through tremendous technological improvements in the form of material design and printing system optimizations. However, there are still several critical issues and problems that needs to be addressed.

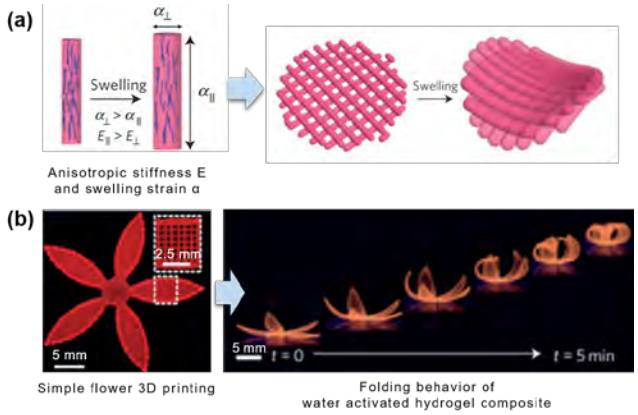

Figure 12. (**A**) Schematic images of cellulose fibrils alignment-induced anisotropic stiffness E and swelling strain α, and (**B**) its water-activated 4D printing effect.(reproduced with permission from [92]. Copyright 2016, Macmillan Ltd).

First of all, hydrogel cross-linking methods that are available in 3D printing systems are severely limited. For the construction of stable 3D structures, hydrogel materials which crosslink rapidly is essential to support each printing layer before they collapse under their own weight, and until now, only photo- and ionic-crosslinking strategies are applicable for 3D printing due to their high crosslinking efficiency. However, the limited materials and printing systems could not meet the stringent requirements demanded by tissue engineering applications. Therefore, material diversity and cross-linking strategies should be the focus of future research.

Secondly, most hydrogel composites are produced from simple mixing of different components at different weight ratios, which can induce severe agglomeration of reinforcements inside the hydrogel matrix. Poorly distributed reinforcements directly affect the performance of the hydrogel composite, thus new strategies for obtaining a uniform distribution or alignment of reinforcements are impertinent for practical applications involving hydrogel composites.

Finally, the alignment or continuity of the reinforcements are also restricted to the X-Y plane because of the layer-by-layer additive fabrication process of 3D printing systems. Printing paths are only allowed in two dimensions(X- and Y-axis), and the mechanical strengthening is also limited to directions parallel with the printing paths. This is the reason why only simple shapes such as rod, bar, and dog-bone have been fabricated and evaluated using one-directional mechanical characterizations. For tissue engineering applications, implanted materials undergo complex loading conditions *in vivo*, and the mechanical properties of hydrogel composites are strongly dependent on their internal microstructure. Therefore, new 3D printing systems focusing on 3D alignment or continuity of internal reinforcements should be developed to improve the mechanical performance of hydrogel composites.

While many problems remain to be unsolved, various fascinating and promising results of the 3D printing system have been reported continuously, and hydrogel composite materials with enhanced printability, mechanical properties, and biological performances have been also designed and proposed. We expect that the classification of 3D printing systems, categorization of hydrogel composite materials, and their applications that have been discussed in this review article will provide a fundamental understanding of hydrogel composite materials and 3D printing systems,

and serve as a platform to design innovative combinations of materials and 3D printing techniques for emerging applications, such as cancer modeling and organ-on-a-chip models.

Conflict of Interest and Funding

No conflict of interest was reported by all authors. This research was supported by AcRF Tier 1 grant 2017-T1-001-246 (RG51/17) from Ministry of Education of Singapore, and Basic Science Research Program (No. 2015R1D1A1A01057311 & 2017R1A6A3A03008914) through the National Research Foundation of Korea (NRF) funded by the Ministry of Science, ICT & Future Planning.

References

1. Wang X, Jiang M, Zhou Z W, *et al.*, 2017, 3D printing of polymer matrix composites: A review and prospective. *Compos B Eng*, 110: 442–458. http://dx.doi.org/10.1016/j.compositesb.2016.11.034
2. Chua C K and Leong K F, 3D printing and additive manufacturing : Principles and applications, 4th ed. Singapore: World Scientific Publishing; 2015.
3. Billiet T, Vandenhaute M, Schelfhout J, *et al.*, 2012, A review of trends and limitations in hydrogel-rapid prototyping for tissue engineering. *Biomaterials*, 33(26): 6020–6041. http://dx.doi.org/10.1016/j.biomaterials.2012.04.050
4. Ballyns J J, Gleghorn J P, Niebrzydowski V, *et al.*, 2008, Image-guided tissue engineering of anatomically shaped implants via MRI and micro-CT using injection molding. *Tissue Eng Part A*, 14(7): 1195–1202. http://dx.doi.org/10.1089/ten.tea.2007.0186
5. Chia H N and Wu B M, 2015, Recent advances in 3D printing of biomaterials. *J Biol Eng*, 9(1): 4 http://dx.doi.org/10.1186/S13036-015-0001-4
6. Seyednejad H, Gawlitta D, Kuiper R V, *et al.*, 2012, *In vivo* biocompatibility and biodegradation of 3D-printed porous scaffolds based on a hydroxyl-functionalized poly(epsilon-caprolactone). *Biomaterials*, 33(17): 4309–4318. http://dx.doi.org/10.1016/j.biomaterials.2012.03.002
7. Wu G H and Hsu S H, 2015, Review: Polymeric-Based 3D printing for tissue engineering. *J Med Bioeng*, 35(3): 285–292. http://dx.doi.org/10.1007/s40846-015-0038-3
8. Utech S and Boccaccini A R, 2016, A review of hydrogel-based composites for biomedical applications: Enhancement of hydrogel properties by addition of rigid inorganic fillers. *J Mater Sci*, 51(1): 271–310. http://dx.doi.org/10.1007/s10853-015-9382-5
9. Gaharwar A K, Peppas N A and Khademhosseini A, 2014, Nanocomposite hydrogels for biomedical applications. *Biotechnol Bioeng*, 111(3): 441–453. http://dx.doi.org/10.1002/bit.25160
10. Xu K, Wang J H, Chen Q, *et al.*, 2008, Spontaneous volume transition of polyampholyte nanocomposite hydrogels based on pure electrostatic interaction. *J Colloid Interface Sci*, 321(2): 272–278. http://dx.doi.org/10.1016/j.jcis.2008.02.024
11. Kabiri K, Omidian H, Zohuriaan-Mehr M J, *et al.*, 2011, Superabsorbent hydrogel composites and nanocomposites: A review. *Polym Compos*, 32(2): 277–289. http://dx.doi.org/10.1002/pc.21046
12. Thoniyot P, Tan M J, Karim A A, *et al.*, 2015, Nanoparticle-Hydrogel composites: Concept, design, and applications of these promising, multi-functional materials. *Adv Sci*, 2(1–2). http://dx.doi.org/10.1002/Advs.201400010
13. Lee J W, Kim S Y, Kim S S, *et al.*, 1999, Synthesis and characteristics of interpenetrating polymer network hydrogel composed of chitosan and poly(acrylic acid). *J Appl Polym Sci*, 73(1): 113–120. http://dx.doi.org/10.1002/(SICI)1097-4628(19990705)73:1<113::AID-APP13>3.0.CO;2-D
14. Ehrburger P and Donnet J B, 1980, Interface in composite-materials. *Philos Trans A Math Phys Eng Sci*, 294(1411): 495–505. http://dx.doi.org/10.1098/rsta.1980.0059
15. Jeong S H, Koh Y H, Kim S W, *et al.*, 2016, Strong and biostable hyaluronic acid-calcium phosphate nanocomposite hydrogel *via in situ* precipitation process. *Biomacromolecules*, 17(3): 841–851. http://dx.doi.org/10.1021/acs.biomac.5b01557
16. Wust S, Godla M E, Muller R, *et al.*, 2014, Tunable hydrogel composite with two-step processing in combination with innovative hardware upgrade for cell-based three-dimensional bioprinting. *Acta Biomater*, 10(2): 630–640. http://dx.doi.org/10.1016/j.actbio.2013.10.016
17. Duan B, Hockaday L A, Kang K H, *et al.*, 2013, 3D Bioprinting of heterogeneous aortic valve conduits with alginate/gelatin hydrogels. *J Biomed Mater Res A*, 101(5): 1255–1264. http://dx.doi.org/10.1002/jbm.a.34420
18. Melchels F P W, Feijen J and Grijpma D W, 2010, A review on stereolithography and its applications in biomedical engineering. *Biomaterials*, 31(24): 6121–6130. http://dx.doi.org/10.1016/j.biomaterials.2010.04.050
19. Bertsch A, Jiguet S, Bernhard P, *et al.*, 2003, Microstereolithography: *A review. Rapid Prototyping Technologies*, 758: 3–15.
20. Beluze L, Bertsch A and Renaud P, 1999, Microstereolithography: A new process to build complex 3D objects. *Design,*

Test, and Microfabrication of Mems and Moems, Pts 1 and 2, 3680: 808–817. http://dx.doi.org/10.1117/12.341277

21. Choi J S, Kang H W, Lee I H, *et al*., 2009, Development of micro-stereolithography technology using a UV lamp and optical fiber. *Int J Adv Manuf Technol*, 41(3–4): 281–286. http://dx.doi.org/10.1007/s00170-008-1461-1
22. Bertsch A, Renaud P, Vogt C, *et al*., 2000, Rapid prototyping of small size objects. *Rapid Prototyp J*, 6(4): 259–266. http://dx.doi.org/10.1108/13552540010373362
23. Sun C, Fang N, Wu D M, *et al*., 2005, Projection micro-stereolithography using digital micro-mirror dynamic mask. *Sens Actuators A Phys*, 121(1): 113–120. http://dx.doi.org/10.1016/j.sna.2004.12.011
24. Ambrosio L, Biomedical composites, 2nd ed. UK: Woodhead Publishing; 2010.
25. Maruo Sand Ikuta K, 2002, Submicron stereolithography for the production of freely movable mechanisms by using single-photon polymerization. *Sens Actuators A Phys*, 100(1): 70–76. http://dx.doi.org/10.1016/S0924-4247(02)00043-2
26. Lee K S, Kim R H, Yang D Y, *et al*., 2008, Advances in 3D nano/microfabrication using two-photon initiated polymerization. *Prog Polym Sci*, 33(6): 631–681. http://dx.doi.org/10.1016/j.progpolymsci.2008.01.001
27. Weiss T, Hildebrand G, Schade R, *et al*., 2009, Two-Photon polymerization for microfabrication of three-dimensional scaffolds for tissue engineering application. *Eng Life Sci*, 9(5): 384–390. http://dx.doi.org/10.1002/elsc.200900002
28. Ostendorf A and Chichkov B N, 2006, Two-photon polymerization: A new approach to micromachining. *Photonics Spectra*, 40(10): 72–80.
29. Hutmacher D W, Sittinger M and Risbud M V, 2004, Scaffold-based tissue engineering: Rationale for computer-aided design and solid free-form fabrication systems. *Trends Biotechnol*, 22(7): 354–362. http://dx.doi.org/10.1016/j.tibtech.2004.05.006
30. Bikas H, Stavropoulos P and Chryssolouris G, 2016, Additive manufacturing methods and modelling approaches: A critical review. *Int J Adv Manuf Technol*, 83(1–4): 389–405. http://dx.doi.org/10.1007/s00170-015-7576-2
31. Anitha R, Arunachalam S and Radhakrishnan P, 2001, Critical parameters influencing the quality of prototypes in fused deposition modelling. *J Mater Process Technol*, 118(1): 385–388. http://dx.doi.org/10.1016/S0924-0136(01)00980-3
32. Xiong Z, Yan Y, Zhang R, *et al*., 2001, Fabrication of porous poly (L-lactic acid) scaffolds for bone tissue engineering via precise extrusion. *Scr Mater*, 45(7): 773–779. http://dx.doi.org/10.1016/S1359-6462(01)01094-6
33. Greulich M, Greul M and Pintat T, 1995, Fast, functional prototypes via multiphase jet solidification. *Rapid Prototyp J*, 1(1): 20–25. http://dx.doi.org/10.1108/13552549510146649
34. Shor L, Güçeri S, Chang R, *et al*., 2009, Precision extruding deposition (PED) fabrication of polycaprolactone (PCL) scaffolds for bone tissue engineering. *Biofabrication*, 1(1): 015003. http://dx.doi.org/10.1088/1758-5082/1/1/015003
35. Torres J, Cotelo J, Karl J, *et al*., 2015, Mechanical property optimization of FDM PLA in shear with multiple objectives. *JOM*, 67(5): 1183–1193. http://dx.doi.org/10.1007/s11837-015-1367-y
36. Yeong W Y, Chua C K, Leong K F, *et al*., 2004, Rapid prototyping in tissue engineering: Challenges and potential. *Trends Biotechnol*, 22(12): 643–652. http://dx.doi.org/10.1016/j.tibtech.2004.10.004
37. Gates R D, Baghdasarian G and Muscatine L, 1992, Temperature stress causes host-cell detachment in symbiotic cnidarians-implications for coral bleaching. *Biol Bull*, 182(3): 324–332. http://dx.doi.org/10.2307/1542252
38. Landers R and Mülhaupt R, 2000, Desktop manufacturing of complex objects, prototypes and biomedical scaffolds by means of computer-assisted design combined with computer-guided 3D plotting of polymers and reactive oligomers. *Macromol Mater Eng*, 282(1): 17–21. http://dx.doi.org/10.1002/1439-2054(20001001)282:1<17::AID-MAME17>3.0.CO;2-8
39. Billiet T, Gevaert E, De Schryver T, *et al*., 2014, The 3D printing of gelatin methacrylamide cell-laden tissue-engineered constructs with high cell viability. *Biomaterials*, 35(1): 49–62. http://dx.doi.org/10.1016/j.biomaterials.2013.09.078
40. Luo Y, Lode A, Akkineni A R, *et al*., 2015, Concentrated gelatin/alginate composites for fabrication of predesigned scaffolds with a favorable cell response by 3D plotting. *RSC Adv*, 5(54): 43480–43488. http://dx.doi.org/10.1039/C5RA04308E
41. Akkineni A R, Luo Y, Schumacher M, *et al*., 2015, 3D plotting of growth factor loaded calcium phosphate cement scaffolds. *Acta Biomater*, 27: 264–274. http://dx.doi.org/10.1016/j.actbio.2015.08.036
42. Yilgor P, Sousa R A, Reis R L, *et al*., 3D plotted PCL scaffolds for stem cell based bone tissue engineering, Macromol Symp, 2008. *Wiley Online Library*, 269:92–99. http://dx.doi.org/10.1002/masy.200850911
43. Landers R and Mulhaupt R, 2000, Desktop manufacturing

of complex objects, prototypes and biomedical scaffolds by means of computer-assisted design combined with computer-guided 3D plotting of polymers and reactive oligomers. *Macromol Mater Eng*, 282(9): 17–21. http://dx.doi.org/10.1002/1439-2054(20001001)282:1<17::Aid-Mame17>3.0.Co;2-8

44. Smay J E, Gratson G M, Shepherd R F, *et al*., 2002, Directed colloidal assembly of 3D periodic structures. *Adv Mater*, 14(18): 1279–1283.
45. Ahn B Y, Duoss E B, Motala M J, *et al*., 2009, Omnidirectional printing of flexible, stretchable, and spanning silver microelectrodes. *Science*, 323(5921): 1590–1593. https://dx.doi.org/10.1126/science.1168375
46. Vozzi G, Previti A, De Rossi D, *et al*., 2002, Microsyringe-based deposition of two-dimensional and three-dimensional polymer scaffolds with a well-defined geometry for application to tissue engineering. *Tissue Eng*, 8(6): 1089–1098. https://dx.doi.org/10.1089/107632702320934182
47. Tartarisco G, Gallone G, Carpi F, *et al*., 2009, Polyurethane unimorph bender microfabricated with pressure assisted microsyringe (PAM) for biomedical applications. *Mater Sci Eng C Mater Biol Appl*, 29(6): 1835–1841. https://dx.doi.org/10.1016/j.msec.2009.02.017
48. Xiong Z, Yan Y, Wang S, *et al*., 2002, Fabrication of porous scaffolds for bone tissue engineering *via* low-temperature deposition. *Scr Mater*, 46(11): 771–776. https://dx.doi.org/10.1016/S1359-6462(02)00071-4
49. Liu L, Xiong Z, Zhang R, *et al*., 2009, A novel osteochondral scaffold fabricated *via* multi-nozzle low-temperature deposition manufacturing. *J Bioact Compat Polym*, 24(1): 18–30. https://dx.doi.org/10.1177/0883911509102347
50. Vadnere M, Amidon G, Lindenbaum S, *et al*., 1984, Thermodynamic studies on the gel-sol transition of some pluronic polyols. *Int J Pharm*, 22(2–3): 207–218. https://dx.doi.org/10.1016/0378-5173(84)90022-X
51. Kim J Y and Cho D-W, 2009, Blended PCL/PLGA scaffold fabrication using multi-head deposition system. *Microelectron Eng*, 86(4): 1447–1450. https://dx.doi.org/10.1016/j.mee.2008.11.026
52. Domingos M, Dinucci D, Cometa S, *et al*., 2009, Polycaprolactone scaffolds fabricated *via* bioextrusion for tissue engineering applications. *Int J Biomater*, 2009(1687–8787) : 239643. https://dx.doi.org/10.1155/2009/239643
53. Lam C, Olkowski R, Swieszkowski W, *et al*., 2008, Mechanical and *in vitro* evaluations of composite PLDLLA/TCP scaffolds for bone engineering. *Virtual Phys Prototyp*, 3(4): 193–197. https://dx.doi.org/10.1080/17452750802551298
54. Lim T, Bang C, Chian K, *et al*., 2008, Development of cryogenic prototyping for tissue engineering. *Virtual Phys Prototyp*, 3(1): 25–31. https://dx.doi.org/10.1080/17452750701799303
55. Bang Pham C, Fai Leong K, Chiun Lim T, *et al*., 2008, Rapid freeze prototyping technique in bio-plotters for tissue scaffold fabrication. *Rapid Prototyp J*, 14(4): 246–253. https://dx.doi.org/10.1108/13552540810896193
56. Lu L, Zhang Q, Wootton D, *et al*., 2010, A novel sucrose porogen-based solid freeform fabrication system for bone scaffold manufacturing. *Rapid Prototyp J*, 16(5): 365–376. https://dx.doi.org/10.1108/13552541011065768
57. Cima M, Sachs E, Fan T, *et al*., Three-dimensional printing techniques. US patent 5387380, 1995 July 2.
58. Mei J, Lovell M Rand Mickle M H, 2005, Formulation and processing of novel conductive solution inks in continuous inkjet printing of 3-D electric circuits. *IEEE Trans Compon Packaging Manuf Technol*, 28(3): 265–273. https://dx.doi.org/10.1109/TEPM.2005.852542
59. Saunders R E, Gough J E and Derby B, 2008, Delivery of human fibroblast cells by piezoelectric drop-on-demand inkjet printing. *Biomaterials*, 29(2): 193–203. https://dx.doi.org/10.1016/j.biomaterials.2007.09.032
60. Nakamura M, Kobayashi A, Takagi F, *et al*., 2005, Biocompatible inkjet printing technique for designed seeding of individual living cells. *Tissue Eng*, 11(11–12): 1658–1666. https://dx.doi.org/10.1089/ten.2005.11.1658
61. Cui X, Dean D, Ruggeri Z M, *et al*., 2010, Cell damage evaluation of thermal inkjet printed Chinese hamster ovary cells. *Biotechnol Bioeng*, 106(6): 963–969. https://dx.doi.org/10.1002/bit.22762
62. Leukers B, Gülkan H, Irsen S H, *et al*., 2005, Hydroxyapatite scaffolds for bone tissue engineering made by 3D printing. *J MATER SCI-MATER M*, 16(12): 1121–1124. https://dx.doi.org/10.1007/s10856-005-4716-5
63. Inzana J A, Olvera D, Fuller S M, *et al*., 2014, 3D printing of composite calcium phosphate and collagen scaffolds for bone regeneration. *Biomaterials*, 35(13): 4026–4034. https://dx.doi.org/10.1016/j.biomaterials.2014.01.064
64. Levy A, Miriyev A, Elliott A, *et al*., 2017, Additive manufacturing of complex-shaped graded TiC/steel composites. *Mater Design*, 118: 198–203. https://dx.doi.org/10.1016/j.matdes.2017.01.024
65. Pfister A, Landers R, Laib A, *et al*., 2004, Biofunctional rapid prototyping for tissue-engineering applications: 3D bioplotting versus 3D printing. *J Polym Sci Pol Chem*, 42(3): 624–638. https:// dx.doi.org/10.1002/pola.10807

66. Boland T, Tao X, Damon B J, *et al*., 2007, Drop-on-demand printing of cells and materials for designer tissue constructs. *Mater Sci Eng C Mater Biol Appl*, 27(3): 372–376. https:// dx.doi.org/10.1016/j.msec.2006.05.047

67. Sun J, Ng J H, Fuh Y H, *et al*., 2009, Comparison of micro-dispensing performance between micro-valve and piezoelectric printhead. *Microsyst Technol*, 15(9): 1437–1448. https:// dx.doi.org/10.1007/s00542-009-0905-3

68. Zustiak S P and Leach J B, 2010, Hydrolytically degradable poly (ethylene glycol) hydrogel scaffolds with tunable degradation and mechanical properties. *Biomacromolecules*, 11(5): 1348–1357. https:// dx.doi.org/10.1021/bm100137q

69. Killion J A, Geever L M, Devine D M, *et al*., 2014, Compressive strength and bioactivity properties of photopolymerizable hybrid composite hydrogels for bone tissue engineering. *Int J Polym Mater Po*, 63(13): 641–650. https:// dx.doi.org/10.1080/00914037.2013.854238

70. Bakarich S E, Gorkin R, Gately R, *et al*., 2017, 3D printing of tough hydrogel composites with spatially varying materials properties. *Addit Manuf*, 14: 24–30. https:// dx.doi.org/10.1016/j.addma.2016.12.003

71. Zhao L, Lee V K, Yoo S-S, *et al*., 2012, The integration of 3-D cell printing and mesoscopic fluorescence molecular tomography of vascular constructs within thick hydrogel scaffolds. *Biomaterials*, 33(21): 5325–5332. http://dx.doi.org/10.1016/j.biomaterials.2012.04.004

72. Hong S, Sycks D, Chan H F, *et al*., 2015, 3D printing of highly stretchable and tough hydrogels into complex, cellularized structures. *Adv Mater*, 27(27): 4035–4040. http://dx.doi.org/10.1002/adma.201501099

73. Markstedt K, Mantas A, Tournier I, *et al*., 2015, 3D bioprinting human chondrocytes with nanocellulose–alginate bioink for cartilage tissue engineering applications. *Biomacromolecules*, 16(5): 1489–1496. http://dx.doi.org/10.1021/acs.biomac.5b00188

74. Rutz A L, Hyland K E, Jakus A E, *et al*., 2015, A multimaterial bioink method for 3D printing tunable, cell-compatible hydrogels. *AdvMater*, 27(9): 1607–1614. http://dx.doi.org/10.1002/adma.201405076

75. Xu M, Wang X, Yan Y, *et al*., 2010, An cell-assembly derived physiological 3D model of the metabolic syndrome, based on adipose-derived stromal cells and a gelatin/alginate/fibrinogen matrix. *Biomaterials*, 31(14): 3868–3877. http://dx.doi.org/10.1016/j.biomaterials.2010.01.111

76. Akkineni A R, Ahlfeld T, Funk A, *et al*., 2016, Highly concentrated alginate-gellan gum composites for 3D plotting of complex tissue engineering scaffolds. *Polymers*, 8(5): 170. http://dx.doi.org/10.3390/polym8050170

77. Boere K W, Blokzijl M M, Visser J,*et al*.,2015, Biofabrication of reinforced 3D-scaffolds using two-component hydrogels. *J Mater Chem B Mater Biol Med*, 3(46): 9067–9078. http://dx.doi.org/10.1039/C5TB01645B

78. Censi R, Schuurman W, Malda J, *et al*., 2011, A printable photopolymerizable thermosensitive p (HPMAm-lactate)-PEG hydrogel for tissue engineering. *Adv Funct Mater*, 21(10): 1833–1842. http://dx.doi.org/10.1002/adfm.201002428

79. Osterbur L, 2013, 3D printing of hyaluronic acid scaffolds for tissue engineering applications [Internet]. Available from: http://hdl.handle.net/2142/44207

80. Wang X, Cui T, Yan Y, *et al*., 2009, Peroneal nerve regeneration using a unique bilayer polyurethane-collagen guide conduit. *J Bioact Compat Polym*, 24(2): 109–127. http://dx.doi.org/10.1177/0883911508101183

81. Mogas-Soldevila L, Duro-Royo J and Oxman N, 2014, Water-based robotic fabrication: Large-Scale additive manufacturing of functionally graded hydrogel composites via multichamber extrusion. *3D Print Addit Manuf*, 1(3): 141–151. http://dx.doi.org/10.1089/3dp.2014.0014

82. Shie M-Y, Chang W-C, Wei L-J, *et al*., 2017, 3D printing of cytocompatible water-based light-cured polyurethane with hyaluronic acid for cartilage tissue engineering applications. *Materials*, 10(2): 136. http://dx.doi.org/10.3390/ma10020136

83. Wang X H, Tolba E, Schroder H C, *et al*., 2014, Effect of bioglass on growth and biomineralization of Saos-2 cells in hydrogel after 3D cell bioprinting. *Plos One*, 9(11): e112497 http://dx.doi.org/10.1371/journal.pone.0112497

84. Sayyar S, Gambhir S, Chung J, *et al*., 2017, 3D printable conducting hydrogels containing chemically converted graphene. *Nanoscale*, 9(5): 2038–2050. http://dx.doi.org/10.1039/c6nr07516a

85. Demirtas T T, Irmak G and Gumusderelioglu M, 2017, A bioprintable form of chitosan hydrogel for bone tissue engineering. *Biofabrication*, 9(3): 035003. http://dx.doi.org/10.1088/1758-5090/Aa7b1d

86. Skardal A, Zhang J X, McCoard L, *et al*., 2010, Dynamically crosslinked gold nanoparticle–Hyaluronan hydrogels. *Adv Mater*, 22(42): 4736. http://dx.doi.org/10.1002/adma.201001436

87. Fedorovich N E, Wijnberg H M, Dhert W J, *et al*., 2011, Distinct tissue formation by heterogeneous printing of osteo- and endothelial progenitor cells. *Tissue Eng Part A*, 17(15–16):

2113–2121. http://dx.doi.org/10.1089/ten.tea.2011.0019

88. Panhuis M I H, Heurtematte A, Small W R, *et al*., 2007, Inkjet printed water sensitive transparent films from natural gum-carbon nanotube composites. *Soft Matter*, 3(7): 840–843. http://dx.doi.org/10.1039/b704368f
89. Heo D N, Castro N J, Lee S J, *et al*., 2017, Enhanced bone tissue regeneration using a 3D printed microstructure incorporated with a hybrid nano hydrogel. *Nanoscale*, 9(16): 5055–5062. http://dx.doi.org/10.1039/c6nr09652b
90. Zhu W, Holmes B, Glazer R I, *et al*., 2016, 3D printed nanocomposite matrix for the study of breast cancer bone metastasis. *Nanomedicine*, 12(1): 69–79. http://dx.doi.org/10.1016/j.nano.2015.09.010
91. Castro N J, O'Brien J and Zhang L G, 2015, Integrating biologically inspired nanomaterials and table-top stereolithography for 3D printed biomimetic osteochondral scaffolds. *Nanoscale*, 7(33): 14010–14022. http://dx.doi.org/10.1039/c5nr03425f
92. Gladman A S, Matsumoto E A, Nuzzo R G, *et al*., 2016, Biomimetic 4D printing. *Nat Mater*, 15(4): 413–418. http://dx.doi.org/10.1038/NMAT4544
93. Narayanan L K, Huebner P, Fisher M B, *et al*., 2016, 3D-Bioprinting of polylactic acid (PLA) nanofiber-alginate hydrogel bioink containing human adipose-derived stem cells. *ACS Biomater Sci Eng*, 2(10): 1732–1742. http://dx.doi.org/10.1021/acsbiomaterials.6b00196
94. Agrawal A, Rahbar N and Calvert P D, 2013, Strong fiber-reinforced hydrogel. *Acta Biomaterialia*, 9(2): 5313–5318. http://dx.doi.org/10.1016/j.actbio.2012.10.011
95. Bakarich S E, Gorkin R, Panhuis M I H, *et al*., 2014, Three-dimensional printing fiber reinforced hydrogel composites. *ACS Appl Mater Interfaces*, 6(18): 15998–16006. http://dx.doi.org/10.1021/am503878d
96. Jin Y, Liu C, Chai W, *et al*., 2017, Self-Supporting nanoclay as internal scaffold mterial for direct printing of soft hydrogelcomposite structures in air. *ACS Appl Mater Interfaces*, 9(20):17456–17465. http://dx.doi.org/10.1021/acsami.7b03613
97. Zhai X, Ma Y, Hou C, *et al*., 2017, 3D-printed high strength bioactive supramolecular polymer/clay nanocomposite hydrogel scaffold for bone regeneration. *ACS Biomater Sci Eng*, 3(6): 1109–1118. http://dx.doi.org/10.1021/acsbiomaterials.7b00224
98. Ahlfeld T, Cidonio G, Kilian D, *et al*., 2017, Development of a clay based bioink for 3D cell printing for skeletal application. *Biofabrication*, 9(3). http://dx.doi.org/10.1088/1758-5090/aa7e96
99. Egorov A A, Fedotov A Y, Mironov A V, *et al*., 2016, 3D printing of mineral-polymer bone substitutes based on sodium alginate and calcium phosphate. *Beilstein J Nanotechnol*, 7(1): 1794–1799. http://dx.doi.org/10.3762/bjnano.7.172
100. Rawat K, Agarwal S, Tyagi A, *et al*., 2014, Aspect ratio dependent cytotoxicity and antimicrobial properties of nanoclay. *Appl Biochem Biotechnol*, 174(3): 936–944. http://dx.doi.org/10.1007/s12010-014-0983-2
101. Mourchid A, Delville A, Lambard J, *et al*., 1995, Phase diagram of colloidal dispersions of anisotropic charged particles: Equilibrium properties, structure, and rheology of laponite suspensions. *Langmuir*, 11(6): 1942–1950. http://dx.doi.org/10.1021/la00006a020
102. Su D, Jiang L, Chen X, *et al*., 2016, Enhancing the gelation and bioactivity of injectable silk fibroin hydrogel with laponite nanoplatelets. *ACS Appl Mater Interfaces*, 8(15): 9619–9628. http://dx.doi.org/10.1021/acsami.6b00891
103. Liu Y, Meng H, Konst S, *et al*., 2014, Injectable dopamine-modified poly (ethylene glycol) nanocomposite hydrogel with enhanced adhesive property and bioactivity. *ACS Appl Mater Interfaces*, 6(19): 16982–16992. http://dx.doi.org/10.1021/am504566v
104. Demirtaş T T, Irmak G and Gümüşderelioğlu M, 2017, A bioprintable form of chitosan hydrogel for bone tissue engineering. *Biofabrication*, 9(3): 035003. http://dx.doi.org/10.1088/1758-5090/aa7b1d
105. Diogo G, Gaspar V, Serra I, *et al*., 2014, Manufacture of β-TCP/alginate scaffolds through a Fab@ home model for application in bone tissue engineering. *Biofabrication*, 6(2): 025001. http://dx.doi.org/10.1088/1758-5082/6/2/025001
106. Kang M-H, Jang T-S, Jung H-D, *et al*., 2016, Poly (ether imide)-silica hybrid coatings for tunable corrosion behavior and improved biocompatibility of magnesium implants. *Bioact Mater*, 11(3): 035003. http://dx.doi.org/10.1088/1748-6041/11/3/035003
107. Lee H, Kim Y, Kim S, *et al*., 2014, Mineralized biomimetic collagen/alginate/silica composite scaffolds fabricated by a low-temperature bio-plotting process for hard tissue regeneration: fabrication, characterisation and *in vitro* cellular activities. *J Mater Chem B Mater Biol Med*, 2(35): 5785–5798. http://dx.doi.org/10.1039/C4TB00931B
108. Wang X, Tolba E, Schröder H C, *et al*., 2014, Effect of bioglass on growth and biomineralization of SaOS-2 cells in hydrogel after 3D cell bioprinting. *PLoS One*, 9(11): e112497. http://dx.doi.org/10.1371/journal.pone.0112497
109. Huey D J, Hu J C and Athanasiou K A, 2012, Unlike bone,

cartilage regeneration remains elusive. *Science*, 338(6109): 917–921. http://dx.doi.org/10.1126/science.1222454

110. Bartnikowski M, Akkineni A R, Gelinsky M, *et al*., 2016, A hydrogel model incorporating 3D-plotted hydroxyapatite for osteochondral tissue engineering. *Materials*, 9(4): 285. http://dx.doi.org/10.3390/ma9040285
111. Kundu J, Shim J H, Jang J, *et al*., 2015, An additive manufacturingbased PCL–alginate–chondrocyte bioprinted scaffold for cartilage tissue engineering. *J Tissue Eng Regen Med*, 9(11): 1286–1297. http://dx.doi.org/10.1002/term.1682
112. Xu T, Binder K W, Albanna M Z, *et al*., 2012, Hybrid printing of mechanically and biologically improved constructs for cartilage tissue engineering applications. *Biofabrication*, 5(1): 015001. http://dx.doi.org/10.1088/1758-5082/5/1/015001
113. Wei J, Wang J, Su S, *et al*., 2015, 3D printing of an extremely tough hydrogel. *RSC Adv*, 5(99): 81324–81329. http://dx.doi.org/10.1039/C5RA16362E
114. Sugihara H, Toda S, Miyabara S, *et al*., 1991, Reconstruction of the skin in three-dimensional collagen gel matrix culture. *In Vitro Cell Dev Biol Anim*, 27(2): 142-146. http://dx.doi.org/10.1007/BF02631000
115. Dorsett-Martin W A, 2004, Rat models of skin wound healing: A review. *Wound Repair Regen*, 12(6): 591–599. http://dx.doi.org/10.1111/j.1067-1927.2004.12601.x
116. Skardal A, Mack D, Kapetanovic E, *et al*., 2012, Bioprinted amniotic fluid-derived stem cells accelerate healing of large skin wounds. *Stem Cells Transl Med*, 1(11): 792–802. http://dx.doi.org/10.5966/sctm.2012-0088
117. Sayyar S, Murray E, Thompson B, *et al*., 2015, Processable conducting graphene/chitosan hydrogels for tissue engineering. *J Mater Chem B Mater Biol Med*, 3(3): 481–490. http://dx.doi.org/10.1039/C4TB01636J
118. Suh J-K and Matthew H W, 2000, Application of chitosan-based polysaccharide biomaterials in cartilage tissue engineering: A review. *Biomaterials*, 21(24): 2589–2598. http://dx.doi.org/10.1016/S0142-9612(00)00126-5
119. Knowlton S, Yenilmez B, Anand S, *et al*., 2017, Photocrosslinking-based bioprinting: Examining crosslinking schemes. *Bioprinting*, 5: 10–18. https:// dx.doi.org/10.1016/j.bprint.2017.03.001
120. Nair K, Gandhi M, Khalil S, *et al*., 2009, Characterization of cell viability during bioprinting processes. *Biotechnol J*, 4(8): 1168–1177. http://dx.doi.org/10.1002/biot.200900004
121. Arslan-Yildiz A, El Assal R, Chen P, *et al*., 2016, Towards artificial tissue models: Past, present, and future of 3D bioprinting. *Biofabrication*, 8(1): 014103.http://dx.doi.org/10.1088/1758-5090/8/1/014103
122. Pereira R Fand Bartolo P J, 2015, 3D bioprinting of photocross-linkable hydrogel constructs. *J Appl Polym Sci*, 132(48): 42458.http://dx.doi.org/10.1002/App.42458
123. Kirchmajer D M, Gorkin R and Panhuis M I H, 2015, An overview of the suitability of hydrogel-forming polymers for extrusion-based 3D-printing. *J Mater Chem B Mater Biol Med*, 3(20): 4105–4117. http://dx.doi.org/10.1039/c5tb00393h
124. Chirag Khatiwala R L, Benjamin Shepherd, Scott Dorfman, *et al.*, 2012, 3D cell bioprinting for regenerative medicine research and therapies. *Gene Ther Regul*, 7(1): 1230004. http://dx.doi.org/10.1142/S1568558611000301
125. Wang Z J, Jin X, Dai R, *et al*., 2016, An ultrafast hydrogel photocrosslinking method for direct laser bioprinting. *RSC Adv*, 6(25): 21099-21104. http://dx.doi.org/10.1039/c5ra24910d
126. Armstrong J P K, Burke M, Carter B M, *et al*., 2016, 3D bioprinting using a templated porous bioink. *Adv Healthc Mater*, 5(14): 1724–1730. http://dx.doi.org/10.1002/adhm.201600022
127. Cui X F, Breitenkamp K, Finn M G, *et al*., 2012, Direct human cartilage repair using three-dimensional bioprinting technology. *Tissue Eng Part A*, 18(11 –12): 1304–1312. http://dx.doi.org/10.1089/ten.tea.2011.0543
128. Fedorovich N E, Oudshoorn M H, van Geemen D, *et al*., 2009, The effect of photopolymerization on stem cells embedded in hydrogels. *Biomaterials*, 30(3): 344–353. http://dx.doi.org/10.1016/j.biomaterials.2008.09.037
129. Folkman J and Hochberg M, 1973, Self-regulation of growth in three dimensions. *J Exp Med*, 138(4): 745–753.
130. Li S, Xiong Z, Wang X, *et al*., 2009, Direct fabrication of a hybrid cell/hydrogel construct by a double-nozzle assembling technology. *J Bioact Compat Polym*, 24(3): 249-265. http://dx.doi.org/10.1016/j.biomaterials.2016.07.038
131. Jia W, Gungor-Ozkerim P S, Zhang Y S, *et al*., 2016, Direct 3D bioprinting of perfusable vascular constructs using a blend bioink. *Biomaterials*, 106: 58–68. http://dx.doi.org/10.1016/j.biomaterials.2016.07.038
132. Skardal A, Zhang J and Prestwich G D, 2010, Bioprinting vessel-like constructs using hyaluronan hydrogels crosslinked with tetrahedral polyethylene glycol tetracrylates. *Biomaterials*, 31(24): 6173–6181. http://dx.doi.org/10.1016/j.biomaterials.2010.04.045
133. Dolati F, Yu Y, Zhang Y, *et al*., 2014, *In vitro* evaluation of carbon-nanotube-reinforced bioprintable vascular conduits. *Nanotechnology*, 25(14): 145101. http://dx.doi.org/10.1088/0957-4484/25/14/145101

134. Gao B, Yang Q Z, Zhao X, *et al*., 2016, 4D bioprinting for biomedical applications. *Trends Biotechnol*, 34(9): 746–756. http://dx.doi.org/10.10164.tibtech.2016.03.004

135. Weiss R A, Izzo E and Mandelbaum S, 2008, New design of shape memory polymers: Mixtures of an elastomeric ionomer and low molar mass fatty acids and their salts. *Macromolecules*, 41(9): 2978–2980. http://dx.doi.org/10.1021/ma8001774

136. Leist S K and Zhou J, 2016, Current status of 4D printing technology and the potential of light-reactive smart materials as 4D printable materials. *Virtual Phys Prototyp*, 11(4): 249–262. http://dx.doi.org/10.1080/17452759.2016.1198630

137. He H Y, Guan J J and Lee J L, 2006, An oral delivery device based on self-folding hydrogels. *J Control Release*, 110(2): 339–346. http://dx.doi.org/10.1016/j.jconrel.2005.10.017

138. Khoo Z X, Teoh J E M, Liu Y, *et al*., 2015, 3D printing of smart materials: A review on recent progresses in 4D printing. *Virtual Phys Prototyp*, 10(3): 103–122. http://dx.doi.org/10.1080/17452759.2015.1097054

139. He Y, Wu Y, Fu J Z, *et al.*, 2016, Developments of 3D printing microfluidics and applications in chemistry and biology: A review. *Electroanalysis*, 28(8): 1658–1678. http://dx.doi.org/10.1002/elan.201600043

140. Lee V K, Lanzi A M, Ngo H, *et al.*, 2014, Generation of multi-scale vascular network system within 3D hydrogel using 3D bio-printing technology. *Cell Mol Bioeng*, 7(3): 460–472. http://dx.doi.org/10.1007/s12195-014-0340-0

RESEARCH ARTICLE

An nMgO containing scaffold: Antibacterial activity, degradation properties and cell responses

Cijun Shuai[1,2,3], Wang Guo[1], Chengde Gao[1], Youwen Yang[1], Ping Wu[4] and Pei Feng[1*]

[1] State Key Laboratory of High Performance Complex Manufacturing, College of Mechanical and Electrical Engineering, Central South University, Changsha, China
[2] Jiangxi University of Science and Technology, Ganzhou, China
[3] Key Laboratory of Organ Injury, Aging and Regenerative Medicine of Hunan Province, Changsha, China
[4] College of Chemistry, Xiangtan University, Xiangtan, China

Abstract: Bone repair failure caused by implant-related infections is a common and troublesome problem. In this study, an antibacterial scaffold was developed via selective laser sintering with incorporating nano magnesium oxide (nMgO) to poly(3-hydroxybutyrate-co-3-hydroxyvalerate) (PHBV). The results indicated the scaffold exerted high antibacterial activity. The antibacterial mechanism was that nMgO could cause oxidative damage and mechanical damage to bacteria through the production of reactive oxygen species (ROS) and direct contact action, respectively, which resulted in the damage of their structures and functions. Besides, nMgO significantly increased the compressive properties of the scaffold including strength and modulus, due to its excellent mechanical properties and uniform dispersion in the PHBV matrix. Moreover, the degradation tests indicated nMgO neutralized the acid degradation products of PHBV and benefited the degradation of the scaffold. The cell culture demonstrated that nMgO promoted the cellular adhesion and proliferation, as well as osteogenic differentiation. The present work may open the door to exploring nMgO as a promising antibacterial material for tissue engineering.

Keywords: Nano magnesium oxide; antibacterial scaffolds; degradation properties; cytocompatibility; mechanical properties

*Correspondence to: Pei Feng, State Key Laboratory of High Performance Complex Manufacturing, College of Mechanical and Electrical Engineering, Central South University, Changsha, 410083, China; fengpei@csu.edu.cn

Received: September 17, 2017; **Accepted**: October 10, 2017; **Published Online**: November 1, 2017

Citation: Shuai C, Guo W, Gao C, *et al.*, 2018, An nMgO containing scaffold: Antibacterial activity, degradation properties and cell responses. *Int J Bioprint*, 4(1): 120. http://dx.doi.org/10.18063/IJB.v4i1.120

1. Introduction

Bone scaffolds are usually susceptible to bacterial infections, which easily result in the failure of bone repair[1–3]. In clinic, administration of antibiotics is a frequently used method for prophylaxis and treatment of infections. However, long-term administration of antibiotics easily causes toxic and adverse effects to the human body such as hypersensitivity and immunosuppression; and the abuse of antibiotics has given rise to serious multiple drug resistance of many pathogenic bacteria[4–7]. Therefore, it is extremely necessary to explore new methods of dealing with the implant-related bacterial infections.

Developing antibacterial scaffolds may be a promising strategy with incorporating antibacterial materials[8–10]. Metallic oxides, including silver oxide, copper oxide, titanium dioxide and magnesium oxide (MgO), have attracted attention owing to their high antibacterial activity and broad antibacterial spectrum[11–13]. Among them, MgO, and especially nanosized MgO (nMgO), is more promising, considering that it has not only strong antibacterial activity but also excellent biocompatibility, which has been recognized as safe by the US Food and Drug Administration (21CFR184.1431)[14]. Besides, its alkaline degradation products may be in favor of constructing weakly alkaline microenvironments for cellular responses; the magnesium ion is widely involved in human metabolisms, playing an significant role in regulating cellular responses[15]. In addition, it has been previously used as a rigid filler for reinforcing polymer[16,17].

Haldorai and Shim[18] prepared chitosan/MgO composites by chemical precipitation method and found the composites showed a much higher killing rate against

Escherichia coli (*E. coli)* compared with chitosan. Yamamoto *et al*.[19] prepared calcium carbonate/nMgO composites *via* thermal decomposition of dolomite and found the composites exerted high antibacterial properties towards *E. coli* and *Staphylococcus aureus*. Ma *et al*.[20] prepared poly(L-lactide)/nMgO composites and found nMgO neutralized the acidic degradation products of poly(L-lactide) and improved its mechanical properties. Nevertheless, studies on MgO-containing composites for biomedical applications are still very lacking, and few papers, to the best of our knowledge, have systematically studied their comprehensive performances, especially in the form of scaffolds.

In this study, nMgO was incorporated to PHBV for developing antibacterial bone scaffolds. Three-dimensional porous PHBV/nMgO scaffolds were prepared by selective laser sintering (SLS). The antibacterial activity of the scaffolds was evaluated, while the antibacterial mechanisms were analyzed and discussed. Moreover, the microstructure, mechanical properties, degradation behaviors and cell responses of the scaffolds were also assessed.

2. Materials and Methods

2.1 Powders Preparation

PHBV with 3 mol% of 3-hydroxyvalerate content, 280 kDa of molecular weight, 1 μm of average particle size and 1.25 g/cm^3 of density (the data were provided by the manufacturer) was obtained from Tianan Biologic Materials Co., Ltd. (Ningbo, China). nMgO with average particle size of 50 nm and density of 3.58 g/cm^3 (the data were provided by the manufacturer) was purchased from Shanghai Macklin Biochemical Co., Ltd. (Ningbo, China).

Five formulations of PHBV/nMgO powders containing 0, 1, 3, 5 and 7 wt% nMgO were prepared mainly through the following procedures[21]: (a) weighing certain amounts of PHBV and nMgO powders according to the designed formulations, and adding them into two beakers containing certain amounts of absolute ethyl alcohol, respectively, followed by magnetically stirring the two solutions for 30 min, respectively; (b) adding the nMgO solution into the PHBV solution, and magnetically stirring the mixed solution for 30 min, followed by ultrasonically dispersing for 30 min; (c) filtering the mixed solution to obtain the mixed powders; (d) drying the mixed powders in vacuum drying oven at 60 °C for 24 h; (e) mechanically milling the dried powders with planetary ball mill for 2 h, and finally obtaining the PHBV/nMgO powders.

2.2 Scaffolds Preparation

Three-dimensional porous scaffolds were prepared *via* a self-developed SLS system, which consisted mainly of a CO_2 laser device (SR 10i, Rofin-Sinar Laser GmbH, Hamburg, Germany) and a galvanometer scanning system (3D scanhead-300-15D, Beijing Century Sunny Technology Co., Beijing, China). Briefly, the laser selectively sinters the powder layers under the control of the scanning system according to the cross-section profiles of the designed parts, forming the solid parts in a layer-by-layer manner[22,23]. The primary processing parameters, *i.e*., laser power, scanning speed, scanning spacing and layer thickness were set as 2 W, 200 mm/s, 0.1 mm and 0.1 mm, respectively. Five formulations of PHBV/nMgO scaffolds containing 0, 1, 3, 5 and 7 wt% nMgO were fabricated, which were denoted as PHBV, PHBV/1%nMgO, PHBV/3%nMgO, PHBV/5%nMgO and PHBV/7%nMgO scaffolds, respectively.

2.3 Microstructures and Mechanical Properties

The phase composition of the PHBV/nMgO scaffolds was analyzed by X-ray diffraction (XRD) (Bruker D8, German Bruker Co., Karlsruhe, Germany). The diffraction data were collected from 5 to 70° at a scan rate of 8°/min using Ni-filtered Cu Kα radiation (λ = 1.5406 Å). The surface morphologies of the PHBV/nMgO scaffolds were analyzed by scanning electron microscope (SEM) (MIRA3, TESCAN, Brno, Czech Republic) installed with energy dispersive spectroscopy (EDS) (X-Max 20, Oxford Instruments, UK) using secondary electron model under 15 kV accelerating voltage. Before the characterization, the specimens were fixed on copper stubs using electrically conductive adhesives, followed by spurting with platinum to increase their conductivity.

The mechanical properties of the PHBV/nMgO scaffolds were assessed by compression tests using a universal testing machine with a 30 kN load cell (MTS Insight 30, MTS Systems Corporation, MN, USA). The specimens (cylinder, 12.7 mm in diameter by 25.4 mm) were compressed to 50% strain at a rate of 1 mm/min[24,25]. The compressive strength and compressive modulus of the scaffolds were determined from the obtained compressive stress-strain curves. Five specimens were tested for each formulation of the scaffolds. The scaffolds with optimal compressive properties were then used to characterize their antibacterial activity, degradation properties and cytocompatibility.

2.4 Antibacterial Activity

E. coli was used as a model bacterium as it is one of the most common bacteria causing orthopedic implant-related infections[26]. The antibacterial activity was evaluated by seeding *E. coli* ATCC 25922 to the PHBV/5%nMgO scaffolds and then observing the

adhesion and proliferation level, with PHBV scaffolds serving as control. The bacterial suspensions were diluted to a concentration of 5×10^5 CFU/mL as this is the clinically relevant concentration in orthopedic infections[27]. Before seeding, the scaffold specimens (diameter 8 mm, thickness 4 mm) were sterilized in XFS-260 autoclave at 120 °C for 20 min, followed by immersing in phosphate buffer solution (PBS) overnight to prewet. Afterwards, the specimens were seeded with the diluted bacterial suspensions and incubated in low glucose Dulbecco's Modified Eagle Medium (DMEM) at 37 °C in 5% CO_2/95% air atmosphere. After 24 h of incubation, the bacterium/scaffold constructs were gently washed using PBS, and then were fixed with 2.5% glutaraldehyde. Subsequently, they were dehydrated with a graded ethanol series, and dried in vacuum drying oven. Afterwards, the dried specimens were installed on copper stubs, sputtering with platinum. Finally, the adhesion and proliferation level of *E. coli* were characterized using a SEM (Phenom ProX, Phenom-World BV, Netherlands) installed with EDS (INCA, Oxford Instruments, UK) under backscattering mode.

Reactive oxygen species (ROS) was reported to play a significant role in exerting the antibacterial activity of some metallic oxide including nMgO[12,13]. Hence, an oxidation-reduction method[28,29] based on reducing nitroblue tetrazolium (NBT) by ROS was employed to detect the production of ROS in the suspensions containing PHBV/5%nMgO scaffolds, with PHBV scaffolds serving as control. Firstly, approximately 50 mg PHBV/5%nMgO scaffold specimens were added into a cap-sealed tube filling with 50 mL PBS containing 2.5×10^{-5} M NBT, followed by incubating at 37 °C in a water bath shaker (SHA-C, Hunan Lichen Instrument Technology Co., Ltd., Changsha, China). After incubating for 1 min, 1 mL of the suspension was aspirated and filtered in order to determine the initial absorbance. After that, another 1 mL of the suspension was regularly aspirated and filtered at a fixed time interval of 10 min until 60 min. The absorbance of the initial filtrates and the filtrates taken out at the fixed time interval was measured with an ultraviolet-visible (UV-vis) spectrophotometer at 259 nm where NBT showed a maximum absorbance. The amount of the produced ROS was proportional to the reduction percentage of NBT, which was calculated by the equation (2.1):

$$\text{Reduction percentage of NBT (\%)} = (A_0-A_t)/A_0\times100 \quad (2.1)$$

where A_0 and A_t represent the absorbance of the initial filtrates and the filtrates taken out at *t* min, respectively. The ROS detection tests were performed in quintuplicate. Besides, a blank control was also set, where no scaffold specimens were added into PBS/NBT solution, in order to exclude the effects of possible self-decomposition of NBT.

2.5 Degradation Properties

The degradation properties of the PHBV/nMgO scaffolds were evaluated by immersing them in PBS (pH = 7.4). Prior to immersion, the initial weights of the specimens were recorded. Approximately 1 g specimen was added into a cap-sealed tube containing 10 mL PBS and incubated in an electronic thermostat water bath at 37 °C. After the predetermined immersion time (7, 14, 21, 28 and 35 days), the specimens were taken out and the PBS was collected. The pH values of the collected PBS were measured using a digital pH meter with a resolution of 0.01 (PHS-3C, Shanghai Xiaosheng Instrument Manufacturing Co., Ltd., Shanghai, China). The specimens were dried in a vacuum drying oven until their weights were constant. The weight loss of the specimens was calculated by the equation (2.2):

$$\text{Weight loss (\%)} = (W_0-W_t)/W_0\times100 \quad (2.2)$$

where W_0 and W_t represents the initial weights and the residual weights of the specimens after t days of immersion, respectively. The pH and weight loss tests were carried out in quintuplicate.

After the weight loss was determined, the specimens were used to characterize the degradation morphologies. Before SEM characterization, the specimens were installed on copper stubs and sputtered with gold. The surface morphologies of the specimens were observed by Phenom ProX SEM using backscattering mode under 15 kV acceleration voltage.

2.6 Cytocompatibility

The cytocompatibility of PHBV/5% nMgO scaffold was evaluated by seeding with MG63 cells (American Type Culture Collection, Manassas, VA, USA) and assessing the cellular responses. The MG63 cells were harvested using trypsin/EDTA, centrifuged at 1×10^3 rpm for 3 min and resuspended in DMEM. The scaffold specimens (diameter 8 mm, thickness 4 mm) were sterilized in an autoclave (XFS-260, Zhejiang Xinfeng Medical Devices Co., Ltd., Shaoxing, China) at 120 °C for 20 min, followed by immersing in PBS overnight to prewet. Afterwards, the specimens were seeded with MG63 cells (at a density of 2×10^3/well, 1×10^5/well and 5×10^5/well for SEM observation, Cell Counting Kit-8 (CCK-8) assay and alkaline phosphatase (ALP) staining, respectively) and incubated in low glucose DMEM supplemented with 10% fetal bovine serum and 1% antibiotic-antimycotic solution at 37 °C in 5% CO_2/95% air atmosphere. After the selected incubation time, the cell-scaffold constructs were sacrificed to assess the cellular adhesion, proliferation and osteogenic

differentiation by SEM observation, CCK-8 assay and ALP staining, respectively.

For evaluating cellular adhesion, the cell/scaffold specimens were gently washed with PBS, followed by fixing with 2.5% glutaraldehyde. Subsequently, a graded ethanol series was used to dehydrate the cells. Afterwards, the specimens were dried in vacuum drying oven, followed by sputtering with platinum. Finally, the cellular morphologies were characterized by Phenom ProX SEM using backscattering mode under 15 kV acceleration voltage. For CCK-8 assay, the MG63 cells were harvested from the scaffold specimens by Trypsin-ethylene diamine tetraacetic acid solution, followed by centrifugation treatment. Afterwards, 0.2 mL of the obtained supernatant was added into 1 mL of fresh culture medium, followed by adding CCK-8 (CK04-13, Dojindo Molecular Technologies, Kimamoto, Japan) solution into it according to the instructions of the manufacturer, which generated an orange formazan product by cellular dehydrogenases. After culture for 4 h at 37 °C, 100 µL of the sample solution was transferred into plate to measure the absorbance with a microplate reader (Beckman, USA) at 450 nm. For ALP staining, the MG63 cells were washed with PBS, fixed with 4% paraformaldehyde for 30 min and then permeated with 0.5% Triton X-100 for 30 min. Subsequently, ALP staining was carried out with 5-bromo-4-chloro-3-indolyl-phosphate/NBT (BCIP/NBT) alkaline phosphatase color development kit (P0321, Shanghai Beyotime Biological Technology Co., Ltd, China) according to the instructions of the manufacturer. Finally, the stained cells were mounted with water-based mounting medium (Boster Biological Technology Co., Ltd., China), followed by observing with light microscope.

2.7 Statistical Analysis

Quantitative data were expressed as the mean ± standard deviation. Levene's test was applied to examine equality of variances. Unpaired two-tailed Student's *t*-test was performed to determine statistical significance. Labels *, ** and *** represent $p < 0.05$, $p < 0.01$ and $p < 0.001$, respectively.

3. Results and Discussion

The three-dimensional porous scaffold model and a representative SLS-fabricated PHBV/nMgO scaffold were shown in Figure 1. It could be seen that the shape and size of the scaffold were consistent with those of the model. The scaffold showed a well ordered and interconnected porous structure. It was considered that the pore size of scaffolds should be large enough to ensure nutrient delivery and tissue ingrowth but not too large to prevent cell migration[30]. Roosa *et al.*[31] found all of the polycaprolactone scaffolds with pore size from 350 to 800 µm could promote bone regeneration and there were no significant differences in new bone formation between them. Similar results were reported by Schek *et al.*[32] who found significant new bone formation for both poly(propylenefumarate)/β-tricalcium phosphate scaffolds with 300 and 800 µm pores, with no statistical differences between them. Hence, the PHBV/nMgO scaffold with pore size of about 400 µm may be beneficial for substance metabolism, cell responses and bone regeneration.

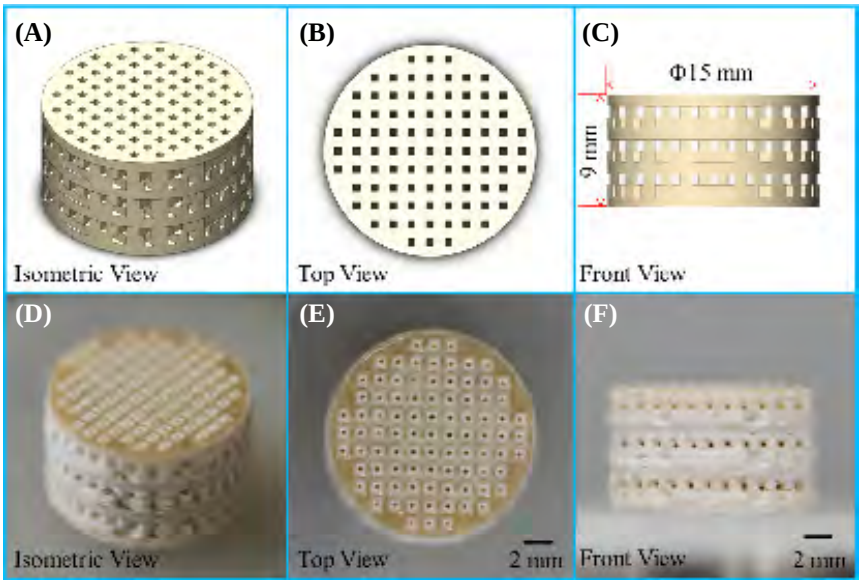

Figure 1. (**A**–**C**) The three-dimensional porous scaffold model and (**D**–**F**) a representative SLS-fabricated PHBV/nMgO scaffold.

The XRD patterns of the PHBV/nMgO scaffolds were plotted in Figure 2. The PHBV scaffold showed strong diffraction peaks at 2θ = 13.4 and 16.8°, which were corresponding to (020) and (110) planes, respectively; additional diffraction peaks at 2θ = 20.1, 21.4, 22.6, 25.5, and 27.1° were also detected, which were assigned to (021), (101), (111), (121), and (040) planes, respectively[33,34]. After incorporating nMgO, the scaffolds showed two new diffraction peaks at 2θ = 42.9 and 62.3°, which were just corresponding to the two main diffraction peaks of MgO assigning to (200) and (220) planes (JCPDS 87-0653), respectively. Moreover, the intensities of the main diffraction peaks of nMgO gradually increased with increasing nMgO content. This indicated nMgO kept thermal stability during the SLS process as it had a very high melting point more than 2800 °C[35].

The compressive strength and compressive modulus of the PHBV/nMgO scaffolds as a function of nMgO content were depicted in Figure 3. In general, they both increased at first but decreased then with the nMgO content increasing from 0 to 7 wt%. The compressive strength and compressive modulus of the PHBV scaffolds were 2.62 and 29.33 MPa, respectively. After incorporating nMgO from 1 to 5 wt%, they keep increasing from 3.37 to 5.14 MPa, and 34.36 to 44.68 MPa, respectively. However, they began to decrease when the nMgO content exceeded 5 wt%. Therefore, the optimal nMgO content was considered to be 5 wt% to obtain the optimal compressive strength and modulus, which were improved by 96.18% and 52.34% compared with the PHBV scaffolds, respectively. It was worth noting that the optimal compressive strength and modulus of the scaffolds was close to that of human trabecular bone (4 to12 MPa and 50 to 500 MPa, respectively[36]).

As the dispersion of fillers in polymer matrix was a significant factor influencing the mechanical properties of polymer composites[37–40], the dispersion of nMgO in PHBV matrix with different nMgO content were characterized using SEM (Figure 4). After incorporation of nMgO, some bright spots appeared in the PHBV matrix; their amounts gradually increased with the nMgO content increasing. The EDS spectrums indicated that the bright spots were just the nMgO incorporated. They kept dispersing uniformly in the PHBV matrix until 5 wt%. However, severe aggregations happened when further increasing the nMgO content. It was well known that excessive nanoparticles would easily result in the occurrence of agglomeration due to the large specific surface area and surface energy[41,42].

The compressive properties of the PHBV/nMgO scaffolds increased with the nMgO content increasing as the total interfacial areas between the fillers and matrix keep increasing. The significant improvements in the mechanical properties of the PHBV/nMgO scaffolds were resulted from strong reinforcing effects of MgO nanoparticles. There were several factors accounting for it: (a) the elastic modulus of MgO was as high as 310 GPa[43], ensuring the applied stress could be transferred to the fillers from the matrix; (b) the nano-sized MgO have extremely high specific surface area, which greatly increased their interfacial areas with the matrix and thus enhanced effectiveness of the stress transfer; (c) the uniform dispersion of MgO nanoparticles in the PHBV matrix maximized its potential in improving the mechanical properties. However, excessive nanoparticles would form severe agglomerations (>5 wt%), which

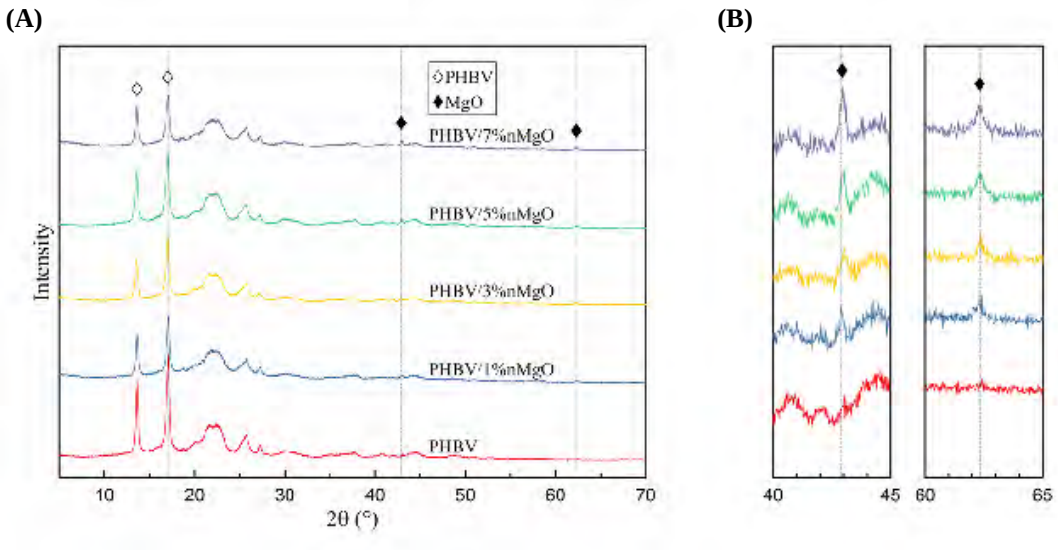

Figure 2. (**A**) The XRD patterns of the PHBV/nMgO scaffolds; (**B**) the enlarged version from 40° to 45° and 60° to

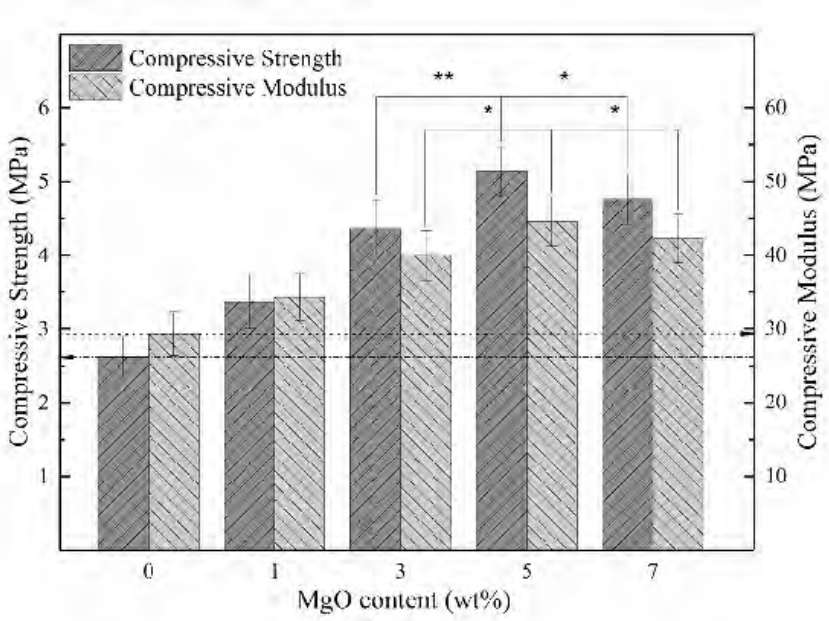

Figure 3. The compressive strength and compressive modulus of the PHBV/nMgO scaffolds as a function of nMgO content

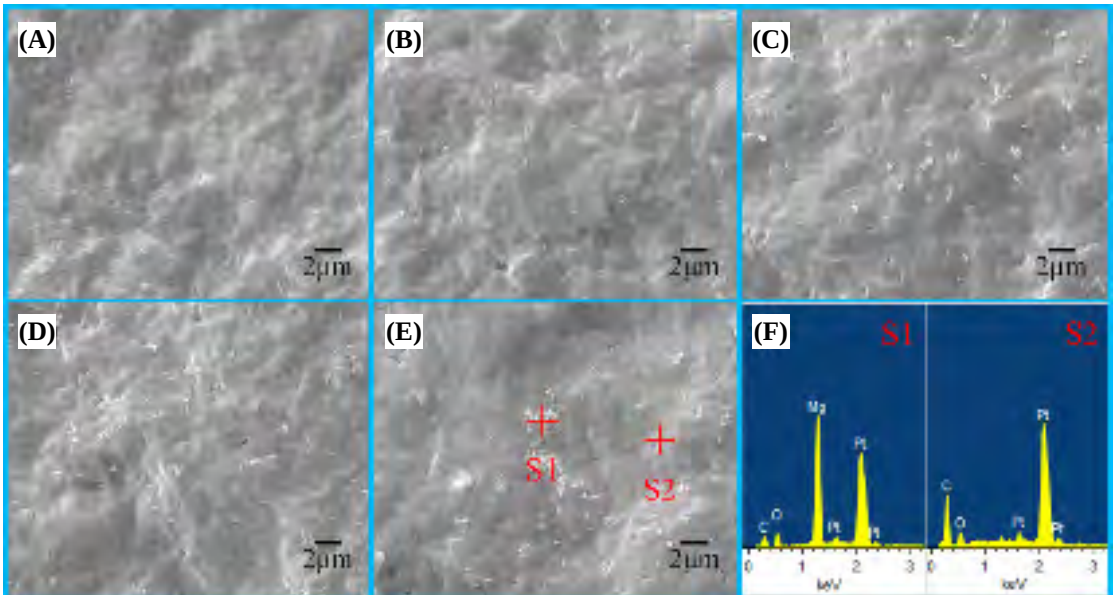

Figure 4. The distribution of nMgO in PHBV matrix with (**A**) 0, (**B**) 1, (**C**) 3, (**D**) 5 and (**E**) 7 wt% nMgO; (**F**) the EDS spectrums of point S1 and S2.

led to a significant decrease of the interfacial areas and strength between the fillers and matrix, thus resulting in the decrease of the reinforcing efficiency. As the PHBV/5%nMgO scaffold showed optimal compressive properties, they were selected to be further evaluated in terms of antibacterial activity, degradation behaviors and cytocompatibility.

The adhesion and proliferation level of *Escherichia coli* (*E. coli*) cultured on the PHBV/5%nMgO and PHBV scaffolds after 24 h were evaluated by SEM (Figure 5). The *E. coli* showed a typical rod shape. It was obvious that large amounts of *E. coli* attached on the PHBV scaffolds and covered almost the entire surface. In contrast, there was only a small amount of *E. coli* attaching on the PHBV/5%nMgO scaffolds. The dramatic decrease of the numbers of *E. coli* indicated that nMgO inhibited the adhesion and proliferation of *E. coli* and killed them. Moreover, it seemed the appearance of the *E. coli* attached on the PHBV/nMgO scaffolds was abnormal, suggesting them suffered structural damage from the antibacterial action of nMgO (Figure 5D). The results indicated the incorporation of nMgO imparted strong antibacterial activity to the scaffolds.

As ROS production was reported to play a significant

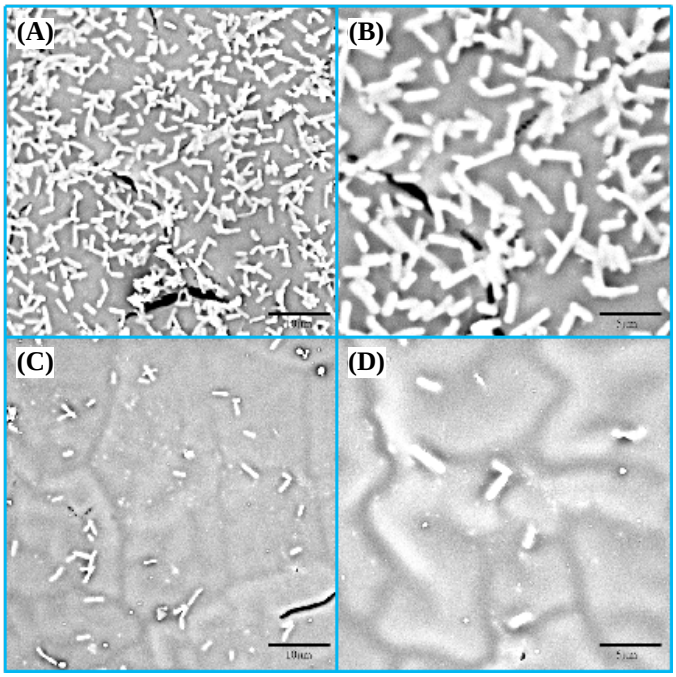

Figure 5. The morphologies of *Escherichia coli* cultured on (**A**, **B**) PHBV and (**C**, **D**) PHBV/5%nMgO scaffolds after 24 h.

role in exerting the antibacterial activity of some metallic oxide including nMgO[44–46]. Hence, the production of ROS from the PHBV/nMgO scaffolds was indirectly determined by calculating the reduction percentage of NBT. As shown in Figure 6, there was almost no reduction of NBT for PHBV scaffolds, indicating they did not produce ROS. Actually, a slight reduction of ROS could be observed, which was resulted from the decomposition of NBT itself as shown in the blank control. In contrast, there happened significant reduction of NBT for the PHBV/nMgO scaffolds. Meanwhile, the reduction of NBT gradually increased with incubation time increasing. The results demonstrated nMgO promoted the production of ROS.

The production of ROS may be attributed to a sequential oxidation-reduction reactions occurred at the surface of nMgO[47]. In detail, nMgO could be hydrated with water and form $Mg(OH)_2$ on its surface, leading to the formation of surface bound electron-hole pairs, which would subsequently decompose into surface trapped electrons and localized holes[48,49]. They were typical oxide catalysts and would promote molecular oxygen (O_2) to produce ROS *via* single electron reduction[50]. It was worth noting that ROS was a strong oxidant. When its concentration exceeded the scavenging ability of the antioxidant defense system of bacteria,

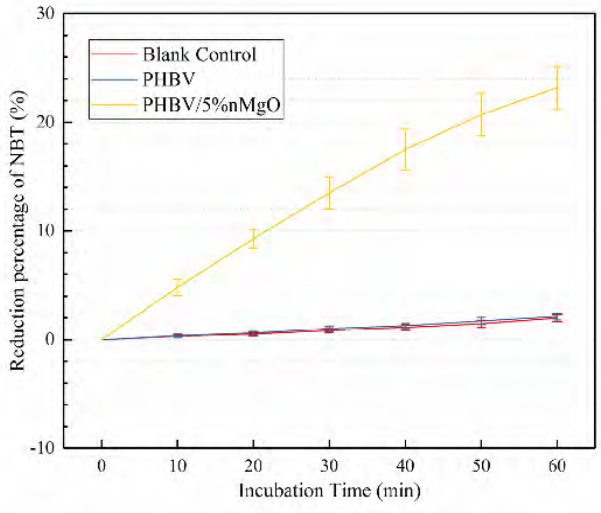

Figure 6. Reduction percentage of NBT with different incubation time for PHBV/5%nMgO and PHBV

they would compel them generate oxidative stress, which subsequently led to the damage of the structure and functions of bacteria[51,52]. Besides, the contact action of the MgO nanoparticles on bacteria would make them generate mechanical stress, resulting in the deformation and damage of the bacterial structure[53,54]. In addition, there were large amounts of active sites on MgO nanoparticles[55], enabling them easily absorb to the bacteria; the enrichment of nanoparticles on the bacteria would increase their membrane permeability[56]. The possible antibacterial mechanisms of nMgO were summarized in detail in Figure 7.

The mass loss and pH for the PHBV/5%nMgO and PHBV scaffolds after immersion in PBS for different days were shown in Figure 8A and 8B, respectively. The mass loss of both of the scaffolds gradually increased with immersion time prolonging, but it was obvious that the mass loss of the PHBV/5%nMgO scaffolds was larger than that of the PHBV scaffolds. After 35 days, the mass loss of the PHBV/5%nMgO scaffolds was 12.68%, which was almost double that of the PHBV scaffolds. In contrast, the change trends of pH for the PHBV and PHBV/5%nMgO scaffolds were significantly different; the pH for the former decreased gradually while that of the latter increased gradually with immersion time increasing. After 35 days, the pH for the PHBV and PHBV/5%nMgO scaffolds were 6.85 and 7.63, respectively, resulting in a weakly acid and weakly alkaline microenvironment, respectively. Besides, the amplitude of pH variation for the PHBV/5%nMgO scaffolds was much smaller than that for the PHBV scaffolds. This was mainly ascribed to the alkaline degradation products of MgO, which exerted neutralization effect against the acid degradation products of PHBV. These results indicated nMgO could promote the degradation of the PHBV scaffolds and neutralize their acid degradation products.

The surface microtopography of PHBV/5%nMgO and PHBV scaffolds after immersion were characterized by SEM (Figure 9) to explain the results of mass loss and pH. It was clear that the surface morphologies of the PHBV/5%nMgO scaffolds were significantly different from that of PHBV scaffolds. In general, the surfaces of PHBV scaffolds after immersion were smooth if the microvoids and microcracks on them were neglected. For PHBV/5%nMgO scaffolds, many micropores appeared on the surface after 7 days of immersion. With the degradation time prolonging, their quantity and size gradually increased. After 35 days of degradation, large amounts of pores formed on the surface, resulting in a microporous structure.

The micropores were resulted from the degradation of MgO nanoparticles as well as the subsequent collapse of the PHBV matrix. It was known that MgO would be hydrolyzed with water to form $Mg(OH)_2$, but a strange thing was that it seemed no $Mg(OH)_2$ particles appeared on the surface. Nevertheless, the EDS mapping results (Figure 9G) indicated that there obviously existed element Mg after degradation, which belonged to $Mg(OH)_2$ and/or MgO in the PHBV matrix. The "disappearance" of $Mg(OH)_2$ was attributed to its dissolution and outflow into PBS solutions. When

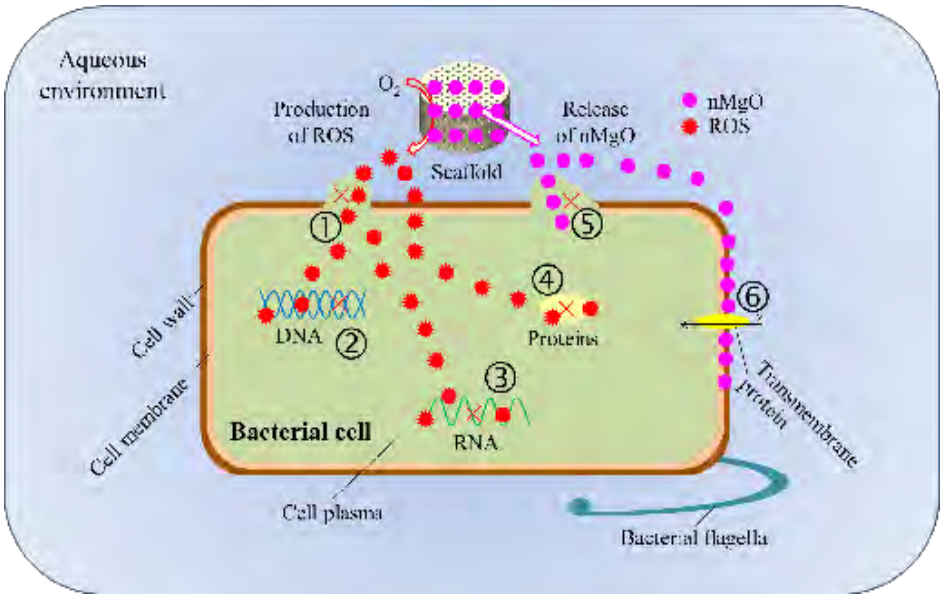

Figure 7. Possible antibacterial mechanisms of the PHBV/nMgO scaffolds: (1) oxidative damage of cell wall and membrane of bacteria resulted by ROS; (2) oxidative damage of DNA and inhibition of its transcription resulted by ROS; (3) oxidative damage of RNA and inhibition of its translation resulted by ROS; (4) oxidative damage and activity inhibition of proteins resulted by ROS; (5) mechanical damage of cell wall and/or membrane of bacteria resulted by the contact action of nMgO; (6) change of membrane permeability of bacteria resulted by the enrichment of nMgO.

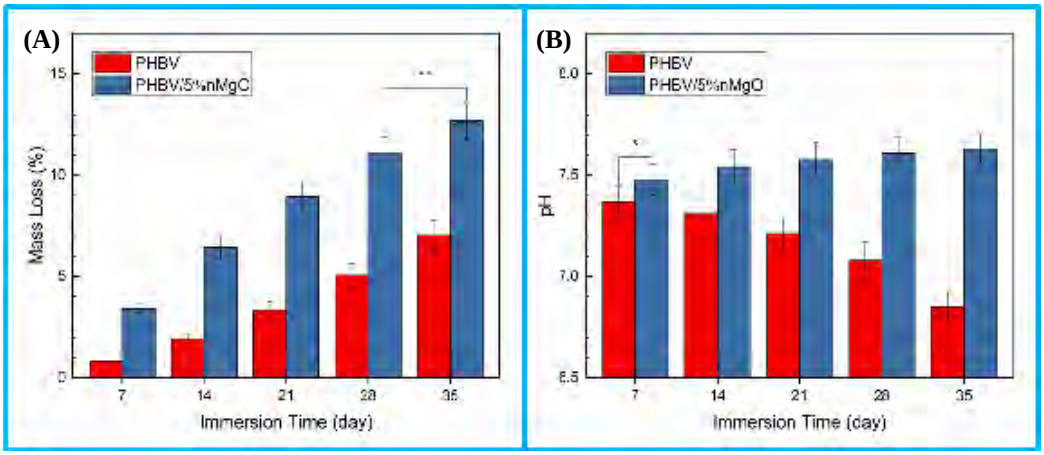

Figure 8. The (**A**) mass loss and (**B**) pH for the PHBV/5%nMgO and PHBV scaffolds as a function of immersion

MgO was hydrated with water to form $Mg(OH)_2$, its crystal lattice would transform from cubic structure to hexagonal structure, which resulted in significant volume expansion[57]. Meanwhile, crystal growth pressure and water-absorbing swelling pressure of $Mg(OH)_2$ would further promote the volume expansion[58]. This would lead to the deterioration of the interface adhesion between the particles and matrix, thus making them easy to outflow and leave large amounts of micropores in the matrix. In return, the pores would significantly increase the specific surface area of the matrix and make water permeate more easily, thus promoting the degradation of the scaffolds.

The cytocompatibility of PHBV/5%nMgO scaffolds was evaluated in terms of cellular adhesion, proliferation and osteogenic differentiation. The adhesion morphology of MG63 cells on PHBV/5%nMgO and PHBV scaffolds after culture for 1, 3 and 5 days was shown in Figure 10. MG63 cells showed an elongated shape and anchored to the surface of the PHBV scaffolds with lamellipodia after 1 day of culture. Some of them gathered together and formed clusters on day 3. On day 5, most regions of the PHBV scaffolds were covered with cell clusters. As for PHBV/5%nMgO scaffolds, some of MG63 cells fused together on the surfaces as soon as on day 1. After 5 days of culture, the entire regions of the PHBV/5%nMgO scaffolds were almost fully covered with MG63 cells, forming thicker cell clusters than that

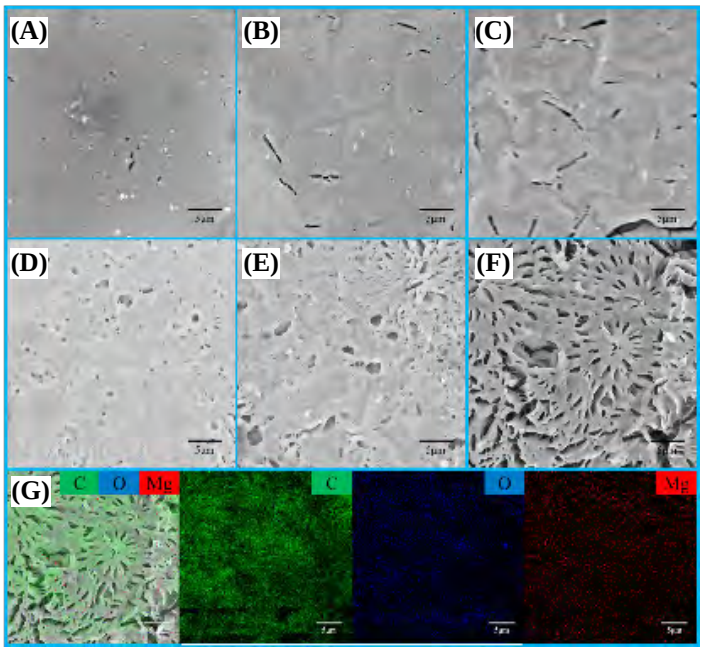

Figure 9. The surface microtopography of (**A**, **B**, **C**) PHBV scaffolds and (**D**, **E**, **F**) PHBV/5%nMgO scaffolds after immersion in PBS for (**A**, **D**) 7, (**B**, **E**) 21 and (**C**, **F**) 35 days; (**G**) the EDS mapping images of carbon, oxygen and magnesium elements for the PHBV/5%nMgO scaffolds after 35 days of immersion.

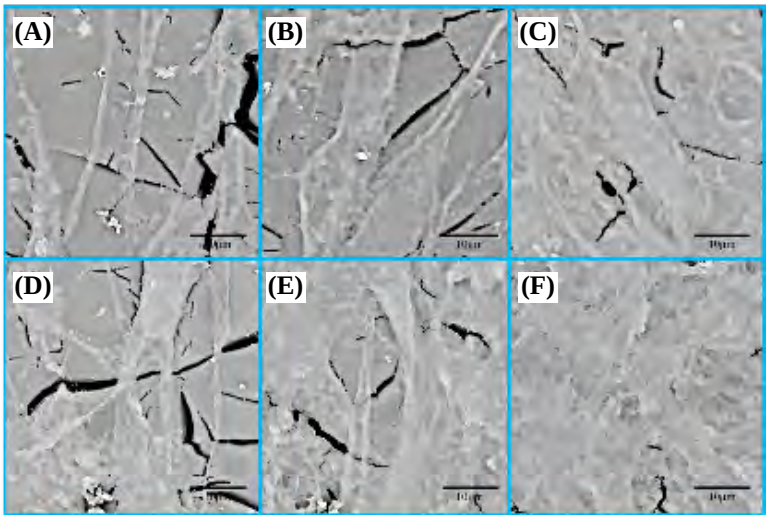

Figure 10. The adhesion morphology of MG63 cells on (**A**, **B**, **C**) PHBV and (**D**, **E**, **F**) PHBV/5%nMgO scaffolds after culture for (**A**, **D**) 1, (**B**, **E**) 3 and (**C**, **F**) 5 days.

on the PHBV scaffolds. The SEM results indicated the addition of MgO promoted the cellular adhesion and proliferation of MG63 cells on the scaffolds.

The proliferation level of MG63 cells on PHBV/5% nMgO and PHBV scaffolds after culture for 1, 3 and 5 days was evaluated by CCK-8 assay (Figure 11). The absorbance is directly proportional to the number of cells according to the principle[59]. It was clear that the number of MG63 cells gradually increased during the whole culture period, for both of the scaffolds. There were significant differences in cell numbers between the adjacent culture time for the PHBV/5% nMgO scaffolds. More importantly, the cell numbers on the PHBV/5% nMgO scaffolds were more than that on the PHBV scaffolds, with significant differences being observed. The CCK-8 assay results suggested the addition of nMgO promoted the proliferation of MG63 cells on the scaffolds.

The osteogenic differentiation of MG63 cells on the PHBV/5% nMgO and PHBV scaffolds was evaluated by ALP staining assay as ALP was widely recognized as a marker for osteogenic differentiation[60]. The number of cells staining positive gradually increased with culture time increasing for both of the PHBV/5% nMgO and PHBV scaffolds (Figure 12). This was attributed either to the maturation of seeded cells or to that of the newly proliferated cells. Furthermore, the cells staining positive on the PHBV/5% nMgO scaffolds were much more than that on the PHBV scaffolds. The ALP staining results indicated the addition of nMgO improved the ability of the scaffolds to induce osteogenic differentiation of MG63 cells.

Ion release from biomaterials was one of the main factors influencing cellular responses[61,62]. It was known that many metal ions could act as co-enzyme factors, thus influencing signal pathways and stimulating cellular responses[63]. In particular, Mg^{2+} could initiate activation of integrins through attaching to the sites on their α-chain[64,65]. It is noted that integrins play an important role in modulating cellular functions such as cellular adhesion, migration, proliferation, differentiation of all human cells as the transduce signals could regulate expression of related genes[66,67]. In the presence of water in the culture medium, the MgO nanoparticles in the matrix would be hydrated with water to form $Mg(OH)_2$. The product would further hydrolyze and ionize into Mg^{2+} and OH^-. Hence, the Mg^{2+} could be released from the scaffolds and be finally utilized by MG63 cells, stimulating their cellular responses.

4. Conclusions

PHBV/nMgO scaffolds fabricated *via* SLS showed interconnected and well-ordered microporous structures. The incorporation of nMgO imparted strong antibacterial activity to the PHBV scaffolds. The antibacterial mechanism was that nMgO could promote the production of ROS and mechanically contact with bacteria. Besides, the compressive strength and compressive modulus of the PHBV scaffolds were increased by 96.18% and 52.34% with addition of 5 wt% nMgO, respectively. Moreover, nMgO could neutralize the acid degradation products of PHBV and promote the degradation of the scaffolds. In addition, nMgO stimulated the cellular adhesion, proliferation and osteogenic differentiation. This study may provide preliminary guidance for applying nMgO as an attractive antibacterial material for bone tissue engineering.

Conflict of Interest and Funding

No conflict of interest was reported by the authors. The

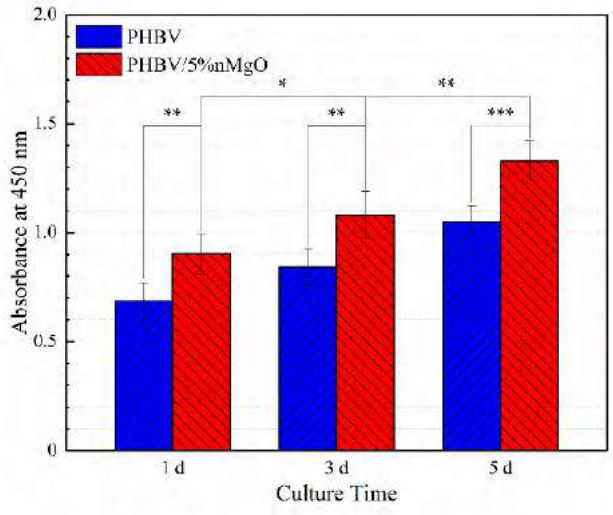

Figure 11. The absorbance for the MG63 cells on the PHBV/5%nMgO and PHBV scaffolds after culture for 1, 3 and 5 days.

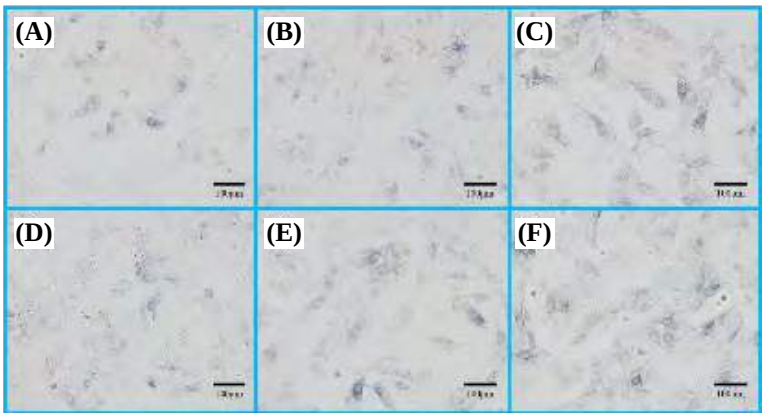

Figure 12. The ALP staining images for (**A**, **B**, **C**) PHBV and (**D**, **E**, **F**) PHBV/5%nMgO scaffolds after culture for (**A**, **D**) 1, (**B**, **E**) 3 and (**C**, **F**) 5 days.

authors gratefully acknowledge the following projects and funds for the financial support: (1) The Natural Science Foundation of China (51575537, 81572577, 51705540); (2) Overseas, Hong Kong, and Macao Scholars Collaborated Researching Fund of National Natural Science Foundation of China (81428018); (3) Hunan Provincial Natural Science Foundation of China (2016JJ1027); (4) The Project of Innovation-driven Plan of Central South University (2016CX023); (5) The Open-End Fund for the Valuable and Precision Instruments of Central South University; (6) The fund of the State Key Laboratory of Solidification Processing at NWPU (SKLSP201605); (7) The Project of State Key Laboratory of High Performance Complex Manufacturing, Central South University, and (8) National Postdoctoral Program for Innovative Talents (BX201700291).

References

1. Zimmerli W, 2014, Clinical presentation and treatment of orthopaedic implant-associated infection. *J Intern Med*, 276(2): 111–119. http://dx.doi.org/10.1111/joim.12233
2. Saidin S, Chevallier P, Abdul Kadir M R, *et al.*, 2013, Polydopamine as an intermediate layer for silver and hydroxyapatite immobilisation on metallic biomaterials surface. *Mater Sci Eng C Mater Biol Appl*, 33(8): 4715–4724. http://dx.doi.org/10.1016/j.msec.2013.07.026
3. Lorenzetti M, Dogsa I, Stosicki T, *et al.*, 2015, The influence of surface modification on bacterial adhesion to titanium-based substrates. *ACS Appl Mater Interfaces*, 7(3): 1644–1651. http://dx.doi.org/10.1021/am507148n
4. Overbye K, Barrett J, 2005, Antibiotics: Where did we go wrong? *Drug Discov Today*, 10(1): 45–52. http://dx.doi.org/10.1016/s1359-6446(04)03285-4

5. Londonkar R L, Madire Kattegouga U, Shivsharanappa K, *et al.*, 2013, Phytochemical screening and *in vitro* antimicrobial activity of *Typha angustifolia* Linn leaves extract against pathogenic gram negative micro organisms. *J Pharm Res*, 6(2): 280–283. http://dx.doi.org/10.1016/j.jopr.2013.02.010
6. Trampuz A, Zimmerli W, 2006, Antimicrobial agents in orthopaedic surgery. *Drugs*, 66(8): 1089–1106. http://dx.doi.org/10.2165/00003495-200666080-00005
7. Goodman S B, Yao Z, Keeney M, *et al.*, 2013, The future of biologic coatings for orthopaedic implants. *Biomaterials*, 34(13): 3174–3183. http://dx.doi.org/10.1016/j.biomaterials.2013.01.074
8. Yang S, Zhang Y, Yu J, *et al.*, 2014, Antibacterial and mechanical properties of honeycomb ceramic materials incorporated with silver and zinc. *Mater Des*, 59: 461–465. http://dx.doi.org/10.1016/j.matdes.2014.03.025
9. Yazdimamaghani M, Vashaee D, Assefa S, *et al.*, 2014, Hybrid macroporous gelatin/bioactive-glass/nanosilver scaffolds with controlled degradation behavior and antimicrobial activity for bone tissue engineering. *J Biomed Nanotechnol*, 10(6): 911–931. http://dx.doi.org/10.1166/jbn.2014.1783
10. Sánchez-Salcedo S, Shruti S, Salinas A J, *et al.*, 2014, *In vitro* antibacterial capacity and cytocompatibility of SiO_2–CaO–P_2O_5 meso-macroporous glass scaffolds enriched with ZnO. *J Mater Chem B*, 2(30): 4836–4847. http://dx.doi.org/10.1039/c4tb00403e
11. Vargas-Reus M A, Memarzadeh K, Huang J, *et al.*, 2012, Antimicrobial activity of nanoparticulate metal oxides against peri-implantitis pathogens. *Int J Antimicrob Agents*, 40(2): 135–139. http://dx.doi.org/10.1016/j.ijantimicag.2012.04.012
12. Dizaj S M, Lotfipour F, Barzegar-Jalali M, *et al.*, 2014, Antimicrobial activity of the metals and metal oxide nanoparticles. *Mater Sci Eng C Mater Biol Appl*, 44: 278–284. http://dx.doi.org/10.1016/j.msec.2014.08.031
13. Li Y, Zhang W, Niu J, *et al.*, 2012, Mechanism of photogenerated reactive oxygen species and correlation with the antibacterial properties of engineered metal-oxide nanoparticles. *ACS Nano*, 6(6): 5164–5173. http://dx.doi.org/10.1021/nn300934k
14. Krishnamoorthy K, Moon J Y, Hyun H B, *et al.*, 2012, Mechanistic investigation on the toxicity of MgO nanoparticles toward cancer cells. *J Mater Chem*, 22(47): 24610–24617. http://dx.doi.org/10.1039/c2jm35087d
15. Staiger M P, Pietak A M, Huadmai J, *et al.*, 2006, Magnesium and its alloys as orthopedic biomaterials: A review. *Biomaterials*, 27(9): 1728–1734. http://dx.doi.org/10.1016/j.biomaterials.2005.10.003
16. De Silva R T, Mantilaka M M, Ratnayake S P, *et al.*, 2017, Nano-MgO reinforced chitosan nanocomposites for high performance packaging applications with improved mechanical, thermal and barrier properties. *Carbohydr Polym*, 157: 739–747. http://dx.doi.org/10.1016/j.carbpol.2016.10.038
17. Zhao Y, Liu B, You C, *et al.*, 2016, Effects of MgO whiskers on mechanical properties and crystallization behavior of PLLA/MgO composites. *Mater Des*, 89: 573–581. http://dx.doi.org/10.1016/j.matdes.2015.09.157
18. Haldorai Y, Shim J-J, 2014, An efficient removal of methyl orange dye from aqueous solution by adsorption onto chitosan/MgO composite: A novel reusable adsorbent. *Appl Surf Sci*, 292: 447–453. http://dx.doi.org/10.1016/j.apsusc.2013.11.158
19. Yamamoto O, Ohira T, Alvarez K, *et al.*, 2010, Antibacterial characteristics of $CaCO_3$–MgO composites. *Mater Sci Eng B*, 173(1–3): 208–212. http://dx.doi.org/10.1016/j.mseb.2009.12.007
20. Ma F, Lu X, Wang Z, *et al.*, 2011, Nanocomposites of poly(L-lactide) and surface modified magnesia nanoparticles: Fabrication, mechanical property and biodegradability. *J Phys Chem Solids*, 72(2): 111–116. http://dx.doi.org/10.1016/j.jpcs.2010.11.008
21. Feng P, Peng S, Wu P, *et al.*, 2016, A space network structure constructed by tetraneedlelike ZnO whiskers supporting boron nitride nanosheets to enhance comprehensive properties of poly (L-lacti acid) scaffolds. *Sci Rep*, 6: 33385. http://dx.doi.org/10.1038/srep33385
22. Lee J M, Sing S L, Tan E Y S, *et al.*, 2016, Bioprinting in cardiovascular tissue engineering: A review. *Int J Bioprint*, 2(2): 27–36. http://dx.doi.org/10.18063/IJB.2016.02.006
23. Murphy C, Kolan K, Li W, *et al.*, 2017, 3D bioprinting of stem cells and polymer/bioactive glass composite scaffolds for bone tissue engineering. *Int J Bioprint*, 3(1): 54–64. http://dx.doi.org/10.18063/IJB.2017.01.005
24. Eshraghi S, Das S, 2010, Mechanical and microstructural properties of polycaprolactone scaffolds with 1-D, 2-D, and 3-D orthogonally oriented porous architectures produced by selective laser sintering. *Acta Biomater*, 6(7): 2467–2476. http://dx.doi.org/10.1016/j.actbio.2010.02.002
25. Eshraghi S, Das S, 2012, Micromechanical finite-element modeling and experimental characterization of the compressive mechanical properties of polycaprolactone–hydroxyapatite composite scaffolds prepared by selective laser sintering for bone tissue engineering. *Acta Biomater*, 8(8): 3138–3143. http://dx.doi.org/10.1016/j.actbio.2012.04.022

26. Amalric J, Mutin P H, Guerrero G, *et al*., 2009, Phosphonate monolayers functionalized by silver thiolate species as antibacterial nanocoatings on titanium and stainless steel. *J Mater Chem*, 19(1): 141–149. http://dx.doi.org/10.1039/b813344a
27. Simchi A, Tamjid E, Pishbin F, *et al*., 2011, Recent progress in inorganic and composite coatings with bactericidal capability for orthopaedic applications. *Nanomedicine*, 7(1): 22–39. http://dx.doi.org/10.1016/j.nano.2010.10.005
28. Ye L, Liu J, Jiang Z, *et al*., 2013, Facets coupling of BiOBr-g-C_3N_4 composite photocatalyst for enhanced visible-light-driven photocatalytic activity. *Appl Catal B*, 142–143: 1–7. http://dx.doi.org/10.1016/j.apcatb.2013.04.058
29. Wu D, Wang B, Wang W, *et al*., 2015, Visible-light-driven BiOBr nanosheets for highly facet-dependent photocatalytic inactivation of *Escherichia coli*. *J Mater Chem A*, 3(29): 15148–15155. http://dx.doi.org/10.1039/c5ta02757h
30. Bruzauskaite I, Bironaite D, Bagdonas E, *et al*., 2016, Scaffolds and cells for tissue regeneration: Different scaffold pore sizes-different cell effects. *Cytotechnology*, 68(3): 355–369. http://dx.doi.org/10.1007/s10616-015-9895-4
31. Roosa S M, Kemppainen J M, Moffitt E N, *et al*., 2010, The pore size of polycaprolactone scaffolds has limited influence on bone regeneration in an *in vivo* model. *J Biomed Mater Res A*, 92(1): 359–368. http://dx.doi.org/10.1002/jbm.a.32381
32. Schek R M, Wilke E N, Hollister S J, *et al*., 2006, Combined use of designed scaffolds and adenoviral gene therapy for skeletal tissue engineering. *Biomaterials*, 27(7): 1160–1166. http://dx.doi.org/10.1016/j.biomaterials.2005.07.029
33. Ten E, Jiang L, Wolcott M P, 2012, Crystallization kinetics of poly(3-hydroxybutyrate-co-3-hydroxyvalerate)/cellulose nanowhiskers composites. *Carbohydr Polym*, 90(1): 541. http://dx.doi.org/10.1016/j.carbpol.2012.05.076
34. Shuai C, Guo W, Gao C, *et al*., 2017, Calcium silicate improved bioactivity and mechanical properties of poly(3-hydroxybutyrate-co-3-hydroxyvalerate) scaffolds. *Polymers*, 9(5): 175. http://dx.doi.org/10.3390/polym9050175
35. Yin Y, Zhang G, Xia Y, 2002, Synthesis and characterization of MgO nanowires through a vapor-phase precursor method. *Adv Funct Mater*, 12(4): 293–298. http://dx.doi.org/10.1002/1616-3028(20020418)12:4<293::aid-adfm293>3.0.co;2-u
36. Hutmacher D W, Schantz J T, Lam C X, *et al*., 2007, State of the art and future directions of scaffold-based bone engineering from a biomaterials perspective. *J Tissue Eng Regen Med*, 1(4): 245–260. http://dx.doi.org/10.1002/term.24
37. Ning N-y, Yin Q-j, Luo F, *et al*., 2007, Crystallization behavior and mechanical properties of polypropylene/halloysite composites. *Polymer*, 48(25): 7374–7384. http://dx.doi.org/10.1016/j.polymer.2007.10.005
38. Li H Y, Tan Y Q, Zhang L, *et al*., 2012, Bio-filler from waste shellfish shell: Preparation, characterization, and its effect on the mechanical properties on polypropylene composites. *J Hazard Mater*, 217–218: 256–262. http://dx.doi.org/10.1016/j.jhazmat.2012.03.028
39. He F, Fan J, Lau S, 2008, Thermal, mechanical, and dielectric properties of graphite reinforced poly(vinylidene fluoride) composites. *Polym Test*, 27(8): 964–970. http://dx.doi.org/10.1016/j.polymertesting.2008.08.010
40. Maity J, Jacob C, Das C K, *et al*., 2008, Direct fluorination of Twaron fiber and the mechanical, thermal and crystallization behaviour of short Twaron fiber reinforced polypropylene composites. *Compos Part A Appl Sci Manuf*, 39(5): 825–833. http://dx.doi.org/10.1016/j.compositesa.2008.01.009
41. Peng D, Qin W, Wu X, *et al*., 2015, Improvement of the resistance performance of carbon/cyanate ester composites during vacuum electron radiation by reduced graphene oxide modified TiO_2. *RSC Adv*, 5(94): 77138–77146. http://dx.doi.org/10.1039/c5ra11113g
42. Liu G, Zhou T, Liu W, *et al*., 2014, Enhanced desulfurization performance of PDMS membranes by incorporating silver decorated dopamine nanoparticles. *J Mater Chem A*, 2(32): 12907. http://dx.doi.org/10.1039/c4ta01778a
43. Lee S-W, Han S M and Nix W D, 2009, Uniaxial compression of fcc Au nanopillars on an MgO substrate: The effects of prestraining and annealing. *Acta Mater*, 57(15): 4404–4415. http://dx.doi.org/10.1016/j.actamat.2009.06.002
44. Applerot G, Lellouche J, Lipovsky A, *et al*., 2012, Understanding the antibacterial mechanism of CuO nanoparticles: Revealing the route of induced oxidative stress. *Small*, 8(21): 3326–3337. http://dx.doi.org/10.1002/smll.201200772
45. Applerot G, Lipovsky A, Dror R, *et al*., 2009, Enhanced antibacterial activity of nanocrystalline ZnO due to increased ROS-mediated cell injury. *Adv Funct Mater*, 19(6): 842–852. http://dx.doi.org/10.1002/adfm.200801081
46. Sawai J, Kojima H, Igarashi H, *et al*., 2000, Antibacterial characteristics of magnesium oxide powder. *World J Microbiol Biotechnol*, 16(2): 187–194. http://dx.doi.org/10.1023/A:1008916209784
47. Krishnamoorthy K, Manivannan G, Kim S J, *et al*., 2012, Antibacterial activity of MgO nanoparticles based on lipid peroxidation by oxygen vacancy. *J Nanopart Res*, 14(9): 1063. http://dx.doi.org/10.1007/s11051-012-1063-6

48. Sterrer M, Diwald O, Knözinger E, 2000, Vacancies and electron deficient surface anions on the surface of MgO nanoparticles. *J Phys Chem B*, 104(15): 3601–3607. http://dx.doi.org/10.1021/jp993924l

49. Berger T, Sterrer M, Stankic S, *et al*., 2005, Trapping of photogenerated charges in oxide nanoparticles. *Mater Sci Eng C*, 25(5–8): 664–668. http://dx.doi.org/10.1016/j.msec.2005.06.013

50. Sterrer M, Berger T, Diwald O, *et al*., 2003, Energy transfer on the MgO surface, monitored by UV-induced H_2 chemisorption. *J Am Chem Soc*, 125(1): 195–199. http://dx.doi.org/10.1021/ja028059o

51. Long T C, Saleh N, Tilton R D, *et al*., 2006, Titanium dioxide (P25) produces reactive oxygen species in immortalized brain microglia (BV2): Implications for nanoparticle neurotoxicity. *Environ Sci Technol*, 40(14): 4346–4352. http://dx.doi.org/10.1021/es060589n

52. Xia T, Kovochich M, Brant J, *et al*., 2006, Comparison of the abilities of ambient and manufactured nanoparticles to induce cellular toxicity according to an oxidative stress paradigm. *Nano Lett*, 6(8): 1794–1807. http://dx.doi.org/10.1021/nl061025k

53. Jin T, He Y, 2011, Antibacterial activities of magnesium oxide (MgO) nanoparticles against foodborne pathogens. *J Nanopart Res*, 13(12): 6877–6885. http://dx.doi.org/10.1007/s11051-011-0595-5

54. Yamamoto O, Sawai J, Kojima H, *et al*., 2002, Effect of mixing ratio on bactericidal action of MgO–CaO powders. *J Mater Sci Mater Med*, 13(8): 789–792. http://dx.doi.org/10.1023/A:1016179225955

55. Jeevanandam P, Klabunde K, 2002, A study on adsorption of surfactant molecules on magnesium oxide nanocrystals prepared by an aerogel route. *Langmuir*, 18(13): 5309–5313. http://dx.doi.org/10.1021/la0200921

56. He Y, Ingudam S, Reed S, *et al*., 2016, Study on the mechanism of antibacterial action of magnesium oxide nanoparticles against foodborne pathogens. *J Nanobiotechnol*, 14(1): 54. http://dx.doi.org/10.1186/s12951-016-0202-0

57. Salomao R, Bittencourt L, Pandolfelli V, 2007, A novel approach for magnesia hydration assessment in refractory castables. *Ceram Int*, 33(5): 803–810. http://dx.doi.org/10.1016/j.ceramint.2006.01.004

58. Mo L, Deng M, Tang M, *et al*., 2014, MgO expansive cement and concrete in China: Past, present and future. *Cem Concr Res*, 57: 1–12. http://dx.doi.org/10.1016/j.cemconres.2013.12.007

59. Shan D, Shi Y, Duan S, *et al*., 2013, Electrospun magnetic poly (L-lactide) (PLLA) nanofibers by incorporating PLLA-stabilized Fe_3O_4 nanoparticles. *Mater Sci Eng C*, 33(6): 3498–3505. http://dx.doi.org/10.1016/j.msec.2013.04.040

60. Marom R, Shur I, Solomon R, *et al*., 2005, Characterization of adhesion and differentiation markers of osteogenic marrow stromal cells. *J Cell Physiol*, 202(1): 41–48. http://dx.doi.org/10.1002/jcp.20109

61. Wang F, Zhai D, Wu C, *et al*., 2016, Multifunctional mesoporous bioactive glass/upconversion nanoparticle nanocomposites with strong red emission to monitor drug delivery and stimulate osteogenic differentiation of stem cells. *Nano Res*, 9(4): 1193–1208. http://dx.doi.org/10.1007/s12274-016-1015-z

62. Zhang J, Zhu Y, 2014, Synthesis and characterization of CeO_2-incorporated mesoporous calcium-silicate materials. *Microporous Mesoporous Mater*, 197: 244–251. http://dx.doi.org/10.1016/j.micromeso.2014.06.018

63. Hoppe A, Guldal N S, Boccaccini A R, 2011, A review of the biological response to ionic dissolution products from bioactive glasses and glass-ceramics. *Biomaterials*, 32(11): 2757–2774. http://dx.doi.org/10.1016/j.biomaterials.2011.01.004

64. Yamniuk A P, Vogel H J, 2005, Calcium- and magnesium-dependent interactions between calcium- and integrin-binding protein and the integrin αIIb cytoplasmic domain. *Protein Sci*, 14(6): 1429–1437. http://dx.doi.org/10.1110/ps.041312805

65. Zreiqat H, Howlett C, Zannettino A, *et al*., 2002, Mechanisms of magnesium-stimulated adhesion of osteoblastic cells to commonly used orthopaedic implants. *J Biomed Mater Res A*, 62(2): 175–184. http://dx.doi.org/10.1002/jbm.10270

66. Bouvard D, Pouwels J, De Franceschi N, *et al*., 2013, Integrin inactivators: Balancing cellular functions *in vitro* and *in vivo*. *Nat Rev Mol Cell Biol*, 14(7): 430–442. http://dx.doi.org/10.1038/nrm3599

67. Bourboulia D, Stetler-Stevenson W G, 2010, Matrix metalloproteinases (MMPs) and tissue inhibitors of metalloproteinases (TIMPs): Positive and negative regulators in tumor cell adhesion. *Semin Cancer Biol*, 20(3): 161–168. http://dx.doi.org/10.1016/j.semcancer.2010.05.002

RESEARCH ARTICLE

Coaxial nozzle-assisted electrohydrodynamic printing for microscale 3D cell-laden constructs

Hongtao Liang, Jiankang He*, Jinke Chang, Bing Zhang, Dichen Li

State key laboratory for manufacturing systems engineering, Xi'an Jiaotong University, Xi'an, China

Abstract: Cell printing has found wide applications in biomedical fields due to its unique capability in fabricating living tissue constructs with precise control over cell arrangements. However, it is still challenging to print cell-laden 3D structures simultaneously with high resolution and high cell viability. Here a coaxial nozzle-assisted electrohydrodynamic cell printing strategy was developed to fabricate living 3D cell-laden constructs. Critical process parameters such as feeding rate and stage moving speed were evaluated to achieve smaller hydrogel filaments. The effect of $CaCl_2$ feeding rate on the printing of 3D alginate hydrogel constructs was also investigated. The results indicated that the presented strategy can print 3D hydrogel structures with relatively uniform filament dimension (about 80 μm) and cell distribution. The viability of the encapsulated cells was over 90%. We envision that the coaxial nozzle-assisted electrohydrodynamic printing will become a promising cell printing strategy to advance biomedical innovations.

Keywords: electrohydrodynamic printing; cell printing; bioprinting; biofabrication; tissue engineering

*Correspondence to: Jiankang He, State Key Laboratory for Manufacturing Systems Engineering, Xi'an Jiaotong University, Xi'an 710049, China; jiankanghe@mail.xjtu.edu.cn

Received: October 1, 2017; **Accepted**: November 13, 2017; **Published Online**: November 22, 2017

Citation: Liang H, He J, Chang J, *et al*., 2018, Coaxial nozzle-assisted electrohydrodynamic printing for microscale 3D cell-laden constructs. *Int J Bioprint*, 4(1): 127. http://dx.doi.org/10.18063/IJB.v4i1.127

1. Introduction

In the past decades, cell printing has been extensively studied in biomedical fields due to its unique capability in precise patterning of biological components such as living cells in a controlled manner[1–3]. Several bioprinting techniques have been developed mainly including microextrusion-based printing, inkjet printing and laser-assisted printing[4–6]. However, there are some drawbacks of these existing strategies in fabricating complex three-dimensional (3D) structures with relatively high resolution and high cell viability in a costly effective way. For example, inkjet cell printing employs thermal or piezoelectric effect to print cell-hydrogel droplets, which affects cell viability and limits low cell concentration[4,7]. Laser-assisted printing commonly requires costly equipment and cannot fabricate 3D constructs[6,8]. Microextrusion-based cell printing has the drawbacks of low printing resolution as well as the side effect of flow-induced shear stress on cell viability[9–11].

Electrohydrodynamic jetting or printing recently attracts extensive attentions in fabricating high-resolution features based on the principle of electrohydrodynamically induced material flows[12–18]. Several process parameters had been investigated to achieve stable electrohydrodynamic printing process, such as applied voltage, moving speed, feeding rate of materials and inter diameter of nozzle[19–26]. Recent explorations indicate that biomaterials like living cells and hydrogels can be electrohydrodynamically printed and maintained their viability[27–30]. For example, Gasperini *et al*. further fabricated hollow cylindrical cell-laden structures using an electrohydrodynamic bioprinter[31]. Yao *et al*. fabricated 3D cell-laden alginate structures with the help of aerosol crosslinking mechanism by combining electrohydrodynamic printing and traditional extrusion-based cell printing[32]. However, the size of these electrohydrodynamically printed hydrogel filaments was commonly larger than 200 μm.

We previously developed a novel electrohydrodynamic cell printing strategy that can fabricate cell-laden constructs with microscale resolution (<100 μm) and high cell viability (>95%)[33]. However, alginate filaments were mainly crosslinked by the calcium ions diffused from the collecting substrate of agarose hydrogel, which limited the layer number of the electrohydrodynamically printed hydrogel smaller than 20. Here a coaxial nozzle-

assisted electrohydrodynamic cell printing process was further presented aiming to fabricate 3D cell-laden constructs with high resolution and high cell viability. The printed alginate filament can be instantly crosslinked by the calcium chloride solution flowed from the coaxial nozzle during the 3D electrohydrodynamic printing process.

2. Materials and Methods

2.1 Materials

Alginate with medium viscosity (2000 mPa·s) was purchased from Sigma (United Kingdom). Calcium chloride powder was bought from Aladdin (Shanghai, China). Agarose powder with low melting temperature (87–89 °C) was bought from Biowest (Spain). 3% (w/v) alginate solution was prepared by dissolving alginate powder into phosphate buffer saline (PBS). 2% (w/v) agarose solution with 3% (w/v) calcium chloride was prepared by dissolving agarose and calcium chloride powders in tris-buffered saline (TBS) at 100 °C. 1% (w/v) calcium chloride solution was prepared by dissolving calcium chloride powder into TBS at room temperature. Flat agarose hydrogel with a thickness of 3 mm was prepared by casting agarose solution in a petri dish. For electrohydrodynamic cell printing, rat myocardial cell lines (H9C2, ATCC) were added into alginate solution with a density of 1×10^6 cells mL^{-1}.

2.2 Coaxial Nozzle-Assisted Electrohydrodynamic Cell Printing Platform

A house-made electrohydrodynamic printing platform was used which mainly consists of three components: a high-voltage generator (ZGF-30/5, Welldone, Shanghai, China), a multi-channel syringe pump system (TJ-2A, Longer Pump, Baoding, China) and a high-resolution x-y-z movement stage (Xiamen Heidelstar Co., China). Alginate solution and calcium chloride solution were loaded into two 1 mL syringes which were separately controlled by the syringe pump. A coaxial printing nozzle was mounted onto the z-axis and connected with the positive terminal of a high-voltage generator. The core inlet of the nozzle was connected with the syringe loaded with alginate solution while the sheath inlet of the nozzle was connected with the syringe loaded with calcium chloride solution respectively *via* soft tubes as shown in Figure 1. Insulating petri dish and agarose hydrogel with calcium ions were sequentially placed on the grounded x-y moving stage as the collecting substrate. The distance between the coaxial nozzle and the collecting substrate was fixed at 200 μm.

To initialize the electrohydrodynamic printing process, high voltage was applied and the syringe pump was opened to simultaneously feed alginate solution and calcium chloride solution into the coaxial nozzle. The electrohydrodynamically printed alginate solution was instantly crosslinked in contact with calcium chloride solution to form hydrogel filaments and deposit onto the collecting substrate. The deposition of alginate hydrogel filaments could be flexibly controlled to fabricate complex patterns by directing the movement of x-y stage according to a user-specific design. A 3D hydrogel structure can be further electrohydrodynamically printed by precisely stacking the alginate filaments in a layer-by-layer manner.

2.3 Effect of Applied Voltage on the Width of the Printed Filaments

To tightly attach the printed hydrogel filament to the collecting substrate, calcium chloride solution was not supplied in the printing of the first three layers. The electrohydrodynamically printed alginate filament was crosslinked by the calcium ions in agarose hydrogel.

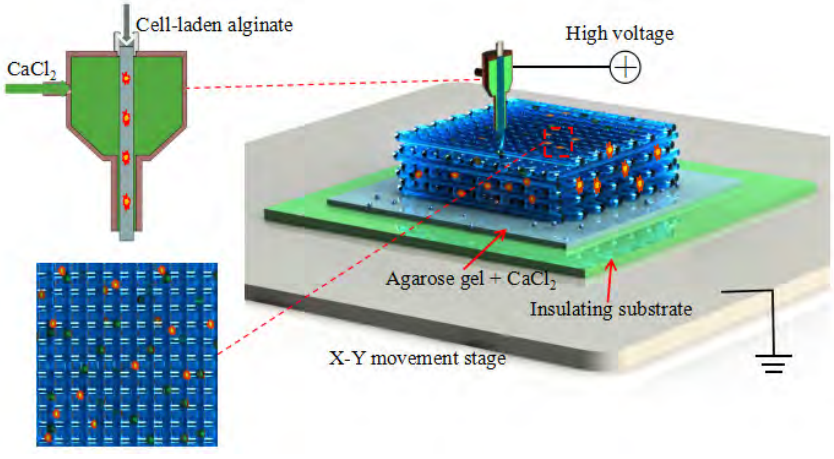

Figure 1. Schematic of coaxial nozzle-assisted electrohydrodynamic printing for microscale cell-laden constructs

We firstly compared the width of the printed filaments with or without applied voltage under different nozzle diameter when alginate feeing rate and stage moving speed were fixed at 600 μL/h and 15 mm/s, respectively. Three kinds of coaxial nozzles were used with the core/sheath diameter of 160/500 μm (30G/21G), 260/840 μm (25G/18G) and 410/1010 μm (22G/17G). The morphology and width of the printed filaments were characterized with an inverted fluorescence microscope (ECLIPSE Ti, Nikon, Japan). For each condition, three samples were separately printed with nine locations totally measured.

2.4 Effect of Process Parameters on the Width of Electrohydrodynamically Printed Filaments

The effect of alginate feeding rate and stage moving speeding on the width of the electrohydrodynamically printed filaments was studied when the applied voltage and nozzle-to-substrate distance were fixed at 4.5 kV and 200 μm. Alginate feeding rate of gradually increased from 200 μL/h to 1000 μL/h when the stage moving speed was fixed at 30 mm/s. The moving speed changed from 15 mm/s to 35 mm/s when alginate feeding rate was fixed at 400 μL/h. The morphology of the printed filaments was characterized and the filament width was expressed as mean ± standard deviation.

2.5 Effect of $CaCl_2$ Feeding Rate on the Electrohydrodynamic Printing of 3D Constructs

To fabricate 3D hydrogel constructs using the presented electrohydrodynamic printing method, it is necessary to simultaneously feed alginate and $CaCl_2$ solutions using the coaxial nozzle to ensure instant crosslinking when the layer number is over 3. The effect of $CaCl_2$ feeding rate on the maximum layer number of the printed constructs was investigated. $CaCl_2$ feeding rate varied in the range of 0–300 μL/h and the maximum layer number was recorded when the electrohydrodynamic printing process became unstable.

2.6 Characterization of the Electrohydrodynamically Printed 3D Hydrogel Constructs

3D hydrogel constructs with different layer number of 10, 30, 50 and 70 were electrohydrodynamically printed. The macro/microscopic images of the resultant constructs were viewed with a digital camera (Nikon, Japan) or optical microscope. The 3D profiles of the printed constructs were reconstructed using a confocal laser scanning microscope (OLS4000, Olympus, USA), based on which the construct height was quantified. The electrohydrodynamically printed constructs with 50 layers were further freeze-dried in a lyophilizer (FD-1A-50, Biocool, Beijing, China) for three days. The microstructures were observed with scanning electron microscope (SEM, SU8010, Hitachi, Japan).

2.7 Electrohydrodynamic Printing of 3D Cell-Laden Constructs

To demonstrate the capability of the presented strategy for cell printing, 3D cell-laden constructs with a layer number of 30 were electrohydrodynamically printed. To evaluate cell viability, Live/Dead assay (Thermo Fisher Scientific, USA) was performed according to the manufacture's specifications. The 3D fluorescent images of the constructs were reconstructed with a confocal microscopy (Nikon, Japan). Cell number and cell viability at specific layer of 5, 15 and 25 were quantified. The quantified data is expressed as mean ± standard deviation. Statistical analysis was performed using analysis of variance in Microsoft Excel software. Values of $p < 0.05$ was considered to be statistically significant.

3. Results and Discussion

Figure 2A–F show the morphology of alginate filaments electrohydrodynamically printed by different nozzle diameter without/with applied voltage. When the voltage was not applied, the width of the printed filaments gradually increased from 166.15 ± 2.67 μm to 196.78 ± 4.87 μm as the core nozzle diameter changed from 160 μm to 410 μm. When the voltage of 4.5 kV was applied, the width of the electrohydrodynamically printed filaments increased from 144.24 ± 4.82 μm to 167.33 ± 7.40 μm as the nozzle diameter increased. In all cases, the width of the electrohydrodynamically printed filaments was obviously smaller than that of extrusion-based printing filaments as shown in Figure 2G. This indicated that applied voltage could decrease the width of the printed filaments. Previous studies also indicated that a thinner Taylor cone could be achieved under a higher voltage, which can decrease line width during the printing process[19,20]. Therefore, in the following experiment, applied voltage of 4.5 kV and the coaxial nozzle with core diameter of 160 μm and sheath diameter of 500 μm were used to achieve relatively smaller filaments.

Figure 3A shows the filament morphology as well as the measured width of the electrohydrodynamically printed filaments under fixed stage moving speed of 30 mm/s and different alginate feeding rate. When the alginate feeding rate was lower than 400 μL/h, the printed filaments were discontinuous. As the alginate feeding rate increased from 400 μL/h to 1000 μL/h, the filament width significantly increased from 92.53 ± 2.75 μm to 137.70 ± 2.99 μm. When alginate feeding rate was fixed at 400 μL/h, the printed filament was straight and continuous and the filament width significantly decreased from 122.24 ± 4.42 μm to 92.53 ± 2.75 μm as

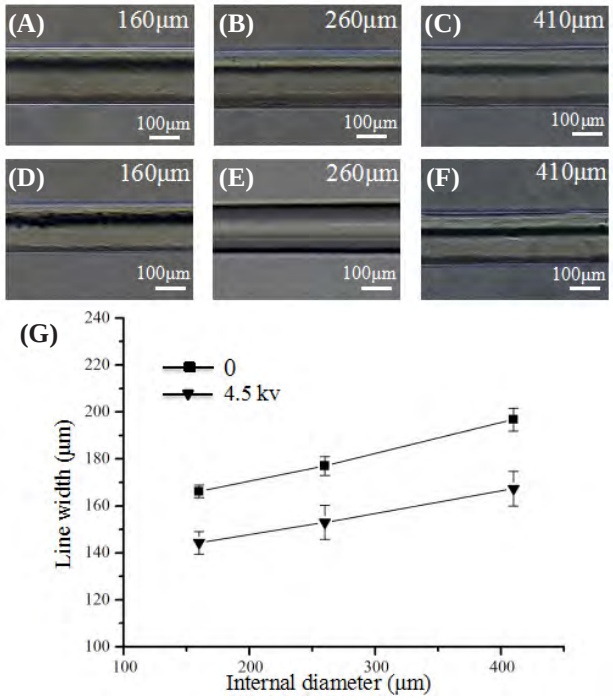

Figure 2. Effect of high voltage on width of electrohydrodynamically printed filament. (**A**–**C**) Morphology of the extruded filaments as the core nozzle diameter changed from 160 μm to 410 μm. (**D**–**E**) Morphology of the electrohydrodynamically printed filaments with the voltage of 4.5 kV as the core nozzle diameter changed from 160 μm to 410 μm. (**G**) Quantification of the width of the printed filament.

stage moving speed changed from 10 mm/s to 30 mm/s in Figure 3B. When the moving speed was over 30 mm/s, the printing filaments became discontinuous. The smallest filament (<100 μm) was achieved when the feeding rate of alginate and stage moving speed were fixed at 400 μL/h and 30 mm/s, respectively.

To test the feasibility of using coaxial nozzle-assisted electrohydrodynamic printing to fabricate 3D hydrogel constructs, multilayer structures were further printed with $CaCl_2$ feeding rate of 300 μL/h after the first three layers were completed. However, it was found that the electrohydrodynamic printing process became unstable with discontinuous alginate filaments when the stage moving speed was 30 mm/s (Supplementary Movie 1). Continuous alginate filaments can be achieved when the stage moving speed decreased to 15 mm/s (Supplementary Movie 2). This was mainly caused by the flow of $CaCl_2$ solution during the electrohydrodynamic printing process. Therefore, a lower stage moving speed of 15 mm/s was used to print the 3D constructs.

The effect of $CaCl_2$ feeding rate on the electrohydrodynamic printing of 3D constructs was investigated. Figure 4A shows the microscopic images of the printed constructs with a layer number of 13 when $CaCl_2$ feeding rate is zero. It was obviously observed that the printed alginate solution was not instantly crosslinked at the top layer due to diffusion-based limitation of calcium ions and was prone to form aggregates at the crossed sites. When $CaCl_2$ feeding rate increased from 100 μL/h to 300 μL/h, more layers of alginate filaments could be electrohydrodynamically printed as shown in Figure 4B–D. The printing layer number was mainly determined by $CaCl_2$ feeding rate. Figure 4E shows the relationship between the maximum printing layer and $CaCl_2$ feeding rate. Alginate hydrogel constructs with the maximum printing layer number of 73 can be fabricated when $CaCl_2$ feeding rate was fixed at 300 μL/h. In addition, calcium chloride solution could fill in the pore of the 3D constructs as the layer number increased. Therefore, the printed cell-laden filaments were always immersed into the liquid environment during the electrohydrodynamic printing process, which might reduce the side effect of water evaporation on the cell viability.

3D alginate hydrogel constructs with different layer number were electrohydrodynamically printed when alginate feeding rate, stage moving speed and $CaCl_2$ feeding rate were fixed at 400 μL/h, 15 mm/s and 300

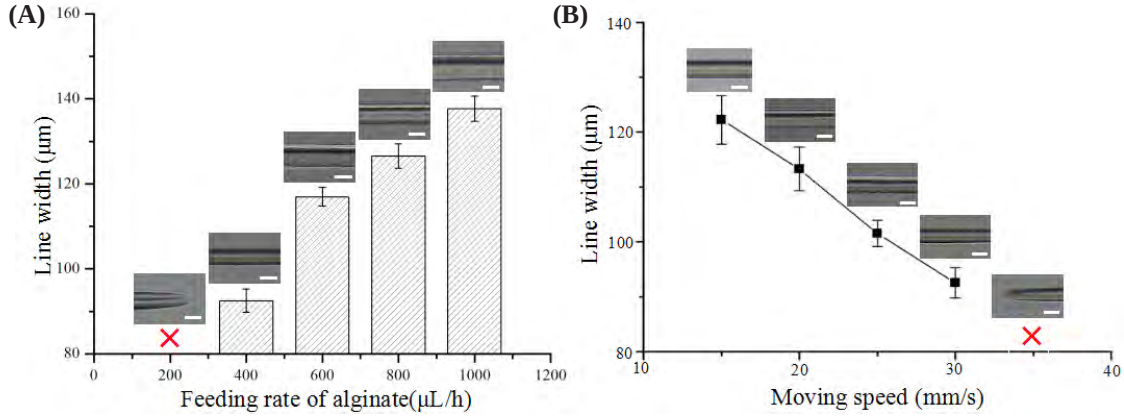

Figure 3. Effect of process parameters on the width of the electrohydrodynamically printed filaments. (**A**) Quantification of filament width as alginate feeding rate changed from 200 μL/h to 1000 μL/h. (**B**) Quantification of filament width as stage moving speed changed from 15 mm/s to 35 mm/s.

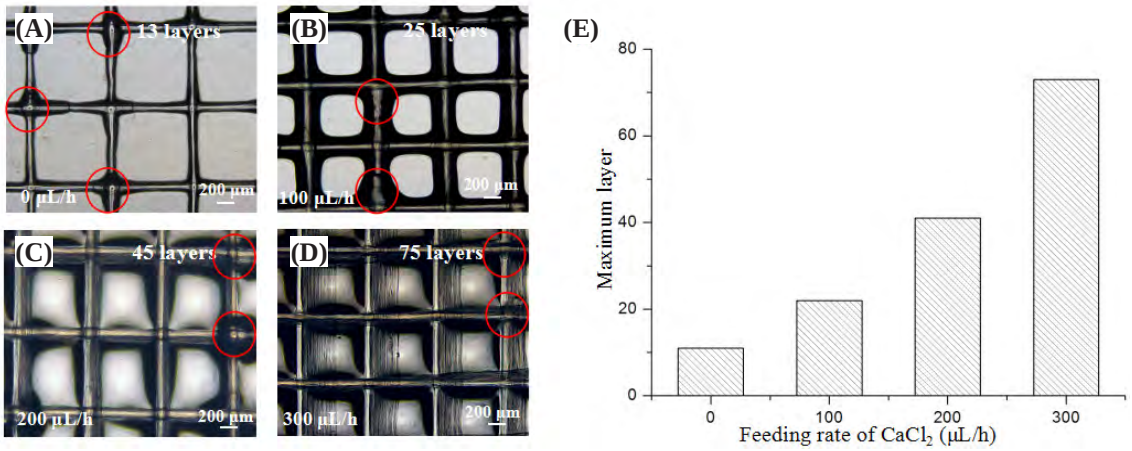

Figure 4. Effect of $CaCl_2$ feeding rate on the maximum printing layer number of the 3D constructs. (**A**–**D**) Microscopic images of the printed constructs with a layer number of 13, 25, 45 and 75 in corresponding to $CaCl_2$ feeding rate of zero, 100 μL/h, 200 μL/h and 300 μL/h. (**E**) The relationship between maximum printing layer number and $CaCl_2$ feeding rate.

μL/h, respectively. Figure 5A–D show the printed structures with the layer number of 10, 30, 50 and 70. The thickness of the printed constructs significantly increased as the layer number increased. This indicated that the electrohydrodynamically printed alginate from the core nozzle can be instantly crosslinked by calcium ions from the sheath nozzle to form tiny filaments with a relatively uniform diameter of 80 μm. In addition, the calcium chloride solution around the hydrogel filaments can significantly decrease the evaporation of water inside printed constructs, which might be important for cell viability. Figure 5E–H show the 3D profiles of the electrohydrodynamically printed constructs with the layer number of 10, 30, 50 and 70. The printed filaments were successfully stacked up to form 3D constructs in a layer-by-layer manner. The measured height for the printed constructs increased from 172.73 ± 9.93 μm to 1464.53 ± 14.46 μm as the layer number increased from 10 to 70 (Figure 5I). In all cases, the average height for each layer was about 18.53 ± 1.32 μm, which

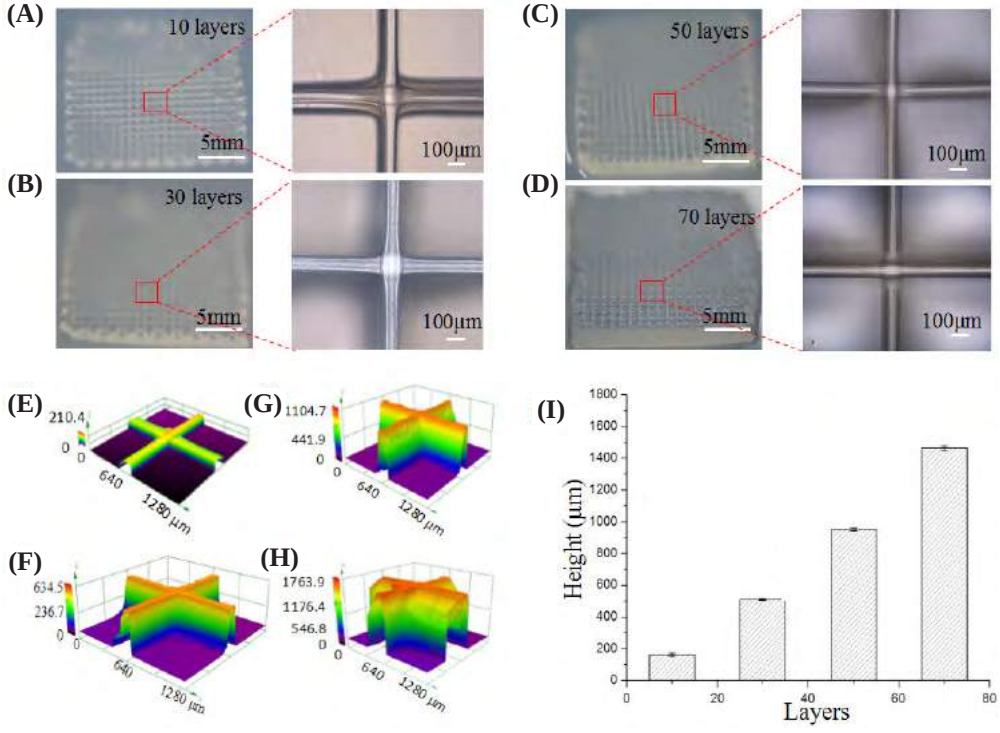

Figure 5. Electrohydrodynamic printing of 3D constructs with different layer number. (**A**–**D**) Photos and microscopic images of the constructs with the layer number of 10, 30, 50 and 70. (**E**–**H**) 3D profiles of the printed constructs with the layer number of 10, 30, 50 and 70. (**I**) Quantification of the construct height with different layer number.

further verified that the printed alginate solution could be instantly crosslinked to form hydrogel filament with uniform dimension. Since the height of each layer was close to the size of living cells, it might enable to print the filaments with single layer of cells in the vertical direction for high-resolution cell printing.

Figure 6 shows the SME images of the electrohydrodynamically printed hydrogel construct with a layer number of 50. The printed filaments at neighbor layers were tightly merged together, which maintained structural integrity after freeze drying. The diameter of the freeze-dried filaments was about 70 μm, slightly smaller than that of the freshly printed hydrogel filaments due to shrinking during the freeze-drying process. Together, these results indicated that the introduction of coaxial nozzle in the electrohydrodynamic printing process significantly enhance the capability to fabricate 3D hydrogel constructs.

Cell-laden hydrogel constructs with a layer number of 30 were finally electrohydrodynamically printed as shown in Figure 7A. Figure 7B shows fluorescent images of the cell-laden constructs (top view) stained with Live/Dead assay. The cells were completely confined inside the hydrogel filaments and most cells kept alive (green).

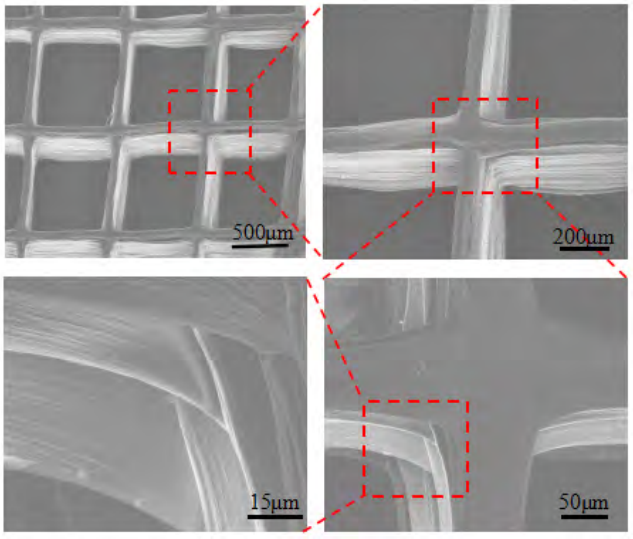

Figure 6. SEM images of the electrohydrodynamically printed construct with a layer number of 50 after freeze drying

Figure 7C illustrates the 3D profile of the printed cell-laden constructs. The height of the obtained structure was about 500 μm. Figure 7D–F show cell distribution at specific layer of 5, 15 and 25, respectively. The electrohydrodynamically printed cells were uniformly distributed among layers (p = 0.26) and the average cell number for each layer was about 70 (Figure 7G). There is no significant difference in cell viability among layers as shown in Figure 7H (p = 0.20). The cell viability was higher than 90%. These results indicated that the coaxial nozzle-assisted electrohydrodynamic printing strategy could effectively fabricate the 3D cell-laden constructs with high resolution, uniform cell distribution and high cell viability.

4. Conclusion

In summary, coaxial nozzle-assisted electrohydrodynamic printing technique was successfully developed to fabricate microscale 3D cell-laden alginate constructs. Process parameters such as applied voltage, alginate feeding rate, stage moving speed and $CaCl_2$ feeding rate were systematically studied to stably print microscale hydrogel filaments with 2D/3D organizations. 3D hydrogel constructs with the maximum layer number of 73 can be electrohydrodynamically printed in a layer-by-layer manner. The height of the printed constructs was approximately 1464.53 ± 14.46 μm and the filament dimension maintained relatively uniform (80 μm in width and 18.5 μm in height). Cell-laden constructs with uniform cell distribution and high cell viability (>90%) was finally achieved. However, it is still challenging to fabricate higher complex heterogeneous 3D living constructs with multiple cell types and hydrogel compositions. In addition, the presented coaxial nozzle-assisted electrohydrodynamic printing should be further explored to solve these problems.

Conflict of Interest and Funding

No conflict of interest was reported by the authors. This work was supported by the National Natural Science Foundation of China (51422508, 51675412), Shaanxi Key Research and Development Program (2017ZDXM-GY-058) and the Fundamental Research Funds for the Central Universities.

References

1. Kang H-W, Lee S J, Ko I K, *et al.*, 2016, A 3D bioprinting system to produce human-scale tissue constructs with structural integrity. *Nat Biotechno*, 34(3): 313–319. http://dx.doi.org/10.1038/nbt.3413
2. Jordan S M, Kelly R S, Michael T Y, *et al.*, 2012, Rapid casting of patterned vascular networks for perfusable engineered three-dimensional tissues. *Nat Mater*, 11(9): 768–774. http://dx.doi.org/10.1038/nmat335733
3. Falguni P, Jinah J, Dong-Heon H, *et al.*, 2014, Printing three-dimensional tissue analogues with decellularized extracellular matrix bioink. *Nat Commun*, 5: 3935. http://dx.doi.org/10.1038/ncomms4935
4. Sean V M, Anthony A, 2014, 3D bioprinting of tissues and organs. *Nat Biotechnol*, 32(8): 773–785. http://dx.doi.org/10.1038/nbt.2958

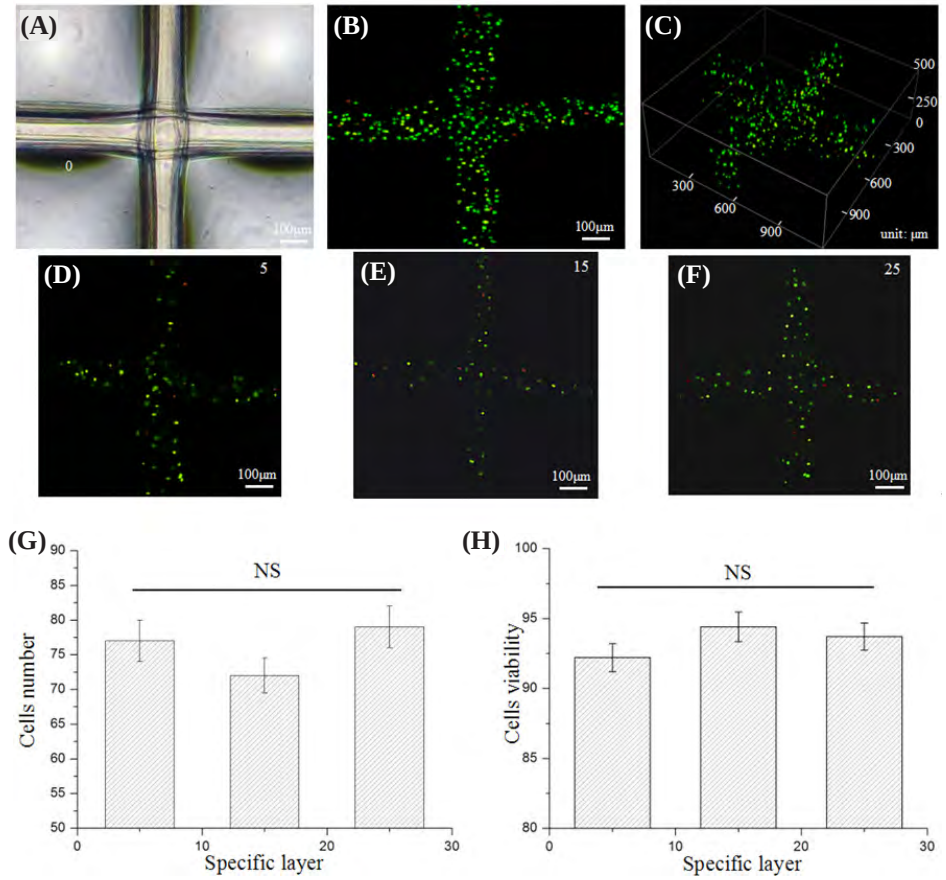

Figure 7. Electrohydrodynamic printing of 3D cell-laden constructs with a layer number of 30. (**A**) Microscopic images of the printed cell-laden constructs. (**B**–**C**) Fluorescent images (top view and 3D profile) of the electrohydrodynamically printed cell-laden constructs. (**D**–**F**) Cell distribution at specific layer of 5, 15 and 25. (**G**) Quantification of cell number at specific layer of 5, 15 and 25. (**H**) Quantification of cell viability at specific layer of 5, 15 and 25. "NS" indicates non-significance.

5. Malda J, Jetze V, Ferry P M, *et al*., 2013, 25th Anniversary article: Engineering hydrogels for biofabrication. *Adv Mater*, 25(36): 5011–5028. http://dx.doi.org/10.1002/adma.201302042
6. Thomas B, Mieke V, Jorg S, *et al*., 2012, A review of trends and limitations in hydrogel-rapid prototyping for tissue engineering. *Biomaterials*, 33(26): 6020–6041. http://dx.doi.org/10.1016/j.biomaterials.2012.04.050
7. Xu T, Zhao W Z, Zhu J M, *et al*., 2013, Complex heterogeneous tissue constructs containing multiple cell types prepared by inkjet printing technology. *Biomaterials*, 34(1): 130–139. http://dx.doi.org/10.1016/j.biomaterials.2012.09.035
8. Lothar K, Andrea D, Sabrina S, *et al*., 2012, Skin tissue generation by laser bioprinting. *Biotechnology*, 109(7): 1855–1863. http://dx.doi.org/10.1002/bit.24455
9. Zhu W, Ma X Y, Gou M L, *et al*., 2016, 3D printing of functional biomaterials for tissue engineering. *Curr Opin Biotechnol*, 40: 103–112. http://dx.doi.org/10.1016/j.copbio.2016.03.014
10. Ning LQ, Chen X B, 2017, A brief review of extrusion-based tissue scaffold bio-printing. *Biotechnol J*, 12(8): 1600671. http://dx.doi.org/10.1002/biot.201600671
11. Koo Y, Kim G, 2016, New strategy for enhancing *in situ* cell viability of cell-printing process *via* piezoelectric transducer-assisted three-dimensional printing. *Biofabrication*, 8(2): 025010. http://dx.doi.org/10.1088/1758-5090/8/2/025010
12. Zhang B, He J K, Li X, *et al*., 2016, Micro/nanoscale electrohydrodynamic printing: From 2D to 3D. *Nanoscale*, 8(34): 15376–15388. http://dx.doi.org/10.1039/c6nr04106j
13. He J K, Xu FY, Cao Y, *et al*., 2015, Towards microscale electrohydrodynamic three-dimensional printing. *J Phys D Appl Phys*, 49(5): 055504. http://dx.doi.org/10.1088/0022-3727/49/5/055504
14. He J K, Xu F Y, Dong R N, *et al*., 2016, Electrohydrodynamic 3D printing of microscale poly (ε-caprolactone) scaffolds with multi-walled carbon nanotubes. *Biofabrication*, 9(1): 015007.

http://dx.doi.org/10.1088/1758-5090/aa53bc

15. Mao M, He J K, Li X, *et al.*, 2017, The emerging frontiers and applications of high-resolution 3D printing. *Micromachines*, 8(4): 113. http://dx.doi.org/10.3390/mi8040113
16. Onses M S, Sutanto E, Ferreira P M, *et al*., 2015, Mechanisms, capabilities, and applications of high-resolution electrohydrodynamic jet printing. *Small*, 11(34): 4267–4266. http://dx.doi.org/10.1002/smll.201500593
17. Lee H, Seong B, Jang Y, *et al*., 2014, Direct alignment and patterning of silver nanowires by electrohydrodynamic jet printing. *Small*, 10(19): 3918–3922. http://dx.doi.org/10.1002/smll.201400936
18. Ahmad Z, Rasekh M, Edirisinghe M, 2010, Electrohydrodynamic direct writing of biomedical polymers and composites. *Macromol Mater Eng*, 295(4): 315–319. http://dx.doi.org/10.1002/mame.200900396
19. Parajuli D, Koomsap P, Parkhi A A, *et al*., 2016, Experimental investigation on process parameters of near-field deposition of electrispinning-based rapid prototyping. *Virtual Phys Prototyp*, 11(3):193–207. http://dx.doi.org/10.1080/17452759.2016.1210314
20. Wei C, Dong J, 2013, Direct fabrication of high-resolution three-dimensional polymeric scaffolds using electrohydrodynamic hot jet plotting. *J Micromech Microeng*, 23(2): 025017. http://dx.doi.org/10.1088/0960-1317/23/2/025017.
21. Zheng G, Sun L L, Wang X, *et al*., 2016, Electrohydrodynamic direct-writing microfiber patterns under stretching. *Appl Phys A Mater Sci Process*, 122(2): 1–9. http://dx.doi.org/10.1007/s00339-015-9584-3
22. Chanthakulchan A, Koomsap P, Parkhi, *et al*., 2015, Environmental effects in fiber fabrication using electrispinning-based rapid prototyping. *Virtual Phys Prototyp*, 10(4): 227–237. http://dx.doi.org/10.1080/17452759.2015.1112411
23. Chanthakulchan A, Koomsap P, Auyson K, *et al*., 2015, Development of an electrospinning-based rapid prototyping for scaffold fabrication, *Rapid Prototyp J*, 21(3): 329–339. http://dx.doi.org/10.1108/RPJ-11-2013-0119
24. Bisht GS, Ciulin C, Alireza M, *et al*., 2011, Controlled continuous patterning of polymeric nanofibers on three-dimensional substrates using low voltage near-field electrospinning. *Nano Lett*, 11(4): 1831–1837. http://dx.doi.org/10.1021/nl2006164
25. Li J L, Cai YL, Guo Y L, *et al*., 2014, Fabrication of three-dimensional porous scaffolds with controlled filament orientation and large pore size *via* an improved E-jetting technique. *J Biomed Mater Res B Appl Biomater*, 102B(4): 651–658. http://dx.doi.org/10.1002/jbm.b.33043
26. Bu N, Huang Y G, Wang X M, *et al*., 2012, Continuous tunable and oriented nanofiber direct-written by mechano-electrospinning. *Mater Manuf Process*, 27(12): 1318–132. http://dx.doi.org/10.1080/10426914.2012.700145
27. Jayasinghe S N, 2013, Cell electrospinning: A novel tool for functionalizing fibres, scaffolds and membranes with living cells and other advanced materials for regenerative biology and medicine. *Analyst*, 138(8): 2215–2223. http://dx.doi.org/10.1039/c3an36599a
28. Zhao X, He J K, Xu F Y, *et al*., 2016, Electrohydrodynamic printing: A potential tool for high-resolution hydrogel/cell patterning. *Virtual Phys Prototyp*, 11 (1): 57–63. http://dx.doi.org/10.1080/17452759.2016.1139378
29. Ehler E, Jayasinghe S N, 2014, Cell electrospinning cardiac patches for tissue engineering the heart. *Analyst*, 139(18): 4449–4452. http://dx.doi.org/10.1039/c4an00766b
30. Jayasinghe S N, Qureshi, A N, Eagles, P A, *et al*., 2006, Electrohydrodynamic jet processing: An advanced electric-field-driven jetting phenomenon for processing living cells. *Small*, 2(2): 216–219. http://dx.doi.org/10.1002/smll.200500291
31. Gasperini L, Manigiglio D, Motta A, *et al*., 2015, An electrohydrodynamic bioprinter for alginate hydrogels containing living cells. *Tissue Eng Part C Methods*, 21(2): 123–132. http://dx.doi.org/10.1089./ten.tec.2014.0149
32. Yeo M, Ha J H, Lee H, *et al*., 2016, Fabrication of hASCs-laden structures using extrusion-based bioprinting supplemented with an electric field. *Acta Biomater*, 38: 33–43. http://dx.doi.org/10.1016/j.actbio.2016.04.017
33. He J K, Zhao X, Chang J K, *et al*., 2017, Microscale electrohydrodynamic bioprinting with high viability. *Small*: 1702626. http://dx.doi.org/10.1002/smll.201702626

RESEARCH ARTICLE

Mechanism for corrosion protection of β-TCP reinforced ZK60 *via* laser rapid solidification

Youwen Deng[1#], Youwen Yang[2#], Chengde Gao[2], Pei Feng[2], Wang Guo[2], Chongxian He[2], Jian Chen[1], Cijun Shuai[2,3,4*]

[1] Department of Emergency Medicine, the Second Xiangya Hospital, Central South University, Changsha, China
[2] State Key Laboratory of High Performance Complex Manufacturing, Central South University, Changsha, China
[3] Jiangxi University of Science and Technology, Ganzhou, China
[4] Key Laboratory of Organ Injury, Aging and Regenerative Medicine of Hunan Province, Changsha, China

Abstract: It remains the primary issue to enhance the corrosion resistance of Mg alloys for their clinical applications. In this study, β-tricalcium phosphate (β-TCP) was composited with Mg-6Zn-1Zr (ZK60) using laser rapid solidification to improve the degradation behavior. Results revealed rapid solidification effectively restrained the aggregation of β-TCP, which thus homogenously distributed along grain boundaries of α-Mg. Significantly, the uniformly distributed β-TCP in the matrix promoted the formation of apatite layer on the surface, which contributed to the formation of a compact corrosion product layer, hence retarding the further degradation. Furthermore, ZK60/8β-TCP (wt. %) composite showed improved mechanical strength, as well as improved cytocompatibility. It was suggested that laser rapidly solidified ZK60/8β-TCP composite might be a potential materials for tissue engineering.

Keywords: laser rapid solidification; ZK60/β-TCP composite; degradation behavior; microstructure

*Correspondence to: Cijun Shuai, State Key Laboratory of High Performance Complex Manufacturing, Central South University, Changsha 410083, China; shuai@csu.edu.cn
#These authors contributed equally to this work.

Received: September 29, 2017; **Accepted**: November 6, 2017; **Published Online**: November 21, 2017

Citation: Deng Y, Yang Y, Gao C, *et al*., 2018, Mechanism for corrosion protection of β-TCP reinforced ZK60 *via* laser rapid solidification. *Int J Bioprint*, 4(1): 124. http://dx.doi.org/10.18063/IJB.v4i1.124

1. Introduction

Magnesium (Mg) alloys have been considered as a new generation of degradable implant materials due to their inherent biofiguredegradability and appropriate mechanical properties[1]. Mg, as one of the essential elements in body, participates in a large number of metabolic reactions, especially in bone metabolism[2]. There have been extensive studies on various Mg alloys as absorbable biomaterials, including AZ31 (Mg-based alloy with 3% Al 1% Zn)[3], WE[4] and Mg-6Zn-1Zr (ZK60) alloys[5]. Among these, ZK60 presents superior strength and good biocompatibility, attracting great attention for its applications in tissue engineering[6]. Unfortunately, ZK60 degrades too rapidly in internal environments, resulting in severe problems including excessive inflammatory response, hydrogen gas accumulation, alkalization of body fluids and premature mechanical failure[7].

Recently, enforcement by utilizing bioceramic materials has been reported to be an effective method to enhance the corrosion resistance of Mg alloys. For example, Campo *et al*.[8] reported that Mg-HAP exhibited improved corrosion resistance compared with Mg. Wan *et al*.[9] also reported that the addition of 45s bioglass into Mg significantly reduced the corrosion rate for Mg. Feng and Han[10] fabricated Mg-based composites reinforced with calcium polyphosphate, which exhibited controllable degradation rates. However, previous study also revealed that the incorporated bioceramic easily segregated together in the Mg matrix even at a low content. He *et al*.[11] observed the agglomeration of tricalcium phosphate (TCP) particles occurred in as-extruded Mg-3Zn-0.8Zr/1.5TCP (wt. %). Liu *et al*.[12] investigated microstructure of the as-casted Mg–3Zn–1Ca/1β-TCP (wt. %), also revealing the agglomeration of the β-TCP particles in the sample. It is well known that the agglomeration of incorporated bioceramic can cause the formation of pores and defects, thus deteriorating the corrosion behavior and mechanical properties of Mg

matrix. Meanwhile, the conventional processes, also including powder metallurgy[13], are difficult to prepare porous Mg alloys with complex shapes.

In the present study, laser melting technology is proposed to overcome the agglomeration of incorporated bioceramic. Laser melting technology is a typical rapid solidification which has an extremely high cooling rate over 10^5 K/s, which allows the solidification can be completed in an extremely short period of time[14]. In this condition, the ceramic particles which originally uniformly dispersed in the liquid pool cannot agglomerate in such a short time, thus homogenously distributing in the matrix. Meanwhile, the rapid solidification is able to refine the microstructure, which is also beneficial to enhance the corrosion resistance of Mg alloys[15]. Another study on Ti–TiB composites further confirmed that laser melting was an effective method that could produce almost fully dense composites with bioceramic enforcement[16]. On the other hand, laser melting technology can fabricate porous Mg alloys[17]. To the best of our best knowledge, there are few publications studying on the corrosion behavior of laser rapidly solidified biocaremic reinforced Mg alloys.

In this study, β-TCP was introduced to ZK60 to improve its degradation behavior *via* laser rapid solidification. β-TCP had good bioactivity as well as good wettability with the Mg alloy[18]. ZK60/β-TCP composites with different contents of β-TCP (0–12 wt. %) were prepared. And the microstructure features, degradation behavior and mechanical properties were investigated.

2. Materials and Methods

2.1 Materials

β-TCP powder with a size of approximately 200 nm (Figure 1A) was obtained from Kunshan Chinese Technology New Materials Co. Ltd., China. Spherical ZK60 powder was purchased from Tangshan Weihao Materials Co. Ltd., China. The chemical composition was as follows: 6.63 wt. % of Zn, 0.56 wt. % of Zr and balanced Mg. The size of the ZK60 powder was <50 μm (Figure 1B). The ZK60 alloy powder was composited with 0, 4, 8 and 12 wt. % of β-TCP powder, respectively, followed by ball milling under a protective gas (0.3 vol. % SF_6 and 99.7 vol. % CO_2) at a rotation speed of 150 rpm. After ball milling for 2 h, the small β-TCP particles uniformly adhered to the surface of large ZK60 particles (Figure 1C and Figure 1D). The homogeneity of the powder could improve the flowability and allow for improved packing of powder, thus reducing the formation of defects[19].

2.2 Fabrication of the Composites

The ZK60/*x*β-TCP (*x* = 0, 4, 8 and 12 wt. %) composites were fabricated by a home-made laser melting system, which comprised of a powder delivery device, a three-dimensional motion platform and a fiber laser[17]. In the laser melting process, a high energy laser beam scanned the powder layer, forming a solid layer. Then, the formed solid layer was covered with a new layer of powder. The cycle continued before the samples (8×8×8 mm^3) were achieved. The samples were fabricated at a laser power of 80 W, a scanning rate of 300 $mm \cdot s^{-1}$ and a layer thickness of 0.1 mm. All procedures were performed under a protective argon atmosphere.

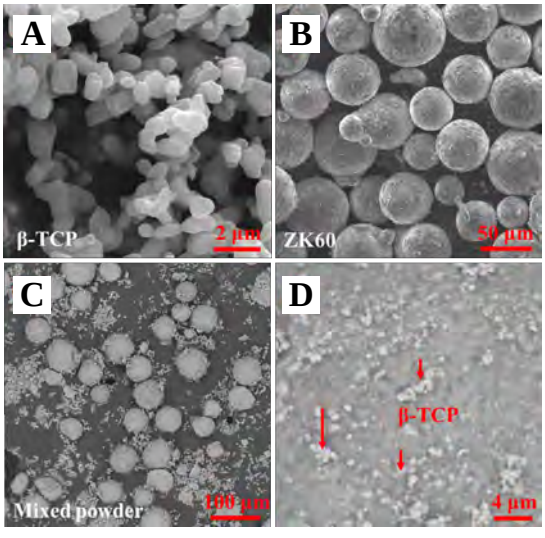

Figure 1. Original powders: (**A**) β-TCP powder; (**B**) ZK60 powder; (**C**) ZK60/8β-TCP (wt. %) mixed powder; and (**D**) the surface on ZK60 particle in mixed powder.

2.3 Microstructure Characterization

The microstructure was analyzed by scanning electron microscopy (SEM; JSM-5600LV, Japan). The sample was prepared as follows: the ZK60/*x*β-TCP composites were successively grounded with abrasive papers (500, 1000 and 2000 grit), and polished with diamond grits. The phase composition of the composites was identified using an X-ray diffractometer (XRD, D8-Advance, Germany). The condition was set using Cu Kα radiation at 15 mA and 30 kV. Scans were performed with 2θ range of 5° to 80° at a scanning rate of 8°·min^{-1}.

The relative density of the laser rapidly solidified composites was studied using Image-Pro Plus 6.0 software. After grinded and polished, optical micrographs of each sample were obtained. The obtained optical micrographs were then turned into the gray mode. A proper threshold value of gray scale was determined as gray scale of the pores. Then, the area percentage of pores was obtained by calculating the area ratio of the marked regions to the whole micrograph. Triplicate tests were conducted for each sample.

2.4 Immersion Test

The immersion experiments were conducted to access the corrosion behavior of the ZK60/*x*β-TCP composites. Simulated body fluid (SBF) served as the degradation medium. The pH variations of the SBF were recorded during the immersion for 10 days. In addition, the corrosion surface of the composites was observed by SEM after immersion for 7 days. The chemical composition was analyzed by energy dispersive spectroscopy (EDS, JSM-5910LV, Japan). Weight loss method was used to obtain the quantified data on the degradation behavior of Mg-based composite. The weight of the samples after the corrosion test was measured after removal of the corrosion products in chromic acid. An average of three measurements was taken for each group. The *in vitro* corrosion rate was calculated according to the equation:

$$C = M_{loss}/(qAT)$$

where C was the corrosion rate in mm/year, M_{loss} was the weight loss, q was the density of the material, A was the initial immersion surface area and T was the immersion time.

2.5 Mechanical Properties

The compressive strength was assessed by a universal testing machine (WD-01, Shanghai Zhuoji instruments Co. Ltd., China) at a loading rate of 0.5 mm·min^{-1}. The test samples with the size of 3×3×6 mm^3 were prepared according to the ASTM-E9-09. Three identical samples were used for the compressive tests. Besides, indentation tests were performed to evaluate the hardness of the composite by a hardness tester (Taiming Optical Instrument Corporation, China). The applied load and loading time were 0.98 N and 15 seconds, respectively. Triplicate tests were conducted for each sample.

2.6 *In Vitro* Cell Culture

MG-63 cells were used for the *in vitro* cell culture. Dulbecco's modified eagle medium (DMEM) with 10% fetal bovine serum, 100 U·mL^{-1} penicillin and 100 mg·mL^{-1} streptomycin were used as culture medium. ZK60/*x*β-TCP samples were immersed in DMEM for 3 days to prepare extracts (surface area to extracts volume 1.25 cm^2·mL^{-1}) in humidified atmosphere (5% CO_2, 37 °C).

MG-63 cells were first cultured in DMEM in a 24-well plate. After 4 h, the cell culture media were substituted by previously prepared extracts. Cells were cultured in a humidified atmosphere for 1 day (5% CO_2, 37 °C). Subsequently, the cells were gently rinsed with phosphate buffered saline (PBS) and then stained with Calcein-AM and Ethidium homodimer-1 reagents (15 min, 37 °C). After gently rinsing with PBS, the specimens were mounted onto glass slides and then observed by fluorescence microscopy (BX60, Olympus, Japan).

Besides, CCK-8 assay was used to assess cell viability of MG-63 cells cultured in extracts of ZK60/*x*β-TCP composites. The MG-63 cells were seeded onto the 96-well plate (cells density 1×10^5 per mL) and cultured for 1 day. Then, the cell culture media were substituted by prepared extracts, with DMEM serving as control. After cultured for 1, 3 and 5 days, cells were incubated with 10 μL CCK-8 (5 mg/mL, Sigma-Aldrich, St. Louis, MO, USA) for 2 h, then the absorbance was measured at 450 nm by paradigm detection platform (BECK MAN, S. Kraemer Boulevard Brea, CA). The obtained optical density (O.D.) values were proportional to the live cell numbers.

2.7 Statistical Analysis

Quantitative data were presented as mean ± standard deviation, and analyzed using the STATA (Data Analysis and Statistical Software). Statistical significance was defined when the p-value was <0.05.

3. Results and Discussion

3.1 Microstructure

The typical microstructures of the laser rapidly solidified ZK60/*x*β-TCP composites were presented in Figure 2. For ZK60, only a small amount of second phases (MgZn intermetallic phase) distributed in Mg matrix (Figure 2A). After composited with 4 wt. % β-TCP, divorced slender

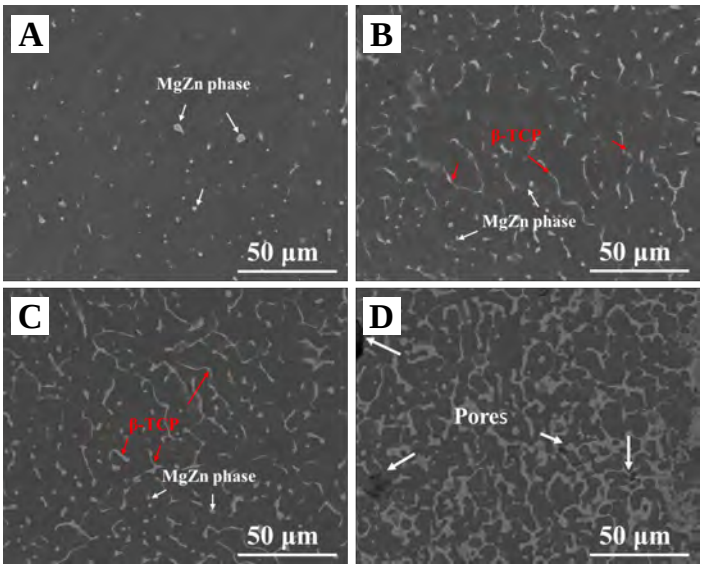

Figure 2. SEM of the ZK60/xβ-TCP composites: (**A**) dot like MgZn phase distributed in ZK60; (**B**) divorced slender β-TCP phase uniformly distributed along grains boundaries in ZK60/4β-TCP; (**C**) continuous slender β-TCP phase in ZK60/8β-TCP; (**D**) pores were observed in ZK60/12β-TCP.

β-TCP phase was observed uniformly distributing along grains boundaries (Figure 2B). For ZK60/8β-TCP, more slender β-TCP phases homogeneously precipitated along the grain boundaries, compared with ZK60/4β-TCP (Figure 2C). While β-TCP content was up to 12 wt. %, the precipitated β-TCP was considerably coarsened and agglomerated, forming a continuous network structure. Besides, some pores were observed in the matrix of ZK60/12β-TCP (Figure 2D).

The relative density of laser-melted ZK60/*x*β-TCP composites was investigated, with results shown in Figure 3. Laser-melted ZK60 obtained a high level of relative density of 98.8 ± 0.6%. After composited with β-TCP, ZK60/4β-TCP and ZK60/8β-TCP still reached a high relative density of 97.6 ± 1.1% and 97.2 ± 1.8%, respectively, with no significant difference among ZK60, ZK60/4β-TCP and ZK60/8β-TCP ($p > 0.05$). However, a considerable decrease of relative density to 88.5 ± 3.5% was observed with a further increase of β-TCP to 12 wt. %. The significantly lower relative density of ZK60/12β-TCP as compared with ZK60/8β-TCP indicated that the agglomeration of β-TCP particles deteriorated the densification behavior of Mg matrix during solidification.

The obtained XRD patterns of β-TCP/ZK60 composites were shown in Figure 4. Compared with the ZK60, besides the diffraction peaks corresponding to α-Mg, the diffraction peaks of β-TCP were also detected in the β-TCP/*x*ZK60 composite. In addition, the diffraction peaks of β-TCP became stronger with β-TCP increasing. The XRD results also demonstrated that no other new phases formed, indicating that no chemical

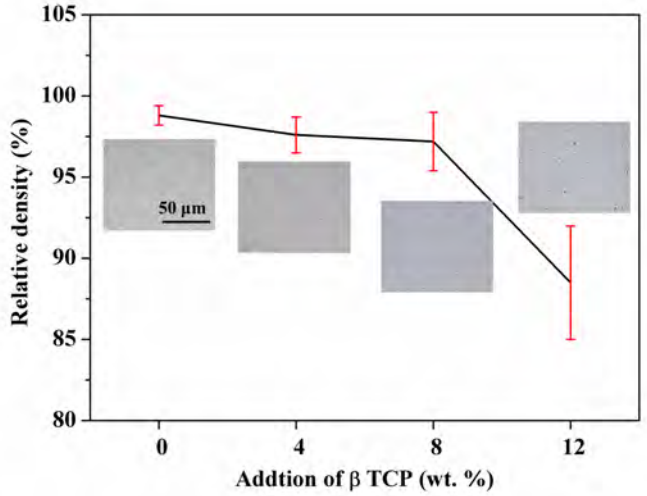

Figure 3. The relative density of the ZK60/xβ-TCP composites. The insets were the corresponding optical images.

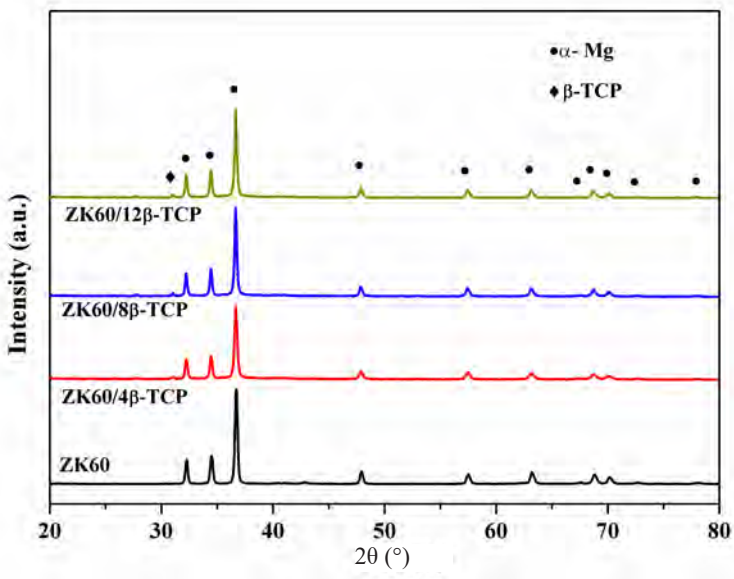

Figure 4. XRD patterns of the ZK60/xβ-TCP composites

reactions occurred between β-TCP and Mg alloys during the laser melting.

3.2 Mechanical Properties

The obtained compressive strength of laser-melted ZK60/*x*β-TCP composites was shown in Figure 5A. ZK60 exhibited a relatively low compressive strength of 111.8 ± 6.8 Mpa. After composited with 8 wt. % β-TCP, the compressive strength was gradually improved to 207.4 ± 7.7 Mpa. However, a further increase of β-TCP to 12 wt. % resulted in a dramatically decrease of compressive strength to 167.4 ± 12.2 Mpa. Besides, the hardness of the laser rapidly solidified ZK60/β-TCP composites was also obtained, with results shown in Figure 5B. It could be observed that the hardness of ZK60/*x*β-TCP composites significantly increased with β-TCP increasing. ZK60 exhibited a low hardness of 82.4 ± 3.8 HV, while ZK60/4β-TCP, ZK60/8β-TCP and ZK60/12β-TCP had an enhanced hardness of 97.6 ± 4.5 Hv, 127.2 ± 5.7 Hv and 153.4 ± 12.2 Hv, respectively.

3.3 Degradation Behavior

The degradation behavior of the ZK60/*x*β-TCP composites was evaluated by immersion tests in SBF. Moreover, the pH variation of the SBF for ZK60/*x*β-TCP composites as a function of soaking time was presented in Figure 6A. It could be seen that the pH values of SBF for different composites had similar change tendency during the immersion period, increasing quickly at the first 48 h and stabilizing during further immersion. After immersed for 240 h, the obtained pH value of SBF for ZK60/8β-TCP exhibited a lowest value of 9.42 ± 0.09, as compared with SBF for ZK60 (10.25 ± 0.12), ZK60/4β-TCP (9.73 ± 0.13) and ZK60/12β-TCP (10.69 ± 0.10). The increase of pH value was due to the generation of OH^- resulting from the degradation of Mg. Thus, it was indicated that ZK60/8β-TCP showed the highest corrosion resistance. The corrosion rates of the ZK60/*x*β-TCP composites were calculated based on weight loss (Figure 6B). Clearly, ZK60/8β-TCP showed a decreased corrosion rate of 0.58 ± 0.11 mm/year, as compared with ZK60 (1.83 ± 0.25 mm/year), ZK60/4β-TCP (1.63 ± 0.18 mm/year) and ZK60/12β-TCP (2.14 ± 0.34 mm/year).

In order to further study the effect of β-TCP on the degradation behavior, the corrosion surface of the soaked samples were studied by SEM (Figure 7). After immersed for 7 days, a compact film formed on the surface of the ZK60/8β-TCP composite, while loose corrosion product film with obvious cracks formed on the surface of the ZK60. As for the ZK60/12β-TCP, some huge gaps appeared in local areas on the surface. The EDS analysis indicated that the degradation products on ZK60 were mainly composed of Mg and O (Figure 7E), indicating a large amount of $Mg(OH)_2$ coated on the surface of ZK60. Significantly, large amounts of calcium and phosphorus were detected on the surface of the composite (Figure 7F). EDS revealed that the calcium/phosphate atom ratio of the product on the ZK60/8β-TCP composite was 1.617, which was close to that of apatite (1.67)[20]. Thus, it was reasonable to conclude that more apatite deposited on the surface of ZK60/*x*β-TCP composites. In addition, the deposition of apatite resulted in a more compact corrosion surface film on Mg matrix (Figure 7B and Figure 7C).

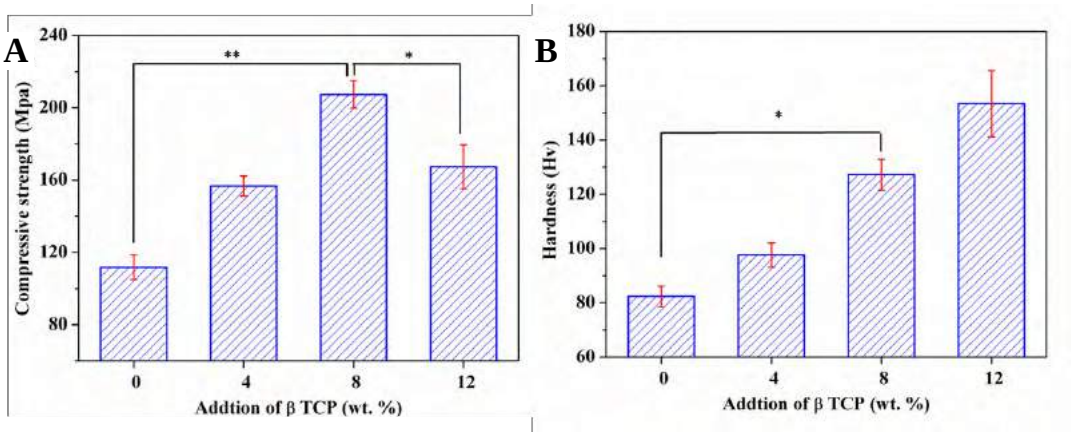

Figure 5. The (**A**) compressive strength and (**B**) hardness of the ZK60/xβ-TCP composites. ($n = 3$, $^{*}p < 0.05$, $^{**}p < 0.01$).

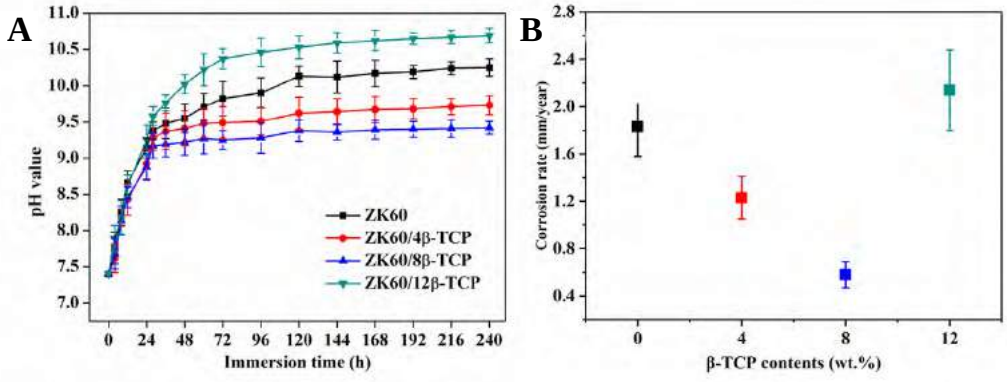

Figure 6. (**A**) The pH variation of SBF after immersion of ZK60/xβ-TCP composites and (**B**) calculated corrosion rate based on weight loss.

3.4 *In Vitro* Cell Response

Fluorescent images of the live/dead assay were presented in Figure 8. Live cells were indicated by the fluorescent green, while dead cells were indicated by the fluorescent red. It could be observed that cells cultured in the extracts of ZK60/8β-TCP presented a typical fusiform shape after 1 day culture (Figure 8C), suggesting their normal cell growth. As a comparison, cells cultured in ZK60 and ZK60/12β-TCP clearly showed a contraction of round shape (Figure 8A and Figure 8D), indicating its unhealthy growth. Meanwhile, a few of dead cells were observed for ZK60 and ZK60/12β-TCP. It should be noted that both ZK60/4β-TCP and ZK60/8β-TCP presented more live cells compared with ZK60 specimens, indicating an improved cytocompatibility of incorporating β-TCP into ZK60.

CCK-8 assay was used to determine the cell viability as a function of culture time, with results shown in Figure 9. Obviously, the cell activity gradually increased with the culture time increasing for all groups. At days 1, 3 and 5, significant differences in O.D. values ($p <$ 0.05) were observed between ZK60/8β-TCP and ZK60. Besides, all the ZK60/*x*β-TCP composites exhibited higher O.D. values than ZK60, indicating better cell viability. Clearly, ZK60/8β-TCP showed higher cell viability than ZK60, ZK60/4β-TCP and ZK60/12β-TCP.

4. 4. Discussion

4.1 The Effect of Laser Rapid Solidification on Microstructure

Laser melting technology is able to process various biomaterials, including bioceramics and biometals. Nevertheless, bioceramics, such as hydroxyapatite, TCP and 45s bioglass, exhibit a too low mechanical strength for bone implant. Furthermore, bioceramic usually has a high viscosity and low fluidity, which impaired the density of laser processed part[21]. While Mg alloys exhibit suitable mechanical strength but poor corrosion resistance. Thus, substantial efforts have been devoted to fabricating bioceramic reinforced Mg alloys as candidates for bone implants. For instance, some researchers had fabricated β-TCP reinforced Mg-based

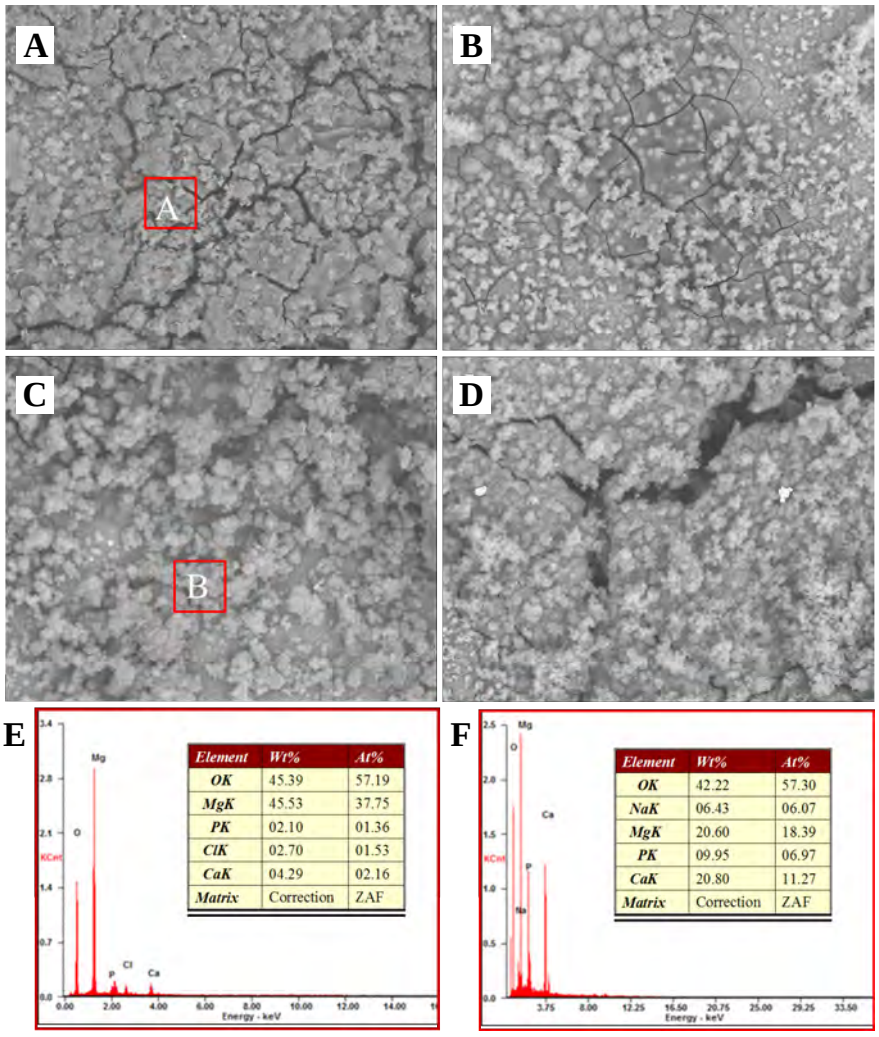

Figure 7. Corrosion surface of laser rapidly solidified ZK60/xβ-TCP composites: (**A**) ZK60; (**B**) ZK60/4β-TCP; (**C**) ZK60/8β-TCP; and (**D**) ZK60/12β-TCP. (**E**) EDS results of region A; (**F**) EDS results of region B.

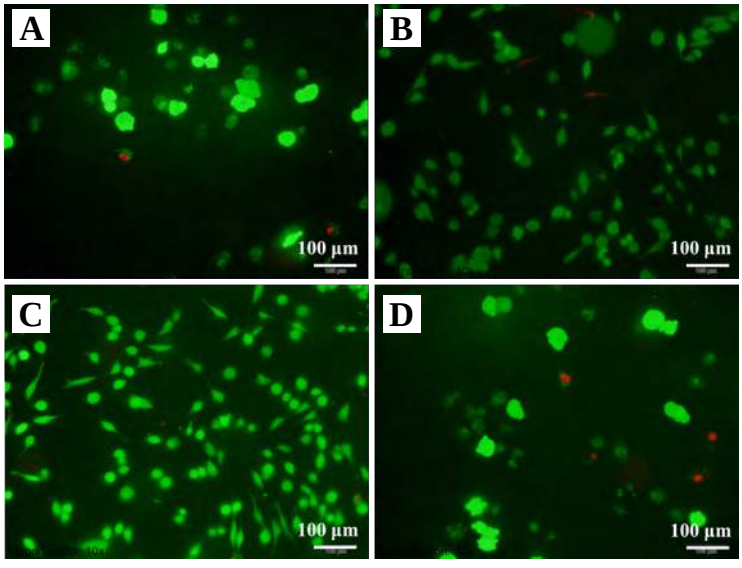

Figure 8. Fluorescence micrograph of live/dead dye-stained MG-63 cells after 1 day culture in the extracts of ZK60/xβ-TCP. (**A**) ZK60, (**B**) ZK60/4β-TCP, (**C**) ZK60/8β-TCP and (**D**) ZK60/12β-TCP.

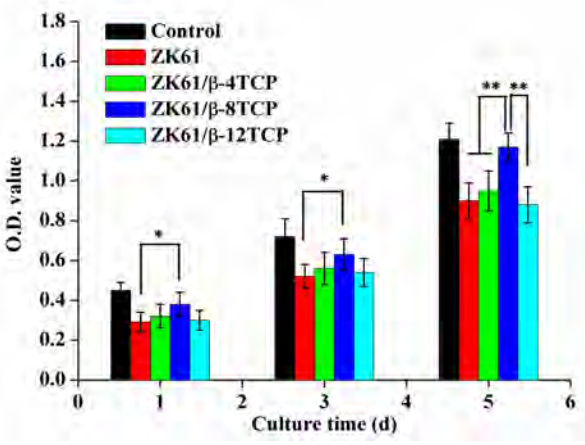

Figure 9. CCK-8 assay for MG-63 cells cultured in the extracts of ZK60/xβ-TCP composites for 1, 3 and 5 days. ($n = 3$, $*p < 0.05$, $**p < 0.01$).

composites by conventional techniques. Unfortunately, agglomeration phenomenon of β-TCP occurred even at a low content of 1.5 wt. % in casting process[11]. Huang *et al.*[22] reported that β-TCP aggregated in the matrix of casted Mg–2Zn–0.5Ca/1β-TCP at a lower content of 1 wt. %. Yan *et al.*[23] fabricated a kind of Mg-Zn/β-TCP composite by powder metallurgy, and also observed the aggregation of β-TCP in Mg matrix. The physical differences between β-TCP and α-Mg would be used to explain the agglomeration of β-TCP in the Mg matrix. β-TCP possessed a rhombohedral structure (lattice parameters a, b = 1.04352 nm, c = 3.7403 nm, a, β = 90° and γ = 120°), while α-Mg had a hexagonal structure (lattice parameters a, b = 0.32092 nm and c = 0.52105 nm)[24]. According to the heterogeneous nucleation theory, such a difference in crystal structure made it extremely difficult for α-Mg to nucleate on the surfaces of β-TCP particles. Thus, most of the β-TCP particles would be pushed by the growing front of α-Mg grains during the solidification. In equilibrium solidification with a low cooling rate, the β-TCP particles would be squeezed out continuously by slowly-advancing solid/liquid interfaces, finally gathered at the crystal interface and caused component segregation.

Combined processes have been reported to overcome the agglomeration of β-TCP in Mg matrix. For example, a melt shearing technology combined with high-pressure die casting was applied to fabricated β-TCP/Mg composite[12]. Besides, powder metallurgy, hot extrusion and aging treatment were combined to fabricated β-TCP/Mg-Zn composites[23]. In this study, laser rapid solidification, as one step process, was proposed to solve the problem. SEM images clearly showed that β-TCP homogeneously distributed along grains boundaries in Mg matrix, with β-TCP contents up to 8 wt. % (Figure 2). In laser rapid solidification, the velocity of the solid/liquid interface was extremely high, which was believed to be far faster than the movement of β-TCP particles. In this condition, the β-TCP particles would be captured by the solid/liquid interface and remained the original uniform distribution. On the other hand, laser rapid solidification could also cause a grain refinement with a high density of grains boundaries[6]. More grain boundaries would provide more distribution space for β-TCP particles, thus avoiding the aggregation of β-TCP particles.

4.2 The Effect of β-TCP on Mechanical Properties

Mechanical tests revealed that the incorporation of β-TCP significantly improved the compressive strength and hardness of ZK60. The increased compressive strength of ZK60/*x*β-TCP composites was due to: (I) a good interface bonding between the α-Mg grains and β-TCP particles gave rise to effective load transfer from α-Mg matrix to β-TCP particles, which possessed better load-bearing capacity[25]; (II) the homogeneously distributed β-TCP would serve as an obstacle to the dislocation movement and then ended up with dislocation pile ups; (III) the addition of β-TCP particles as second phase inhibited the growth of α-Mg grains, resulting in fine grain strengthening. However, the compressive strength of the ZK60/*x*β-TCP composites decreased with β-TCP further increasing to 12 wt. %. For ZK60/12β-TCP, excess β-TCP aggregated at the grain boundaries and formed coarsened second phase, which weakened the bonding interface between the α-Mg grains and adjacent β-TCP particles. A large number of pores and defects formed in the matrix, thus reducing the compressive strengths of the composite. Besides, the enhanced hardness was primarily attributed to that hard β-TCP particles acted as reinforcement phases, which impeded the dislocation movement.

4.3 The Effect of β-TCP on Degradation Behavior

It was well known that Mg had a lively chemical property. As Mg based alloys were exposed to aqueous solution, Mg would degrade according to the following chemical reactions[26]:

$$\text{Anodic: } Mg \rightarrow Mg^{2+} + 2e^{-} \quad (4.1)$$

$$\text{Cathodic: } 2H_2O + 2e^{-} \rightarrow H_2\uparrow + 2OH^{-} \quad (4.2)$$

$$\text{Product formation: } Mg^{2+} + 2OH^{-} \rightarrow Mg(OH)_2\downarrow \quad (4.3)$$

Hence a heavy layer of $Mg(OH)_2$, which exhibited a porous structure, was observed on the surface of ZK60 (Figure 7A). Meanwhile, the Cl^- ions contained in SBF could transformed $Mg(OH)_2$ into resoluble $MgCl_2$ as follows[16]:

$$Mg(OH)_2 + 2Cl^{-} \rightarrow MgCl_2 + 2OH^{-} \quad (4.4)$$

Thus, the coated $Mg(OH)_2$ layer could not provide an effective protection for the inner fresh Mg matrix from further degradation. Compared with ZK60, ZK60/8β-TCP had an enhanced corrosion resistance. This could be confirmed by the reduced pH value of SBF after immersion of ZK60/8β-TCP composite. The enhanced corrosion resistance of ZK60/8β-TCP was due to a more protective film formed on the corrosion surface. The β-TCP distributed in Mg matrix would dissolve in the aqueous solution as follows[27]:

$$3Ca_3(PO_4)_2 + H_2O \rightarrow HPO_4^{2-} + OH^{-} + 9Ca^{2+} + 5PO_4^{3-} \quad (4.5)$$

The released calcium ion and phosphate ion favored for the formation of apatite layer on surface. On the other hand, the β-TCP usually acted as the apatite nuclei leading to the deposition of apatite spontaneously[28]. Therefore, a large amount of apatite deposited on the surface and filled the pores of $Mg(OH)_2$ layer. As a result, a more compact surface film formed and effectively retarded the further degradation.

It should be noted that the corrosion rate accelerated as the β-TCP content increased up to 12 wt. %. This was because too much β-TCP aggregated at the grain boundaries and reduced the relative density of the matrix. As a consequence, the strongly corrosive Cl^- ion easily invaded into the matrix, which accelerated the degradation.

4.4 *In Vitro* Cell Response of ZK60/xβ-TCP

In the presented study, the extracts of ZK60/*x*β-TCP were utilized to mimic the environment during implantation. *In vitro* cell culture experiments indicated that MG-63 cells exhibited better growth in extracts of ZK60/8β-TCP than in that of ZK60. The improved cytocompatibility of ZK60/8β-TCP was believed to be closely related to the enhanced corrosion resistance. As shown in Figure 6A, the pH value significantly increased during the immersion due to the rapid degradation of Mg-based composites. In general, a weak alkaline environment with pH value ranging from 7.4 to 7.8 was more suitable for cell survival. An increased pH would significantly impair the enzyme activity, thus affecting the transport of substance for cell membrane. Meanwhile, a high pH value with high Mg^{2+} and OH^- concentration led to a too high osmotic pressure in culture medium[29]. Thus, the significantly increased pH had obvious inhibitory effects on cell proliferation. For ZK60/8β-TCP, the pH value and ion concentration (Mg^{2+}, OH^-) in culture medium were considerably reduced compared with ZK60, resulting in more appropriate pH value and osmolality for cell proliferation. Besides, the released Ca^{2+} caused by the degradation of β-TCP should also be responsible for the improvement of cytocompatibility for ZK60/8β-TCP. Ca, as a nutrient element for the human body, is essential in chemical signaling with cells[30]. Li *et al*. also reported that Ca^{2+} enhanced the proliferation of bone-derived cell[31]. Thus, the release of Ca^{2+} from ZK60/8β-TCP might exert a positive effect on the cell growth and proliferation.

5. Conclusions

In this study, β-TCP was composited with ZK60 *via* laser rapid solidification with an aim to improve the degradation behavior. It was revealed that laser rapid solidification restrained the segregation of β-TCP particles in Mg matrix. In addition, β-TCP particles uniformly distributed along grains boundaries in ZK60/8β-TCP. The results showed that the laser rapidly solidified ZK60/8β-TCP had an enhanced corrosion resistance and mechanical properties as compared with ZK60. Besides, the results of *in vitro* cell culture assays also revealed that ZK60/8β-TCP composite had an improved cytocompatibility to MG-63 cells. It was suggested that ZK60/8β-TCP was a potential biodegradable implant.

Conflict of Interest and Funding

No conflict of interest was reported by the authors. The authors gratefully acknowledge the following projects and funds for the financial support: (1) The Natural Science Foundation of China (51575537, 81572577, 51705540, 81472058); (2) Hunan Provincial Natural Science Foundation of China (2016JJ1027); (3) The Project of Innovation-driven Plan of Central South University (2016CX023); (4) The Open-End Fund for the Valuable and Precision Instruments of Central South University; (5) The fund of the State Key Laboratory of Solidification Processing at NWPU (SKLSP201605);

(6) The Project of State Key Laboratory of High Performance Complex Manufacturing, Central South University, and (7) National Postdoctoral Program for Innovative Talents (BX201700291).

References

1. Chen Y, Xu Z, Smith C, *et al*., 2014, Recent advances on the development of magnesium alloys for biodegradable implants. *Acta Biomater*, 10(11): 4561–4573. http://dx.doi.org/ 10.1016/j.actbio.2014.07.005
2. Tie D, Guan R, Liu H, *et al*., 2016, An *in vivo* study on the metabolism and osteogenic activity of bioabsorbable Mg–1Sr alloy. *Acta Biomater*, 29: 455–467. http://dx.doi.org/10.1016/j.actbio.2015.11.014
3. Yazdani M, Yazdani M, Afshar A, *et al*., 2017, Electrochemical evaluation of AZ 31 magnesium alloy in two simulated biological solutions. *Anti-Corros Method M*, 64(1): 103–108. http://dx.doi.org/10.1108/ACMM-02-2016-1649
4. Ge S, Wang Y, Tian J, *et al*., 2016, An *in vitro* study on the biocompatibility of WE magnesium alloys. *J Biomed Mater Res B Appl Biomater*, 104(3): 482–487. http://dx.doi.org/10.1002/jbm.b.33388
5. Feng A and Han Y, 2010, The microstructure, mechanical and corrosion properties of calcium polyphosphate reinforced ZK60A magnesium alloy composites. *J Alloys Compd*, 504(2): 585–593. http://dx.doi.org/10.1016/j.jallcom.2010.06.013
6. Shuai C, Yang Y, Wu P, *et al*., 2017, Laser rapid solidification improves corrosion behavior of Mg-Zn-Zr alloy. *J Alloys Compd*, 691: 961–969. https://doi.org/10.1016/j.jallcom.2016.09.019
7. Li N, Zheng Y, 2013, Novel magnesium alloys developed for biomedical application: A review. *J Mater Sci Technol*, 29(6): 489–502. https://doi.org/10.1016/j.jmst.2013.02.005
8. Del Campo R, Savoini B, Munoz A, *et al*., 2014, Mechanical properties and corrosion behavior of Mg–HAP composites. *J Mech Behav Biomed Mater*, 39: 238–246. https://doi.org/10.1016/j.jmbbm.2014.07.014
9. Wan Y, Cui T, Li W, *et al*., 2016, Mechanical and biological properties of bioglass/magnesium composites prepared *via* microwave sintering route. *Mater Des*, 99: 521–527. https://doi.org/10.1016/j.matdes.2016.03.096
10. Feng A and Han Y, 2011, Mechanical and *in vitro* degradation behavior of ultrafine calcium polyphosphate reinforced magnesium-alloy composites. *Mater Des*, 32(5): 2813–2820. https://doi.org/10.1016/j.matdes.2010.12.054
11. He S-Y, Yue S, Chen M-F, *et al*., 2011, Microstructure and properties of biodegradable β-TCP reinforced Mg-Zn-Zr composites. *Trans Nonferrous Met Soc China*, 21(4): 814–819. https://doi.org/10.1016/S1003-6326(11)60786-3
12. Liu D, Zuo Y, Meng W, *et al*., 2012, Fabrication of biodegradable nano-sized β-TCP/Mg composite by a novel melt shearing technology. *Mater Sci Eng C*, 32(5): 1253–1258. https://doi.org/10.1016/j.msec.2012.03.017
13. Yazdimamaghani M, Razavi M, Vashaee D, *et al*., 2016, *In vitro* analysis of Mg scaffolds coated with polymer/hydrogel/ceramic composite layers. *Surf Coat Technol*, 301: 126–132. https://doi.org/10.1016/j.surfcoat.2016.01.017
14. Xie D, Zhao J, Qi Y, *et al*., 2013, Decreasing pores in a laser cladding layer with pulsed current. *Chin Opt Lett*, 11(11): 111401. https://doi.org/10.3788/COL201311.111401.
15. Liang Y-J, Li J, Li A, *et al*., 2017, Solidification path of single-crystal nickel-base superalloys with minor carbon additions under laser rapid directional solidification conditions. *Scr Mater*, 127: 58–62. https://doi.org/10.1016/j.scriptamat.2016.08.039
16. Banerjee R, Collins P Cand Fraser H L, 2002, Laser deposition of *in situ* Ti–TiB composites. *Adv Eng Mater,* 4(11): 847–851. https://doi.org/10.1002/1527-2648(20021105)4:11<847::AID-ADEM847>3.0.CO;2-C
17. Yang Y, Wu P, Lin X, *et al*., 2016, System development, formability quality and microstructure evolution of selective laser-melted magnesium. *Virtual Phys Prototyp*, 11(3): 1–9. http://dx.doi.org/10.1080/17452759.2016.1210522
18. Pillai R S, Frasnelli M, Sglavo V M, 2017, HA/β-TCP Plasma Sprayed Coatings on Ti Substrate for Biomedical Applications. *Ceram Int*. https://doi.org/10.1016/j.ceramint.2017.08.113
19. Sutton A T, Kriewall C S, Ming C L, *et al*., 2016, Powder characterisation techniques and effects of powder characteristics on part properties in powder-bed fusion processes. *Virtual Phys Prototyp*, 12(1): 3–29. http://dx.doi.org/10.1080/17452759.2016.1250605
20. Ivanchenko P, Delgado-López J M, Iafisco M, *et al*., 2017, On the surface effects of citrates on nano-apatites:

Evidence of a decreased hydrophilicity. *Sci Rep*, 7:8901. http://dx.doi.org/10.1038/s41598-017-09376-x

21. Sing S L, Yeong W Y, Wiria F E, *et al*., 2017, Direct selective laser sintering and melting of ceramics: A review. *Rapid Prototyp J*, 23(3): 611–623. http://dx.doi.org/10.1108/RPJ-11-2015-0178
22. Huang Y, Liu D, Anguilano L, *et al*., 2015, Fabrication and characterization of a biodegradable Mg–2Zn–0.5 Ca/1β-TCP composite. *Mater Sci Eng C*, 54: 120–132. http://dx.doi.org/10.1016/j.msec.2015.05.035
23. Yan Y, Kang Y, Li D, *et al*., 2017, Improvement of the mechanical properties and corrosion resistance of biodegradable β-Ca_3 (PO_4) 2/Mg-Zn composites prepared by powder metallurgy: The adding β-Ca_3 $(PO_4)_2$, hot extrusion and aging treatment. *Mater Sci Eng C*, 74: 582–596. http://dx.doi.org/10.1016/j.msec.2016.12.132
24. Yashima M, Sakai A, Kamiyama T, *et al*., 2003, Crystal structure analysis of β-tricalcium phosphate $Ca_3(PO_4)_2$ by neutron powder diffraction. *J Solid State Chem*, 175(2): 272–277. http://dx.doi.org/10.1016/S0022-4596(03)00279-2
25. Garoushi S K, Hatem M, Lassila L V, *et al*., 2015, The effect of short fiber composite base on microleakage and load-bearing capacity of posterior restorations. *Acta Biomater Odontol Scand*, 1(1): 6–12. http://dx.doi.org/10.3109/23337931.2015.1017576
26. Agarwal S, Curtin J, Duffy B, *et al*., 2016, Biodegradable magnesium alloys for orthopaedic applications: A review on corrosion, biocompatibility and surface modifications. *Mater Sci Eng C*, 68: 948–963. http://dx.doi.org/10.1016/j.msec.2016.06.020
27. Geng F, Tan L, Jin X, *et al*., 2009, The preparation, cytocompatibility, and *in vitro* biodegradation study of pure β-TCP on magnesium. *J Mater Sci Mater Med*, 20(5): 1149–1157. http://dx.doi.org/10.1007/s10856-008-3669-x
28. Kokubo T, 1996, Formation of biologically active bone-like apatite on metals and polymers by a biomimetic process. *Thermochim Acta*, 280–281: 479–490. http://dx.doi.org/10.1016/0040-6031(95)02784-X
29. Zhang L, Pei J, Wang H, *et al*., 2017, Facile preparation of poly (lactic acid)/brushite bilayer coating on biodegradable magnesium alloys with multiple functionalities for orthopedic application. *ACS Appl Mater Interfaces*, 9(11): 9437–9448. http://dx.doi.org/10.1021/acsami.7b00209
30. Ilich J Z and Kerstetter J E, 2000, Nutrition in bone health revisited: A story beyond calcium. *J Am Coll Nutr*, 19(6): 715–737. http://dx.doi.org/10.1080/07315724.2000.10718070
31. Li Z, Gu X, Lou S, *et al*., 2008, The development of binary Mg–Ca alloys for use as biodegradable materials within bone. *Biomaterials*, 29(10): 1329–1344. http://dx.doi.org/10.1016/j.biomaterials.2007.12.021

RESEARCH ARTICLE

Pre-clinical evaluation of advanced nerve guide conduits using a novel 3D *in vitro* testing model

Mehri Behbehani[1], Adam Glen[1], Caroline S. Taylor[1], Alexander Schuhmacher[2], Frederik Claeyssens[1], John W. Haycock[1]

[1] Department of Materials Science and Engineering, The University of Sheffield, UK

[2] Faculty of Applied Chemistry, Reutlingen University, Germany

Abstract: Autografts are the current gold standard for large peripheral nerve defects in clinics despite the frequently occurring side effects like donor site morbidity. Hollow nerve guidance conduits (NGC) are proposed alternatives to autografts, but failed to bridge gaps exceeding 3 cm in humans. Internal NGC guidance cues like microfibres are believed to enhance hollow NGCs by giving additional physical support for directed regeneration of Schwann cells and axons. In this study, we report a new 3D *in vitro* model that allows the evaluation of different intraluminal fibre scaffolds inside a complete NGC. The performance of electrospun polycaprolactone (PCL) microfibres inside 5 mm long polyethylene glycol (PEG) conduits were investigated in neuronal cell and dorsal root ganglion (DRG) cultures *in vitro*. Z-stack confocal microscopy revealed the aligned orientation of neuronal cells along the fibres throughout the whole NGC length and depth. The number of living cells in the centre of the scaffold was not significantly different to the tissue culture plastic (TCP) control. For *ex vivo* analysis, DRGs were placed on top of fibre-filled NGCs to simulate the proximal nerve stump. In 21 days of culture, Schwann cells and axons infiltrated the conduits along the microfibres with 2.2 ± 0.37 mm and 2.1 ± 0.33 mm, respectively. We conclude that this *in vitro* model can help define internal NGC scaffolds in the future by comparing different fibre materials, composites and dimensions in one setup prior to animal testing.

Keywords: 3D model; intraluminal scaffold; peripheral nerve; regenerative medicine; microfibres

*Correspondence to: John W Haycock, Department of Materials Science and Engineering, Sir Robert Hadfield Building, Mappin Street, S1 3JD, UK; j.w.haycock@sheffield.ac.uk

Received: September 29, 2017; **Accepted:** November 22, 2017; **Published Online:** December 20, 2017

Citation: Haycock J W, 2018, Pre-clinical evaluation of advanced nerve guide conduits using a novel 3D *in vitro* testing model. *Int J Bioprint,* 4(1): 123. http://dx.doi.org/10.18063/IJB.v4i1.123.

1. Introduction

Injuries to peripheral nerves can affect the general public in all age groups, mostly caused by domestic, industrial or traffic accidents. Severe transection injuries are often life-changing and may result in defects of motor and sensory function. These injuries can often be repaired through a self-regeneration mechanism after Wallerian degeneration takes place[1]. However, a major concern is the increasing risk of incomplete functional and motor recovery with increasing degree of injury[2]. Current clinical treatments of complete peripheral nerve transection injuries comprise of surgical end-to-end suturing, allografting or the use of nerve guidance conduits depending on nerve gap size and severity of injury. Despite its reputation as the gold standard, autografts suffer from several major drawbacks: the sacrifice of a healthy nerve, donor site morbidity, at least two surgical interventions on donor and injury site, potential size discrepancy between harvested nerve and injured nerve and possible functional mismatch when treating

motor nerve lesions with commonly used sensory sural nerve grafts[3-5].

In recent years, bioengineers have focused on the development of NGCs to provide an alternative treatment to autografts, where different materials and designs were explored resulting in a number of devices that have seen FDA approval (Neuroflex/ Neuromatrix®, NeuraGen®, AxoGuard®, Avance®, Neu-rolac® or SaluTunnel®). However, these commercial NGCs lack internal guidance structures and cannot exceed injury gaps greater than 3 cm, which is shorter than the defined critical nerve gap of 4 cm in humans[6,7]. To this date, no other commercial solution has been presented. Therefore, key challenges now focus on enhancement of NGCs by including internal conduit guidance structures for targeted axon regeneration through the nerve gap to maximise the number of regenerating axons and therefore the regeneration outcome. Aligned fibres of a natural or synthetic material can be one approach to improve hollow nerve guides[8-11] by mimicking the natural regeneration guidance cues of bands of Büngner, where Schwann cells and fibroblasts form aligned bands between the proximal and distal nerve end to guide axons to their target effectors[12]. With adjustment of the fibre density in the NGC lumen, specific regeneration needs can be addressed like varying axon numbers in nerves. In comparison, hollow nerve guides only provide outer guidance for the injured nerve to keep both nerve stumps connected but cannot provide relevant internal guidance support for regenerating cells and tissue. Furthermore, fibre containing conduits would not require an adaption of nerve fascicles and blood vessels between the proximal stump and the conduit which is necessary when using autografts[13].

Newly developed NGC scaffold designs, which have seen *in vivo* implantation, have compared favourably to hollow conduits and autografts[8,14-16]. However, new designs have, for the most part, not been directly compared to previous generation NGCs, or to currently used nerve conduits. Furthermore, with advanced NGC improvements more adequate evaluation techniques are required. More complex NGC structures, such as those that comprise of two components, like an additional internal scaffold, would greatly benefit from novel assessment techniques like *in vitro* evaluations in three dimensions, instead of relying on data retrieved from *in vitro* analysis on flat material films. We therefore hypothesized that the evaluation of intraluminal nerve guide scaffolds (*e.g.* microfibres) can be directly conducted in whole nerve conduits in order to provide a prospective platform for comparison of different internal NGC scaffolds. The effectiveness of the model was determined by neuronal cell culture and primary rat dorsal root ganglion explants in conjunction with cellular responses investigated using three-dimensional z-stack confocal and two-photon imaging.

2. Methods

2.1 Conduit Fabrication

Three-dimensional conduits were fabricated by microstereolithography. Polyethylene glycoldiacrylate (Mn = 575 g/mol, Sigma, Poole, U.K.) was mixed with 4% diphenyl-(2,4,6-trimethylbenzoyl)-Phosphineoxide/2 -hydroxy-2-methylpropiophenone 50/50 photoinitiator (wt/wt, Sigma) to obtain a photocurable version of the target polymer. A cross sectional image of the required conduit size (1.2 mm internal diameter, 250 µm wall thickness) was uploaded to a digital micromirror device (Texas Instruments Incorporated, USA, associated software: ALP-3 Basic, ViALUX GmbH), which comprised of a range of mirrors, where each 20 µm size mirror represented a 1:1 object-to-image size ratio. The beam of a 10 mW 405 nm laser (Vortran Laser Technology Inc, USA) was expanded and aligned while running through a spatial filter and a mirror set. The beam then reached the digital micromirror device and was reflected in the shape of the uploaded cross section image. The liquid prepolymer was placed under a motorized z-axis translation stage (Thorlabs Ltd, UK, associated software: APT software), which was mounted at the liquid-air interface. Controlled by velocity and acceleration, the z-stage moved down into the bulk material where the irradiated regions were polymerized. Once the final length of the structure was reached, the laser power was turned off and the stage returned to its origin, carrying the complete 3D conduit structure. Unreacted prepolymer was washed off with isopropyl alcohol (IPA, Fisher Scientific UK). All fabricated structures were washed in IPA for 7 days to ensure full removal of unreacted prepolymer and added photoinitiator.

2.2 Microfibre Fabrication

The fabrication of 5 µm PCL fibres (referred to as microfibres) was conducted using electrospinning. A plastic syringe (Becton Dickinson) was filled with 10% PCL solution (wt/wt, Sigma Aldrich Co, U.K.) in dichloromethane (Fisher Scientific U.K.) and topped with a 20G blunt stainless-steel needle. The needle

was connected to a high voltage supply (Genvolt UK) and the polymer-loaded syringe placed in the mount of a programmable syringe pump (WPI Europe) and constantly pumped through with a flow rate of 4 ml/hr. Polymer jet formation was achieved by a voltage of 15 kV. The formed fibres were collected on an earthed rotating aluminium collector (IKA Works) wrapped in aluminium foil with a rotation speed of 2000 rpm.

2.3 Characterisation of Microfibres

Gold coated electrospun fibre samples were imaged using a XL-20 scanning electron microscope (SEM, Koninklijke Philips N.V.) operating at 15 kV. On each aluminium fibre sheet, three parallel arranged squares were analysed regarding fibre diameter and density. The fibre diameter was analysed using a ruler tool in the SEM related XL software. The amount of fibres per 50 µm were counted and averaged over all images.

2.4 Combination of Conduit and Microfibers

Approximately 6000–7000 PCL microfibres were threaded per PEG conduit. The fibre sheets were cut to the required width and 1–2 cm of the fibres were manually lifted off in the direction of the fibre alignment. These fibres were twisted between the fingers, where the twisted end was used in a similar manner to a needle. PEG NGCs were threaded onto PCL fibres (non-bunched end) like pearls on a chain and fibre excess was cut with scissors. A schematic of the workflow can be found in Figure 1.

2.5 Cell Culture in Whole Nerve Guides

NG108–15 neuroblastoma × glioma rat/mouse hybrid neuronal cells (Public Health England, UK) were cultured in whole nerve guides with a cell concentration of 6 × 10^5 cells in proliferation medium, containing of Dulbecco's Modified Eagle Medium (DMEM, Sigma), 10% foetal bovine serum (FBS, v/v, Biosera), 0.25 mg/mL amphotericin (Sigma), 200 mM L-glutamine (Sigma), 100 units/mL penicillin and 100 mg/mL streptomycin (Sigma) for 4 days. Cells were seeded with 15 µL of cell suspension by directly pipetting on top of the fibres in the conduits. The NGCs were transferred to the designed culturing setup in a 6-well plate and cells were allowed to attach at 37 °C for 30 minutes before wells were filled with proliferation medium. Neuronal NG108–15 cells were used between passage 14–20 and cultured at 37 °C in a humidified 95% air and 5% CO_2 atmosphere.

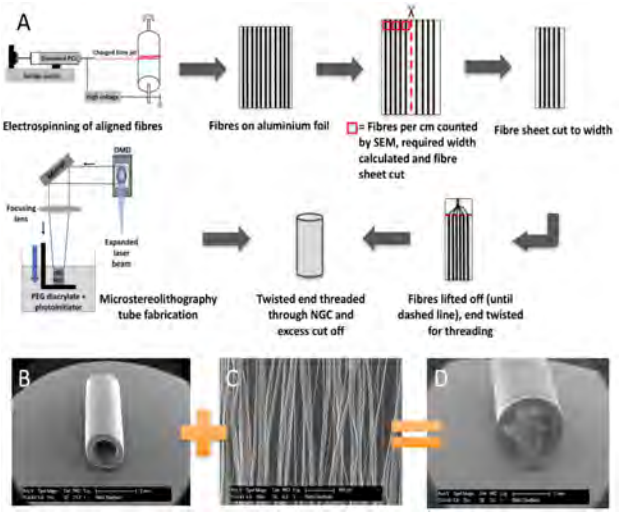

Figure 1. (**A**) Schematic workflow of the production of PCL microfibres using electrospinning, following the procedures of Daud *et al.*[18], the analysis and threading procedure of microfibres and the fabrication of PEG conduits by microstereolithography, following the procedures of Pateman *et al.*[17] SEM micrographs illustrating components of the nerve guide testing device; (**B**) A 5 mm long hollow PEG NGC, fabricated by microstereolithography, and (**C**) PCL microfibres spun by electrospinning. (**D**) Conduit and microfibres were combined into a final testing nerve guide device.

2.6 F-actin Labelling of Neuronal Cells

NG108-15 neuronal cells were fixed with 3.7% paraformaldehyde (PFA, v/v in distilled water, Sigma) in whole NGCs for 3 h. For further staining procedures, the PCL microfibre filling was carefully removed from the NGC by using forceps and fixed on an objective slide. Cell membrane permeabilisation was conducted with 0.1% Triton X-100 (w/v, Sigma) in phosphate buffered saline (PBS, Thermo Scientific) for one hour. Cytoskeleton's F-actin was visualised by using phalloidin conjugated to tetramethylrhodamine (TRITC) (v/v 1:1000 dilution in PBS, Sigma), and cell nuclei were labelled with 4',6-diamidino-2-phenylindole (DAPI, 300 nM, Sigma) for 1 h at room temperature.

2.7 Live/Dead Cell Staining of Neuronal Cells

To distinguish live and dead neuronal cells visually, living cells were stained green by using 0.02% Syto 9 (v/v, Thermo Fisher Scientific) and dead cells red by using 0.03% propidium iodide (v/v, Thermo Fisher Scientific) in serum-free medium (proliferation medium deprived from serum). Cells were incubated

in the staining solution for 60 min at 37 °C. Confocal imaging was conducted in PBS immediately after staining (details below).

2.8 Dorsal Root Ganglion Isolation and Culture

Male Wistar rats aged 10–12 weeks were sacrificed by cervical dislocation (schedule I procedure, UK Home Office). Rats were skinned and the spine was removed. DRGs were extracted after the spine was cut open, dorsal side facing up, and the spinal cord and meninges were removed. The nerve roots of each DRG were trimmed and explant DRG bodies placed on top of the nerve guides (one DRG body per conduit), which were held in place by the described setup. DRGs were incubated at 37 °C for 15 min to allow attachment. Afterwards, samples were fully covered with proliferation medium and incubated at 37 °C in a humidified 95% air and 5% CO_2 atmosphere for 21 days.

2.9 βIII-tubulin and S100β Labelling of Dorsal Root Ganglia

In order to reveal neuron-specific protein βIII-tubulin and Schwann cell-specific protein S100β immunolabelling was conducted. After fixation with 3.7% PFA for 3 h and permeabilising cell membranes with 0.1% Tween X-100 for 1 h, protein binding sites were blocked with 3% bovine serum albumin (BSA, w/v in PBS, Fluka) for 30 min and subsequently washed with PBS. Anti-βIII-tubulin primary mouse antibody (1:200 in 1% v/v BSA, Promega, G7121) and anti S100β primary rabbit antibody (1:600 in 1% v/v BSA, Abcam, Ab868) were added to the samples for 48 h at 4 °C, followed by three washes in PBS. The secondary antibodies, horse anti-mouse lgG conjugated to Texas Red (1:1000 in 1% BSA; Vector Laboratories, TI-200) and goat anti-rabbit lgG conjugated to fluorescein isothiocyanate (FITC) (1:1000 in 1% BSA; Vector Laboratories, F1-1000) were added to the samples and incubated for 120 min at room temperature. Before imaging, samples were washed, then resubmerged in PBS.

2.10 Confocal and 2-photon Laser Microscopy

For imaging samples, a Zeiss LSM 510 META confocal microscope (Carl Zeiss Ltd, UK) with a 543 nm and a 488 nm laser was used. DAPI stained samples were imaged using an additional 2-photon 780 nm laser (Chameleon Ultra III, Coherent Inc, USA). Samples were arranged in a 6-well plate or were fixed on a glass microscope slide and imaged in PBS using a 10× magnification ZeissW Plan Achromat water-dipping objective lens. For imaging FITC- and SYTO 9-labelled samples incident and excitation wavelengths of λex = 488 nm/λem = 525 nm were used, and wavelengths of λex = 543 nm/λem = 576 nm to image Texas Red, TRITC and propidium iodide-labelled samples. Cell nuclei were visualized at λex = 780 nm/λem = 480 nm. Images were stitched together and analysed using Zeiss LSM Image Browser software and Image J 1.49 (National Institute of Health, USA).

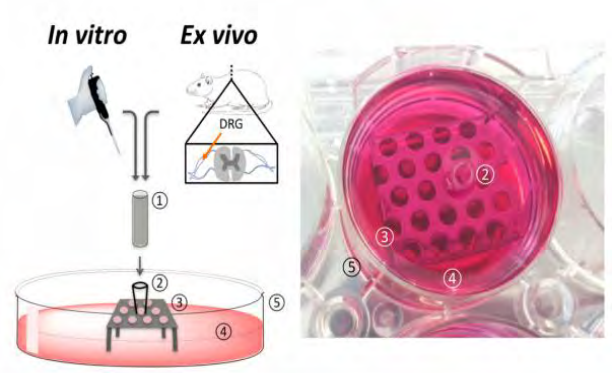

Figure 2. (Left) Schematic of the designed 3D model setup to evaluate the internal nerve guide scaffolds *in vitro* and *ex vivo*. (Right) Photograph of the experimental setup. Cell cultivation was conducted directly inside the incorporated scaffolds. For *ex vivo* analysis, dorsal root ganglia (DRGs), isolated from rat spines, were placed on top of the scaffolds. The test NGC device (1) was fitted with an adapter. (2) To a perforated metal plate. (3) And secured in a well of a commercial 6-well plate (5). In order to perform cell culture experiments, wells were filled with culture medium. (4) Until NGCs were covered.

2.11 Statistics

Data are shown as mean ± SD of three independent experiments, where each experiment has been conducted in triplicate, except for the analysis of microfibres using DRGs, where each experiment had a sample size of four. Statistical differences were tested by ordinary one-way ANOVA Tukey's multiple comparisons test and differences were considered significant when $p \leq 0.05$.

3. Results

The aim of this study was to develop a 3D model to test microfibres as a potential intraluminal guide in nerve conduits *in vitro* with an imaging technique that advances beyond more traditional and time consuming approaches like sample sectioning and histology. The major finding of the study describes a model that

supported the culturing of primary and non-primary neuronal and Schwann cells by following standard cell culture protocols in a more complex, multilayered environment represented by the conduit scaffold architecture under investigation

3.1 Design of the *In Vitro* Testing Setup and Example Device

The developed 3D model used a PEG nerve guide conduit filled with PCL microfibres, based on the procedures developed by Pateman *et al*.,[17] and Daud *et al.*[18]. Figure 1A shows a detailed schematic of the production of PEG conduits with an internal PCL microfibre scaffold. PEG conduits, fabricated by microstereolithography, measured 5 mm in length and had an internal diameter of 1.2 mm with a wall thickness of 250 µm (Figure 1B). The internal lumen diameter was designed to fit a rat dorsal root ganglion for *ex vivo* conduit testing. PCL was electrospun to aligned fibres (Figure 1C), which had an average fibre diameter of 5 ± 0.2 µm. The example device was fabricated by combining the above to a PEG NGC with an internal aligned fibre scaffold to investigate cell's behaviour in response to the introduced internal guide in a ready-to-implant device (Figure 1D). PCL microfibres inside example PEG conduits were tested using a developed testing setup that comprised of two components, a stainless steel perforated metal plate and a polystyrene adapter to match conduit size and the metal stage (Figure 2). Metal stages and polystyrene adapters were sterilised by autoclaving and 70% ethanol treatment respectively. The setup was compatible to a standard 6-well plate and could be used to investigate different conduit sizes, where conduit length analysis was only limited by the well height.

3.2 Cell Orientation Analysis in the 3D Nerve Guide Architecture

In order to successfully analyse the behaviour of neuronal cells on internal NGC scaffolds, key questions of cell attachment and distribution on the scaffolds needs to be answered. Neuronal NG108-15 cells were cultured for 4 days and their morphology investigated by revealing cell nuclei and cytoskeleton with DAPI and F-actin-binding phalloidin. Figure 3A shows an SEM image of the experimental NGC device comprising PCL microfibres inside the lumen of a tubular PEG conduit. Neuronal cells were seeded on internal fibre scaffolds in whole NGCs using the described setup (Figure 2) and followed standard cell seeding procedures by directly applying the cell suspension on the nerve guide scaffold without the need of a pump perfusion system for the supply of medium. As shown in Figures 3B and 3C, neuronal cell orientation on the internal fibre scaffold was compared to cells on TCP. In monolayer, cells are randomly arranged and evenly attached to the TCP substrate (Figure 3B).

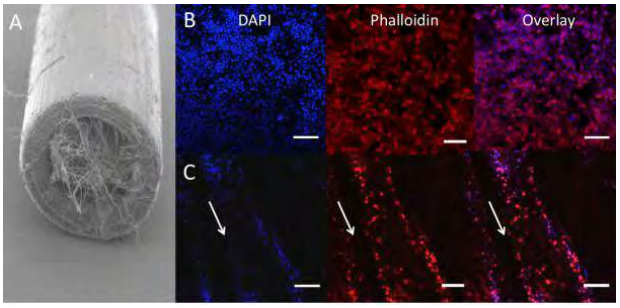

Figure 3. Confocal microscopy images of neuronal cells in nerve guides filled with PCL microfibres. (**A**) Neuronal NG108–15 cells were cultured in 5 mm long PEG NGCs with an internal aligned PCL microfibre scaffold in proliferation medium for 4 days. Neurons were labelled with F-actin-binding phalloidin-TRITC (red) and DAPI (blue) to reveal cytoskeletons and nuclei respectively. (**B**) TCP was used as a flat substrate control, on which neurons were randomly orientated. (**C**) Neurons cultured in whole NGCs orientated with the PCL fibre alignment inside whole PEG nerve guides. Arrows indicate the direction of microfibres in the NGCs. Scale bars = 20 µm.

In Figure 3C, it is clearly demonstrated how neuronal cells changed their orientation when introduced to an aligned scaffold inside the conduit. Due to the restricted growth area, neurons attached along the fibre direction and appeared as cellular bands. Additionally, culture complexity was reached through several microfibre layers inside the NGC, where neurons could attach and elongate in two dimensions on the microfibre scaffold with cell-cell chemical communication in a three-dimensional environment. The distribution of neuronal cells inside the experimental NGC device was evaluated by z-stack confocal microscopy to capture the complete multilayered internal conduit architecture. Microscope images were taken from three different positions of the fibre scaffolds (Figure 4A) and stacked together to 3D projections for analysis. From the data in Figure 4B, it is apparent that neuronal cells attached along the microfibres on all three positions imaged. Despite the presence of neurons in the entire fibre scaffold, attachment was also found on the different fibre layers illustrated in the 3D projections (Figure 4B). Aligned neuronal attachment was detected both in fibre depth

(illustrated by single images) and along the whole tube (illustrated by images taken on three different positions) (Figure 4B). Together, these results provide insight into neuronal attachment, alignment and distribution on PCL microfibres incorporated into NGCs when using the developed culture model, where neurons orientated like they would do as bands of Büngner in peripheral nerve regeneration *in vivo*.

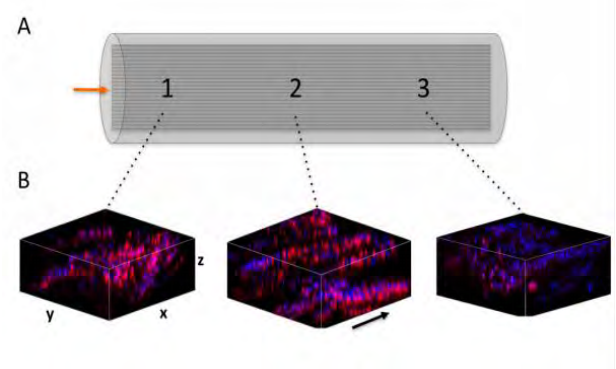

Figure 4. 3D confocal microscopy images of neuronal cell distribution on aligned PCL fibres in whole nerve guides. The incidence of neuronal NG108–15 cells were evaluated on three different positions throughout the NGC and neurons revealed by phalloidin- TRITC and DAPI. For confocal microscopy, the fibres were taken out of the tube and mounted on a glass microscope slide. (**A**) Graphical representation of an NGC with incorporated aligned fibres. The arrow indicates the position where cells were seeded in the tubes. Imaging was conducted in three different positions on the fibres (illustrated by numbers). (**B**) 3D z-projection confocal images of neuronal cell distribution on microfibres inside NGCs. Z-stack images (depth: ~400 µm) were taken at three different positions as illustrated in A. Arrow indicates the direction of microfibres in the NGCs

3.3 Cell Survival Inside Microfibre-filled NGCs

Cell viability not only plays an important role for the *in vitro* analysis and evaluation of cell behaviour and properties but is also crucial in the injury site to maintain as many viable cells as possible to increase effectiveness of tissue regeneration. In the described model, neuronal cells were seeded with greater numbers per area than on flat monolayer substrates and were surrounded by the conduit walls structurally mimicking a peripheral nerve whereas in contrast, monolayer cultured cells are exposed to an open system with unrestricted medium supply. Based on these culturing differences, a comparative overview staining of live and dead neuronal cells was conducted between cells on monolayer TCP substrates or PCL respectively, and cells, which were cultured on PCL microfibre scaffolds inside NGCs (Figure 5A–C). Neuronal cells attached and expanded in different patterns on the three different substrates. On TCP, neurons distributed evenly over the entire monolayer substrate (Figure 5A), where cells on PCL films showed a clumped arrangement (Figure 5B). Neurons cultured on microfibres inside the NGC device formed aligned cellular bands in the direction of the fibres (Figure 5C).

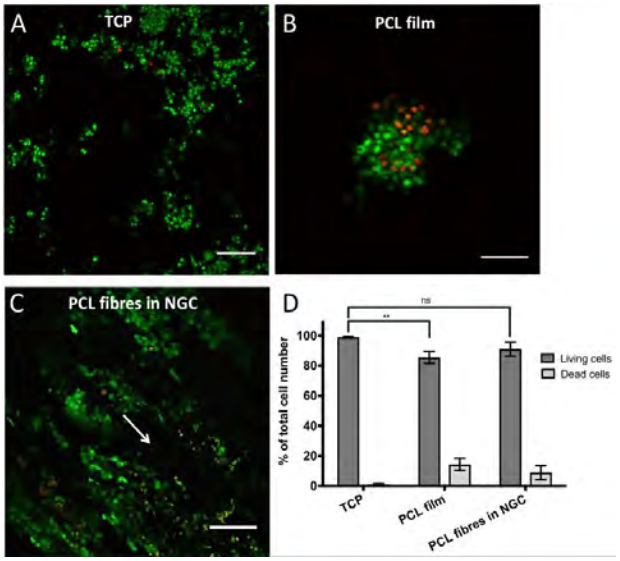

Figure 5. Overview of live and dead neuronal cells in the proposed 3D model. NG108–15 neuronal cells were cultured on TCP (**A**), PCL films (**B**) and on PCL microfibres inside the NGC test device (**C**) for 4 days. Live cells were identified with Syto 9 (green) and dead cells with propidium iodide (red). Cell imaging on fibres was conducted in the centre of the scaffold in z-stacks (depth 400 µm) and was illustrated as maximum intensity images. Arrow indicates the fibre orientation in NGCs. (**D**) shows the percentile distribution of living (dark bars) and dead cells (light bars) in the three different conditions (**A–C**). Living cells on TCP accounted 98.9 ± 0.6 %, on PCL films 85.6 ± 3.9 % and 91 ± 4.6 % on microfibres in NGCs in relation to the total cell population. No significant (ns) differences between data points of living cells on TCP and microfibres inside NGCs could be found, where significance was seen between TCP and PCL films. Data points of living cells were analysed by one-way ANOVA (**p < 0.01). Scale bar = 150 µm."

Additionally, the ratio of viable neuronal cells varied between 85% and 99%, where the highest numbers of living cells could be seen, with more than 90% viability, on microfibres in NGCs and on the flat TCP control. No significant differences could be seen between living or dead neuronal cells cultured on microfibres inside the NGC device and the TCP control. However, a significant decrease in living

neuronal cells was observed between PCL films and TCP. Taken together, microfibres supported the alignment of neuronal cells, yielded in living cell numbers greater than 90% and yielded in higher numbers of living cells compared to the flat PCL control.

3.4 *Ex vivo* dorsal root ganglion culture

Schwann cell proliferation and migration from the proximal to the distal nerve stump is one major key event in peripheral nerve regeneration to provide guidance for re-growing axons in order to successfully reinnervate target effectors on distal site. Simulating the proximal injury site *in vitro*, a rat dorsal root ganglion was placed on top of the example NGC device for investigations on internal scaffold performance by analysing Schwann cell proliferation and axon outgrowth along the microfibre scaffold from the explant towards the tube end (illustrated in Figure 6A). Dorsal root ganglia have been chosen as they accommodate sensory neuronal cell bodies, Schwann cells and fibroblastic cells, and represent a more *in vivo* like environment with primary cells in a co-culture arrangement. In order to analyse the success of the dissection procedure and the ability of microfibres to support DRG outgrowth, DRGs survival and attachment to the NGC device were analysed. The number of attached DRGs to the conduit scaffolds was determined visually and was normalised to the total number of isolated DRGs. In addition, the number of DRGs were counted, where microfibres supported the outgrowth of cells from the DRG body and numbers expressed in relation to all dissected DRGs. More than 90% of all isolated DRGs from male Wistar rats, in the age of 10–12 weeks, attached to the nerve guides using the described setup where more than 80% of the explants showed positive labelling for S100β and βIII tubulin away from the ganglion body (Figure 6C). In order to analyse the cell outgrowth distance from the DRG body towards the tube end, the incorporated PCL microfibre scaffold was removed from the conduit after 21 days of culture and Schwann cells labelled for S100β (green fluorescent signal) and axons for βIII tubulin (red fluorescent signal) (Figure 6B).

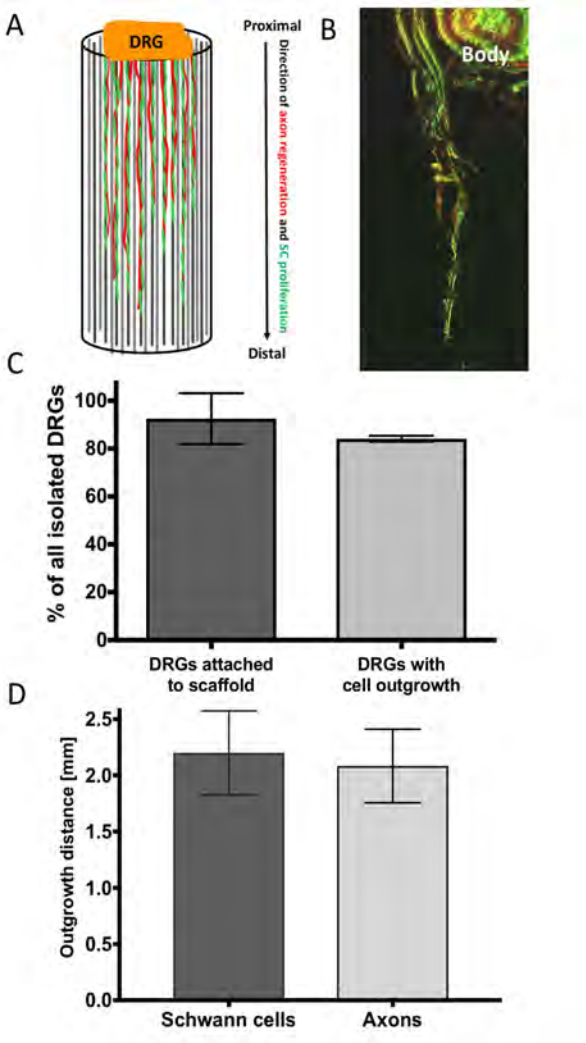

Figure 6. *Ex vivo* evaluation of microfibres in whole nerve guides. DRGs were placed on top of the NGC test devices to evaluate the performance of the microfibre scaffold by analysing the outgrowth behaviour of cells along the scaffold. (**A**) Graphical illustration of the outgrowth of proliferating/ migrating Schwann cells (SC, illustrated in green) and the extension of axons from sensory neuronal cell bodies (illustrated in red) from the DRG body (proximal site) along the microfibres to the tube end (distal site). (**B**) Confocal microscopy z-projection (depth: ~500 µm) of the outgrowth of Schwann cells (immunocytochemically-labelled for S100β, green) and axons (immunocytochemically-labelled for βIII-tubulin, red) along PCL microfibres in a 5 mm long PEG NGC. (**C**) *Ex vivo* performance of the developed culture setup. From all isolated DRGs 91.6 ± 11.8 % attached to the NGC test device using the proposed setup, from which 85% showed an outgrowth of cells into the test conduit. (**D**) In the 5 mm long NGC devices, Schwann cells proliferated in average 2.2 ± 0.37 mm into the conduits, where axons grew out 2.1 ± 0.33 mm in 21 days of culture.

Green fluorescence from axons βIII tubulin could be seen simultaneously where Schwann cells were located. The co-localization could be identified by an overlay of green and red fluorescent signals appearing in a yellow-orange colour (Figure 6B). The distance that neuronal and Schwann cells infiltrated into the conduit was defined as the last detectable signal seen distant from the DRG body. The distance of outgrown cells was of particular importance as demonstrating the microfibres efficiency to support cell infiltration in a simulated nerve lesion *in vitro*. Schwann cells migrated and proliferated 2.2 ± 0.37 mm along the aligned microfibre scaffold inside the NGCs, where neuronal cells showed the extension of axons by 2.1 ± 0.33 mm (Figure 6D). Together, Schwann cells and axons infiltrated 43 % of the 5 mm long conduit *in vitro* in 21 days.

4. Discussion

Most cell-based research is acquired via experiments in monolayer cultures and largely assumes that these monolayer cultures reflect the physiology of tissue. To this day, cell cultivation in a monolayer is the traditional way of culturing cells. Cultivation in monolayers has proved to be simple, convenient and lead to relatively fast results. However, for some time, only *in vitro* 2D cultivation models and *in vivo* animal models were available and used for early stage medical device evaluation[19–21]. Between both models there is a large gap in relation to the physiological relevance. Monolayer cultures are far away from the biological behaviour in the human body, especially when cell lines were chosen over primary cells, and animal studies, whilst representing a whole organism and metabolism, are not human. Though animal studies can mirror human biological responses, they do not always reproduce human physiology[22]. Especially the dominant use of rat sciatic nerve injury models to study NGCs, which have limitations when translating results to humans[23]. Rats are too small in size to enable the study of human critical nerve gap lengths of > 4 cm and homogenous in-bred strains reduce the variability between results. Another concern that may result in mistranslation is the attempt to compare experiments of healthy animals versus sick patients, who normally suffer from multiple injuries besides the injury to a peripheral nerve due to traffic, industrial or domestic accidents. Additionally, there is a regulatory and ethically driven effort to reduce the number of animals used in medical research.

3D *in vitro* models are of increasing interest because of their "closer-to-*in-vivo*" behaviour with higher physiological relevance. In 3D models, cells can be cultivated in three dimensions like in their natural environment in tissues and organs. In neurosciences, 3D models are mostly devoted to the central nervous system to study the neuronal network and signalling pathways, brain barriers, disorders and the effects of neurotoxins (reviewed by[24,25]). Studies on peripheral nerve injuries, and nerve guides in particular, would benefit from *in vitro* 3D models due to the discussed limitations of animal injury models, 2D *in vitro* cultures and the lack of published data. Today there is an increased need for 3D models on internal NGC scaffolds. In particular, hollow NGCs have shown their limitations in repairing nerve gaps exceeding 3 cm and improvement on this matter is urgently needed. Different attempts have been made to study internal scaffolds for NGCs in a three-dimensional environment but documentation on a 3D *in vitro* model to test different scaffolds in one setup prior to animal implantation is still missing. In support of this notion, we developed an *in vitro* 3D DRG model that allows the investigation of different internal fibre scaffolds inside an NGC. In order to ensure that the microfibre scaffold supported cell growth and viability throughout the entire conduit length and depth, cell culture was conducted prior to DRG cultures. The developed system showed an *in vitro* 3D environment, which was based on the final implantable product and therefore more likely mimicked physiological relevant conditions. The morphology and viability of neuronal cells on microfibres inside a tubular nerve guide using the proposed setup was examined, where neuronal morphology remained unchanged throughout the entire nerve guide and where cells showed similar and not significantly different viability rates compared to the flat TCP control. This is of particular interest as it was previously mentioned that even thin 3D scaffolds showed a much lower cell growth in the centre of those structures due to the lack of nutrient and oxygen diffusion to the scaffold core[26–29]. Herein, the number of living cells inside the centre of the microfibre scaffold measured more than 90%.

DRGs are an effective tool for the evaluation of internal scaffolds in NGCs as described in this study. They are easy to harvest, demonstrate a primary

multi-cell type source and their anatomical morphology is suitable to simulate the proximal nerve stump after nerve injury when placed on top of an NGC. Additionally, DRGs contain three main cell types: sensory neurons, which are surrounded by satellite glial cells, Schwann cells and fibroblasts, which are arranged in a collagen-dominant extracellular matrix[30]. Evaluating NGC scaffolds using DRGs therefore allows axon-glia communication, approximates the native peripheral nerve environment and contains the major cell components, which take part in peripheral nerve regeneration. During Wallerian degeneration, Schwann cells and fibroblasts proliferate and migrate from both the proximal and the distal nerve stump into the nerve lesion and provide a chemical and physical guide for regenerating axons[1,31]. The close association of Schwann cells and axons was also observed in this study (yellow fluorescent signal in Figure 6B). In addition, Schwann cells proliferated further than the axons regenerated (Figure 6D), suggesting Schwann cells direct extending axons. The use of DRGs as an evaluation tool for peripheral nerve repair studies is not a new idea and was presented by several research groups in the past[18,32–34]. However, the described *in vitro* assessment methods are mainly confined to the evaluation of a single internal NGC scaffold. The current study suggests using DRGs to evaluate multiple scaffold structures inside the NGC, where the model is not restricted to the evaluation of a single conduit design. Additionally, this study showed the use of DRGs to simulate the proximal nerve stump when placed on top of the NGC device. It should also be mentioned that several NGCs can be tested at once by only sacrificing one animal compared to the direct *in vivo* implantation of a single NGC in a single animal. The presented model may therefore act in terms of the refinement and the reduction of the 3Rs in animal testing[35], showing an advantage from an ethical point of view, but is also advantageous in terms of time and resources.

The hollow nerve conduits in this study were fabricated by microstereolithography from PEG. Microstereolithography is a micro-structuring technique for complex 3D structuring with advantages of high resolution and fast manufacturing times for nerve regeneration[17,36]. Herein, PEG conduits were used as a non-degradable test-conduit device for the analysis of the intraluminal microfibre scaffold. This model can be used with any other kind of hollow nerve guide and is not restricted to the use of PEG NGCs. Combinations of different hollow NGCs and internal scaffolds can also be studied. The size of the conduits studied were directly relevant to a common fibular critical gap injury in a mouse model[17] and provide a basis for longer injury gaps of rat sciatic (>10mm), and human trials thereafter. The microfibres used in this study were fabricated by electrospinning. Electrospinning is a controlled and fast fibre fabrication method, which allows the spinning of highly aligned or random oriented nano and microfibres, which have seen different applications in tissue engineering[37–39]. A range of fibre diameters (1, 5 and 8 µm) were extensively studied by Daud *et al*., where NG108–15 neuronal cells formed the longest neurites in co-culture experiments together with primary Schwann cells when grown on 5 µm fibres[18]. Additionally, PCL was chosen in respect to its bioresorbable properties and FDA approval[40] as well as its great suitability for peripheral nerve repair[18,41–43]. Besides PCL microfibres, a range of other internal NGC scaffolds have been suggested as being suitable candidates to enhance hollow nerve conduits in nerve repair (summarised by[44,45]). The comparison of different NGC scaffold candidates would be beneficial for the broad research community to identify an optimal internal guide for hollow NGCs. In this context, the developed 3D DRG model is of value in the process of identifying internal NGC scaffolds. It is of note that more than 90% of all DRG explants attached to NGCs in the developed model. In our experience, the attachment of DRGs to scaffolds is normally poor, typically around 20%. Furthermore, the proposed removal step of the microfibres from the conduit is an easy and fast method for sample imaging and is to our knowledge a new technique to image fibre scaffolds in NGCs. With this technique common confocal microscopy is still feasible without the need of time consuming sectioning processes like cryosectioning or paraffin embedding. The advantage of this technique is the maintenance of the intraluminal guide complexity where z-stack microscopy can reveal Schwann cell migration and axon sprouting through the whole depth of the internal scaffold, together with simple but accurate assessment of cell health using live/dead analysis along the full length of a scaffold to be investigated. Therefore, not only can internal fibre scaffolds of different materials and diameter be investigated but also different fibre densities inside NGCs. Scaffolds, which are too highly packed can result in cell necrosis in the scaffold core which can lead to direct failure of cell ingrowth[26–29]. In this model, such packing densities could easily be identified prior to *in vivo* implantation and might therefore also reduce the number of animals.

5. Conclusion

This study presented a novel DRG *in vitro* model that allows the testing of intraluminal fibre scaffolds inside nerve guides for the use in peripheral nerve repair. This model can be used to assess the performance of different fibre scaffold candidates in one experimental setup. Fibres of different dimensions like nano or microfibres, different diameter, materials and packing densities can be studied. The migration and proliferation of Schwann cells as well as the extensions of axons from the DRG body into the NGC serve as evaluation tools. Additionally, cell infiltration into the scaffold architecture can be studied, looking particularly on cell outgrowth length and cell viability in the scaffold core. Therefore, the current model has a major advantage of evaluating biomaterial chemistry and medical device design prototypes, and consequently may result in the refinement of leading candidate designs prior to further, more detailed, *in vivo* analysis.

Acknowledgments

We are grateful to the EPSRC (U.K.) for funding of a studentship to MB (EP/L505055/1). This work was co-funded by the Erasmus+ Programme of the European Union and the European Community's Seventh Framework Programme (FP7–NMP–2013–SME–7) for NEURIMP under grant agreement no 604450. Confocal and 2-photon microscopy was performed at the University of Sheffield (U.K.) Kroto Research Institute Confocal Imaging Facility, with thanks to Dr. Nicola Green for microscopy assistance.

Conflict of interest

The authors do not have a conflict of interest.

References

1. Rotshenker S, 2011, Wallerian degeneration: The innate-immune response to traumatic nerve injury. *J Neuroinflammation*, 8 (1): 1–14. http://doi.org/10.1186/1742–2094–8–109
2. Sunderland S, 1951, A classification of peripheral nerve injuries producing loss of function. *Brain*, 74(4): 491–516.
3. Brenner M J, Hess J R, Myckatyn T M, *et al*., 2006, Repair of motor nerve gaps with sensory nerve inhibits regeneration in rats. *Laryngoscope*, 116(9): 1685–1692. http://doi.org/10.1097/01.mlg.0000229469.31749.91
4. Hallgren A, Bjorkman A, Chemnitz A, *et al*., 2013, Subjective outcome related to donor site morbidity after sural nerve graft harvesting: A survey in 41 patients. *BMC Surg,* 13 (1): 1–7. http://doi.org/10.1186/1471-2482–13–39
5. Deumens R, Bozkurt A, Meek M F, *et al*., 2010, Repairing injured peripheral nerves: Bridging the gap. *Prog Neurobiol,* 92(3): 245-276. http://doi.org/10.1016/j.pneurobio.2010.10.002
6. Meek M F, Coert J H, 2008, US Food and Drug Administration /Conformit Europe-approved absorbable nerve conduits for clinical repair of peripheral and cranial nerves. *Ann Plast Surg*, 60(1): 110–116. http://doi.org/10.1097/SAP.0b013e31804d441c
7. Kehoe S, Zhang X F, Boyd D, 2012, FDA approved guidance conduits and wraps for peripheral nerve injury: A review of materials and efficacy. *Injury,* 43(5): 553–572. http://doi.org/10.1016/j.injury.2010.12.030
8. Ma F, Xiao Z, Meng D, *et al*., 2014, Use of natural neural scaffolds consisting of engineered vascular endothelial growth factor immobilized on ordered collagen fibers filled in a collagen tube for peripheral nerve regeneration in rats. *Int J Mol Sci,* 15(10): 18593–18609. http://doi.org/10.3390/ijms151018593
9. Koh H S, Yong T, Teo W E, *et al*., 2010, *In vivo* study of novel nanofibrous intra-luminal guidance channels to promote nerve regeneration. *J Neural Eng,* 7(4): 046003. http://doi.org/10.1088/1741–2560/7/4/046003
10. Jeffries E M, Wang Y, 2013, Incorporation of parallel electrospun fibers for improved topographical guidance in 3D nerve guides. *Biofabrication,* 5(3): 035015. http://doi.org/10.1088/1758–5082/5/3/035015
11. Ngo T T, Waggoner P J, Romero A A, *et al*., 2003, Poly(L-lactide) microfilaments enhance peripheral nerve regeneration across extended nerve lesions. *J Neurosci Res*, 72(2): 227–238. http://doi.org/10.1002/ jnr.10570
12. Faroni A, Mobasseri S A, Kingham P J, *et al*., 2015, Peripheral nerve regeneration: Experimental strategies and future perspectives. *Adv Drug Deliv Rev*, 82–83: 160–167. http://doi.org/10.1016/j.addr.2014.11.010
13. Griffin M F, Malahias M, Hindocha S, *et al*., 2014, Peripheral nerve injury: Principles for repair and regeneration. *Open Orthop J*, 8: 199–203. http://doi.org/10.2174/1874325001408010199
14. Toba T, Nakamura T, Shimizu Y, *et al*., 2001, Regeneration of canine peroneal nerve with the use of a polyglycolic acid-collagen tube filled with laminin-soaked collagen sponge: A comparative study of collagen sponge and collagen fibers as filling materials for nerve conduits. *J Biomed Mater Res*, 58(6): 622–630.

15. Wang X, Hu W, Cao Y, *et al*., 2005, Dog sciatic nerve regeneration across a 30-mm defect bridged by a chitosan/PGA artificial nerve graft. *Brain*, 128(Pt 8): 1897–1910. http://doi.org/10.1093/brain/awh517
16. Daly W T, Yao L, Abu-rub M T, *et al*., 2012, The effect of intraluminal contact mediated guidance signals on axonal mismatch during peripheral nerve repair. *Biomaterials*, 33(28):6660–6671.http://doi.org/10.1016/j.biomaterials.2012.06.002
17. Pateman C J, Harding A J, Glen A, *et al*., 2015, Nerve guides manufactured from photocurable polymers to aid peripheral nerve repair. *Biomaterials*, 49: 77–89. http://doi.org/10.1016/j.biomaterials.2015.01.055
18. Daud M F, Pawar K C, Claeyssens F, *et al*., 2012, An aligned 3D neuronal-glial co-culture model for peripheral nerve studies. *Biomaterials*, 33(25): 5901–5913. http://doi.org/10.1016/j.biomaterials.2012.05.008
19. Edelman D B, Keefer E W, 2005, A cultural renaissance: *In vitro* cell biology embraces three-dimensional context. *Exp Neurol*, 192(1): 1. http://doi.org/10.1016/j.expneurol.2004.10.005
20. Pampaloni F, Reynaud E G, Stelzer E H, 2007, The third dimension bridges the gap between cell culture and live tissue. *Nat Rev Mol Cell Biol*, 8(10): 839–845. http://doi.org/ 10.1038/nrm2236
21. Ravi M, Paramesh V, Kaviya S R, *et al*., 2015, 3D cell culture systems: Advantages and applications. *J Cell Physiol*, 230(1): 16–26. http://doi.org/10.1002/jcp.24683
22. Mazzoleni G, Di Lorenzo D, Steimberg N, 2009, Modelling tissues in 3D: The next future of pharmaco-toxicology and food research?. *Genes Nutr,* 4(1): 13–22. http://doi.org/10.1007/s12263–008–0107–0
23. Kaplan H M, Mishra P, Kohn J, 2015, The overwhelming use of rat models in nerve regeneration research may compromise designs of nerve guidance conduits for humans. *J Mater Sci Mater Med*, 26(8): 226. http://doi.org/10.1007/s10856–015–5558–4
24. Teixeira F G, Vasconcelos N L, Gomes E D, *et al*., 2016, Bioengineered cell culture systems of central nervous system injury and disease. *Drug Discov Today*, 21(9): 1456–1463. http://doi.org/10.1016/j.drudis.2016.04.020
25. Bosi S, Rauti R, Laishram J, *et al*., 2015, From 2D to 3D: Novel nanostructured scaffolds to investigate signalling in reconstructed neuronal networks. *Sci Rep*, 5: 9562. http://doi.org/10.1038/srep09562
26. Dunn J C, Chan W Y, Cristini V, *et al*., 2006, Analysis of cell growth in three-dimensional scaffolds. *Tissue Eng*, 12(4): 705–716. http://doi.org/10.1089/ten.2006.12.705
27. Sodian R, Hoerstrup S P, Sperling J S, *et al*., 2000, Tissue engineering of heart valves: *In vitro* experiences. *Ann Thorac Surg,* 70(1): 140–4.
28. Burg K J, Holder W D, Jr., Culberson C R, *et al*., 2000, Comparative study of seeding methods for three-dimensional polymeric scaffolds. *J Biomed Mater Res*, 52(3): 576.
29. Yang T H, Miyoshi H, Ohshima N, 2001, Novel cell immobilization method utilizing centrifugal force to achieve high-density hepatocyte culture in porous scaffold. *J Biomed Mater Res*, 55(3): 379–86.
30. Krames E S, 2015, The dorsal root ganglion in chronic pain and as a target for neuromodulation: A review. *Neuromodulation*, 18(1): 24–32. http://doi.org/10.1111/ner.12247
31. Gaudet A D, Popovich P G, Ramer M S, 2011, Wallerian degeneration: Gaining perspective on inflammatory events after peripheral nerve injury. *J Neuroinflammation*, 8: 110. 10.1186/1742–2094–8–110. http://doi.org/10.1186/1742-2094-8-110
32. Bozkurt A, Brook G A, Moellers S, *et al*., 2007, *In vitro* assessment of axonal growth using dorsal root ganglia explants in a novel three-dimensional collagen matrix. *Tissue Eng*, 13(12): 297–299. http://doi.org/10.1089/ten.2007.0116
33. Rangappa N, Romero A, Nelson K D, *et al*., 2000, Laminin-coated poly (L-lactide) filaments induce robust neurite growth while providing directional orientation. *J Biomed Mater Res*, 51(4): 625–634.
34. Huval R M, Miller O H, Curley J L, *et al*., 2015, Microengineered peripheral nerve-on-a-chip for preclinical physiological testing. *Lab Chip*, 15(10): 22–32. http://doi.org/10.1039/c4lc01513d
35. Graham M Land Prescott M J, 2015, The multifactorial role of the 3Rs in shifting the harm-benefit analysis in animal models of disease. *Eur J Pharmacol,* 759: 19–29. http://doi.org/10.1016/j.ejphar.2015.03.040
36. Cho D W, Kang H W, 2012, Microstereolithographybased computer-aided manufacturing for tissue engineering. Methods *Mol Biol,* 868: 341–356. http://doi.org/10.1007/978–1–61779–764–4_21
37. Kim Y T, Haftel V K, Kumar S, *et al*., 2008, The role of aligned polymer fiber-based constructs in the bridging of long peripheral nerve gaps. *Biomaterials,* 29(21): 31–27. http://doi.org/10.1016/j.biomaterials.2008.03.042
38. Kwak S, Haider A, Gupta K C, *et al*., 2016, Micro/Nano multilayered scaffolds of PLGA and collagen by alternately electrospinning for bone tissue engineering. *Nanoscale Res Lett,* 11(1): 323. http://doi.org/10.1186/s11671–016–1532–4
39. Tan Z, Wang H, Gao X, *et al*., 2016, Composite vascular grafts with high cell infiltration by co-electrospinning.

Mater Sci Eng C Mater Biol Appl, 67: 369–377. http://doi.org/10.1016/j.msec.2016.05.067

40. Woodruff M A, Hutmacher D W, 2010, The return of a forgotten polymer-Polycaprolactone in the 21st century. *Prog Polym SCI*, 35(10): 1217–1256. http://doi.org/10.1016/j.progpolymsci.2010.04.002
41. Nectow A R, Marra K G, Kaplan D L, 2012, Biomaterials for the development of peripheral nerve guidance conduits. *Tissue Eng Part B Rev,* 18(1): 40–50. http://doi.org/10.1089/ten.TEB.2011.0240
42. Hopkins T M, Little K J, Vennemeyer J J, *et al*., 2017, Short and long gap peripheral nerve repair with magnesium metal filaments. *J Biomed Mater Res A,* 105(11): 3148–3158. http://doi.org/10.1002/jbm.a.36176
43. Shahriari D, Shibayama M, Lynam D, *et al*., 2017, Peripheral nerve growth within a hydrogel microchannel scaffold supported by a kink-resistant conduit. *J Biomed Mater Res A*, 105(12): 3392–3399. http://doi.org/10.1002/jbm.a.36186
44. Jiang X, Lim S H, Mao H Q, *et al*., 2010, Current applications and future perspectives of artificial nerve conduits. *Experimental Neurology*, 223(1): 86–101. http://doi.org/10.1016/j.expneurol.2009.09.009
45. Daly W, Yao L, Zeugolis D, *et al.*, 2012, A biomaterials approach to peripheral nerve regeneration: Bridging the peripheral nerve gap and enhancing functional recovery. *J R Soc Interface*, 9(67): 202–221. http://doi.org/10.1098/rsif.2011.0438

RESEARCH ARTICLE

Formation of cell spheroids using Standing Surface Acoustic Wave (SSAW)

Yannapol Sriphutkiat, Surasak Kasetsirikul, Yufeng Zhou*

Singapore Centre for 3D Printing (SC3DP), School of Mechanical and Aerospace Engineering, Nanyang Technological University, Singapore

Abstract: 3D bioprinting becomes one of the popular approaches in the tissue engineering. In this emerging application, bioink is crucial for fabrication and functionality of constructed tissue. The use of cell spheroids as bioink can enhance the cell-cell interaction and subsequently the growth and differentiation of cells in the 3D printed construct with the minimum amount of other biomaterials. However, the conventional methods of preparing the cell spheroids have several limitations, such as long culture time, low-throughput, and medium modification. In this study, the formation of cell spheroids by SSAW was evaluated both numerically and experimentally in order to overcome the aforementioned limitations. The effects of excitation frequencies on the cell accumulation time, diameter of the formed cell spheroids, and subsequently, the growth and viability of cell spheroids in the culture medium over time were studied. Using the high-frequency (23.8 MHz) excitation, cell accumulation time to the pressure nodes could be reduced in comparison to that of the low-frequency (10.4 MHz) excitation, but in a smaller spheroid size. SSAW excitation at both frequencies does not affect the cell viability up to 7 days, > 90% with no statistical difference compared with the control group. In summary, SSAW can effectively prepare the cell spheroids as bioink for the future 3D bioprinting and various biotechnology applications (*e.g.*, pharmaceutical drug screening and tissue engineering).

Keywords: standing surface acoustic wave (SSAW); cell spheroid; cell viability; bioink; interdigital transducer (IDT)

*Correspondence to: Yufeng Zhou, Singapore Centre for 3D Printing (SC3DP), School of Mechanical and Aerospace Engineering, Nanyang Technological University, 50 Nanyang Ave, 639798, Singapore; Email: yfzhou@ntu.edu.sg

Received: November 28, 2017; **Accepted:** December 14, 2017; **Published Online:** January 17, 2017

Citation: Sriphutkiat Y, Kasetsirikul S, Zhou Y F, 2018, Formation of cell spheroids using Standing Surface Acoustic Wave (SSAW). *Int J Bioprint*, 4(1): 130. http://dx.doi.org/10.18063/IJB.v4i1.130

1. Introduction

3D bioprinting has attracted great attention in the field tissue engineering and regenerative medicine; different types of cells and extracellular matrix (ECM) proteins can be deposited simultaneously to form complex tissue-engineered constructs for skin[1,2] perfusable blood vessels[3], cartilage[4], bone[5], neuronal[6] and cardiac tissue[7]. 3D bioprinting has a capability to fabricate complicated structures in high accuracy and reproducibility in the aspect of the shape, size, internal porosity, and interconnectivity[8-10]. One of the essential components of 3D bioprinting is the use of bioink which consists of multiple types of cells and various biomaterials. The requirements for appropriate and excellent bioink include printability, biocompatibility, and bioactivity[11]. Cells suspension in the gelatin is usually used as the bioink. However, the cells in the monolayer condition were found to grow slowly and loss functionality after culture for a long time[12-15]. In contrast, cell viability and differentiated functions in a cell spheroid, accumulation of hundreds of cells in the shape of a sphere, could be maintained for prolonged periods of time. Retention in 3D structure, establishment of cell-cell contacts, and presence of extracellular matrix (ECM) are important reasons for spheroidal aggregation[16-18]. Currently, cell spheroids are used extensively in the study of tissue anatomy, drug screening[19,20], toxicology[21], and cell proliferation and

differentiation[22,23] because they represent more similar *in vivo* biological behaviors. Therefore, cell spheroids could be an alternative format of the bioink. More importantly, such novel bioink enhances cell-cell interaction, growth, differentiation, and resistance to the environment because of the high cell density in the construct. As a result, the printed vascular construct shows a better cell-cell interaction and differentiation[24,25]. Additionally, tissue construct printed using the cell spheroids could minimize the inclusion of biomaterials[26], enhance the growth in the natural condition, and reduce the potential biodegradation which may release the toxic or unnatural byproducts[25].

The current methods of forming cell spheroids, such as using the U-bottom plate, cell hanging drop[27], dielectrophoresis[28] and magnetic-assisted assembly[29], require additional chemicals to modify the cell culture medium or the use of a complex device or complicated fabrication process, but in low throughput. Although rotating cell culture[30], using non-adhesive surface[31], and cell culturing in scaffold[32] can improve the throughput, they are still time-consuming and tedious with inconsistent production of cell spheroids in size. Microvalve-based printer is another high-throughput method to form cell spheroids, but low cell viability and inhomogeneity were found[33,34]. In comparison, microparticle manipulation by the acoustic wave has been utilized in the field of lab-on-a-chip because of its advantages of non-invasiveness, low power consumption, free labeling, biocompatibility, and high throughput. Standing wave generated from the bulk acoustic wave (BAW) could trap the individual cells loaded into a certain device to the pressure nodes and then form cell spheroids[35]. However, excitation frequency for BAW is quite low (mostly below 4 MHz), resulting in weak acoustic radiation force, low throughput, and domination of acoustic streaming and temperature instability at the high power. In the recent year, surface acoustic wave (SAW) was introduced in the microparticle manipulation[36]. In comparison to BAW, SAW has the advantages of high excitation frequency, high throughput, low power consumption, less excessive heat and disturbance of acoustic streaming, simple manufacture of device in arbitrary design, and large range of operating parameters. However, the effect of excitation frequency on the formation of cell spheroids by standing surface acoustic wave (SSAW) and their biological characteristics has not been explored. As the distance between pressure nodes in the standing acoustic field is half of the wavelength, which is inversely proportional to the excitation frequency, and the acoustic radiation force applied to the microparticles is proportional to the frequency, the preparation time and size of cell spheroids is highly dependent on the excitation frequency. In addition, acoustic exposure at high intensity may produce significant biological effects, such as damages to the cell membrane[37], apoptosis, and necrosis for the reduced cell viability. Furthermore, the fluid medium may also be heated up by the acoustic exposure due to the energy absorption, especially in a small cavity at high power output and high acoustic frequency, which may harm biological cells[38,39].

In this study, the effects of excitation frequency on the formation of cell spheroids (accumulation time and size) and their biological characteristics (growth and cell viability) in the culturing afterward were studied. The motion of cells by SSAW for the formation of cell spheroids was simulated and then compared with the experimental results. It is hypothesized that the high-frequency excitation could reduce the accumulation time, but size of cell spheroids as well. The potential damage of acoustic exposure to the formed cell spheroids was evaluated up to 7 days after the production. Our study may be able to provide the guideline for the preparation of cell spheroids by SSAW as bioink for the future biotechnical applications.

2. Materials and Methods

2.1 Governing Equation

In the fluid, the motion of cells in the acoustic field depends on the resultant forces from acoustophoresis and Stroke drag. The Stokes drag force applied to the cells is due to the velocity differences between fluid and cells[40].

$$F_D = 6\pi\mu r\,(v_f - v_p) \tag{1}$$

where r is the radius of cell in the shape of a sphere, v_f and v_p are the velocities of fluid and cells, respectively, μ is the dynamic viscosity. As cells have different physical properties from fluid media, the propagation of an acoustic wave causes the cells to oscillate and pulsate, which leads to monopole and dipole scattering expressed in the resultant acoustic radiation force[41].

$$\mathrm{F_r} = \frac{4}{3}\pi \mathrm{r^3}\,\nabla\left[\mathrm{f_{mono}}\frac{1}{2}\mathrm{k_0 p_{prop}^2} - \mathrm{f_{dip}}\frac{3}{4}\rho_0 \mathrm{v_{prop}^2}\right]$$

$$\mathrm{f_{mono}} = 1 - \frac{\mathrm{k_p}}{\mathrm{k_f}},\quad \mathrm{f_{dip}} = \frac{\rho_\mathrm{p} - \rho_\mathrm{f}}{\rho_\mathrm{p} + \rho_{\mathrm{f}/2}} \tag{2}$$

where ρ_p and ρ_f are the density of cell and fluid, k_p and k_f are the compressibility of particle and fluid, f_{mono} and f_{dip} are the dimensionless scattering coefficients for the monopole and dipole, respectively, and k_0 is the acoustic wave number. In the acoustic standing wave field, the acoustic radiation force acting on the cell is simplified as

$$\mathrm{F_r} = -\left(\frac{\pi \mathrm{r^3}\beta_\mathrm{f}}{3}\right)\mathrm{p_0^2 k}\phi \sin\left(2\mathrm{k_0 y}\right) \tag{3}$$

where p_0 is an acoustic pressure, ϕ is an acoustic contrast factor given by

$$\phi = f_{mono} + \frac{3}{2} f_{dip} = \frac{5\rho_p - 2\rho_f}{2\rho_p + \rho_f} - \frac{\beta_p}{\beta_f} \quad (4)$$

The transverse motion of cells across the channel width under the action of the acoustic radiation force is governed by Newton's second law. As the cells are much smaller than the dimension of the microchannel, their longitudinal motion is assumed to follow the fluid streamlines. Particle motion was simulated by solving the ordinary differential equation (ODE) above using the fourth order Runge-Kutta method in Matlab (MathWorks, Natick, MA, USA). Material properties used in the simulation are listed in Table 1, and the schematic diagram is same as that in our previous study[42].

Table 1. Material properties used in simulation at the temperature of 27 ℃

Water	density, ρ_w	997 kg/m^3
	speed of sound, c_w	1497 m/s
	viscosity, μ_w	0.890 mPa.s
	compressibility, κ_w	448 TPa^{-1}
Biological cells	density, ρ_p	1075 kg/m^3
	speed of sound, c_p	1600 m/s
	compressibility, κ_p	428 TPa^{-1}
Poly-dimethylsiloxane (PDMS, 10:1)	density,ρ_{PDMS}	920 kg/m^3
	speed of sound, c_{PDMS}	1076.5 m/s
Lithium niobate ($LiNbO_3$)	density,ρ_{LNB}	4650 kg/m^3
	speed of sound, c_{LNB}	3997 m/s

2.2 Device Fabrication

Two pairs of identical interdigital transducers (IDTs) aligned perpendicular to each other were fabricated by positive photoresist lift-off process. The process started with hexamethyldisilazane (HMDS) treatment followed by coating the photoresist (AZ9260, MicroChemicals GmbH, Germany) in the thickness of about 5-µm on the surface of the $LiNbO_3$ wafer in the thickness of 500-µm (Y-128° propagating, University Wafer, Boston, MA, USA). The $LiNbO_3$ wafer was cured with UV to weaken the photoresist which was further developed with AZ-developer (400K, MicroChemicals GmbH, Germany). After that, the wafer was sputtered with a layer of 20 nm-Cr and 400 nm-Au, and the photoresist was removed by acetone (Aik Moh, Singapore). There are 20 strips in the width of 150 µm in each IDT with an aperture size of 2 cm.

The poly-dimethylsiloxane (PDMS) microfluidic cavity was fabricated using the soft-lithography and mould-replica techniques. PDMS (Sylgard 184, Dow Corning, Midland, MI, USA) was fixed with elastomer base in a ratio of 10:1 and then poured on the mould in the length of 3 mm, the width of 3 mm, and the height of 100 µm. The PDMS cavity was degassed in a vacuum chamber (3608-1CE, ThermoFisher Scientific, Waltham, MA, USA) at 60 °C for 4 h. Then the PDMS cavity was bonded directly on $LiNbO_3$ by oxygen plasma (Harrick Plasma, Ithaca, NY, USA) treatment and then rest at 60 °C in the vacuum chamber for 10 min.

2.3 Experimental Setup

The PDMS cavity was punched with two holes for inlet and outlet. Prior to loading cells, the PDMS cavity was filled with 2% bovine serum albumin (BSA, Thermo Fisher Scientific) for 15 min to coat the cavity surface in order to reduce the cell adhesion. Many pressure nodes in the shape of grid with the size of half wavelength, which is determined by the excitation frequency of SAW and speed of sound propagating in the $LiNbO_3$ wafer, are generated inside the PDMS cavity after SAW excitation. The cells suspension was filled into a 3 mL syringe that was driven by a syringe pump (NE-1000, New era pump systems, Farmingdale, NY, USA) to the PDMS cavity through the inlet. The accumulation of cells and formation of cell spheroids in the cavity was observed under an optical microscope (CKX-41, Olympus, Tokyo, Japan) at 40× magnification and captured by a digital camera (QIC-F-CLR-12-C, QImaging, Surrey, BC, Canada), and the size of formed cell spheroid was quantitatively determined using digital image software (ImageJ, National Institute of Health, Bethesda, MD, USA). A sinusoidal signal of at the frequency of 10.4 or 23.8 MHz was generated (AFG3000, Tektronix, Beaverton, OR, USA), amplified (25A250A, Amplifier Research, Souderton, PA, USA) and supplied to these two pairs of IDTs at an output power of 0.7 Watt for the acoustic excitation. During the excitation of SSAW for about 30 min, the device (PDMS cavity on the $LiNbO_3$ wafer) was placed on a lab-made cooling plate to reduce the generated excessive heat. The cooling plate consists of a Peltier plate (thermoelectric cooler in the size of 4×4 cm, Robot R Us, Singapore), heat sink, and 5V DC brushless fan (Robot R Us). After the formation, the cell spheroids were transferred out from the PDMS cavity by pumping 1×phosphate-buffered saline (PBS) solution through the inlet at a flow rate of 2 µL/min. Then the collected cell spheroids from the outlet were observed under the same optical microscope.

2.4 Cell Preparation

HepG2 cells, immortalized human liver carcinoma cell line (HB-8065™, ATCC®, Manassas, VA, USA), were cultured in HyClone™ Dulbecco's modified eagle's medium (DMEM, GE Healthcare Life Sciences, HyClone Laboratories,

Logan, UT, USA) containing 10% fetal bovine serum (FBS, Gibco, Waltham, MA, USA) and 1% antibiotic-antimycotic solution, including 10,000 units/mL of penicillin, 10,000 µg/mL of streptomycin, and 25 µg/mL of amphotericin B (Gibco), in a cell culture flask (t75, ThermoFisher Scientific). The cells were incubated at 37 °C in a humidified incubator (Heracell 150i, ThermoFisher Scientific) under the condition of 5% CO_2. The culture medium was changed every two or three days depending on the initial seeding. Achieving 80% confluence, the cell was dissociated using 0.25% Trypsin 1 mM EDTA.4Na (Lonza, Basel, Switzerland), centrifuged at 1,000 RPM (SL 8 small benchtop centrifuge, ThermoFisher Scientific) for 5 min at room temperature, and subsequently re-suspended in the culture medium in a concentration of 2×10^6 cells/mL and a volume of about 400 µL. Cell density was estimated using hemocytometer (Hausser scientific hemocytometer, ThermoFisher Scientific). Live/dead cell viability assays (L3224, L/D kit for mammalian cells, ThermoFisher Scientific) consisting of calcein-AM and ethidium homodimer-1 were used to stain the cells. The samples in 5 random areas were captured by the optical microscope and processed with ImageJ using the established protocols[43,44] to count the live and dead cells stained in green and red, respectively. The cell spheroids were then cultured in ultralow attachable culture dish (#3262 Corning®, Thermo Fisher Scientific) to minimize the cell attachment. The spheroid size and cell viability were measured daily for 7 days[36,45].

3. Results and Discussion

3.1 Numerical Simulation of Cell Motion by SSAW

Using a network analyzer (HP8510B, Agilent Technologies, Santa Clara, CA, USA), the S_{12} frequency response of IDTs (transmission coefficient) shows several peaks[42]. Trajectories of biological cells excited by low-frequency (10.4 MHz) and high-frequency (23.8 MHz) were simulated and compared. It is assumed that all individual cells were distributed uniformly across the PDMS cavity and do not gather before reaching the pressure node. In this simulation, the motion of cells and the time required to reach the equilibrium state are highly dependent on the equivalent force applied to them and their initial location. It is found that the trajectory motion of cells in the SSAW field can be fitted by an exponential rise curve and the rising rate is dependent on the initial distance to the pressure node and acoustic operating parameters, such as the excitation frequency and power (see Figure 2). The correlationbetween acoustics parameters (*e.g.*, excitation frequency, power output) and cell motion by SSAW was listed in Table 2. Firstly, the cell motion across the cavity by either low- and high-frequency SSAW at different initial positions is shown in Figures 2A and B. It is clear that using the high-frequency excitation could accumulate the cells much more quickly. The effects of output power and cell diameter on the trajectory motion of cell were also investigated if the distance between the initial position and pressure node is fixed as 42 µm which is one-quarter of wavelength or the distance from anti-pressure node to adjacent pressure node at the high-frequency excitation. Referring to Eq.2, acoustic radiation force is proportional to the volume of the cell (or cube of cell diameter in the shape of a sphere) and the power (or square of acoustic pressure). Large cells reach the pressure node in a short time because of large acoustic radiation force applied to them (see Figure 2C). At the high-frequency excitation, the cells in a diameter of 8 µm, 10 µm, and 15 µm at the acoustic excitation power of 1.0 W reach the pressure node after 6.26 s, 4.01 s, and 1.78 s, respectively. In comparison, the corresponding values at the low-frequency excitation are 13.58 s, 8.70 s, and 3.87 s, respectively, almost twice as those at the high frequency. In addition, the motion time required to reach the pressure node also decreases with the output power (see Figure 2D).

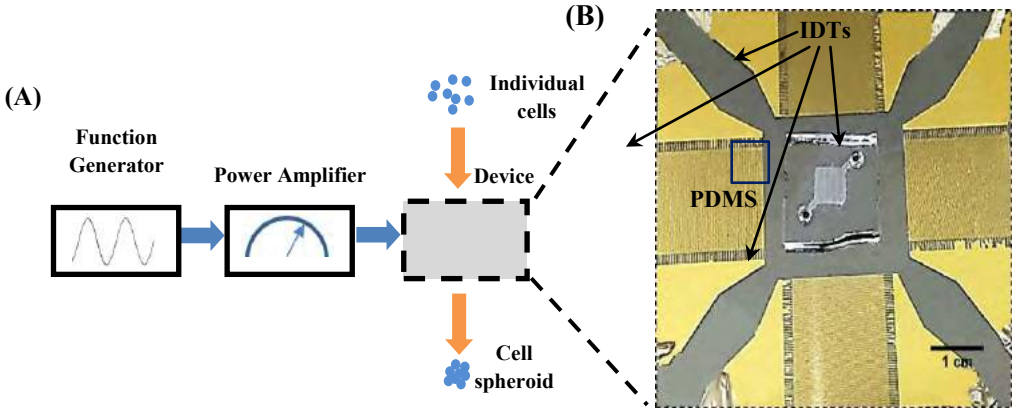

Figure 1. (**A**) Schematic diagram of experimental setup of forming cell spheroids by SSAW and (**B**) zoomed photo showing two pairs of interdigital transducers (IDTs) and PDMS cavity.

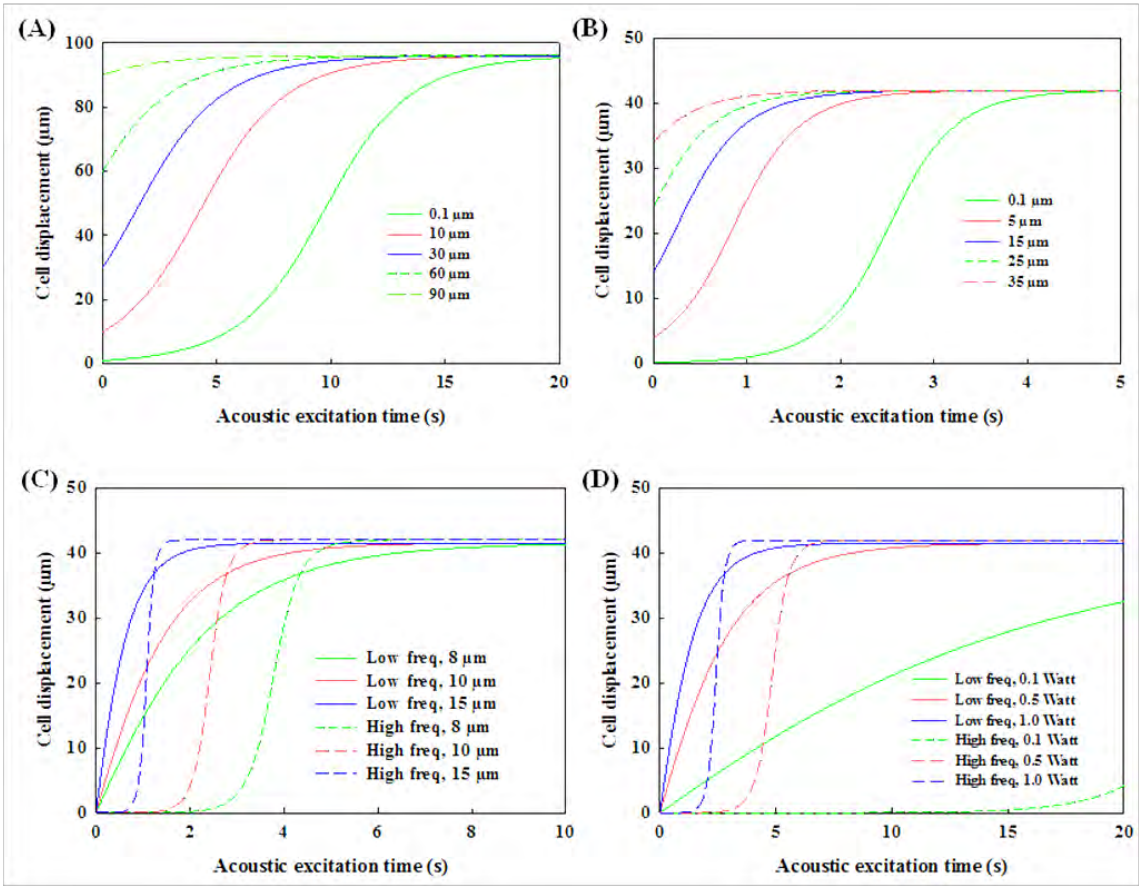

Figure 2. Numerical simulation of **(A)** 10 μm-cell trajectory excited by low- (10.4 MHz) and **(B)** high- (23.8 MHz) frequency standing surface acoustic wave across the cavity at the power of 0.5 W from different initial positions to the pressure nodes, and **(C)** the effect of thediameter of cell (8 μm, 10 μm, and 15 μm) at the excitation power of 1.0 W and **(D)** the effect of excitation power (0.1 W, 0.5 W, and 1.0 W) on motion of 10-μm diameter cellat thelow and high frequency with the same initial distance to the corresponding pressure node of 42 μm.

Table 2. Correlation between acoustic parameters and cell motion by SSAW

Parameters	Distance between pressure nodes	Cell motion velocity	Time to reach pressure node	Size of cell spheroid
Excitation frequency	Decrease	Increase	Decrease	Decrease
Power output	Constant	Increase	Decrease	Constant
Cell diameter	Constant	Increase	Decrease	Increase

At the high frequency, cells in the diameter of 10 μm reach the pressure node at 37.79 s, 8.00 s, and 4.01 s at the output power of 0.1W, 0.5W, and 1.0W, respectively. In comparison, the corresponding values at the low-frequency excitation are 89.27s, 17.37s, and 8.70s, respectively. The enhancement of high-frequency excitation for cells in different sizes at varied output power is similar, ~2.2 fold, which is slightly lower than the ratio of excitation frequency (2.4 fold).

The trajectory motion of microparticles, either solid microspheres or cells, by the SSAW is able to be calculated and validated[46,47]. The high output power and large size of microparticles have already been found to enhance the motion velocity of microparticles[42,48]. In comparison to the solid microparticles in the similar size, cells usually have lower compressibility and density so that their motion speed is slower[49,50]. In order to reduce the time of reaching the pressure node higher output power is required, which leads to high temperature elevation of the substrate during the IDTs excitation. Another potential side effect of acoustic manipulation of cells is due to the mechanical impact. However, previous studies show that acoustic excitation at the power of about 0.87 W does not decrease the cell viability significantly, but occasionally could even enhance the cell activities[38,51]. Moreover, the initial location is one of the important factors for the cell accumulation time. The distribution of an acoustic radiation force from the standing waves is not uniform across the microchannel width[52], pointing from the anti-pressure node toward the pressure node. Both pressure nodes and anti-pressure node locations have the lowest magnitude of acoustic radiation force in the standing wave field. Thus, cells located nearby the anti-

pressure node have the low initial acceleration, especially at the high-frequency excitation and low output power in comparison to that at the low-frequency excitation and the same output power input (see 0.1 W in Figure 2D).

It is noted that if the height of PDMS cavity is larger than the half wavelength of SSAW excitation multiple pressure nodes will be generated in the vertical direction. The magnitude and distribution of these pressure nodes in the central region of the cavity are quite uniform, but not at the edge[53]. Those cells accumulated at the middle region of pressure nodes are in the suspension and may have low possibility of attachment to the cavity. However, higher PDMS cavity may not allow the accurate measurement of the size of cell spheroids aligned vertically, but increase the production, which will be evaluated later.

3.2 Formation of Cell Spheroids by SSAW

Cell spheroids were gathered and formed from suspended individual cells under acoustic excitation, usually within 30 sec. The diameter of spheroids relies on the number of cells in the adjacent region of pressure nodes. The distance between pressure nodes in the PDMS cavity, which is the half wavelength and inverse proportional to the excitation frequency, is one of the important factors for the size of produced cell spheroids. In this experiment, both low- and high-frequency excitations could accumulate cells at the pressure nodes successfully (see Figure 3). However, the size of cell spheroids and number of accumulated cells at each pressure nodes are not exactly same. The main reason may be non-uniform cell distribution in the PDMS cavity[54] with low Reynold number, <20 (see Figure 3C). Accumulation of cells and subsequently, the formation of cell spheroids is a quite complicated phenomenon involving several factors, such as cell aggregation[55], lateral shear force[56], and culture medium (*e.g.*, nutrients[57], growth factor[58], and waste[57]). Initial average size of cell spheroids generated by the low-frequency excitation is slightly larger than the reported value in the previous study[36] at the same cell density (2×10^6 cells/mL), 32.8 ± 4.3 μm *vs.* 18.8 ± 3.0 μm. Low-frequency could gather more cells from a wide region due to its large wavelength for the generation of larger cell spheroids. Overall, it is a tradeoff between the size and accumulation speed of cell spheroids. New strategies or techniques are desired to produce large uniform cell spheroids in a short time. It is noted that low power output (*e.g.*, 0.1 W) was applied after the cell spheroid formation for 30–90 min in order to allow sufficient ECM being secreted to hold them in place and avoid the sedimentation. No mergence of cell spheroids was found inside the PDMS cavity at the cell density used in this study. Afterwards, the spheroids are stable enough for handling and transferring.

During the excitation, most cells initially move toward and gather with the others at the nearby pressure nodes. However, it is found that some cells locate slightly away from the pressure nodes, which may be due to attachment of cells on the surface of PDMS cavity or $LiNbO_3$ wafer and curved wave front of SSAW inside the cavity. Cells attachment on the surface of microchannel is a common issue due to complicated surface properties[59,60]. Briefly, the attractive forces from the surface are stronger than the combination of electrostatic repulsion force and acoustic streaming forces applied to the cell[61]. Subsequently, cells could not move and follow the acoustic radiation force. When the waves travel through PDMS and fluid medium at a long distance, acoustic attenuates particularly at the high frequency is not spatially uniform because of the heterogeneous properties distribution of each medium. The diffraction waves generated from the flat IDTs lead to the slightly curved wave front, but the flat grid in the numerical simulation. In addition, cell density may also determine the magnitude of force required to tightly pack cells into spheroid. In the recent study, during of cells High cell density results in the formation of large cell were found located away from the pressure node at high cells density[36]. Furthermore, cell density is an important issue. spheroids, but also high possibility of cell attachment and

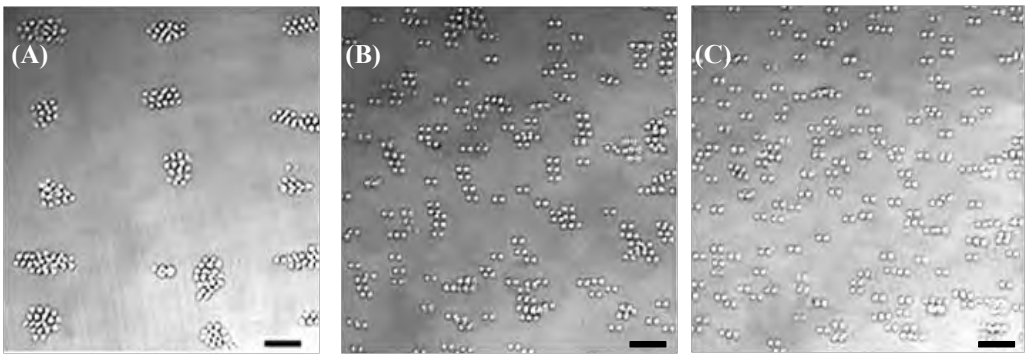

Figure 3. Accumulation of HepG2 cells by SSAW at the frequency of **(A)** 10.4 MHz, **(B)** 23.8 MHz, and **(C)** distribution of suspended cells without excitation, scale bar of 50 μm.

cell spheroid may also be possible using SSAW at the excitation frequency of 7.4 MHz at the cell density of clogging at the outlet of cavity when collecting them. Some cell spheroids generated are about 200 µm. Such a large 30×10^6 cells/mL.

3.3 Growth of Cell Spheroids

After the acoustic excitation, cell spheroids were collected and cultured in the incubator for up to 7 days to monitor their growth. All formed cell spheroids grow quite well (see Figure 4). After 7 days of culture, the cell spheroids prepared by the low-frequency excitation increase from 32.8±4.3 µm to 58.7±9.2 µm (1.79 fold) while those prepared by the high-frequency excitation increase from 18.8±3.0 µm to 38.5±7.9 µm (2.05 fold) as shown in Figure 4A. In addition, the collected cell spheroids in the petri dish were not found to merge with each other during the 7-day culturing.

Overall, growth trends of cell spheroids generated by both low-frequency and high-frequencyexcitations are similar. The slope of growth seems slightly steeper after 5 days of cell culture. The cell spheroids generated by the high-frequency excitation have a slightly faster growth rate (2.05 fold in 7 days) than that by the low-frequency excitation (1.79 fold in 7 days). For large cell spheroids, the cells at the center may be less exposed to the nutrient and oxygen from the culture medium[62–64], which may slow down cell growth and lead to necrotic death[65]. After being transferred out of the PDMS cavity and collected in a culture dish, the fresh cell spheroids have clear outlines of individual cells. After 4 h, the cells in the formed spheroids start to merge with the adjacent cells. Within a day, the cell outlines in the spheroid become blurred, showing the significant cell mergence. On day 3, all cells inside the spheroid merge almost completely with the disappearance of cell outlines, especially those at the center. After that, there are no more significant changes in the morphology of the formed cell spheroids.

3.4 Cell Vability

Cell viability of HepG2 was measured on day 1, 3, 5, and 7 to investigate the influence of acoustic excitation on the formed cell spheroids. The cells undergone SSAW excitation showed a clear accumulation with adjacent cells comparing with those wihtout acosutic excitation, but without significant difference on the cell viabilities (see red fluorescent intensity in Figure 5). On day 0, the cell outlines in the cell spheroids were still clear. After 7 days of cell culture, cell spheroids became more compact and round with cell viability of 94% (see Figure 5C). Although the cell viability decreased slightly over such a period, there are always no significant differences between the cells in

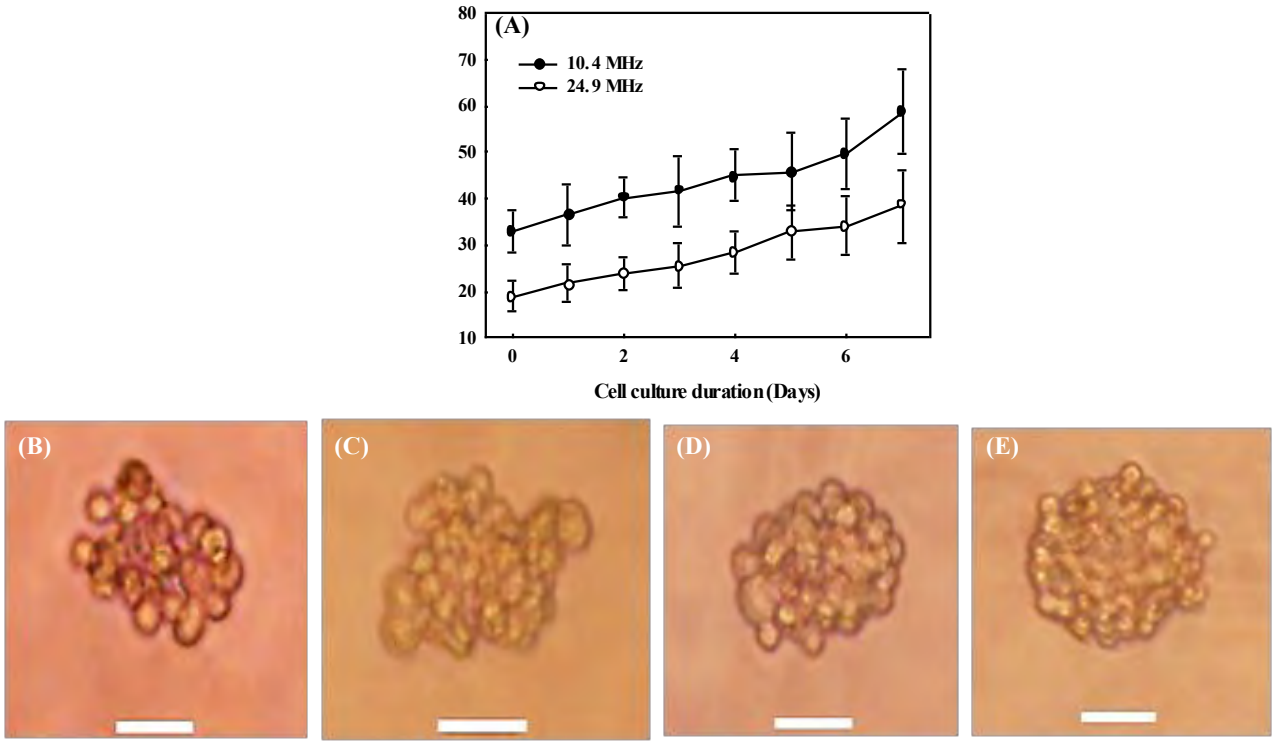

Figure 4. Progressive growth of the cell spheroids after the formation by SSAW **(A)** at 10.4 MHz (solid circle) and 23.8 MHz (hollow circle) over seven days of culture, and representative photo of cell spheroid of 10.4 MHz at **(B)** hour 0 (immediately after the formation), **(C)** hour 4, on **(D)** day 1, and **(E)** day 3 with a scale bar of 20 µm.

acoustically formed cell spheroids and suspended HepG2 the control group (p = 0.492, 0.849, 0.566, and 0.492 on day 1, 3, 5, 7, respectively, all p> 0.05, see Figure 5D). Both experimental and control group had high cell viability over 90% which represents healthy cell condition and suggests the safety of our approach. It is found that the cell viability by the high-frequency excitation was slightly lower than that by the low-frequency excitation despite without statistical difference (p< 0.05), which may be due to greater acoustic radiation force applied to the cells. The slight decrease of cell viability over time is due to the cell spheroids being cultured in non-attachable environment. If transferred to a scaffold, cell spheroids will be able to grow into a stable construct.

There are two major contributions to the death of cell spheroids formed after acoustic manipulation: temperature and magnitude of acoustic radiation force applied to the cells during the acoustic excitation for approximately 30 min continuously. As the cell viability is highly sensitive to the environment temperature, a lab-built cooling plate was placed underneath the $LiNbO_3$ substrate to release the excessive heat and control the temperature in order to reduce the thermal effects on the viability of the formed cell spheroids. The temperature of PDMS cavity was measured to be around 26 °C by an infrared thermometer (MAX IR Thermometer, Fluke, Everett, WA USA). Nevertheless, the acoustic radiation force at the pressure node for the generation of cell spheroid has a theoretical magnitude of 0. In this experiment, the cell spheroids in the diameter range of about 15 μm to 70 μm were over 90% in viability after at least 7 days of cell culture. This result is in good agreement with previous studies[36,66,67] where the cell spheroids in diameter below 100 μm could survive at a very high percentage (over 85%). However, large cell spheroids may also result in some dead cells at the center after incubation for a long time. Such limitation of spheroid size is dependent on the type of cells and the conditions of cell culture. As for hepatocyte, the mostly viable spheroid diameter could reach about 120-180 μm[66–70]. Since oxygen is difficult to permeate through the thick cell structure, further increase in size results in a depletion of oxygen (hypoxic conditions) and causes cell necrosis in the core of large spheroids[65,71].

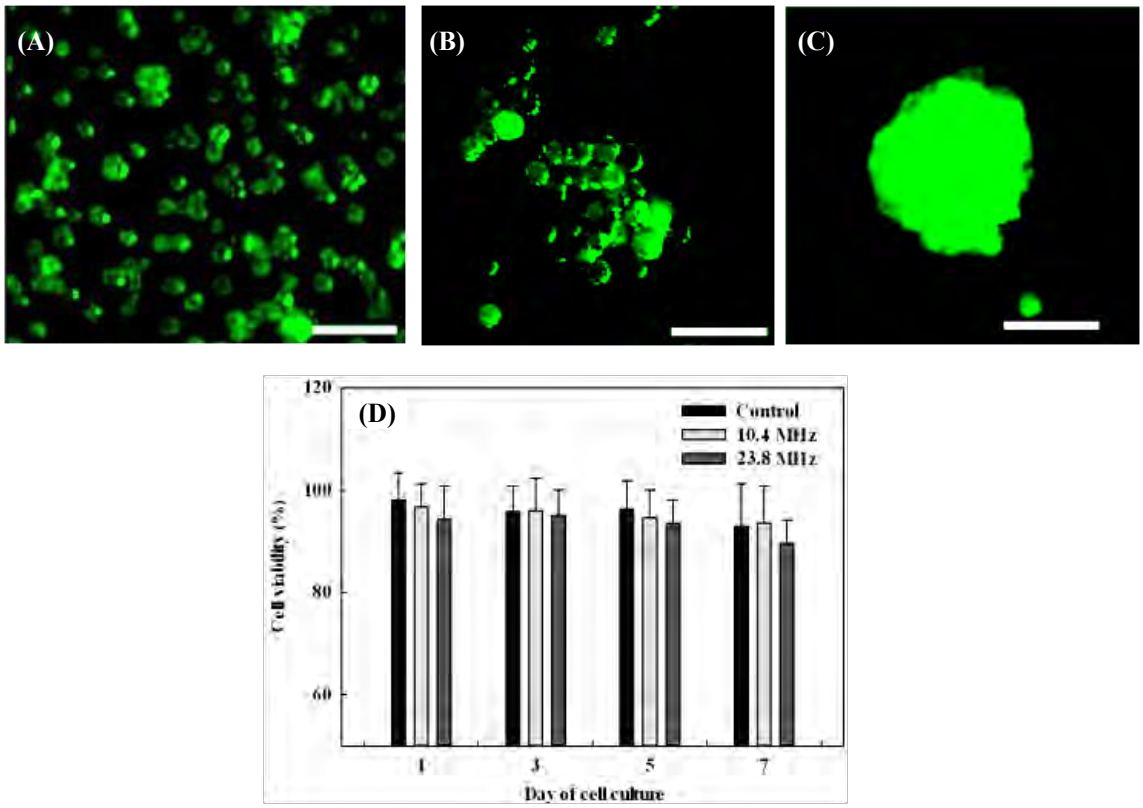

Figure 5. Cells stained with live/dead assay, **(A)** individual HepG2 cellswithout acoustic excitation in the control group, in the formed cell spheroids by the acoustic excitation on **(B)** day 0, **(C)** day 7, and **(D)** thepercentage of cell viability of cells with and without acoustic excitation on day 1, 3, 5, and 7.

4. Conclusion

In this study, the device with PDMS cavity and IDTs to form cell spheroids by SSAW was developed, and its performance was evaluated. The effects of excitation frequency on the accumulation time and the size of cell spheroids immediately after the formation and growth and cell viability after culturing for up to 7 days were studied. The cell accumulation time by SSAW using the high-frequency (23.8 MHz) excitation could be reduced by ~2.5 fold compared to that using the low-frequency (10.4 MHz) frequency excitation in the simulation. Size of cell spheroids formed by the high-frequency excitation is smaller than that by the low-frequency excitation by about 43% on day 0 and 34% on day 7, respectively. The viability of HepG2 cell spheroids is over 90% up to 7 days of cell culture and similar to the control group, which illustrates no influence of acoustic manipulation and suggests the acoustically prepared cell spheroids as good candidate of bioink. In the future, this technology could be applied for various biotechnology applications (*e.g.*, drug testing, tissue engineering, and 3D bioprinting).

Conflict of Interest

No conflict of interest was reported by all the authors.

Acknowledgments

This study was partially funded by Academic Research Fund (AcRF) Tier 1 (RG171/15), Ministry of Education, Singapore, and A*STAR-P&G Biomedical Research Council Strategic Positioning Fund (BMRC SPF, APG 2013/045A).

References

1. Ng W L, Wang S, Yeong W Y, *et al.*, 2016, Skin bioprinting: Impending reality or fantasy? *Trends Biotechnol*, 35(3): 278. http://dx.doi.org/10.1016/j.tibtech.2016.04.006
2. Ng W L, Tan J, Yeong W Y, *et al*., 2018, Proof-of-concept: 3D bioprinting of pigmented human skin constructs. *Biofabrication*, 10.
3. Suntornnond R, Tan E Y S, An J, *et al.*, 2017, A highly printable and biocompatible hydrogel composite for direct printing of soft and perfusable vasculature-like structures. *Sci Rep*, 7(1): 16902. http://dx.doi.org/10.1038/s41598–017–17198–0
4. Olubamiji A D, Izadifar Z, Si J L, *et al.*, 2016, Modulating mechanical behaviour of 3D-printed cartilage -mimetic PCL scaffolds: Influence of molecular weight and pore geometry. *Biofabrication*, 8(2): 025020. http://dx.doi.org/10.1088/1758–5090/8/2/025020
5. Sing S L, An J, Yeong W Y, *et al.*, 2016, Laser and electron-beam powder-bed additive manufacturing of metallic implants: A review on processes, materials and designs. *J Orthop Res*, 34(3): 369–385. http://dx.doi.org/10.1002/jor.23075
6. Zhuang P, Sun A X, An J, *et al.*, 2018, 3D neural tissue models: From spheroids to bioprinting. *Biomaterials*, 154: 113–133. http: //dx. doi. org/ 10.1016/j.biomaterials.2017.10.002
7. Lee J M, Sing S L, Tan E Y S, *et al.*, 2016, Bioprinting in cardiovascular tissue engineering: A review. *Int J Bioprint*,2: 27–36. http://dx.doi.org/10.18063/Ijb.2016.02.006
8. Kolesky D B, Truby R L, Gladman A, *et al.*, 2014, 3D bioprinting of vascularized, heterogeneous cell-laden tissue constructs. *Adv Mater*, 26(19): 3124–3130. http://dx.doi.org/10.1002/adma.201305506
9. Murphy S V, Atala A, 2014, 3D bioprinting of tissues and organs. *Nat Biotechnology*, 32(8): 773–785. http://dx.doi.org/10.1038/nbt.2958
10. Mehrban N, Teoh G Z, Birchall M A, 2016, 3D bioprinting for tissue engineering: Stem cells in hydrogels. *Int J Bioprint*, 2: 6–19. http://dx.doi.org/10.18063/Ijb.2016.01.006
11. Ji S, Guvendiren M, 2017, Recent advances in bioink design for 3D bioprinting of tissues and organs. *Front Bioeng Biotechnol*, 5: 23. http://dx.doi.org/10.3389/fbioe.2017.00023
12. Lin R Z, Chang H Y, 2008, Recent advances in three-dimensional multicellular spheroid culture for biomedical research. *Biotechnol J*, 3(9–10): 1172–1184. http://dx.doi.org/10.1002/biot.200700228
13. Page H, Flood P, Reynaud E G, 2013, Three-dimensional tissue cultures: Current trends and beyond. *Cell Tissue Res*, 352(1): 123–131. http://dx.doi.org/10.1007/s00441–012–1441–5
14. LeCluyse E L, Bullock P L, Parkinson A, 1996, Strategies for restoration and maintenance of normal hepatic structure and function in long-term cultures of rat hepatocytes. *Adv Drug Deliv Rev*, 22(1): 133–186. http://dx.doi.org/10.1016/S0169–409x(96)00418–8
15. Shepherd J A, Kerlikowske K, Ma L, *et al.*, 2011, Volume of mammographic density and risk of breast cancer. *Cancer Epidemiol Biomarkers Prev*, 20(7):1473–1482. http://dx.doi.org/10.1158/1055–9965.EPI–10–1150

16. Yuasa C, Tomita Y, Shono M, *et al.*, 1993, Importance of cell aggregation for expression of liver functions and regeneration demonstrated with primary cultured hepatocytes. *J Cell Physiol*, 156(3):522–530. http://dx.doi.org/10.1002/jcp.1041560311
17. Takabatake H, Koide N, Tsuji T, 1991, Encapsulated multicellular spheroids of rat hepatocytes produce albumin and urea in a spouted bed circulating culture system. *Artif Organs*, 15(6):474–80.
18. Landry J, Bernier D, Ouellet C, *et al.*, 1985, Spheroidal aggregate culture of rat liver cells: Histotypic reorganization, biomatrix deposition, and maintenance of functional activities. *J Cell Biol*, 101(3): 914–923. http://dx.doi.org/https://doi.org/10.1083/jcb.101.3.914
19. Edmondson R, Broglie J J, Adcock A F, *et al.*, 2014, Three-dimensional cell culture systems and their applications in drug discovery and cell-based biosensors. *Assay Drug Dev technol*, 12(4): 207–218. http://dx.doi.org/10.1089/adt.2014.573
20. Imamura Y, Mukohara T, Shimono Y, *et al.*, 2015, Comparison of 2D-and 3D-culture models as drug-testing platforms in breast cancer. *Oncol Rep*, 33(4): 1837–1843. http://dx.doi.org/10.3892/or.2015.3767
21. Xu J S, Ma M W, Purcell W M, 2003, Characterisation of some cytotoxic endpoints using rat liver and HepG2 spheroids as *in vitro* models and their application in hepatotoxicity studies. I. Glucose metabolism and enzyme release as cytotoxic markers. *Toxicol Appl Pharmacol*, 189(2): 112–119. http://dx.doi.org/10.1016/S0041–008x(03)00089–9
22. Mandal B B, Kundu S C, 2009, Cell proliferation and migration in silk fibroin 3D scaffolds. *Biomaterials*, 30(15): 2956–2965. http://dx.doi.org/10.1016/j.biomaterials.2009.02.006
23. Young E W, Beebe D J, 2010, Fundamentals of microfluidic cell culture in controlled microenvironments. *Chem Soc Rev*, 39(3): 1036–1048. http://dx.doi.org/10.1039/b909900j
24. Norotte C, Marga F S, Niklason L E, *et al.*, 2009, Scaffold-free vascular tissue engineering using bioprinting. *Biomaterials*, 30(30): 5910–5917. http://dx.doi.org/10.1016/j.biomaterials.2009.06.034
25. Ozbolat I T, Yu Y, 2013, Bioprinting toward organ fabrication: Challenges and future trends. *IEEE Trans Biomed Eng*, 60(3): 691–699. http://dx.doi.org/10.1109/TBME. 2013.2243912
26. Lee J, Sato M, Kim H, *et al.*, 2011, Transplantation of scaffold-free spheroids composed of synovium-derived cells and chondrocytes for the treatment of cartilage defects of the knee. *Eur Cell Mater*, 22: 275–290. http://dx.doi.org/https://doi.org/10.22203/ecm.v022a21
27 Timmins N E, Dietmair S, Nielsen L K, 2004, Hanging-drop multicellular spheroids as a model of tumour angiogenesis. *Angiogenesis*, 7(2): 97–103. http://dx.doi.org/10.1007/s10456–004–8911–7
28. Albrecht D R, Underhill G H, Wassermann T B, *et al.*, 2006, Probing the role of multicellular organization in three-dimensional microenvironments. *Nat Methods*, 3(5):369–375. http://dx.doi.org/10.1038/nmeth873
29. Souza G R, Molina J R, Raphael R M, *et al.*, 2010, Three-dimensional tissue culture based on magnetic cell levitation. *Nat Nanotechnol*, 5(4): 291–296, http://dx.doi.org/10.1038/nnano.2010.23
30. Ingram M, Techy G B, Saroufeem R, *et al.*, 1997, Three-dimensional growth patterns of various human tumor cell lines in simulated microgravity of a NASA bioreactor. *In Vitro Cell Dev Biol Anim*, 33(6): 459–466. http://dx.doi.org/10.1007/s11626–997–0064–8
31. Napolitano A P, Chai P, Dean D M, *et al.*, 2007, Dynamics of the self-assembly of complex cellular aggregates on micromolded nonadhesive hydrogels. *Tissue Eng*, 13(8): 2087–2094. http://dx.doi.org/10.1089/ten.2006.0190
32. Semino C E, Merok J R, Crane G G, *et al.*, 2003, Functional differentiation of hepatocyte-like spheroid structures from putative liver progenitor cells in three-dimensional peptide scaffolds. *Differentiation*, 71(4–5): 262–270. http://dx.doi.org/10.1046/j.1432–0436.2003.7104503.x
33. Ng W L, Lee J M, Yeong W Y, *et al.*, 2017, Microvalve-based bioprinting–Process, bio-inks and applications. *Biomater Sci*,5(4): 632–647. http://dx.doi.org/10.1039/c6bm00861e
34. Faulkner-Jones A, Greenhough S, King J A, *et al.*, 2013, Development of a valve-based cell printer for the formation of human embryonic stem cell spheroid aggregates. *Biofabrication*, 5(1): 015013. http://dx.doi.org/10.1088/1758–5082/5/1/015013
35. Bazou D, Kearney R, Mansergh F, *et al.*, 2011, Gene expression analysis of mouse embryonic stem cells following levitation in an ultrasound standing wave trap. *Ultrasound Med Biol*, 37(2): 321–330. http://dx.doi.org/10.1016/j.ultrasmedbio.2010.10.019
36 Chen K, Wu M, Guo F, *et al.*, 2016, Rapid formation of size-controllable multicellular spheroids *via* 3D acoustic tweezers. *Lab Chip*, 16(14): 2636–2643. http://dx.doi.org/10.1039/c6lc00444j

37. Collins D J, Morahan B, Garcia-Bustos J, *et al.*, 2015, Two-dimensional single-cell patterning with one cell per well driven by surface acoustic waves. *Nat Commun*, 6: 8686. http://dx.doi.org/10.1038/ncomms9686
38. Wiklund M, 2012, Acoustofluidics 12: Biocompatibility and cell viability in microfluidic acoustic resonators. *Lab Chip*, 12(11): 2018–2028. http://dx.doi.org/10.1039/c2lc40201g
39. Ohlin M, Iranmanesh I, Christakou A E, *et al.*, 2015, Temperature-controlled MPa-pressure ultrasonic cell manipulation in a microfluidic chip. *Lab Chip*, 15(16): 3341–3349. http://dx.doi.org/10.1039/c5lc00490j
40. Glynne-Jones P, Hill M, 2013, Acoustofluidics 23: Acoustic manipulation combined with other force fields. *Lab Chip*, 13(6): 1003–1010. http://dx.doi.org/10.1039/c3lc41369a
41. Bruus H, 2012, Acoustofluidics 7: The acoustic radiation force on small particles. *Lab Chip*, 12(6): 1014–1021. http://dx.doi.org/10.1039/c2lc21068a
42. Sriphutkiat Y, Zhou Y, 2017, Particle manipulation using standing acoustic waves in the microchannel at dual-frequency excitation: Effect of power ratio. *Sensor Actuat A Phys*, 263: 521–529. http://dx.doi.org/10.1016/j.sna.2017.07.023
43. Burgess A, Vigneron S, Brioudes E, *et al.*, 2010, Loss of human Greatwall results in G2 arrest and multiple mitotic defects due to deregulation of the cyclin B-Cdc2/PP2A balance. *Pro Nati Acad Sci*, 107(28): 12564–12569. http://dx.doi.org/10.1073/pnas.0914191107
44. McCloy R A, Rogers S, Caldon C E, *et al.*, 2014, Partial inhibition of Cdk1 in G2 phase overrides the SAC and decouples mitotic events. *Cell Cycle*, 13(9): 1400–1412. http://dx.doi.org/10.4161/cc.28401
45. Cui X, Hartanto Y, Zhang H, 2017, Advances in multicellular spheroids formation. *J R Soc Interface*, 14: 20160877.
46. Chen Y, Li P, Huang P H, *et al.*, 2014, Rare cell isolation and analysis in microfluidics. *Lab Chip*, 14(4): 626–645. http://dx.doi.org/10.1039/c3lc90136j
47. Ding X, Peng Z, Lin S C, *et al.*, 2014, Cell separation using tilted-angle standing surface acoustic waves. *Pro Nati Acad Sci USA*, 111(36): 12992–12997. http://dx.doi.org/10.1073/pnas.1413325111
48. Sriphutkiat Y, Zhou Y, 2017, Particle accumulation in a microchannel and its reduction by a standing surface acoustic wave (SSAW). *Sensors*, 17(1): 106. http://dx.doi.org/10.3390/s17010106
49. Hartono D, Liu Y, Tan P L, *et al.*, 2011, On-chip measurements of cell compressibility *via* acoustic radiation. *Lab Chip*, 11(23): 4072–4080. http://dx.doi.org/10.1039/c1lc20687g
50. Nama N, Barnkob R, Mao Z, *et al.*, 2015, Numerical study of acoustophoretic motion of particles in a PDMS microchannel driven by surface acoustic waves. *Lab Chip*, 15(12): 2700–2709. http://dx.doi.org/10.1039/c5lc00231a
51. Burguillos M A, Magnusson C, Nordin M, *et al.*, 2013, Microchannel acoustophoresis does not impact survival or function of microglia, leukocytes or tumor cells. *Plos One*, 8: e64233. http://dx.doi.org/10.1371/journal.pone.0064233
52. Ding X Y, Shi J J, Lin S C S, *et al.*, 2012, Tunable patterning of microparticles and cells using standing surface acoustic waves. *Lab Chip*, 12(14): 2491–2497. http://dx.doi.org/10.1039/c2lc21021e
53. Devendran C, Albrecht T, Brenker J, *et al.*, 2016, The importance of travelling wave components in standing surface acoustic wave (SSAW) systems. *Lab Chip*, 16(19): 3756–3766. http://dx.doi.org/10.1039/c6lc00798h
54. Squires T, 2005, Microfluidics: Fluid physics at the nanoliter scale. *Rev Mod Phys*, 7(3): 977–1026. http://dx.doi.org/10.1103/RevModPhys.77.977
55. Lee P J, Hung P J, Rao V M, *et al.*, 2006, Nanoliter scale microbioreactor array for quantitative cell biology. *Biotechnol Bioeng*, 94(1): 5–14. http://dx.doi.org/10.1002/bit.20745
56. Wang Z, Kim M C, Marquez M, *et al.*, 2007, High-density microfluidic arrays for cell cytotoxicity analysis. *Lab Chip*, 7(6): 740–745. http://dx.doi.org/10.1039/b618734j
57. Melchels F P, Barradas A M, van Blitterswijk C A, *et al.*, 2010, Effects of the architecture of tissue engineering scaffolds on cell seeding and culturing. *Acta Biomater*, 6(11): 4208–4217. http://dx.doi.org/10.1016/j.actbio.2010.06.012
58 Lichtner R B, Schirrmacher V, 1990, Cellular distribution and biological activity of epidermal growth factor receptors in A431 cells are influenced by cell-cell contact. *J Cell Physiol*, 144(2): 303–312. http://dx.doi.org/10.1002/ jcp.1041440217
59. Henry C, Minier J P, Lefevre G, 2012, Towards a description of particulate fouling: From single particle deposition to clogging. *Adv Colloid Interface Sci*, 185–186: 34–76. http://dx.doi.org/10.1016/j.cis.2012.10.001
60. Mustin B, Stoeber B, 2016, Single layer deposition of polystyrene particles onto planar polydimethylsiloxane substrates. *Langmuir*, 32(1): 88–101. http://dx.doi.org/10.1021/ acs. langmuir.5b02914

61 Devendran C, Albrecht T, Brenker J, *et al.*, 2016, The importance of travelling wave components in standing surface acoustic wave (SSAW) systems. *Lab Chip*, 16(19): 3756–3766. http://dx.doi.org/10.1039/c6lc00798h

62. Drasdo D, Hohme S, 2005, A single-cell-based model of tumor growth *in vitro*: Monolayers and spheroids. *Phys Biol*, 2(3): 133–147. http://dx.doi.org/10.1088/1478-3975/2/3/001

63. Engelberg J A, Ropella G E, Hunt C A, 2008, Essential operating principles for tumor spheroid growth. *BMC Syst Biol*, 2: 110. http://dx.doi.org/10.1186/1752–0509–2–110

64. Zanoni M, Piccinini F, Arienti C, *et al.*, 2016, 3D tumor spheroid models for *in vitro* therapeutic screening: A systematic approach to enhance the biological relevance of data obtained. *Sci Rep*, 6: 19103. http://dx.doi.org/10.1038/srep19103

65. Anada T, Fukuda J, Sai Y, *et al.*, 2012, An oxygen-permeable spheroid culture system for the prevention of central hypoxia and necrosis of spheroids. *Biomaterials*, 33(33): 8430–8441. http://dx.doi.org/10.1016/j.biomaterials.2012.08.040

66. Glicklis R, Merchuk J C, Cohen S, 2004, Modeling mass transfer in hepatocyte spheroids via cell viability, spheroid size, and hepatocellular functions. *Biotechnol Bioeng*, 86(6): 672–680. http://dx.doi.org/10.1002/bit.20086

67. Lee J, Cuddihy M J, Cater G M, *et al.*, 2009, Engineering liver tissue spheroids with inverted colloidal crystal scaffolds. *Biomaterials*, 30(27): 4687–4694. http://dx.doi.org/10.1016/j.biomaterials.2009.05.024

68. Curcio E, Salerno S, Barbieri G, *et al.*, 2007, Mass transfer and metabolic reactions in hepatocyte spheroids cultured in rotating wall gas-permeable membrane system. *Biomaterials*, 28(36): 5487–5497. http://dx.doi.org/10.1016/j.biomaterials.2007.08.033

69. Fukuda J, Okamura K, Nakazawa K, *et al.*, 2003, Efficacy of a polyurethane foam/spheroid artificial liver by using human hepatoblastoma cell line (Hep G2). *Cell Transplant*, 12(1): 51–58. http://dx.doi.org/10.3727/000000003783985151

70. Tamura T, Sakai Y, Nakazawa K, 2008, Two-dimensional microarray of HepG2 spheroids using collagen/polyethylene glycol micropatterned chip. *J Mater Sci Mater M*, 19(5): 2071–2077. http://dx.doi.org/10.1007/s10856–007–3305–1

71. Hirschhaeuser F, Menne H, Dittfeld C, *et al.*, 2010, Multicellular tumor spheroids:An underestimated tool is catching up again. *JBiotechnol*, 148(1):3–15. http://dx.doi.org/10.1016/j.jbiotec.2010.01.012

INTERNATIONAL JOURNAL OF BIOPRINTING

ISSN (print): 2424-7723

ABOUT THE JOURNAL

International Journal of Bioprinting is a biannual, double-blind peer-reviewed, open access journal. This journal focuses on the use of 3D printing technology with materials that incorporate viable living cells or biological elements to produce tissue or biotechnological products. Further discourses and technological advancements in bioprinting are the goals behind acceptance of high-quality basic and applied research: from concept creation to fabrication of the bioprinting process, associated clinical applications as well as social implications.

Whioce Publishing, official publisher for the journal welcomes researchers to submit their papers relevant to bioprinting for consideration via **http://ijb.whioce.com/** For general enquiries and order for prints and reprints, please write in to **IJB@whioce.com** for a fast response.

SUBMIT YOUR PAPERS HERE

WHIOCE
PUBLISHING PTE. LTD.

ABOUT THE PUBLISHER

Whioce Publishing in Singapore is a registered publisher of excellent quality academic journals for an international readership. We deliver exceptional editorial support for the advancement and dissemination of scientific research by linking readers and researchers with networks and industries. We have ambitions to get our journals indexed in prominent databases such as EI, SCI, SSCI and AHCI, thereby aiming to be a first-class knowledge platform for researchers worldwide.

Whioce Publishing also engages in publishing e-books, organizing academic conferences and educational trainings, and providing translational services.

International Journal of Bioprinting is an
independent open access journal published
by Whioce Publishing Pte.Ltd.

WHIOCE PUBLISHING PTE. LTD.
PROVIDING
FIRST-CLASS SCIENTIFIC INFORMATION
FOR TOP SCHOLARS

Whioce Publishing Pte.Ltd.
7030 Ang Mo Kio Avenue 5
#04-15 Northstar@AMK
Singapore 569880
Tel: +65 65702707/65702718
Fax: +65 65702803

See **www.whioce.com/contact** for a full list of offices and contact information.

Whioce Publishing Pte.Ltd. is a company registered in Singapore (No. 201427293E), whose registered office is at 7030 Ang Mo Kio Avenue 5 #04-15 Northstar@AMK Singapore 569880